UNIVERSITÀ DEGLI STUDI DI CAMERINO

School of Advanced Studies

DOCTORAL COURSE IN

Chemical Science

XXXIV cycle

NEW METAL COMPLEXES AND METAL-ORGANIC FRAMEWORKS (MOFS) WITH POTENTIAL BIOLOGICAL APPLICATIONS

PhD Student

Chuanpan Guo

Supervisors

Prof. Fabio Marchetti

Co-supervisors

Prof. Zhihong Zhang

CONTENT

Abbreviations……..……7

CHAPTER 1: Introduction 11

1.1 Metal complexes and MOFs for antibacterial applications 12

1.1.1 Metal complexes for antibacterial applications..... 13

1.1.2 MOF-based materials for antibacterial applications..... 22

1.2 MOF-based platforms for biosensors 29

1.2.1 Monometallic MOF 31

1.2.2 MOF-based composites 33

1.2.3 MOF-based heterostructures 35

1.2.4 MOFs-based derivatives 37

CHAPTER 2: Synthesis, characterization and antibacterial activity of silver(I) complexes with acylpyrazolone ligands 41

2.1 Introduction..... 42

2.2 Experimental section 43

2.2.1 Basic characterizations 43

2.2.2 Synthesis of silver complexes 44

2.2.3 Antimicrobial activity..... 49

2.3 Results and discussion 50

2.3.1 Synthesis and spectroscopy characterization of silver complexes 50

2.3.2 Evaluation of antibacterial activity..... 55

2.4 Conclusion..... 56

CHAPTER 3: Synthesis of neutral and cationic silver(I) phosphino-complexes with pyrazolone ligands 58

3.1 Introduction 59

3.2 Experimental section 59

3.2.1 Basic characterizations 60

3.2.2 Synthesis of silver complexes 60

3.3 Results and discussion 66

3.4 Conclusion 72

CHAPTER 4: Copper-based polymer-metal-organic framework embedded with Ag nanoparticles: long-acting and intelligent antibacterial activity and accelerated wound healing 73

4.1 Introduction 74

4.2 Experimental section 77

4.2.1 Chemicals and regents 77

4.2.2 Synthesis of the polymer ligand 78

4.2.3 Preparation of polyCu-MOF and Cu-MOF 80

4.2.4 Preparation of polyCu-MOF@AgNPs and Cu-MOF@AgNPs hybrids 81

4.2.5 Basic characterizations 81

4.2.6 *In vitro* antibacterial effect 82

4.2.7 Bacterial morphological studies 84

4.2.8 Release behaviors of Cu^{2+} and Ag^{+} ions *in vitro* 84

4.2.9 Detection of the intracellular ROS level 85

4.2.10 Cytotoxicity assay and hemolysis assay *in vitro* 85

4.2.11 Wound disinfection and healing assay *in vivo* 86

4.2.12 Statistical analysis..... 87

4.3 Results and discussion 88

4.3.1 Basic characterizations of polyCu-MOF@AgNPs..... 88

4.3.2 Antibacterial property of polyCu-MOF@AgNPs 100

4.3.3 Antibacterial mechanism of polyCu-MOF@AgNPs.....107

4.3.4 *In vitro* biocompatibility 112

4.3.5 Wound disinfection and healing assay *in vivo* 114

4.4 Conclusion.....117

CHAPTER 5: Semiconductive Cu_xNi_{3-x}(hexahydroxytriphenylene)$_2$ framework for electrochemical aptasensing of C6 glioma cells and epidermal growth factor receptor.....119

5.1 Introduction.....120

5.2 Experimental section 123

5.2.1 Reagents and materials 123

5.2.2 Preparation of $Cu_3(HHTP)_2$, $Ni_3(HHTP)_2$, and $Cu_xNi_{3-x}(HHTP)_2$ 123

5.2.3 Pre-treatment of the bare AE.....124

5.2.4 Preparation of solutions 124

5.2.5 Electrochemical measurements 125

5.2.6 Fabrication of electrochemical aptasensors 126

5.2.7 Real samples.....128

5.2.8 Cytotoxicity and *in vitro* cell uptake 128

5.3 Results and discussion 129

5.3.1 Characterizations of $Cu_3(HHTP)_2$, $Ni_3(HHTP)_2$, and $Cu_xNi_{3-x}(HHTP)_2$ ...129

5.3.2 Biocompatibility of $Cu_3(HHTP)_2$, $Ni_3(HHTP)_2$ and $Cu_xNi_{3-x}(HHTP)_2$.....136

5.3.3 Electrochemical sensing performances of 2D MOFs toward C6 cells 137

5.3.4 Selectivity of the $Cu_xNi_{3-x}(HHTP)_2$-based cytosensor toward C6 cells 142

5.3.5 Detection of C6 cells using the $Cu_xNi_{3-x}(HHTP)_2$-based cytosensor 144

5.3.6 EGFR sensing performances of the $Cu_xNi_{3-x}(HHTP)_2$-based aptasensor..150

5.4 Conclusion.....155

CHAPTER 6: Structural hybridization of bimetallic zeolitic imidazolate framework (ZIF) nanosheets and carbon nanofibers for efficiently sensing α-synuclein oligomers.....157

6.1 Introduction.....158

6.2 Experimental section 160

6.2.1 Materials and reagents 160

6.2.2 Synthesis of CNF and the series of CoMn-ZIF@CNF nanohybrids.....161

6.2.3 Development of the series of CoMn-ZIF@CNF-based aptasensors 162

6.2.4 Electrochemical measurements 163

6.3 Results and discussion 164

6.3.1 Basic characterizations of CoMn-ZIF@CNF nanohybrids 164

6.3.2 Electrochemical sensing performances of the series of CoMn-ZIF@CNF nanohybrids.....174

6.3.3 Optimization of sensing performances for α-Syn oligomers detection 180

6.3.4 Detection sensitivity of the CoMn-ZIF@CNF(1-3)-based aptasensor.....183

6.3.5 Selectivity, reproducibility, stability, and regeneration of the CoMn-ZIF@CNF(1-3)-based aptasensor.....185

6.4 Conclusion.....189

References.....190

List of pubulications 205

Acknowledgements…….207

Abbreviations

MOFs	metal−organic framework
$^1O_2$	singlet oxygen
ROS	reactive oxygen species
Ag NPs	silver nanoparticles
MIC	minimum inhibitory concentrations
NHC	*N*-heterocyclic carbene
Van	vancomycin
PDT	photodynamic therapy
PTT	photothermal therapy
ZIF	zeolitic imidazolate framework
PEG	polyethylene glycol
CCM	curcumin
HA	hyaluronic acid
CS	chitosan
NO	nitric oxide
PB	Prussian blue
NIR	near-infrared
AChE	acetylcholinesterase
GH	galantamine hydrobromide
LOD	limit of detection
l-Tyr	l-tyrosine
MUC1	mucin 1
EIS	electrochemical impedance spectroscopy
SPR	surface plasmon resonance
CEA	carcinoembryonic antigen
CNTs	carbon nanotubes
HQ	hydroquinone
CC	catechol

FE-SEM	field emission scanning electron microscope
H1N1	influenza A virus
SARS-CoV2	severe acute respiratory syndrome coronavirus 2
CDs	carbon dots
HER2	human epidermal growth factor receptor-2
MCF-7 cells	breast cancer cells
AuNPs	gold nanoparticles
PTK7	protein tyrosine kinase-7
CA125	carbohydrate antigen 125
PAN	polyacrylonitrile
GNF	graphene-like nanofiber
OPN	osteopontin
HIV-1	human immune deficiency virus-1
HHTP	2,3,6,7,10,11-hexahydroxytriphenylene
EGFR	epidermal growth factor receptor
α-Syn	α-synuclein
CNFs	carbon nanofibers
ESI-MS	electrospray mass spectra
TGA	thermal gravimetric analysis
DMSO	dimethyl sulfoxide
DMF	*N, N*-dimethylformamide
LB	Luria-Bertani
H_2BDC	1,4-benzenedicarboxylic acid
H_2-DCFDA	2′,7′- dichlorodihydrofluorescein diacetate
PXRD	power X-ray diffraction
FT-IR	Fourier transform infrared
XPS	X-ray photoelectron spectroscopy
HR-TEM	high-resolution transmission electron microscopy

EDS	energy dispersive spectrometer
BET	Brunauer-Emmett-Teller
OD_{600}	optical density at 600 nm
Calcein-AM	calcein acetoxymethyl ester
PI	propidium iodide
CLSM	confocal laser scanning microscope
PBS	phosphate buffer solution
ICP-AES	inductively-coupled plasma atomic emission spectrometry
H&E	hematoxylin and eosin
SAED	diffraction patterns
BEs	binding energies
$\bullet O_2^-$	superoxide
H_2O_2	hydrogen peroxide
•OH	hydroxyl radical
H_2-DCF	dichlorodihydrofluorescein
MTT	3-(4, 5-dimethylthiazol-2-yl)-2, 5-diphenyltetrazolium bromide
DMEM	Dulbecco's Modified Eagle's Medium
L929 cells	normal cells of mice
AE	gold electrode
IgG	immunoglobulin G
BSA	bovine serum albumin
VEGF165	vascular endothelial growth factor 165
AFP	alpha fetoprotein
CA 199	carbohydrate antigen 199
IUPAC	International Union of Pure and Applied Chemistry
CV	cyclic voltammetry

R_s	solution resistance
R_{ct}	charge-transfer resistance
CPE	constant-phase element
W_o	Warburg impedance
DPV	differential pulse voltammetry
PD	Parkinson’s disease
ELISA	enzyme-linked immunosorbent assay
LSPR	localized surface plasmon resonance

CHAPTER 1

Introduction

As a cornerstone of synthetic chemistry, the coordination of organic ligands to ions/clusters has been used to prepare many types of materials, including metal complexes, metal–organic polyhedral, porous coordination polymers, porous coordination networks, and metal–organic frameworks (MOFs) [1]. These metal–organic materials are assembled by metal coordination, hydrogen bonding, electrostatic interactions or π–π stacking [2], exhibiting tunable structures, compositions and properties. Therefore, they are considered as promising candidates in the fields of catalysis, gas adsorption and separation, sensors, functional devices, etc [3]. Notably, biomedical applications have greatly benefited from the progress made by these metal–organic materials in the fields of diagnosis, monitoring, and therapy. Some of the biomedical applications of metal–organic materials include biosensors, biocatalysis, bioimaging, drug delivery, anticancer, antibacterial, and wound healing. This part mainly focuses on different types of metal complexes and MOFs for biomedical applications, specifically, for antibacterial and biosensing applications.

1.1 Metal complexes and MOFs for antibacterial applications

Bacteria are unicellular prokaryotic organisms that are usually only a few micrometers in size and are habit everywhere on Earth and even in extreme environments [4]. According to the structure of the cell wall, bacteria can be divided into two main groups: Gram-negative and Gram-positive [5] bacteria. Most Gram-negative bacteria and some Gram-positive bacteria are pathogenic to humans.

Gram-negative bacteria, with their unique outer membrane, have a thinner peptidoglycan layer than Gram-positive bacteria [6]. Therefore, the two types of bacteria have different tolerance to antibacterial agents. Bacterial infections have always plagued humans and have become one of the most serious public health problems. Despite tremendous advances in modern medicine, bacterial infections still claim about 1.5 million lives each year. In particular, some drug-resistant bacteria have developed compensatory mechanisms to resist antibiotics [7]. Therefore, more efforts are needed to develop new and effective antibacterial agents to protect humans from bacterial infections.

1.1.1 Metal complexes for antibacterial applications

The biological activity of metal complexes has been the subject of numerous studies, especially in the field of antibacterial, due to their prominent advantages [8]. For example, the steric and electronic properties of metal complexes can be tuned by modifying their ligands. In addition, metal complexes can undergo ligand exchange reactions with certain biomolecules [9]. Therefore, metal complexes can provide different antibacterial mechanisms compared to conventional organic antibiotics [10]. The antibacterial mechanisms of metal complexes are often multimodal, which is advantageous for overcoming drug resistance in bacteria. Specifically, they are (1) direct inhibition of protein by metal ions, (2) exchange or release of ligands, (3) generation of singlet oxygen ($^1O_2$) upon photoactivation, (4) generation of reactive oxygen species (ROS), and (5) redox activation and catalytic generation of toxic

species [11]. Many metal complexes have been synthesized, including vanadium, chromium, cadmium, manganese, iron, cobalt, nickel, copper, zinc, palladium, platinum, iridium, and ruthenium. For transition metal ions in the first row, ligand substitution generally occurs more rapidly than elements in the second and third rows. This may indicate that these compounds react more rapidly with components of the medium and are unable to enter bacterial cells [12].

1.1.1.1 Silver-based antibacterial agents

Silver ions and/or silver nanoparticles (Ag NPs) demonstrate excellent antibacterial properties, and can served as metallodrugs in weakening cell wall or interfere with transcription of bacterial DNA, further killing bacteria [13]. Ag-based complexes can not only effectively prevent Ag NPs form agglomerating, but also release Ag ions for a long period of time, thus achieving a sustained antibacterial effect. So far, various Ag complexes have been designed and prepared and further employed as antibacterial agents.

For instance, the antibacterial activity of $[Ag(L)_2(NO_3)]$ (**I**) (L=nicotinaldehyde (3-pyridinecarboxaldehyde)) against bacteria was evaluated by minimum inhibitory concentrations (MIC) and disk diffusion methods [14]. According to the results, the $[Ag(L)_2(NO_3)]$ exhibits a wider spectrum of antimicrobial activities due to the weak metal–ligand bonding (Ag(I)–N and Ag(I)–O). Moreover, another antibacterial agent of $[Ag_2(L)_2](CF_3SO_3)$ (**II**) (L= 2,6-bis(benzothiazole)-pyridine) was prepared, and the antibacterial activity against *Staphylococcus epidermidis* and *Acinetobacter baumannii* was evaluated [15]. The result inflicts that $[Ag_2(L)_2](CF_3SO_3)$ shows more

antimicrobial actions against both types of bacteria, which is attributed to the negative surface potential of bacterial cell walls facilitating the passage of the cationic complexes.

Further, some active molecules also possess intrinsic antibacterial activity, including sulfathiazole, sulfamethoxazole, mafenide, amprenavir, and sulfasalazine. The coordination between metal ions and these active molecules is a promising way to enhance antimicrobial and antiviral activities. For example, [Ag(eMaf)] (**III**) (eMaf=ethyl-mafenide) was prepared by coordination of Ag and ethyl-mafenide through the nitrogen and oxygen atoms in the deprotonated sulfonamide group (SO_2NH). The antibacterial activity of Ag(eMaf) was evaluated against aerobic bacteria, such as *Staphylococcus aureus*, *Burkholderia cepacia*, *S. epidermidis*, and *Pseudomonas aeruginosa* [16]. The MIC values of [Ag(eMaf)] against aerobic bacterial strains *S. aureus*, *B. cepacia*, *S. epidermidis* and *P. aeruginosa* ranged from 21.3 to 170 μmol L^{-1}.

Moreover, stabilization of transition-metal catalysis in various oxidation states during biological activities is critical for the complex. Accordingly, *N*-heterocyclic carbene (NHC) possess good stability thanks to the two existing binds of π- and σ-bond. Two types of Ag(I)-NHC complexes of $[Ag(L_1)_2(Cl)]$ and $[Ag(L_2)_2(Cl)]$ (**IV**) (L_1= 1-methyl-3-(2,5-dimethylphenyl)-acetamideimidazolium,

L_2= 1-benzyl-3-(2,5-dimethylphenyl)-acetamideimidazolium) from the reaction of Ag_2O with the ligands were developed [17]. The antibacterial activity was assessed against *S. aureus* and *Escherichia coli* using azithromycin as a standard antibiotic.

Among them, $[Ag(L_1)_2(Cl)]$ presented better antibacterial activity, which might be due to the change of N-substituents on the ligand would affect the stability of the complexes. The enhancement of sustained release of Ag^+ ions induces by the stability changes is important for the inhibition of bacterial growth. Similarly, $[Ag(L)(PF_6)]$ (**V**) (L= 1,4-bis(3-cyanobenzylbenzimidazol-1-ylmethyl)benzene) was synthesized by reacting the hexafluorophosphate salts with Ag_2O, and the antibacterial activity against *S. aureus* and *E. coli* was determined in comparison with that of $AgNO_3$ and ciprofloxacin [18]. $[Ag(L)(PF_6)]$ had better antibacterial performance compared to silver nitrate, and the MIC values of the complexes against both bacterial strains were in the range of 25–100 μg mL^{-1}.

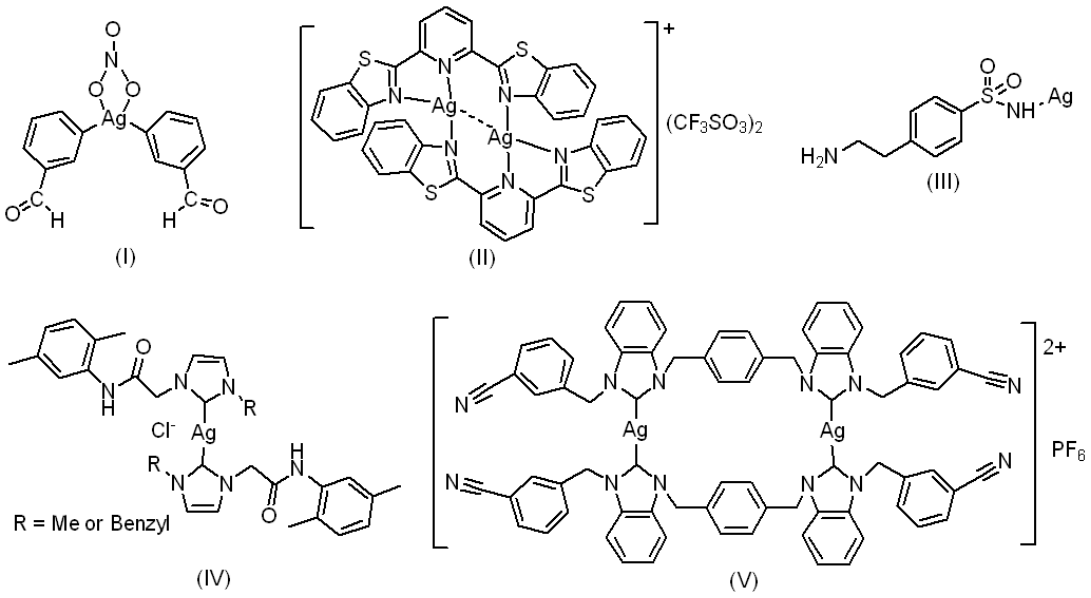

Figure 1. Structure of antibacterial silver complexes [I-V].

1.1.1.2 Copper-based antibacterial agents

Similar to Ag-based complexes as antibacterial agents, cooper-based antibacterial complexes also attract more attention. For example, copper complexes can bind to the

N-7 guanine residue of DNA and further break the DNA strand. Moreover, the ligands composed of metal complexes also have antibacterial activity against bacteria. A Cu (II) complex CuL (**VI**) (L= (E)-2-((2,4-dihydroxybenzylidene)amino)-3-(1H-indol-3-yl)propanoic acid Schiff base) was proposed and investigated for its antibacterial activity against *P. aeruginosa* and *E. co*li [19]. The inhibition of bacterial growth is attributed to the enhanced lipophilic character of the central metal ion by chelating ligand with metal ion. This facilitates subsequent penetration through the lipid layer of the cell membrane.

The stereoelectronic properties of the metal complexes can be adjusted to achieve the specific purposes by introducing substitutions with different electronegativity and size. Additionally, metal complexes prepared by partially replacing the ligands with others are a new strategy for constructing specifically designed complexes. A $[Cu(L^1)(phen)]ClO_4$ (**VII**) (L^1 = NN'O type unsymmetrical tridentate Schiff base ligand, phen=1,10-phenanthroline) was designed and synthesized using $Cu(ClO_4)_2 \cdot 6H_2O$ and co-ligands [20]. The antibacterial test against *S. aureus*, *B. subtilis*, *Salmonella typhi*, and *E. coli* showed that the $[Cu(L^1)(phen)]ClO_4$ complex exhibited higher activity compared to $Cu(ClO_4)_2 \cdot 6H_2O$, indicating that the presence of the ligands is essential for increasing the lipophilicity.

The N- and O- donor sites involve in ligands endow the metal complex with tunable steric and electronic coordination environments on the metal center, affording its excellent antibacterial properties [21]. Two new types of $[Cu(L_1)_2]$ (**VIII**) and $[Cu(L_2)_2]$ (**IX**) (L=Schiff base ligands) were prepared and evaluated for their

antibacterial activity against *Chromobacterium violaceum*, *Shigella flexneri*, *S. aureus*, *P. aeruginosa* and *Streptococcus pyogenes* in comparison with those of the ligand [22]. The two Cu(II) complexes showed more efficient antibacterial activity against all bacterial species than their ligands and the standard drug amikacin. In particular, the MIC values of $[Cu(L_2)_2]$ are lower than those of $[Cu(L_1)_2]$, which may be due to the presence of two extremely hydrophobic t-butyl group in $[Cu(L_2)_2]$.

Moreover, S-donor ligands can also be used to prepare antibacterial agent due to the close structural resemblance to thioamides, which are related to biological systems [23]. Mononuclear complexes with mixed-ligands [CuX(mbtt)(xantphos)] (**X**) (X=Br, I, xantphos=4,5-bis(diphenylphosphano)-9,9-dimethyl-xanthene, mbtt=N-methylbenzothiazole-2-thione) were evaluated for their antibacterial activity against *E. coli*, *Xanthomonas campestris*, *B. subtilis*, and *Bacillus cereus* [24]. Among the compounds, only [CuBr(mbtt)(xantphos)] clearly inhibited the growth of all four bacteria, which was mediated by the generation of ROS and damage to the bacterial membrane. In some cases, the ligand showed no the antibacterial activity. The prepared $[Cu(L)(NO_3)(OH_2)_2]H_2O$ (**XI**) (L=(E)-4-(3-cyano-4,6-dimethylpyridin-2-ylamino)-N'-(1-(2-hydroxyphenyl) ethylidene) benzohydrazide) was evaluated for its antibacterial activity against *E. coli* and *S. aureus* by the well-diffusion method [25]. The ligand possessed very low or almost no antibacterial activity, while the complex showed increased antibacterial activity. This can be attributed to the formation of the complex and the subsequent partially transfer of positive charge to donor atoms in ligand, which induced by the

existence of overlaps between ligands and metal orbitals, further leading to a decreace in the polarity of metal ion. The increased lipophilicity is beneficial to the penetration of complexes into cells, limiting protein synthesis and interfering with cellular respiration.

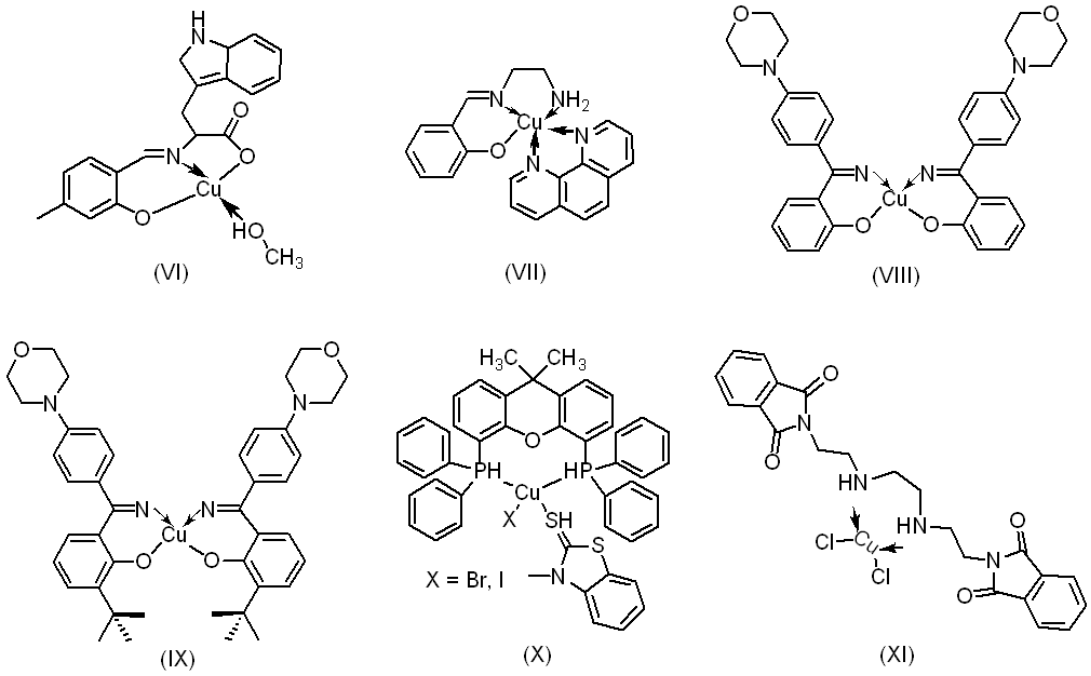

Figure 2. Structure of antibacterial copper complexes [VI-XI].

1.1.1.3 Zinc-based antibacterial agents

The Zn(II) metal ion, a d^{10} electronic system can adopt a versatile coordination number with various types of molecular architectures and topologies that can be produced in the presence of suitable ligands framework. Moreover, the complex containing a thiazole ring shows enhanced biological performance in antibacterial application. A $[Zn(C_{12}H_{10}N_5O_2Cl)Cl_2]$ (**XII**) was employed to text antibacterial activity against *B. subtilis*, *S. aureus*, *P. aeruginosa*, and *E. coli* in comparison to ciprofloxacin. The Zn(II) complexes have good antibacterial properties but less than

ciprofloxacin. The antibacterial activity could be due to the following mechanisms: (a) inhibition of ribonucleoside diphosphate reductase, which supports DNA synthesis; (b) damage to DNA strands by oxidative rupture; (c) by binding to nitrogen bases in DNA to inhibit base replication. A series of metal complexes of type $Zn(L)_2(H_2O)_x$ (**XIII**) (L=2,4-dihalo-6-(substituted thiazol-2-ylimino)methylphenol) were synthesized by employing thiosemicarbazone as primary ligand and heterocyclic nitrogen donor bases as secondary ligand [26]. Both ligands and their complexes exhibited inhibition (MIC > 64 μg mL^{-1}) towards *E. coli* and *S. aureus*. This result may be due to the presence of azomethine and thiazolyl groups in the ligands, which can form hydrogen bonds with the active centers of specific cellular enzymes, thereby interfering with normal cellular processes. The increased activity of complex compared to the free ligand was explained based on chelation theory.

Accordingly, the complexes with specific properties can be prepared by combining imidazole and its derivatives as analogs of nucleic bases, and/or planar aromatic N-containing ligands and its derivatives that are similar to purine and pyrimidine bases. Especially, some complexes can interact with DNA and proteins [27]. Four ternary complexes, $[ZnL_1L_2]$ (L_1=1-((2-hydroxynaphthalen-1-yl)methylene)-4-phenylthiosemicarbazide and L_2=imidazole (**XIV**), 2, 2′-bipyridine (**XV**), 2-methyimidazole (**XVI**) or 4, 4′-bipy (**XVII**)) were synthesized [28]. The antibacterial activity of these complexes were investigated comparison with two standard antibacterial drugs, nalidixic acid and vancomycin (Van). All of these complexes are active, and the antibacterial

mechanisms may include: (1) destruction of cell membranes to alter cell permeability; (2) inactivation of cellular enzymes; (3) denaturation of cellular proteins; (4) interaction with the active biological center of the cell to impair the normal cellular processes. The superior antibacterial activity of complexes **XV** and **XVII** may also be related to the presence of bipyridine, which can impel the complexes to insert into DNA and cause damage.

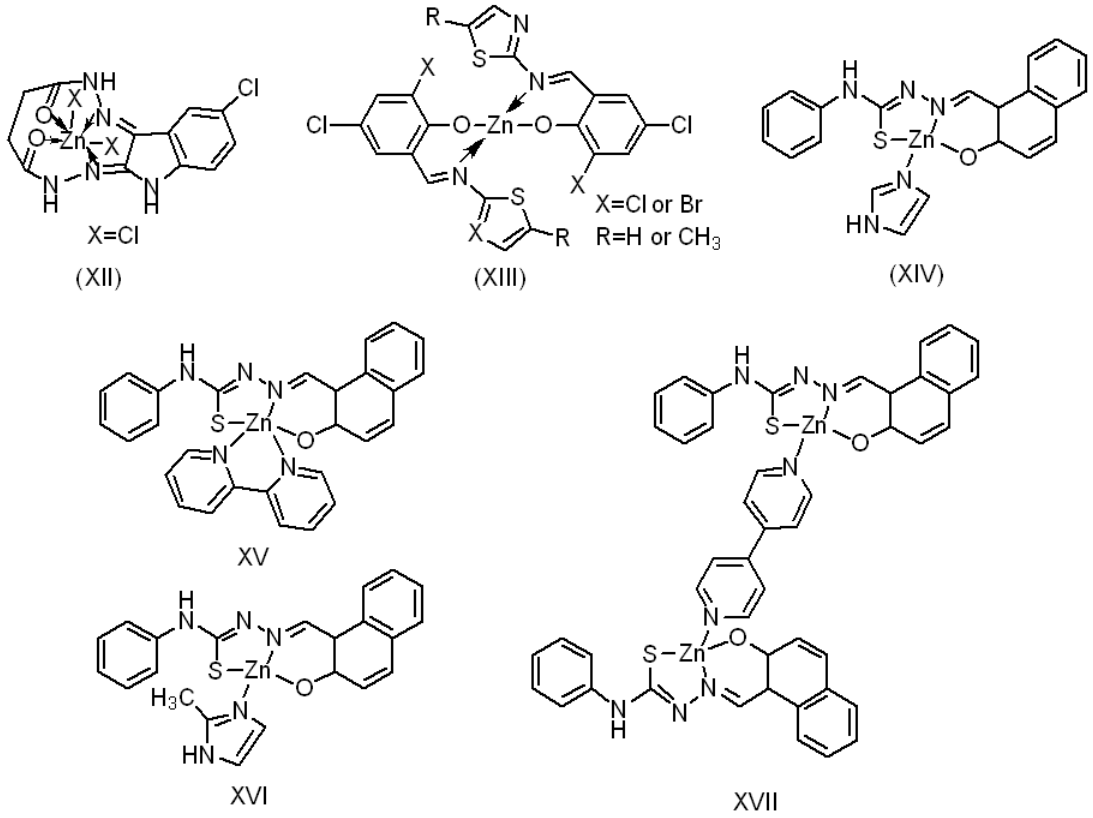

Figure 3. Structure of antibacterial zinc complexes [XII-XVII].

In addition to above mentioned Ag(I), Cu(II), and Zn (II) metal complexes, other metal complexes (such as Mn, Fe, Co, Ni, Ga, Ru, Rh, Pd, Cd, Eu, Re, Ir, Pt, or Au) are also used for antibacterial applications [12]. Amongst, Ru is the most commonly used element with less toxicity to prepare complexes with antibacterial activity,

followed by Ag, Pd and Ir. And only few Ga and Cd complexes have been reported. Pd, Ir, and Pt complexes also show good activities, but these elements are relatively rare and expensive, limiting their use as clinical antibiotics if large doses are required. However, Fe complexes are rarely used as antibacterial agents due to their poor antibacterial activity. The different biological properties and mechanisms of action of each metal complex can be attained, which are depended on the metal ions, ligand, or the geometric shape of complex for the preparation of these metal complexes. Most metal complexes target the cytoplasmic membrane or interfere with protein synthesis, while some metal complexes bind to DNA or directly cause DNA breaks, affecting their antibacterial properties.

1.1.2 MOF-based materials for antibacterial applications

MOFs composed of metal ions and organic linkers are a promising class of porous crystalline materials owning to their large surface area, tunable pore architecture, more effective surface modification, chemical stability and biological activity [29]. Currently, MOFs have attracted more and more attention in the field of antibacterial [30-32]. Compared with other nanomaterials for antibacterial applications, MOFs demonstrate the following advantages: (1) metal nodes in MOFs (such as Ag, Co, Cu, Zn, etc.), which have antibacterial activity and could be gradually released when MOFs degrade, (2) some organic linkers, such as porphyrin and phthalocyanine, which have the potential to combine photodynamic therapy (PDT) and photothermal therapy (PTT) for bacterial infections, (3) the high specific surface

area and porosity facilitate to improve the antibacterial agents loading efficient, (4) stable but degradable structures guarantee the controlled release of antibacterial agents, (5) the free functional groups decorated on MOF surfaces provide opportunities for further functionalization of MOFs, (6) good biocompatibility ensures biosecurity for *in vivo* applications.

1.1.2.1 Individual MOFs

Many individual MOFs have been directly used as antibacterial agents. For example, Hu et al. [33] successfully synthesized two kinds of highly efficient Ag-MOF by synergistically utilizing the antibacterial properties of reactive organic radicals and silver ions. The two Ag-MOFs, Ag-1 and Ag-2 can sustainably release Ag^+ and exhibited similar effective antimicrobial activity against four common Gram-negative and Gram-positive human pathogens and particularly two multidrug resistant bacteria. Zhao's group [34] prepared a 2D Cu-MOF nanosheets with high density of Cu^{2+}/Cu^+ surface active sites, which could decompose H_2O_2 into highly cytotoxic hydroxyl radicals and induce bacteria death. In another work, a Zn-MOF, zeolitic imidazolate framework-8 (ZIF-8), has been synthesized using Zn^{2+} and 2-methylimidazole ligands, exhibited almost complete inactivation of *E. coli* in saline solution under sunlight irradiation for 2 h [35]. The disinfection mechanism of ZIF-8 was mainly attributed to the ROS produced by photocatalysis.

Although MOFs are a hot patch for antibacterial agents, it is difficult to achieve reutilization due to the progressive degradation of MOFs skeletons. Current research focuses on combining MOFs with various matrix (such as hydrogel, polymer, glass,

wood, cotton, silicone rubber etc.) to improve their operability, machinability and reusability [36]. Yao et al. [37] fabricated a Zn-MOF encapsulated methacrylated hyaluronic acid microneedles array through the molding method to promote wound healing. This microneedles array shows excellent antibacterial activity due to the damage capability against the bacteria member and oxidative stress of the zinc ion released from the Zn-MOF. Besides, the degradable photo-crosslinked MeHA matrix presents superior capabilities to continuously release zinc ions and avoid secondary damage to the wound. Rubin et al. [38] engineered a MOF–cotton material for antibacterial applications by growing the MOF $Cu_3(NH_2BTC)_2$ layer-by-layer on the surface of a modified cotton fabric. The obtained cotton swatches can not only kill bacteria by releasing Cu^{2+}, but the materials were also able to significantly reduce the adhesion of bacteria to the surface under both wet and dry conditions. Gwon et al. [39] synthesized a series of bioactive MOF-embedded hydrogels (hydrogel@Cu-MOF 1, hydrogel@Co-MOF 2, and hydrogel@Zn-MOF 3) by UV light-mediated thiolene photopolymerization using diacrylated polyethylene glycol (PEG), 4-arm-thiolated PEG, and MOFs. The antibacterial experiments proved that both hydrogel@Cu-MOF 1 and hydrogel@Co-MOF 2 showed excellent antibacterial activity. Importantly, the hydrogel@Cu-MOF 1 did not exhibit cytotoxic effects, and exhibited 99.9% antibacterial effects at the minimum bactericidal concentration.

1.1.2.2 MOF-based composites

Although MOFs have been employed as effective antibacterial agents, their low stability may lead to excessive release of metal ions, which is harmful to human

tissues, limiting their wide applications. In addition, single-model bactericidal strategy limited the efficiency. Hence, many other materials such as metal nanoparticles, metal oxide, antibiotics, and photosensitizer were selected to synthesize MOFs-based nanocomposites to solve these problems [40].

As well-known antibacterial agents, Ag NPs have been widely explored for antibacterial applications. Therefore, MOFs have been incorporated with Ag NPs to enhance their antibacterial ability. For example, Shakya et al. [41] developed a water-soluble and biocompatible γ-cyclodextrin MOF as a template in which ultrafine Ag NPs were embedded by reaction diffusion to promote antibacterial activity. The CD-MOF based synthetic strategy facilitate reduced particle size and enhanced stability of Ag NPs. Meanwhile, the synthesized Ag NPs are easily dispersible in aqueous media and effectively inhibit bacterial growth. Furthermore, Ag@CD-MOF-treated rats had a 90% reduction in wound size within 10 days, while the blank group required more than 14 days.

The degradation of MOFs under appropriate conditions to achieve controlled release of antibiotics has also been reported. For example, a porous Fe-MOF (MOF-53) was prepared to encapsulate Van through a post-synthesis method. It exhibited a much higher drug-loading ratio (20 wt %) and excellent chemical stability under acidic conditions [42]. This MOF-53(Fe)/Van system showed high antibacterial ratio (99.3%) against *S. aureus*. Duan et al. [43] constructed an Fe-MOF-coated mesoporous silica nanoparticles system to co-deliver β-lactam antibiotics and β-lactamase inhibitors to eliminate antibiotic-resistant bacteria and biofilm. Lin's

group [44] studied a ZIF-8 loaded with small molecular photosensitizer, curcumin (CCM). Then, the CCM@ZIF-8 was decorated with biocompatible polymers hyaluronic acid (HA) and chitosan (CS) by the layer-by-layer self-assembly technique to obtain an antibacterial CCM@ZIF-8@HA@CS nanoparticle. The further surface modification of CCM@ZIF-8 was efficient to improve local positive charge density, which resulted in binding bacteria by electrostatic interactions. Under blue light irradiation for 10 min, the CCM@ZIF-8@HA@CS showed highly effective antibacterial activities toward both *S. aureus* and *E. coli*.

As a biological signal molecule, nitric oxide (NO) is involved in many processes of human physiology and pathology. Recently, more and more studies proves that NO has potent antimicrobial activity and plays a pivotal role in the processes of wound healing. Furthermore, high concentrations of NO are toxic to mammalian cells, so precise control of its release is critical. Zhang et al. [45] fabricated a HKUST-1 as NO-loading vehicle, and the NO-loaded HKUST-1 (NO@HKUST-1) particles were incorporated into the hydrophobic polycaprolactone through the electrospinning method to synthesize the core–shell NO sustained release system. It was demonstrated that NO (1.74 nmol L^{-1} h^{-1}) and copper ions could be released continuously at a low concentration, leading to effective stimulate angiogenesis, promote the angiogenesis, and inhibit inflammation in the wound area.

Beside chemotherapy to kill bacteria, MOFs also exhibit PDT [46] and PTT [47] effect for antibacterial activities. For this, Wu et al. [48] developed a porphyrinic MOF (PCN-224) with $ZrCl_4$ and tetrakis(4-carboxyphenyl porphyrin) (TCPP),

followed by incorporation of Cu^{2+} into the core of the porphyrin ring via hydrothermal method to form metalloporphyrin-MOFs. After Cu^{2+} doping, the PCN-224 exhibited improved photocatalytic property, which effectively enhance the yield of ROS. At the same time, the d-d transition of Cu^{2+} can also enhance its photothermal effect. The PCN-224 doped with 10% Cu^{2+} exhibited the best antibacterial efficiency (99.71%) against *S. aureus* in 20 min. Furthermore, the *in vivo* experimental results showed that Cu_{10}MOF could effectively kill bacteria and promote wound healing. Subsequently, Wu's group [49] designed a series of PB derivatives with tunable photothermal properties by adjusting the doping level of zinc ions that kills methicillin-resistant *S. aureus in vitro* and *in vivo* wound healing model. The photothermal effect could accelerate the ions (Zn^{2+}, Fe^{2+}, and Fe^{3+}) to disrupt intracellular metabolic pathways and improve the bacteria killing efficiency without causing systemic toxicity. The ZnPB-3 demonstrated the highest antibacterial rate against *E. coli*, *S. aureus*, and MRSA biofilm and its mechanism is based on the photothermal effect and release of metal ions.

1.1.2.3 MOF-based heterostructures

Recently, a Prussian blue (PB) MOF has been employed as template for the growth of porphyrin-doped UIO-66-TCPP MOF to prepare a core–shell dual MOF (PB@MOF) [50]. PB MOF, as a photothermal material, has good photothermal effects and biodegradability [51]. As a photoexcited MOF, porphyrin can significantly enhance the transfer of photoexcited electrons from PB, thereby enhancing the photocatalytic performance and the yield of $^1O_2$. Due to the photothermal and

photodynamic synergistic effects of PB@MOF heterostructure, the antibacterial efficacies against *S. aureus* and *E. coli* were 99.31% and 98.68%, respectively, under the dual light irradiation of 808 nm near-infrared (NIR) and 660 nm red light.

1.1.2.4 MOFs-based derivatives

Since MOF derivatives contain abundant graphitic-like structures after carbonization, which offer enormous possibilities for PTT. Therefore, MOF derivatives provide a strategy for the preparation of antibacterial agents with synergistic bactericidal effect, which not only exhibit the ability to release metal ions, but also with PTT performance. Yang et al. [52] reported a silver-doped MOF derivative (C–Zn/Ag) that exhibits effective release of metal ions performance and excellent photo-to-thermal conversion ability for synergistic antimicrobial application. Under NIR irradiation, the C–Zn/Ag can destroy bacterial membranes by photothermal effect. Meanwhile, abundant metal ions can be released to damage bacterial intracellular substances. Antibacterial experiments exhibited that the C–Zn/Ag nanoagents with nearly 100% antibacterial efficiency against *S. aureus* and *E. coli* at concentration of 0.16 mg mL^{-1}.

MOF-based materials have been well developed for antibacterial applications. These MOFs have the advantages of broad antibacterial spectrum, high efficiency, high stability, and fast acting time. It is well known that the antibacterial properties of MOFs are mainly determined by metal ions, and their release control is attributed to their highly ordered three-dimensional structure. Although great progress has been made in the antimicrobial performance of MOFs, there are still some unsolved

problems that need to be developed, such as (i) acceptable toxicology, (ii) controllable degradation of MOFs, and (iii) efficient encapsulation and controllable release of antibacterial molecules.

1.2 MOF-based platforms for biosensors

Recently, numerous biosensors based on diverse MOFs (**Figure 4**) have been developed for detecting diverse targets, such as heavy metal ions, antibiotics, proteins, biomarkers, living cancer cells, and such on, by coupling with diverse determination techniques such as fluorescence, electrochemical, photoelectrochemical, and solid-phase extraction [53]. Among them, electrochemical biosensors combine the sensitivity of electrochemical detection technology with the specificity of a designated biological entity [54].

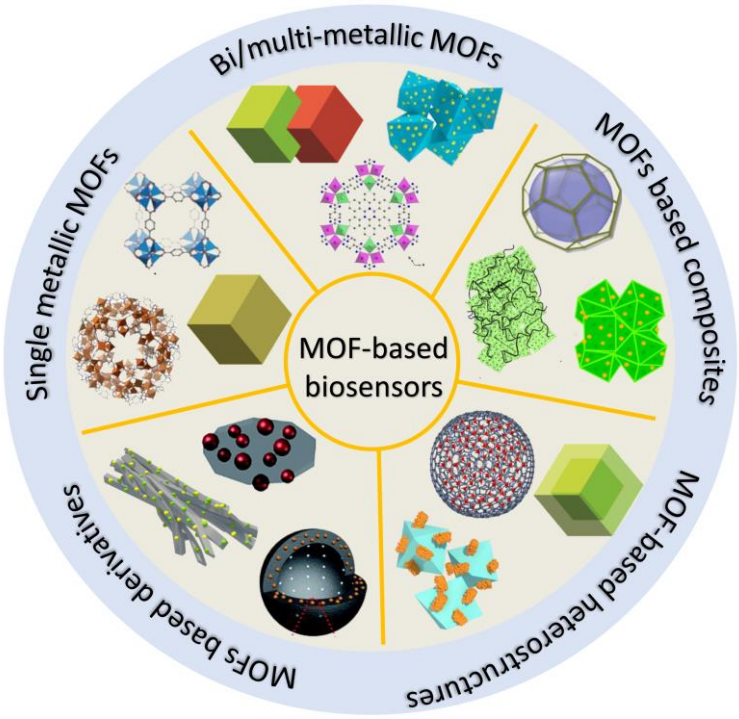

Figure 4. Various MOFs-based biosensors.

Electrochemical biosensors are considered as ideal detection tools because of their cost effectiveness, fast response, high sensitivity, small sample volume requirement, reusability, and easy disposability [55]. Typically, an electrochemical biosensor system usually consists of three integrated components [56]: (i) biorecognition elements, such as aptamers, antibodies, or enzymes, that can specifically interact with the targets, (ii) signal transducers that can generate chemical signals caused by the interaction of biorecognition elements and analytes, and (iii) electronic systems for data management.

The large surface area of MOFs is benefit for anchoring the recognition biomolecules (antibody, aptamer, and DNA, etc.) with high loading capacity through van der Waals force, hydrogen-bonding, π-π* interaction, electrostatic, or hydrophobic interactions [57]. Further, owing to various grafting groups on the surface or in the pore, such as amino or carboxyl groups, MOFs have been used as an ideal platform for the immobilization of recognition biomolecules through covalent linkage [58]. Compared with other traditional sensing platforms, the probes adsorbed on the surface of MOFs, can also penetrate into the interior of MOFs, showing higher sensitivity than other electrochemical biosensors. Due to the large number of probes can be immobilized over MOFs based electrochemical biosensors, almost all active sites within these materials can be occupied, resulting in insignificant non-specific adsorption [57]. MOFs based electrochemical biosensors show high selectivity due to the specific binding of recognition molecules to the target, such as antibody-antigen interaction, G-quadruplex between aptamer strands and different targets. More

importantly, high stability of most MOFs can provide protection of biomolecules under severe environments (such as high temperature, extreme pH value, organic solvents, and toxic substances) [59]. Based on these discussions, MOFs can be rationally designed and synthesized to possess unique properties that are beneficial to the immobilization of biomolecules to construct biosensors with high sensitivity, specificity and stability.

1.2.1 Monometallic MOF

Initially, only monometallic MOFs were directly applied as platforms for electrochemical biosensors to detect different targets. The metal ions used in the construction of MOFs include Zn^{2+}, Zr^{4+}, Cu^{2+}, Al^{3+}, Fe^{3+}, Ti^{4+}, etc. For instance, Zhang et al. [60] prepared a series of 3D Ni-MOFs with different pore sizes, which were used to construct acetylcholinesterase (AChE) biosensors for detection of the chiral drug inhibitor galantamine hydrobromide (GH). Through the combination of Ni-MOFs with intrinsic oxidase-like activity and the high active AChE, a synergistic catalytic effect can be exerted on the hydrolysis of acetylthiocholine chloride, resulting in a rapid sensing response. The matched size and chirality of MOF significantly accelerate the delivery of substrate and enhance the interactions between substrates and biosensor, which enables the optimal Ni-MOF-based platform with highly sensitive for GH detection, with a detection limit (LOD) of 0.31 pM and a wide linear range of $1 \times 10^{-12} \sim 1 \times 10^{-6}$ M. Wu's group [61] prepared a water-stable one-dimensional double-chain Cu-MOF by a hydrothermal method and employed it to

construct an electrochemical biosensor for efficiently recognizing l-tyrosine (l-Tyr) in biomimic environments. Based on the extreme solvent and thermal stability as well as excellent electroconductive character, Cu-MOF showed preferable biosensing ability toward l-Tyr. The biosensor exhibited simple operation and high sensitivity with a LOD of 5.822 μM in the concentration range from 0.01 to 0.09 mM. Our research groups [62] have presented the design and synthesis of two-dimensional Zr-based MOF (denoted as 521-MOF) using polyvinyl pyrrolidone as surfactant. Then, electrochemical biosensor based on 521-MOF was developed for the detection of cancer marker, mucin 1 (MUC1). The 521-MOF-based biosensor has excellent sensing ability for MUC1 with LOD of 0.12 and 0.65 $pg \cdot mL^{-1}$ deduced from electrochemical impedance spectroscopy (EIS) and surface Plasmon resonance spectroscopy (SPR), respectively, within the broad concentration range of MUC1 from 0.001 to 0.5 $ng \cdot mL^{-1}$.

Considering their excellent compatibility with different metal species, bi-/multi-metallic MOFs can be successfully obtained via different synthesis methods. Compared with single metallic MOFs, bimetallic and multimetallic MOFs often show improved sensing performance due to the synergistic effect and electronic effect and enhanced framework water stability [63]. A novel label-free electrochemical biosensor based on bimetallic silver/zinc metal–organic framework (Ag/Zn-MOF) was progressed for direct detection of unamplified hepatitis C virus nucleic acid [64]. Based on the synergistic catalytic effect of silver and zinc, the bimetallic Ag/Zn-MOF MOF was used as a catalyst to oxidize glucose for signal amplification, as well as

platform to immobilize the probes and electroactive materials for signal reporting. Additionally, Zn/Co-ZIF exhibits high selectivity and sensitivity over a linear detection range from 1 fM to100 nM with a detection limit of 0.64 fM. He et al. [65] reported a bifunctional electrochemical aptasensor based on bimetallic NiCo Prussian blue analogue (NiCoPBA) nanocubes for detecting carcinoembryonic antigen (CEA) and corresponding living cancer cells. The CEA-targeted aptamer strands can be strongly immobilized on the surface of NiCo-PBA due to intrinsic cavities, metallic coordination centers, rich C≡N groups, and π-π* interactions. The developed NiCoPBA-based aptasensor can not only be employed to determine CEA, which provides a LOD of 0.74 fg mL^{-1} in a wide linear range from 1.0 fg mL^{-1} to 5.0 ng mL^{-1}, but also can be utilized to directly detect cancer cells with LOD of 47 cells mL^{-1}.

1.2.2 MOF-based composites

Since MOFs usually suffer from some disadvantages such as low conductivity and poor stability, there has been growing interest in integrating MOFs with other functional materials (such as metal nanoparticles, carbon materials, conductive polymers, etc.) to form composites, which is considered a useful method to improve the performance of MOFs and further extend the potential applications of MOFs [66]. Fortunately, MOFs have large surface area and excellent absorption ability, which could be utilized as carriers for these functional components.

As reported, a Ce-MOF/CNTs (carbon nanotubes) nanocomposite was prepared

by a simple solution method and post-treated with the mixed hydrogen peroxide/sodium hydroxide solution [67]. Taking advantage of good electrical conductivity of CNTs, the two-valence of Ce^{3+}/Ce^{4+} after post-processing and the large surface area of MOF, the Ce-MOF/CNTs nanocomposites were used to construct the sensor for the simultaneous electrochemical detection of hydroquinone (HQ) and catechol (CC). The prepared electrochemical sensing platform demonstrates good selectivity, reproducibility, stability, and comparative LOD for the detection of HQ (5.3 μM) and CC (3.5 μM). Recently, Jia et al. [68] has prepared polymer–zirconium-based MOF containing silver nanoparticles (AgNPs@polyUiO-66) as platform for anchoring aptamer to effectively detect respiratory viruses, including influenza A virus (H1N1) and the N-gene of severe acute respiratory syndrome coronavirus 2 (SARS-CoV2). By combining the enhanced electrochemical activity of Ag NPs with the high specific surface area, large pore size, and abundant functionalities of polyUiO-66, a large number of H1N1-targeting antibodies and N gene-targeting aptamers can be adsorbed on the developed platform, respectively. Thereby, the proposed biosensor show amplified electrochemical responses for detecting H1N1 virus and SARS-CoV2 N-gene, with low LOD of 54.7 and 23.4 fg mL^{-1}, respectively, as well as high selectivity, good stability, excellent reproducibility, and acceptable regenerability.

Our research group [69] prepared a bimetallic ZrHf-MOF embedded with abundant carbon dots (CDs) (denoted as CDs@ZrHf-MOF), which was employed to construct an aptasensor for the determination of human epidermal growth factor

receptor (HER2) and living cancer cells. The results reveal that ZrHf-MOF has good biocompatibility, strong fluorescence and high electrochemical activity, because ZrHf-MOF can form high binding interactions of both Zr−O−P and Hf−O−P with the aptamer strands. The CDs@ZrHf-MOF-based electrochemical aptasensor displays excellent sensing performances, giving a LOD of 19 fg mL^{-1} for HER2 (0.001–10 ng mL^{-1}) and 23 cell mL^{-1} for breast cancer cells (MCF-7 cells) (1×10^2-1×10^5 cell mL^{-1}), with good selectivity, stability, reproducibility, and acceptable applicability. A similar strategy was used for detecting HER2, where the electrochemical activity was enhanced by adding gold nanoparticles (Au NPs) into MnFe-PBA network (represented by MnFePBA@AuNPs). The obtained MnFePBA@AuNPs-based electrochemical biosensor was applied for detecting the HER2, showing a low LOD of 0.247 pg·mL^{-1} within HER2 concentration range of 0.001–1.0 ng·mL^{-1}.

1.2.3 MOF-based heterostructures

In order to tune the fundamental properties of MOFs, the exploration hybrids of various MOFs has proven to be a promising strategy to manipulate their compositions and structures. To date, various classes of MOF-based hybrids, such as MOF-on-MOF and MOF@MOF, have been prepared for developing new heterostructures, exploring the formation mechanism of structures, and extending the practical applications of MOFs [70]. These MOF-based hybrids not only maintain the excellent properties of two types of MOFs along with some unexpected synergistic effects, but also

effectively overcome the shortcomings of single MOF, exhibiting different properties from single MOFs.

Based on the cascade primer exchange reaction, a MOF@Pt@MOF nanozyme have been employed for ultrasensitive detection of exosome miRNA [71]. Under the catalysis of the MOF@Pt@MOF multiple-layered nanozyme, hydrogen peroxide can be decomposed into H_2O and O_2, resulting in an amplified electrochemical signal. Thus, the constructed electrochemical biosensors displayed high sensitivity with LOD of 0.29 fM and high specificity, which can distinguish homologous miRNAs with single base mismatch. Zhou's group [72] prepared two types of MOF-on-MOF hybrid i.e., Zn-MOF-on-Zr-MOF and Zr-MOF-on-Zn-MOF, which were exploited as the aptasensor platforms for detecting the cancer marker protein tyrosine kinase-7 (PTK7). The electrochemical results show that the Zr-MOF component was favorable for the immobilization of aptamer, while the Zn-MOF component could greatly stabilize the G-quadruplex formed by aptamer strands and PTK7 due to specific recognition. As compared, the Zn-MOF-on-Zr-MOF-based aptasensor exhibited the superior sensing performance than the Zr-MOF-on-Zn-MOF-based one, giving an LOD of 0.84 pg mL^{-1} with the PTK7 concentration range of 1.0 pg mL^{-1} to 1.0 ng mL^{-1}. The proposed n-MOF-on-Zr-MOF-based biosensor also present high selectivity, good stability, reproducibility, and acceptability in human serum. In our previous work, two kinds of heterostructured bimetallic TbFe-MOF MOFs, i.e., Tb-MOF-on-Fe-MOF and Fe-MOF-on-Tb-MOF have been developed as the platforms for detecting CA125 (carbohydrate antigen 125) and the living cancer cells [73]. The electrochemical

results reveal that the Tb-MOF-on-Fe-MOF-based biosensor displayed higher stability of the formed G-quadruplex of aptamer and CA125. Therefore, the Tb-MOF-on-Fe-MOF-based biosensor shows an ultralow LOD of 58 μU mL^{-1} within a linear range from 100 μU·mL^{-1} to 200 U·mL^{-1}, along with high sensitivity for the detection of MCF-7 cells (LOD=19 cell·mL^{-1}).

1.2.4 MOFs-based derivatives

Thermal decomposition of MOFs is a feasible method to improve their electrochemical activity [74]. In this case, MOFs can be selectively transformed into their respective porous carbons, metals, metal oxides, or their composites by controlling the thermal decomposition conditions [75]. Such MOF-derived nanoporous metal oxides and carbons have high specific surface areas and interconnected pores, which improve the performance of biosensing application [58].

As in our previous work, a zirconium-based MOF (UiO-66) entrapped within the electric spun polyacrylonitrile (PAN) fiber (represented by UiO-66@PAN) was calcinated at different temperatures to obtain a series of zirconium oxide nanoparticles and graphene-like nanofiber (denoted by ZrO_2@GNF) nanohybrids with different morphologies and nanostructures [76]. As compared with ZrO_2@GNF calcined at 500 °C and 900 °C, the ZrO_2@GNF nanohybrid obtained at 700 °C demonstrated superior sensing performance, which exhibited a LOD of 4.76 fg mL^{-1} within an osteopontin (OPN) concentration ranging from 0.01 pg mL^{-1} to 2.0 ng mL^{-1}. Similarly, a bimetallic NiCo-MOF was pyrolyzed into a novel composite consisting of

$NiCo_2O_4$ spinel, CoO, and CNTs (represented by $NiCo_2O_4$/CoO@CNTs) at high temperature 700 °C, which was used as efficient platform for immobilizing the probe DNA of human immune deficiency virus-1 (HIV-1) [63]. The $NiCo_2O_4$/CoO@CNTs-based biosensor displays a LOD of 16.7 fM toward HIV-1 DNA over the linear range of 0.1 pM to 20 nM.

After discussing the applications of pure MOFs, MOF-based composites, MOFs@MOFs and MOF-on-MOF hybrids, and MOF-based derivatives, we can conclude that by tuning the pore size, composition, morphology, and physicochemical properties of MOFs, their functional properties can be enhanced. Depending on the requirements of a specific application, MOF materials with specific structures, texture features, and different properties can be designed to meet the application requirements.

Herein, we focus on the field of metal complexes and metal-organic frameworks with potential biological applications, which is divided into five chapters:

1) Novel silver(I) complexes were synthesized by interaction of a new acylpyrazolone ligand with $AgNO_3$, where imidazole and triphenylphosphine were selected as ancillary donors. The coordination of acylpyrazolonates with silver through the O_2-chelating face and the N_2 of the pyrazole ring in the $[Ag(Q^{PhN2Ph})]_n$ coordination polymers, while the O_2-chelating face was observed in complexes $[Ag(Q^{PhN2Ph})(Miem)_2]$, $[Ag(Q^{PhN2Ph})(imH)]$, $[Ag(Q^{PhN2Ph})(PR_3)_2]$ and $[Ag(Q^{PhN2Ph})(PR_3)]_2$. The antibacterial activity of all Ag(I) compounds were tested against two bacterial strains, *S. aureus* and *E. coli*.

2) Novel silver(I) complexes were synthesized by interaction of two type of pyrazolone ligands with $AgNO_3$, where triphenylphosphine was selected as ancillary donors. By coordination the pyrazolone ligand with silver through the N_2-chelating mode, the cationic species $[Ag(L^{Py,\ Me})(PTA)]NO_3$, $[Ag(L^{Py,\ Me})(PTA)]PF_6$, and $[Ag(L^{Py,\ Ph})(PTA)]NO_3$ were obtained. In the presence of $NaOCH_3$, the neutral species $[Ag(L^{Py,\ Me})(PR_3)]$, $[Ag(L^{Py,\ Me})(PTA)]$, $[Ag(L^{Py,\ Ph})(PR_3)]$, and $[Ag(L^{Py,\ Ph})(PTA)]$ (R=Ph or Cy) were obtained.

3) A novel copper-based polymer-metal-organic framework (polyCu-MOF) was selected as an efficient scaffold for loading Ag NPs (denoted as polyCu-MOF@AgNPs), which was applied as a superior antibacterial agent for wound healing. PolyCu-MOF was prepared by using a polyether ligand containing 1,4-benzenedicarboxylic acid unit as building block, 4,4′-bipyridine as co-ligand, and copper ions as coordination centers. Subsequently, the obtained polyCu-MOF serves as a novel carrier for loading abundant Ag NPs. The antibacterial performances against *S. aureus* and *E. coli*, were investigated using the growth curve and plate colony counting method. The antibacterial properties of Cu-MOF@AgNPs prepared with 1,4-benzenedicarboxylic acid as ligand was also carried out for comparison. After assessing the cytocompatibility and hemocompatibility of polyCu-MOF@AgNPs, wound healing rate, histopathological examinations, and plate counting method were also used to evaluate the *in vivo S. aureus*-infected wound therapeutic effects. The present work not only extends the biomedical application of MOF-based platforms, but also provides a potential and robust strategy for healing

bacteria-infected wounds.

4) A $Cu_xNi_{3-x}(HHTP)_2$ MOF was synthesized with 2,3,6,7,10,11-hexahydroxytriphenylene (HHTP) as linker. This MOF was used as sensitive scaffold for adsorbing aptamer strands toward electrochemical detection of living C6 glioma cells and one of its biomarkers, epidermal growth factor receptor (EGFR). The sensitivity, selectivity, stability, reproducibility, and usability of CoMn-ZIF@CNF(1-3)-based aptasensor were investigated. This sensing strategy based on bimetallic semiconducting MOF shows the great potential to detect other cancer cells for cancer diagnosis.

5) A high-efficiency sensing system for α-synuclein (α-Syn) oligomers was designed based on a novel one dimensional/two dimensional structural nanohybrid (denoted as CoMn-ZIF@CNF) of CoMn-based ZIF nanosheets vertically grown around carbon nanofibers (CNFs). CNFs were prepared by calcining electrospun polyacrylonitrile under Ar/H_2 atmosphere and used as the template for CoMnZIF synthesis, which can remarkably enlarge the electrochemical signal of CoMnZIF@CNF nanohybrid. The series of CoMn-ZIF@CNF nanohybrids were modulated by changing the ratios of precursors $Co(NO_3)_2$ and $Mn(NO_3)_2$ (i.e. 3:1, 1:1, and 1:3) to optimize sensing performances of α-Syn oligomers. The sensitivity, selectivity, stability, reproducibility, and usability of CoMn-ZIF@CNF(1-3)-based aptasensor were further investigated. The efficient strategy of structural hybridization can be used in designing different aptasensors and further extend the application range of ZIFs materials.

CHAPTER 2

Synthesis, characterization and antibacterial activity of silver(I) complexes with acylpyrazolone ligands

2.1 Introduction

Acylpyrazolones are an interesting class of α-diketones, containing a pyrazole fused to a chelating arm. Since the first acylpyrazolone was synthesized by L. Knott in 1883, a variety of acylpyrazolone ligands have been reported [77]. Numerous studies demonstrated that pyrazolone-based compounds contain a variety of coordination atoms such as N and O, which have strong coordination ability and abundant chelating modes. They have the ability to exist either in an enol or keto tautomer forms, which gives them the potential to form different types of interesting coordination compounds [78], such as neutral mononuclear, dinuclear, polynuclear, or ionic species. These metal complexes display catalytic performance, biological activity and enhanced luminescence. Acylpyrazolone ligands have been used as convenient metal extractants or chelating agents for the spectroscopic determination of trace metals [79]. Due to high extracting ability, great separation power, intense color of complex extracts and low solubility, acylpyrazolone ligands are widely used in analytical chemistry for the determination and isolation of almost all metal ions. Similarly, acylpyrazolone ligands are also a very important class of intermediates in drug synthesis, which play an important role in biomedicine due to their high efficiency, low toxicity, and structural diversity.

Recently, many efforts have been devoted on the exploration of the tremendous biological potential of Ag(I) complexes with acylpyrazolone ligands, which can act as broad spectrum antimicrobial agents. Thus they can kill most Gram-positive and Gram-negative bacterial strains [80-82]. Herein, we described the synthesis and

characterization of a number of silver(I) derivatives containing a new acylpyrazolones (**Scheme 2-1**), with N-donor imidazole and 1-methylimidazole, or with the colligating unidentate phosphines such as Ph_3P and Cy_3P in diverse ligand/metal ratios.

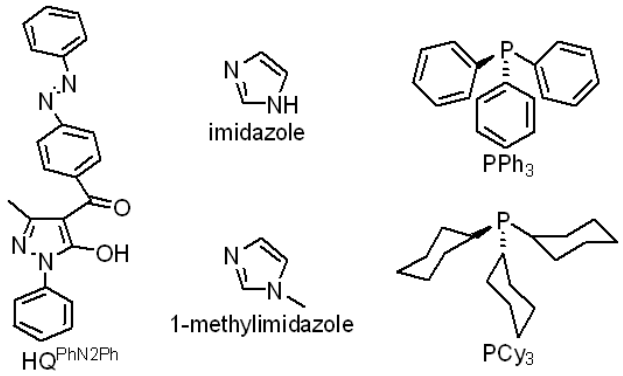

Scheme 1. HQ proligands, imidazoles, and phosphine used in this work.

2.2 Experimental section

2.2.1 Basic characterizations

All chemicals were purchased from Aldrich and used as received. Melting points were taken with a STMP3 Stuart scientific instrument on a capillary apparatus. ^{1}H, $^{13}C\{^{1}H\}$, and $^{31}P\{^{1}H\}$ NMR spectra were recorded with a 500 Bruker Ascend instrument operating(500 MHz for ^{1}H, 125 MHz for ^{13}C, and 202.6 MHz for ^{31}P). IR spectra were recorded from 4000 to 400 cm^{-1} with a PerkinElmer Spectrum Frontier FT-IR instrument. Elemental analyses were performed with a Fisons Instruments 1108 CHNS-O Elemental Analyzer. The positive and negative ion electrospray mass spectra (ESI-MS) were carried out with a Series 1100 MSI detector HP spectrometer, using acetonitrile mobile phase. Thermal gravimetric analysis (TGA) were performed in a N_2 atmosphere with a Perkin-Elmer STA 6000 simultaneous thermal analyzer.

2.2.2 Synthesis of silver complexes

Synthesis of HQ^{PhN2Ph}. Firstly, 3-methyl-1-phenylparazaol-5-one (7.92 mM, 1.38 g) was dissolved in 1,4-dioxane (10 mL), and heated to 80 ℃ to form the clear solution. Subsequently, calcium hydroxide (7.74 mM, 1.89g) was added, following by stirring for 3 h. Then, 4-(phenylazo)benzoyl chloride (7.74 mM, 1.89 g) was dissolved in 1,4-dioxane and drop wised using a separatory funnel. The above solution was heated to 160 ℃ for 2 h. Finally, the mixture was poured into hydrochloric acid solution (2 M, 500 mL) to decompose the calcium complex. The solution color changed from red to brown. The precipitate was separated by filtration and dried under reduced pressure (20℃, 0.1 Torr) to constant weight. Yield: 92.5%. Afterward, it is soluble in dimethyl sulfoxide (DMSO), *N*, *N*-dimethylformamide (DMF), acetone, acetonitrile and chlorinated solvents. ^{1}H NMR ($CDCl_3$): δ=2.18s (3H, C3-C*H*$_3$), 7.35t (*H*20, *J*=7.48 Hz), 7.49-7.59m (*H*9, *H*8, *H*8', *H*19, *H*19'), 7.84d (*H*7, *H*7', *J*=8.28 Hz), 7.91d (*H*18, *H*18', *J*=8.22 Hz), 7.98-8.02m (*H*12, *H*12'), 8.08d (*H*13, *H*13', *J*=8.50 Hz).

Synthesis of $[Ag(Q^{PhN2Ph})]_n$ (1). HQ^{PhN2Ph} (0.2 mM, 76 mg) and NaOMe (0.2 mM, 11 mg) were added to methanol to form suspension. $AgNO_3$ (0.2 mM, 34 mg) was dissolved in water and added to above suspension. After stirring at room temperature for 1 h, the solvent was removed almost on rotary evaporator. Then 10 mL of Et_2O was added to form the precipitate. After filtration, the brown powder was dried in vacuum to constant weight and denoted as derivative **1**. Yield: 85.6%. It is soluble in DMSO. M.p. 234–236 ℃. ^{1}H NMR (DMSO-d_6): δ=2.30s (3H, C3-C*H*$_3$),

7.03t (*H*20, *J*=7.39 Hz), 7.51t (*H*19, *H*19', *J*=7.81 Hz), 7.57-7.65m (*H*8, *H*8', *H*9), 7.80d (*H*7, *H*7', *J*=8.37 Hz), 7.85d (*H*18, *H*18', *J*=8.04 Hz), 7.88-7.95m (*H*12, *H*12', *H*13, *H*13'). $^{13}C\{^{1}H\}$ NMR (DMSO-d_6): δ=17.9s (C3-*C*H_3), 102.5s (*C*4), 120.0s, 121.8s, 123.1s, 123.5s, 128.8s, 130.0s, 130.1s, 132.0s, 140.8s, 145.0s, 152.3s (*C*3), 152.6s, 152.7s, 164.5s (*C*5), 187.1s (*C*O). IR: ≅3049w (νC_{arom}=H), 1609vs, 1592s (νC=O), 1575m, 1503vs, 1429s, 1356m (νC=C, νC=N, νC=N), 1217w, 1063 (w), 940s, 783s, 753m, 683s cm^{-1}. Anal. Calc. for $C_{23}H_{17}AgN_4O_2$: C 56.46, H 3.50, N 11.45. Found: C 54.38, H 3.10, N 10.13. TGA-DTA (mg% vs. °C): heating from 30 to 600 °C with a speed of 8 °C min^{-1}; from 200 to 600 °C progressive decomposition, with a final black residual of 56.6% weight.

Synthesis of Ag(Q^{PhN2Ph})(Meim)$_2$ (2). [Ag(Q^{PhN2Ph})]$_n$ (0.1 mM, 48.9 mg) and 1-Methylimidazole (0.3 mM, 25 mg) were added to methanol. Then, the mixture was stirred at room temperature for 24 h. After that, the solvent was reduced to one third of the original volume on rotary evaporator. Then Et_2O was added to obtain precipitate. After filtration, the brown powder was dried in vacuum to constant weight and denoted as derivative **2**. Yield: 64.3%. It is soluble in methanol, DMSO, DMF, acetonitrile, acetone, and chlorinated solvents. M.p. 121–124 °C. ^{1}H NMR ($CDCl_3$): δ=2.18s (3H, C3-CH_3), 3.68s (6H, CH_3 of 1-methylimidazole), 6.89-7.09m (*H*24, *H*25, *H*29, *H*30), 7.19t (*H*20, *J*=7.29 Hz), 7.51t (*H*19, *H*19', *J*=7.04 Hz), 7.47-7.59m (*H*8, *H*8', *H*9, *H*7, *H*7'), 7.80-7.89m (*H*22, *H*27, *H*18, *H*18'), 7.95d (*H*12, *H*12', *H*13, *H*13', *J*=7.13 Hz). $^{13}C\{^{1}H\}$ NMR ($CDCl_3$): δ=17.4s (C3-*C*H_3), 33.8 (N-*C*H_3) 103.9s (*C*4), 121.5s, 122.3s, 122.9s, 125.0s, 128.8s, 129.1s, 129.4s, 131.2s, 139.4s, 143.5s, 151.8s

(*C*3), 152.7s, 153.4s, 164.3s (*C*5), 190.0s (*C*O). IR: ≅3120w (νC_{arom}=H), 1621m, 1588s ν(C=O), 1496m, 1453vs, 1422s (νC=C, νC=N, νC=N), 1236m, 1216m, 1111s, 1002s, 909s, 737s, 688s, 655vs cm^{-1}. Anal. Calc. for $C_{23}H_{17}AgN_4O_2$: C 56.46, H 3.50, N 11.45. Found: C 54.38, H 3.10, N 10.13. ESI-MS (+, CH_3CN) m/z (%): 83 (100) $[MeimH]^+$, 189 (33) $[Ag(Meim)]^+$, 271 (55) $[Ag(Meim)_2]^+$. TGA-DTA (mg% vs. °C): heating from 30 to 600 °C with a speed of 8 °C min^{-1}; from 120 to 600 °C progressive decomposition, with a final black residual of 24.9% weight.

Synthesis of Ag(Q^{PhN2Ph})(imH) (3). $[Ag(Q^{PhN2Ph})]_n$ (0.1 mM, 48.9 mg) and imidazole (0.2 mM, 13.6 mg) were added to methanol. Then, the mixture was stirred at room temperature for 4 h. After reaction, the solvent was removed completely on rotary evaporator to obtain precipitate. The precipitate was filtered off and washed with methanol. The yellow powder was dried in vacuum to constant weight and denoted as derivate **3**. Yield: 30.7%. It is soluble in DMSO. M.p. 167–168 °C. ^{1}H NMR (DMSO-d_6): δ=2.32s (3H, C3-CH_3), 7.01t (*H*20, *J*=7.03 Hz), 7.18-7.32m (*H*19, *H*19', *H*24, *H*25), 7.56-7.65m (*H*8, *H*8', *H*9), 7.78-7.86m (*H*18, *H*18', *H*7, *H*7'), 7.93d (*H*12, *H*12', *H*13, *H*13', *J*=7.11 Hz), 8.02s (*H*22), 12.80s (N-*H* of imidazole). $^{13}C\{^1H\}$ NMR (DMSO-d_6): δ=17.8s (C3-CH_3), 102.4s (*C*4), 119.2s, 121.7s, 123.0s, 128.7s, 130.0s, 130.1s, 132.0s, 141.2s, 145.4s (*C*3), 151.8s, 152.6s, 164.9s (*C*5), 186.8s (*C*O). IR: ≅3049w (νC_{arom}=H), 1609vs, 1592s ν(C=O), 1501vs, 1451s, 1427s (νC=C, νC=N, νC=N), 1217m, 1064m, 1009m, 939m, 782s, 752s, 682vs, 656s cm^{-1}. Anal. Calc. for $C_{26}H_{21}AgN_6O_2$: C 56.03, H 3.80, N 15.08. Found: C 54.87, H 3.78, N 13.71. TGA-DTA (mg% vs. °C): heating from 30 to 600 °C with a speed of 8 °C min^{-1};

from 200 to 600 °C progressive decomposition, with a final black residual of 55.8% weight.

Synthesis of $Ag(Q^{PhN2Ph})(PPh_3)_2$ (4). Firstly, triphenylphosphine (0.55 mM, 144 mg) was dissolved in methanol. Then, silver nitrate (0.25 mM, 42 mg) was added. After 10 minutes a white precipitate was obtained. The mixture was then added to a suspension of HQ^{PhN2Ph} (0.25 mM, 95 mg) and potassium hydroxide (0.25 mM, 14 mg). After stirring at room temperature for 24 h, the precipitate was filtered off and washed with methanol. The yellow powder was dried in vacuum to constant weight and denoted as derivate **4**. It is soluble in DMSO, DMF and chlorinated solvents. M.p. 184.9–186.2 °C. ^{1}H NMR ($CDCl_3$): δ=1.83s (3H, C3-C*H*$_3$), 7.13t (*H*20, *J*=7.12 Hz), 7.28-7.34m, 7.37-7.46m (32H, *H*19, *H*19' and Ph_3P), 7.49-7.59m (*H*8, *H*8', *H*9, *H*7, *H*7'), 7.91-8.01m (*H*18, *H*18', *H*12, *H*12', *H*13, *H*13'). $^{13}C\{^1H\}$ NMR ($CDCl_3$): δ=17.6s (C3-*C*H$_3$), 111.9s, 122.7s, 123.1s, 123.4s, 128.5s, 128.7s, 128.9s, 129.0s, 129.3s, 130.3s, 131.3s, 132.6s, 132.8s, 134.1s, 134.3s, 140.5s, 152.9s, 153.0s. $^{31}P\{^1H\}$ NMR($CDCl_3$): δ 8.1s (T=298 K), 17.4dd [$^1J(^{31}P–^{109/107}Ag)$=934Hz] (T=233 K). IR: ≅3051w (νC_{arom}=H), 1615m ν(C=O), 1593m, 1478m, 1434m, 1344m, 742s, 692vs, 504vs ν(P-Ph) cm^{-1}. Anal. Calc. for $C_{59}H_{47}AgN_4O_2P_2$: C 69.90, H 4.67, N 5.53. Found: C 69.67, H 4.75, N 5.31. TGA-DTA (mg% vs. °C): heating from 30 to 600 °C with a speed of 8 °C min^{-1}; from 180 to 600 °C progressive decomposition, with a final black residual of 41.5% weight.

Synthesis of $Ag(Q^{PhN2Ph})(PCy_3)_2$ (5). Derivative **5** was prepared by the same method as **4**. It is soluble in methanol, DMSO, DMF, acetonitrile, acetone and

chlorinated solvents. M.p. 116–118 °C. ^{1}H NMR ($CDCl_3$): δ=1.18-1.50m, 1.71-1.95m (66H, C_6H_{11}-P), 1.97s (3H, C3-CH_3), 7.19t (*H*20, *J*=7.40 Hz), 7.41t (*H*19, *H*19', *J*=7.92 Hz), 7.49-7.59m (*H*8, *H*8', *H*9), 7.76d (*H*7, *H*7', *J*=8.16 Hz), 7.93-8.04m (*H*12, *H*12', *H*13, *H*13', *H*18, *H*18'). ^{13}C{^{1}H} NMR ($CDCl_3$): δ=16.6s (C3-*C*H_3), 25.8s, 26.2s, 26.3s, 26.4s, 26.9s, 27.0s, 27.1s, 27.2s, 30.9s, 31.3, 31.8, 31.9, 32.0s, 35.1s, 35.6s ((*C*$_6$H$_{11}$)$_3$P), 104.2s (*C*4), 120.8s, 122.7s, 123.1s, 125.6s, 128.9s, 129.2s, 131.0s, 131.5s, 148.9s (*C*3), 152.6s, 153.8s, 190.9s (*C*O). ^{31}P{^{1}H} NMR($CDCl_3$): δ 43.1dd [^{1}J(^{31}P–^{109}Ag)=768 Hz, ^{1}J(^{31}P–^{107}Ag)=665 Hz] (T=298 K). IR: ≅2920s, 2850s ν(–CH_2–), 1622vs ν(C=O), 1595s, 1499vs, 1430vs, 690vs, 508m cm^{-1}. Anal. Calc. for $C_{59}H_{83}AgN_4O_2P_2$: C 67.48, H 7.97, N 5.34. Found: C 54.45, H 5.99, N 7.25. ESI-MS (+, CH_3CN) m/z (%): 669 (100) $[Ag(PCy_3)_2]^+$, 1157 (65) $[Ag_2(Q^{PhN2Ph})(PCy_3)_2]^+$.

Synthesis of]Ag(Q^{PhN2Ph})(PPh$_3$)]$_2$ (6). Derivative **6** was prepared by the same method as **4**. It is soluble in DMSO, DMF, and chlorinated solvents. M.p. 189–192 °C. ^{1}H NMR ($CDCl_3$): δ= 1.87s (3H, C3-CH_3), 7.20t (*H*20, *J*=7.38 Hz), 7.40-7.61m (20H, *H*8, *H*8', *H*9, *H*19, *H*19' and PPh_3), 7.73d (*H*7, *H*7', *J*=7.74 Hz), 7.95-8.09m (*H*12, *H*12', *H*13, *H*13', *H*18, *H*18'). ^{13}C{^{1}H} NMR ($CDCl_3$): δ=16.9s (C3-*C*H_3), 104.7s (*C*4), 120.5s, 122.4s, 122.7s, 123.0s, 124.7s, 128.6s, 128.7s, 129.1s, 129.2s, 130.9s, 131.4s, 133.9s, 134.1s, 139.2s, 143.7s, 149.0s (*C*3), 152.7s, 153.4s, 191.0s (*C*O). ^{31}P{^{1}H} NMR($CDCl_3$): δ 17.0d [^{1}J(^{31}P–$^{109/107}$Ag)=749 Hz] (T=298 K). IR: ≅3048w (νC_{arom}=H), 1621vs ν(C=O), 1595m, 1503s, 1434vs, 692vs, 517s, 497vs ν(P–Ph) cm^{-1}. Anal. Calc. for $C_{41}H_{32}AgN_4O_2P$: C 65.52, H 4.29, N 7.45. Found: C 64.49, H 4.15, N 6.66. TGA-DTA (mg% vs. °C): heating from 30 to 600 °C with a speed of 8 °C min^{-1};

from 230 to 600 ℃ progressive decomposition, with a final black residual of 56.4% weight.

Synthesis of [Ag(Q^{PhN2Ph})(PCy_3)]$_2$ (7). Derivative **7** was prepared by the same method as **4**. It is soluble in DMSO and DMF, M.p. 182–186 ℃. ^{1}H NMR ($CDCl_3$): δ=1.13-1.33m, 1.62-1.89m (33H, C_6H_{11}-P), 2.27s (3H, C3-CH_3), 7.01t (*H*20, *J*=7.29 Hz), 7.08t (*H*19, *H*19', *J*=8.14 Hz), 7.57-7.65m (*H*8, *H*8', *H*9), 7.78d (*H*7, *H*7', *J*=8.57 Hz), 7.85d (*H*18, *H*18', *J*=8.21 Hz), 7.91-7.97m (*H*12, *H*12', *H*13, *H*13'). ^{13}C{^{1}H} NMR ($CDCl_3$): δ=18.0s (C3-*C*H$_3$), 26.0s, 26.3s, 26.4s, 26.7s, 26.8s, 27.0s, 27.1s, 30.9s, 31.5, 31.6, 34.8s, 35.2s ((*C*$_6$H$_{11}$)$_3$P), 102.6s (*C*4), 120.1s, 121.9s, 123.1s, 123.3s, 125.6s, 128.8s, 130.0s, 131.1s, 132.0s, 140.7s, 145s, 152.1s (*C*3), 152.6s, 152.7s, 164.4s (*C*5), 187.3s (*C*O). ^{31}P{^{1}H} NMR ($CDCl_3$): δ 40.1d [^1J(^{31}P–$^{109/107}$Ag)=711 Hz] (T=298K). IR: ≅2925w, 2850w ν(–CH_2–), 1608vs ν(C=O), 1585s, 1500vs, 1428vs, 686vs cm^{-1}. Anal. Calc. for $C_{41}H_{50}AgN_4O_2P$: C 63.98, H 6.55, N 7.28. Found: C 57.15, H 4.64, N 7.28. TGA-DTA (mg% vs. ℃): heating from 30 to 600 ℃ with a speed of 8 ℃ min^{-1}; from 230 to 600 ℃ progressive decomposition, with a final black residual of 59.5% weight.

2.2.3 Antimicrobial activity

The antibacterial activities of the obtained complexes were tested against *E. coli* (ATCC 25922) and *S. aureus* (ATCC 6538) using oxford cup diffusion inhibition assays. Typically, the melted sterilized Luria-Bertani (LB) agar medium was poured into plastic petri dishes and then cool to room temperature to solidify. Subsequently, the medium containing bacteria (10^6 CFU mL^{-1}) was evenly layered on LB agar plates

by sterile spreader and incubated for 10 min. Afterwards, sterilized Oxford cups (6 mm) were placed on the top of LB agar plates, then 100 µL of complex solutions (50 µg mL^{-1}) were added to each Oxford cup. Finally, the plates were incubated for 24 h at 37 °C. Antibacterial activity was evaluated by the zone of inhibition (mm) around oxford cups using a calliper.

2.3 Results and discussion

2.3.1 Synthesis and spectroscopy characterization of silver complexes

The synthesis of derivatives **1-7** and their structure are shown in the **Scheme 2**. In detail, derivative $Ag(Q^{PhN2Ph})$ (**1**) was prepared by interaction between HQ^{PhN2Ph} and $AgNO_3$ in methanol, in the presence of NaOMe. Subsequently, derivatives **2** and **3** were obtained by mixing methanol suspension of **1** with excess of N-donor such as 1-methylimidazole and imidazole, affording Ag/Q^{PhN2Ph}/imidazole monomuclear derivatives with 1:1:2 composition (derivative **2**) or 1:1:1 (derivative **3**), respectively.

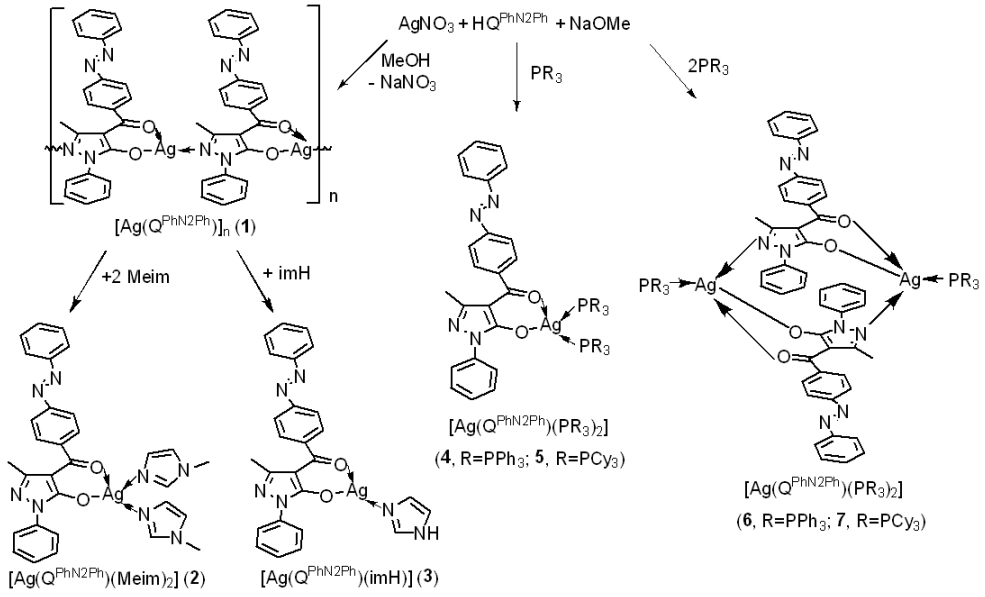

Scheme 2. Synthesis of derivatives **1**–**7**.

Derivatives **4** and **5** were synthesized by reaction of 1 equivalent HQ^{PhN2Ph} with 1 equivalent $AgNO_3$ and 2 equivalent R_3P ligands in methanol, in the presence of NaOMe. Derivatives **6** and **7** were obtained from the interaction of HQ^{PhN2Ph} with equimolar amounts of $AgNO_3$ and R_3P ligands.

Derivatives **1**–**7** are stable in air, **1**, **4**, **6** and **7** show higher melting points than **2**, **3** and **5**. The polynuclear structure of **1** has been proposed based on their insolubility in most organic solvents, apart from DMSO. Derivatives **2** and **4**–**6** are soluble in DMSO, DMF and chlorinated solvents, in the case of **5**, also in methanol, acetonitrile, and acetone. Derivative **3** is only soluble in DMSO. Derivative **7** is soluble in DMSO and DMF. The mononuclear structures of **2-5** and dinuclear structures of **6-7** have been established on the basis of their relevant dates mentioned in the experimental section.

The IR spectrum **1** shows that HQ^{PhN2Ph} is coordinated to two silvers through one oxygen atom of carbonyl group and one nitrogen atom of pyrazole ring after deprotonation, and the characteristic peaks shift lower frequencies after coordination. IR data of derivatives **2-7** show two strong absorptions in the range 1585–1625 cm^{-1} due to C=O stretching vibration [81]. Compared with HQ^{PhN2Ph}, carbonyl ν(C=O) band of derivatives **2-7** shifts to lower frequency (**Figure 5**), indicating chelation of silver through carbonyl groups bearing on Q^{PhN2Ph}.

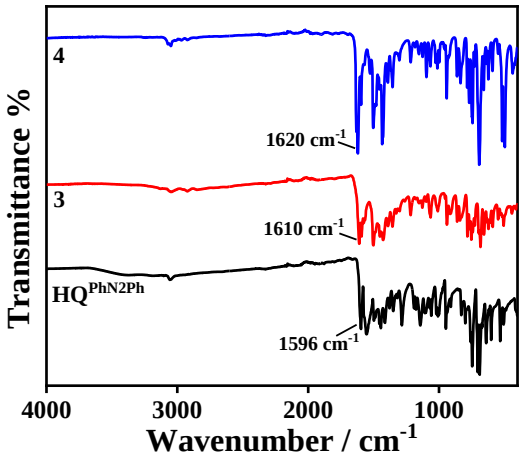

Figure 5. IR spectra of derivatives **3** and **4** compared to that of ligand HQ^{PhN2Ph}.

In the ^{1}H and ^{13}C NMR spectra, derivatives **1**, **3**, and **7** were measured in DMSO-d_6. While derivatives **2** and **4**-**6** carried out in $CDCl_3$. As show in **Figures 6** and **7**, the integration ratio of H resonances of Q^{PhN2Ph} and imidazole ligand is in accordance with the expected ratio of 1:2 (derivative **2**) or 1:1 (derivative **3**).

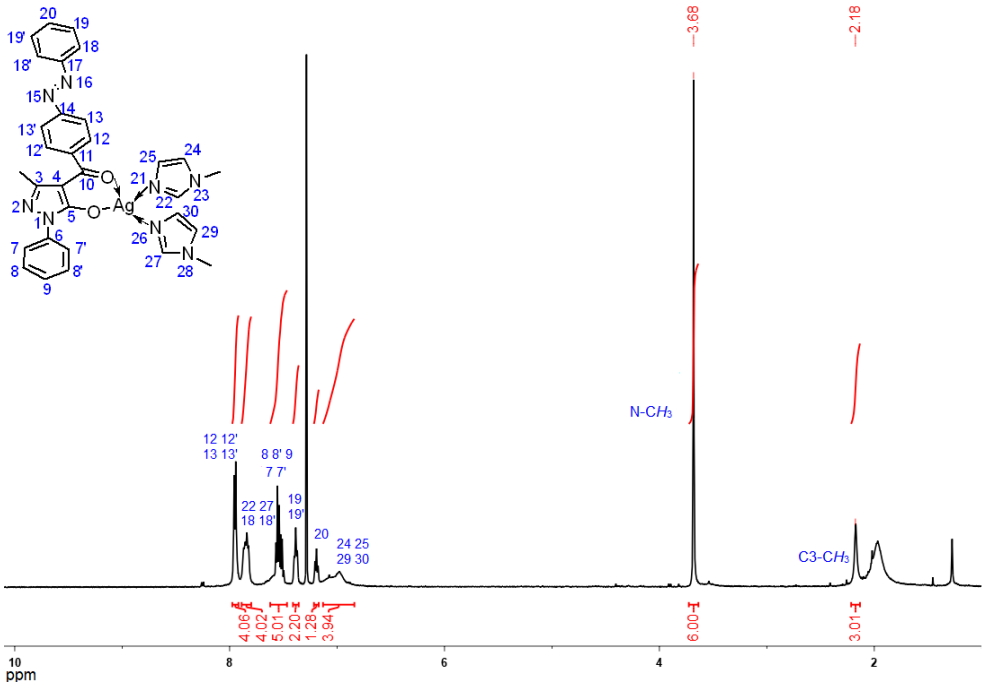

Figure 6. ^{1}H NMR spectrum of $[Ag(Q^{PhN2Ph})(Meim)_2]$, **2**.

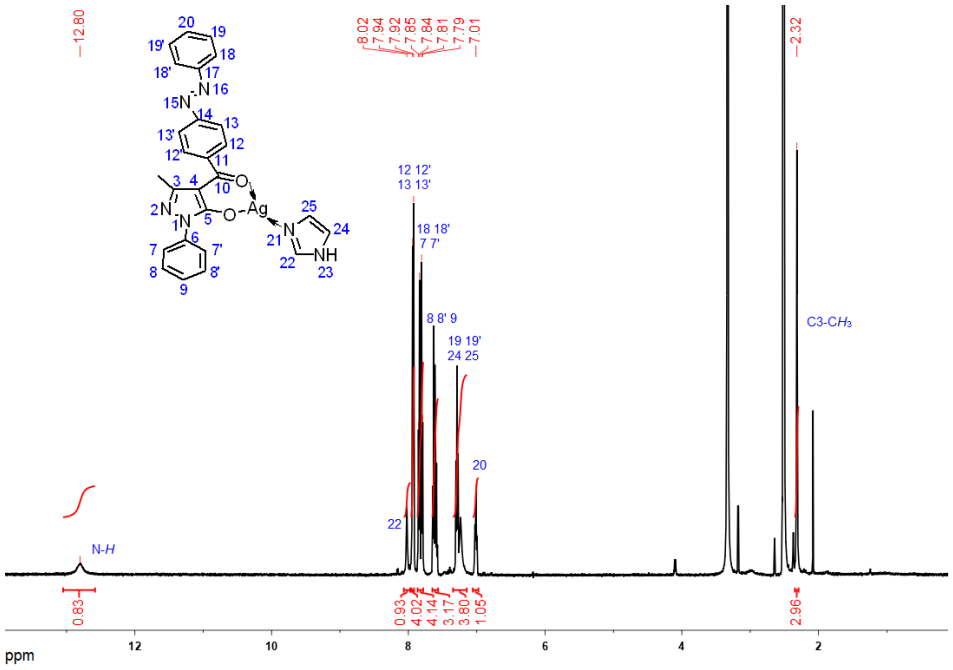

Figure 7. ^{1}H NMR spectrum of [Ag(Q^{PhN2Ph})(imH)], **3**.

The proton spectra of derivatives **4-7** show one set of resonances for Q^{PhN2Ph} and PR_3 with the integrations in accordance with the formulation proposed. The ^{1}H spectra of **4** and **6** have been presented in **Figures 8** and **9**, respectively.

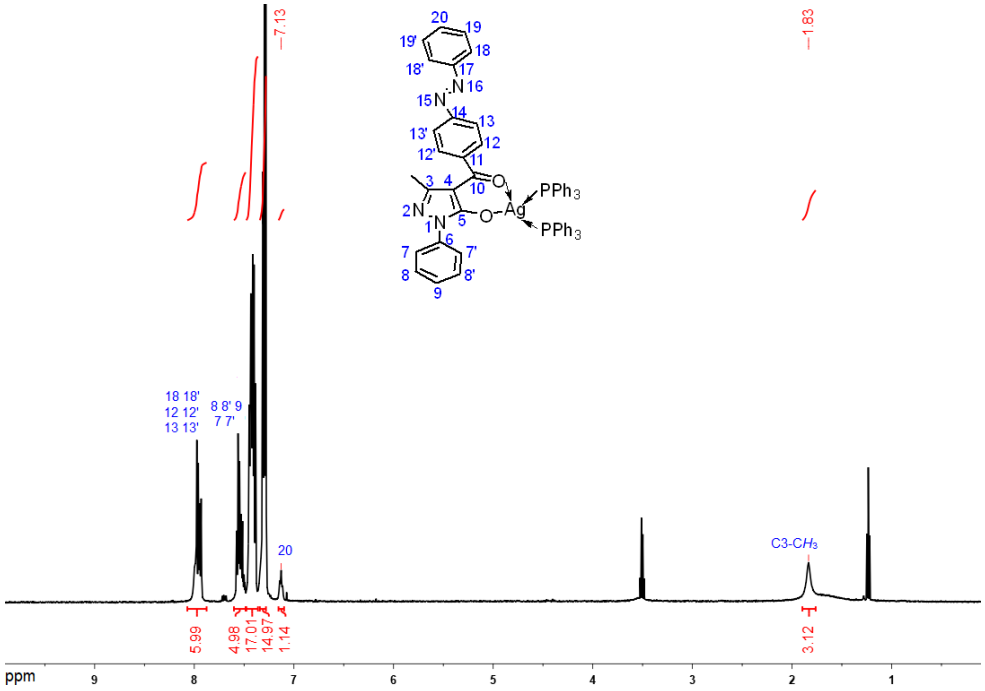

Figure 8. ^{1}H NMR spectrum of [Ag(Q^{PhN2Ph})(PPh_3)$_2$], **4**.

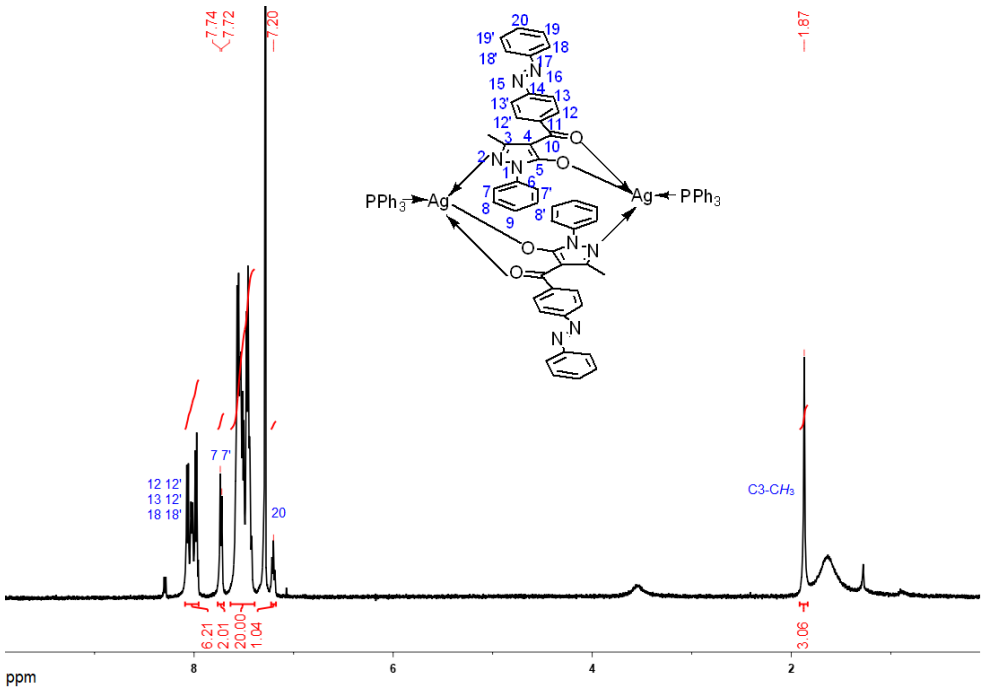

Figure 9. ^{1}H NMR spectrum of [Ag(Q^{PhN2Ph})(PPh$_3$)]$_2$, **6**.

Moreover, in the ^{31}P NMR studies at 25 °C have been recorded for **4**-**7**, also at -40 °C for **4**. The ^{31}P NMR spectrum of **4** shows only one single resonance at room temperature, which is observed at around 8 ppm, while on cooling the sample this signal becomes a double resonance. The loss of Ag−P information at room temperature may be related to the partial dissociation of the ligand. The ^{31}P NMR spectra of **6** and **7** show double resonance at room temperature at 17.0 and 40.1 ppm, respectively. While the signal for **5** is double doublets at room temperature, due to the coupling of ^{31}P nucleus to the NMR active isotopes of silver with spin 1/2, ^{107}Ag and ^{109}Ag, from which it is possible to determine $^{1}J(^{31}P–^{109}Ag)$ and $^{1}J(^{31}P–^{107}Ag)$ coupling constants. The coupling constant values ^{1}J(P–Ag) are indicative of the number of phosphine ligands bonded.

ESI-MS spectra of **2** and **5** were measured in acetonitrile. The signals correspond to species containing the ligand Q^{PhN2Ph} and silver. TGA analyses show that **1**–**7** are thermally stable species, with decomposition after 120 ℃ for **2**, at approximately 180 ℃ for **4**, over 200 ℃ for **1**, **3**, **5**-**7**.

2.3.2 Evaluation of antibacterial activity

The antibacterial activities of HQ^{PhN2Ph} ligand and derivatives **1**-**7** against *S. aureus* and *E. coli* were investigated by the inhibition zones obtained from oxford cup diffusion method. As shown in **Figure 10**, derivatives **1**-**7** exhibit significant inhibitory effects on both *S. aureus* and *E. coli*. While HQ^{PhN2Ph} only slightly inhibits the growth of bacterial. Obviously, these silver(I) complexes display better antibacterial performance against *E. coli* than those against *S. aureus*. This different behavior for Gram-positive and Gram-negative strains can be explained by their different cell wall structures. Because gram-negative bacteria have thinner cell walls than gram-positive bacteria, they are less protective against attack by chemical agents

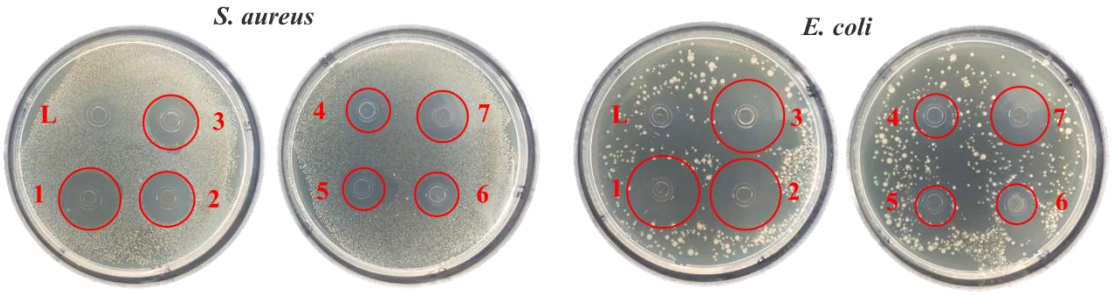

Figure 10. Photograph of inhibition zone of HQ^{PhN2Ph} and derivatives **1**-**7** against strain *S. aureus* and *E. coli*.

The inhibitory effects of these samples are summarized in **Table 1**. The derivatives **1-3** exhibit slightly larger inhibition zones ranging from 18 to 20 mm against *S. aureus* and 22 to 25 mm against *E. coli* at a sample concentration of 50 μg mL^{-1}. This may be due to the more stable structure of phosphorous coordinated compounds, which is not easy to release Ag^{+}. The superior antimicrobial activity of complexes **1**–**3** relative to **4**–**7** can be explained by the less crowded coordination environments in **1**–**3** with respect to the 4-coordinate Ag(I) centers in **4**–**7**, which afford different thermodynamic stability and different ability to release Ag^{+} ions.

Table 1. Inhibition zone of HQ^{PhN2Ph} and derivatives **1-7**.

	Ligand	**1**	**2**	**3**	**4**	**5**	**6**	**7**
S. aureus	**8**	**18**	**19**	**20**	**13**	**12**	**13**	**17**
E. coli	**8**	**23**	**22**	**25**	**15**	**13**	**13**	**24**

2.4 Conclusion

Novel silver(I) complexes were synthesized by interaction of a new acylpyrazolone ligand with $AgNO_3$, where imidazole, 1-methylimidazole and triphenylphosphine were selected as ancillary donors. The coordination of acylpyrazolonates with silver through the O_2-chelating face and the N_2 of the pyrazole ring in the $[Ag(Q^{PhN2Ph})]_n$ coordination polymers, while the O_2-chelating face was observed in complexes $[Ag(Q^{PhN2Ph})(Miem)_2]$, $[Ag(Q^{PhN2Ph})(imH)]$, $[Ag(Q^{PhN2Ph})(PR_3)_2]$ and $[Ag(Q^{PhN2Ph})(PR_3)]_2$. The antibacterial activity of

$[Ag(Q^{PhN2Ph})]_n$, $[Ag(Q^{PhN2Ph})(Miem)_2]$, and $[Ag(Q^{PhN2Ph})(imH)]$ is higher than that of $[Ag(Q^{PhN2Ph})(PR_3)_2]$ and $[Ag(Q^{PhN2Ph})(PR_3)]_2$ (R=PPh_3 or PCy_3) against both *S. aureus* and *E. coli*, possibly due to the more stable structures of 4-coordinate Ag(I) centers, which reduce the Ag^+ release.

CHAPTER 3

Synthesis of neutral and cationic silver(I) phosphino-complexes with pyrazolone ligands

3.1 Introduction

4-Acyl-5-pyrazolones are a variation of classical α-diketonates with a pyrazole fused to the chelating moiety, and are known for their selective extraction properties toward several metal ions [83]. They generally chelate metal centers in an unsymmetrical manner due to the different donor capabilities of their oxygen atoms [84]. Furthermore they have been shown to be able to bind to soft metal acceptors through the nitrogen of pyrazole. The peripheral groups of these ligands can be easily substituted, in which the substituents ranging from electron-withdrawing groups to electrondonating ones, thereby tuning their steric and electronic features [85].

The coordination chemistry of classical 4-acyl-5-pyrazolones with silver(I) has been studied previously, and it was shown that Ag(I) can bind not only to the oxygen atoms of 4-acyl-5-pyrazolonates but also to the nitrogen of the pyrazole [86,87]. Here, we used two types of 4-acyl-5-pyrazolones (**Scheme 3**). The two ligands are endowed with two completely different potential chelating surfaces in opposite directions through the binding of the pyridine ring to the pyrazole. The N_2-chelating moiety is similar to those of N,N'-aromatic bidentate ligands.

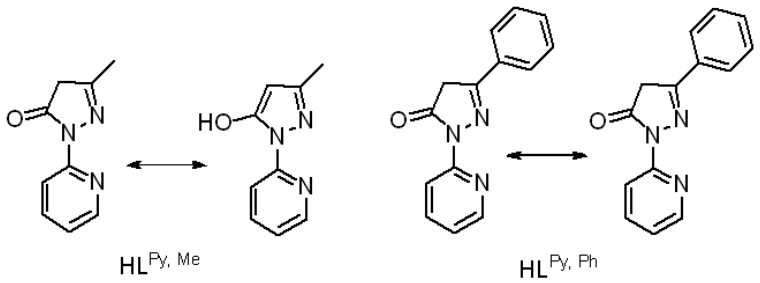

Scheme 3. $HL^{Py, Me}$ and $HL^{Py, Ph}$ used in this work.

3.2 Experimental section

3.2.1 Basic characterizations

All chemicals were purchased from Aldrich and used as received. Melting points were taken with a STMP3 Stuart scientific instrument on a capillary apparatus. ^{1}H, $^{13}C\{^{1}H\}$, and $^{31}P\{^{1}H\}$ NMR spectra were recorded with a 500 Bruker Ascend instrument operating(500 MHz for ^{1}H, 125 MHz for ^{13}C, and 202.6 MHz for ^{31}P). IR spectra were recorded from 4000 to 400 cm^{-1} with a PerkinElmer Spectrum Frontier FT-IR instrument. Elemental analyses were performed with a Fisons Instruments 1108 CHNS-O Elemental Analyzer. The ESI-MS were carried out with a Series 1100 MSI detector HP spectrometer, using acetonitrile mobile phase. TGA were performed in a N_2 atmosphere with a Perkin-Elmer STA 6000 simultaneous thermal analyzer. X-ray data were collected on an Oxford Xcalibur Gemini Eos diffractometer equipped with graphite-monochromated Cu-Kα radiation (λ = 1.5418 Å).

3.2.2 Synthesis of silver complexes

Synthesis of [Ag($L^{Py, Me}$)(PTA)]NO_3 (8). Firstly, $HL^{Py, Me}$ (112 mg, 0.64 mmol) was dissolved in MeOH (10 ml), and then $AgNO_3$ (54 mg, 0.32 mmol) was added to above solution. After 10 min stirring, PTA (50 mg, 0.32 mmol) was added. The mixture was stirred at room temperature for another 1h. A pink precipitate was filtered off, washed with MeOH, dried under vacuum to constant weight, and denoted as derivative **1**. Yield: 66%. It is soluble in H_2O, DMSO, and DMF. M.p. 201–204 °C. ^{1}H NMR (D_2O): δ 2.15s (3H, C3-CH_3), 4.27s, 4.56d (*J*=13.14 Hz), 4.67d (*J*=13.35 Hz, 14H, *H*4 and PTA), 7.21t (*H*9, *J*=6.16 Hz), 7.88t (*H*10, *J*=7.96 Hz), 8.03d (*H*11,

J=8.60 Hz), 8.28d (*H*8, *J*=4.66 Hz). $^{13}C\{^{1}H\}$ NMR (DMSO-d_6): δ 14.5s (C3-CH_3), 34.0s (*C*4), 50.2s, 72.3s, 72.4s, 89.0s, 102.1s, 113.8s, 121.0s, 141.0s, 149.6s (*C*3), 160.0s (*C*O). $^{31}P\{^{1}H\}$ NMR(D_2O): δ -76.2s (T=298 K). IR: ≅2920s, ν(–CH_2–), 1601vs (νC=O), 1582w, 1418s, 1284vs, 1240s, 1014vs, 978vs, 951vs, 765vs, 749s, 602s, 582s, 570m cm^{-1}. Anal. Calc. for $C_{15}H_{21}AgN_7O_4P$: C 35.87, H 4.21, N 19.52. Found: C 34.99, H 4.05, N 18.51. TGA-DTA (mg% vs. °C): heating from 30 to 600 °C with a speed of 8 °C min^{-1}; from 230 to 600 °C progressive decomposition, with a final black residual of 44.4% weight.

Synthesis of [Ag($L^{Py, Me}$)(PF_6)]NO_3 (9). Derivative **9** was prepared by the same method as **8**. Yield: 68.2%. It is soluble in DMSO, DMF, and acetonitrile. M.p. 203–206 °C. ^{1}H NMR (DMSO-d_6): δ 2.24s (3H, C3-CH_3), 4.32-4.67m (14H, *H*4 and PTA), 7.33t (*H*10, *J*=6.00 Hz), 8.03d (*H*10, *J*=7.94 Hz), 8.42-8.47m (*H*8, *H*11). $^{13}C\{^{1}H\}$ NMR (DMSO-d_6): δ 14.4s (C3-CH_3), 50.6s, 50.7s, 72.5s, 72.6s, 102.1s, 113.8s, 121.1s, 140.9s, 149.3s (*C*3), 160.0s (*C*O). $^{31}P\{^{1}H\}$ NMR(DMSO-d_6): δ -80.4s, -144.2s (sept, PF_6, T=298 K). IR: ≅2940s, ν(–CH_2–), 1605m (νC=O), 1572w, 1473m, 1439m, 832vs ν(P-F), 556s cm^{-1}. Anal. Calc. for $C_{15}H_{21}AgF_6N_6OP_2$: C 30.79, H 3.62, N 14.36. Found: C 31.92, H 3.70, N 13.57. ESI-MS (+, CH_3CN) m/z (%): 176 (50) $[HL^{py, Me}]^+$, 441 (100) $[Ag(HL^{py, Me})(PTA)]^+$, 971 (40) $[Ag(HL^{py, Me})(PTA)]_2^+$. TGA-DTA (mg% vs. °C): heating from 30 to 600 °C with a speed of 8 °C min^{-1}; from 230 to 600 °C progressive decomposition, with a final black residual of 39.1% weight.

Synthesis of [Ag($L^{Py, Me}$)(PPh_3)] (10). Firstly, $HL^{Py, Me}$ (88 mg, 0.5 mmol) was dissolved in MeOH (10 ml), then KOH (28 mg, 0.5 mmol) was added for

deprotonation. Afterward, $AgNO_3$ (85 mg, 0.5 mmol) and PPh_3 (131 mg, 0.5 mmol) were added to above solution. After stirring at room temperature overnight, the solvent was removed almost on rotary evaporator to obtain precipitate. Finally, the yellow powder was dried under vacuum to constant weight and denoted as derivative **10**. It is soluble in MeOH and chlorinated solvents and only slightly soluble in DMSO, DMF, and acetone. M.p. 198–202 °C. ^{1}H NMR ($CDCl_3$): δ 2.19s (3H, C3-C*H*$_3$), 5.07s (*H*4), 6.91t (*H*9, *J*=6.23 Hz), 7.43-7.59m (15H, H_{arom} of PPh_3), 7.75t (*H*10, *J*=6.23 Hz), 8.02d (*H*11, *J*=4.01 Hz), 9.14s (*H*8). ^{13}C{^{1}H} NMR ($CDCl_3$): δ 16.6s (C3-*C*H$_3$), 87.6s (*C*4), 114.0s, 118.0s, 129.3s, 129.4s, 130.7s, 131.0s, 131.2s, 133.7s, 133.8s, 139.3s, 147.0s (*C*3), 151.3s (*C*6), 153.5s (*C*O). ^{31}P{^{1}H} NMR($CDCl_3$): δ 18.7s (T=298 K), 18.6d [^{1}J(^{31}P–$^{109/107}$Ag)=652 Hz] (T=273 K), 18.5d [^{1}J(^{31}P–$^{109/107}$Ag)=669 Hz] (T=253 K), 18.4dd [^{1}J(^{31}P–^{109}Ag)=727 Hz, ^{1}J(^{31}P–^{107}Ag)=630 Hz] (T=223 K). IR: ≅3046w (νC$_{Ar}$=H), 1607m (νC=O), 1580m, 1471m, 1433m, 1345s (νC=C, νC=N, νC=N), 741s, 696vs, 494vs ν(P-Ph) cm^{-1}. Anal. Calc. for $C_{27}H_{23}AgN_3OP$: C 59.58, H 4.26, N 7.72. Found: C 58.89, H 4.29, N 7.95. ESI-MS (+, CH_3OH) m/z (%): 546 (88) [Ag(HL$^{py, Me}$)(PPh_3)]$^{+}$, 914 (100) [Ag$_2$(L$^{py, Me}$)(PPh_3)$_2$]$^{+}$, 1097 (15) [Ag$_3$(L$^{py, Me}$)$_2$(PPh_3)$_2$]$^{+}$. TGA-DTA (mg% vs. °C): heating from 30 to 600 °C with a speed of 8 °C min^{-1}; from 180 to 600 °C progressive decomposition, with a final black residual of 19.0% weight.

Synthesis of [Ag(L$^{Py, Me}$)(Cy$_3$P)] (11). Derivative **11** was prepared by the same method as **10**. It is soluble in DMSO, DMF and chlorinated solvents and only slightly soluble in MeOH. M.p. 169–172 °C. ^{1}H NMR ($CDCl_3$): δ 2.21s (3H, C3-C*H*$_3$),

1.71-2.02 and 1.20-1.51m (33H, H_{arom} of PCy_3), 5.13s (*H*4), 6.99s (*H*9), 7.73t (*H*10, *J*=7.58 Hz), 8.14s (*H*11), 9.04s (*H*8). $^{13}C\{^1H\}$ NMR ($CDCl_3$): δ 16.4s (C3-*C*H_3), 26.0s, 26.1s, 26.3s, 26.4s, 26.9s, 27.0s, 27.1s, 27.2s, 31.4s, 32.0s, 32.1s, 32.2s, 35.1s, 35.6 ((C_6H_{11})$_3$P), 87.1s (*C*4), 114.1s, 118.47s, 139.0s (*C*3), 146.8s, 151.2s (*C*5), 153.1s (*C*O). $^{31}P\{^1H\}$ NMR($CDCl_3$): δ 43.2dd [$^1J(^{31}P–^{109}Ag)$=702 Hz, $^1J(^{31}P–^{107}Ag)$=608 Hz] (T=298 K). IR: ≅2920s, 2850s ν(–CH_2–), 1604s ν(C=O), 1582m, 1462vs, 1434vs, 1345s, 767s, 734s cm^{-1}. Anal. calc. (%) for $C_{27}H_{41}AgN_3OP$: C 57.65 H 7.35, N 7.47. Found: C 53.14, H 7.07, N 8.17. ESI-MS (+, CH_3OH) m/z (%): 563 (100) $[Ag(HL^{py,\ Me})(PCy_3)]^+$, 950 (48) $[Ag_2(L^{py,\ Me})(PCy_3)_2]^+$. TGA-DTA (mg% vs. °C): heating from 30 to 6008C with a speed of 8 °C min^{-1}; from 240 to 600 °C progressive decomposition, with a final black residual of 24.3% weight.

Synthesis of [Ag($L^{Py,\ Me}$)(PTA)] (12). Derivative **12** was prepared by the same method as **10**. It is soluble in DMSO and DMF and only slightly soluble in MeOH, acetonitrile, acetone, and chlorinated solvents. M.p. 152–155 °C. ^1H NMR (DMSO-d_6): δ 2.05s and 2.15s (3H, C3-CH_3), 4.36d (6H, *J*=2.25 Hz, PTA), 4.42s, 4.45s, 4.60s, and 4.62s (6H, PTA), 7.06t (*H*9, *J*=6.15 Hz), 7.82t (*H*10, *J*=7.88 Hz), 8.29dd (*H*11, *J*=5.35 Hz), 8.34s (*H*4), 8.81d (*H*8, *J*=8.14 Hz). $^{13}C\{^1H\}$ NMR (DMSO-d_6): δ 16.7s (C3-*C*H_3), 50.8, 50.9s (*C*-P of PTA), 72.6, 72.7s (*C* of PTA), 112.4 (C*4*), 118.1, 139.6, 148.7, 151.1s (*C3*), 152.6s, 165.4s (*C*O). $^{31}P\{1H\}$ NMR(DMSO-d_6): δ -80.4s (T=298 K). IR: ≅2920s, ν(–CH_2–), 1602vs (νC=O), 1582 s, 1349vs, 1012vs, 968vs, 950vs, 747v, 583vs cm^{-1}. Anal. calc. (%) for $C_{15}H_{20}AgN_6OP$: C 41.02, H 4.59, N 19.13. Found: C 34.28, H 3.95, N 16.11.

TGA-DTA (mg% vs. °C): heating from 30 to 600 °C with a speed of 8 °C min^{-1}; from 180 to 600 °C progressive decomposition, with a final black residual of 75% weight.

Synthesis of [Ag($L^{Py, Ph}$)(PTA)]NO_3 (13). Derivative **13** was prepared by the same method as **8**. It is soluble in DMSO and DMF. M.p. 202.8–205.4 °C. ^{1}H NMR (DMSO-d_6): δ 4.21d (6H, *J*=7.96 Hz, PTA), 4.51d (3H, *J*=12.77 Hz, PTA), 4.64d (3H, *J*=12.44 Hz, PTA)), 6.03s (*H*4), 7.31-7.53m (*H*10, *H*14, *H*15, *H*15', *H*9), 7.21t (*J*=6.16 Hz), 7.91d (*H*13, *H*13', *J*=7.23 Hz), 8.03t (*H*11, *J*=8.51 Hz), 8.51d (*H*8, *J*=5.54 Hz). ^{13}C{^{1}H} NMR (DMSO-d_6): δ 72.2s, 49.8s (PTA), 86.4s (*C*4), 101.2s, 113.8s, 121.4s, 126.2s, 128.6s, 129.2s, 148.2s, 152.2s (*C*3), 160.5s (*C*O). ^{31}P{^{1}H} NMR(DMSO-d_6): δ -81.9s (T=298 K). IR: ≅2941w, ν(–CH_2–), 1602s ν(C=O), 1572w, 1473s, 1305vs, 1242s, 1025s, 971s, 950vs, 771s, 745s, 566s cm^{-1}. Anal. Calc. for $C_{20}H_{23}AgN_7O_4P$: C 42.57, H 4.11, N 17.38. Found: C 45.04, H 4.32, N 16.83. TGA-DTA (mg% vs. °C): heating from 30 to 600 °C with a speed of 8 °C min^{-1}; from 230 to 600 °C progressive decomposition, with a final black residual of 66.1% weight.

Synthesis of [Ag($L^{Py, Ph}$)(PPh_3)] (14). Derivative **14** was prepared by the same method as **11**. It is soluble in DMSO, DMF and chlorinated solvents and only slightly soluble in MeOH, acetonitrile, and acetone. M.p. 216–220 °C. ^{1}H NMR ($CDCl_3$): δ 5.52s (*H*4), 6.97-7.06m (3H, H_{arom} of PPh_3), 7.20t (*H*9, *J*=7.45 Hz), 7.32-7.38m, 7.40-7.45m (12H, H_{arom} of PPh_3), 7.49-7.54m (*H*15, *H*14, *H*14'), 7.79-7.84m (*H*10, *H*13, *H*13), 8.08d (*H*11, *J*=5.29 Hz), 9.24d (*H*8, *J*=8.28 Hz). 13C{^{1}H} NMR ($CDCl_3$): δ 86.3s (*C*4), 114.6s, 118.2s, 126.5s, 128.1s, 128.2s, 129.1s, 129.2s, 130.8s, 131.2s, 131.5s, 133.6s, 133.7s, 139.3s, 146.9s 151.7 (*C*3), 155.5s (*C*O). ^{31}P{^{1}H}

NMR($CDCl_3$): δ 17.4s (T=298 K), 15.9s (T=273 K), 17.4d [$^1J(^{31}P–^{109/107}Ag)$=662 Hz] (T=253 K), 17.4dd [$^1J(^{31}P–^{109}Ag)$=733 Hz, $^1J(^{31}P–^{107}Ag)$=635 Hz] (T=223 K). IR: ≅3054w (νC_{Ar}=H), 1605s (νC=O), 1584m, 1466s, 1435s, 1347m (νC=C, νC=N, νC=N), 774s, 740s, 696vs, 526s, 507s ν(P-Ph), 487s cm^{-1}. Anal. calc. (%) for $C_{32}H_{25}AgN_3OP$: C 63.38, H 4.16, N 6.93. Found: C 61.91, H 4.54, N 6.88. ESI-MS (+, CH_3OH) m/z (%): 607 (15) $[Ag(HL^{py,\ Ph})(PPh_3)]^+$, 976 (100) $[Ag_2(L^{py,\ Ph})(PPh_3)_2]^+$, 1321 (15) $[Ag_3(L^{py,\ Me})_2(PPh_3)_2]^+$. TGA-DTA (mg% vs. °C): heating from 30 to 600 °C with a speed of 8 °C min^{-1}; from 230 to 600 °C progressive decomposition, with a final black residual of 24.4% weight.

Synthesis of [Ag($L^{Py,\ Ph}$)(Cy_3P)] (15). Derivative **15** was prepared by the same method as **11**. It is soluble in MeOH, DMSO, DMF, acetone, and chlorinated solvents and only slightly soluble in acetonitrile. M.p. 119–120 °C. ^1H NMR ($CDCl_3$): δ 1.13-1.33, 1.39-1.51 and 1.71-1.99m (33H, H_{arom} of Pcy_3), 5.53s (*H*4), 7.05s (*H*9), 7.35s (*H*15, *H*14, *H*14'), 7.82d (*H*13, *H*13', *H*11, *J*=5.22 Hz), 8.19s (*H*10), 9.17s (*H*8). 13C{^1H} NMR ($CDCl_3$): δ 25.9s, 26.2s, 26.4s, 26.9s, 27.0s, 27.1s, 27.2s, 31.2s, 31.9s, 32.0s, 35.1s, 35.6 ((C_6H_{11})$_3$P), 86.3s (*C*4), 114.2s, 118.8s, 126.6s, 129.3s, 139.3s (*C*3), 146.5s (*C*O). $^{31}P\{^1H\}$ NMR($CDCl_3$): δ 42.2dd [$^1J(^{31}P–^{109}Ag)$=711 Hz, $^1J(^{31}P–^{107}Ag)$=615 Hz] (T=298 K). IR: ≅2920m, 2850m ν(–CH_2–), 1603s ν(C=O), 1471vs, 1435s, 1345s, 769s, 738s, 694s, 661s cm^{-1}. Anal. calc. (%) for $C_{32}H_{43}AgN_3OP$: C 61.54, H 6.94, N 6.73. Found: C 57.37, H 6.58, N 7.59. ESI-MS (+, CH_3OH) m/z (%): 626 (100) $[Ag(HL^{py,\ Ph})(PCy_3)]^+$, 1012 (90) $[Ag_2(L^{py,\ Ph})(PCy_3)_2]^+$. TGA-DTA (mg% vs. °C): heating from 30 to 600 °C with a speed of 8 °C min^{-1}; from

230 to 600 °C progressive decomposition, with a final black residual of 24.7% weight.

Synthesis of [Ag($L^{Py, Ph}$)(PTA)] (16). Derivative **16** was prepared by the same method as **11**. It is soluble in DMSO and DMF and only slightly soluble in MeOH, acetonitrile, acetone, and chlorinated solvents. M.p. 210–215 °C. ^{1}H NMR (DMSO-d_6): δ 4.21s (6H, *J*=2.25 Hz, PTA), 4.41d, 4.55d (6H, *J*=2.25 Hz, PTA), 5.15s (*H*4), 7.14t (*H*9, *J*=6.17 Hz), 7.35-7.51m (*H*10, *H*14, *H*14', *H*15), 7.85-7.90m (*H*13, *H*13'), 8.37d (*H*11, *J*=4.84 Hz), 8.99d (*H*8, *J*=8.70 Hz). ^{13}C{^{1}H} NMR (DMSO-d_6): δ 50.9, 51.0s (*C*-P of PTA), 72.7, 72.8s (C of PTA), 84.4s (*C*4), 113.2s, 118.8s, 126.4, 128.8, 129.1, and 129.s (C_{arom} of $HL^{Py, Ph}$), 134.9s, 140.1s, 149.2s, 151.2s, 153.9s (*C*3), 166.7 (*C*O). ^{31}P{1H} NMR(DMSO-d_6): δ -81.8s (T=298 K). IR: ≅2937w, ν(–CH_2–), 1604s ν(C=O), 1570m, 1471s, 1346vs,1013s, 970s, 949s, 768s, 745s, 698s, 666vs cm^{-1}. Anal. calc. (%) for $C_{20}H_{22}AgN_6OP$: C 47.92, H 4.42, N 16.77. Found: C 39.79, H 3.69, N 14.96. TGA-DTA (mg% vs. °C): heating from 30 to 600 °C with a speed of 8 °C min^{-1}, with a final black residual of 46.3% weight.

3.3 Results and discussion

The synthesis of derivatives **8-16** and their structure are shown in **Schemes 4** and **5**. In detail, derivatives **8** and **9** have been synthesized by reaction of $HL^{Py, Me}$ with PTA and AgX (X = NO_3 or PF_6) in methanol, respectively. Subsequently, derivatives **10**-**12** were obtained by interaction of $HL^{Py, Me}$ with $AgNO_3$ and several phosphorus donors (PPh_3, PCy_3, and PTA) with different electronic and steric features in methanol, in the presence of NaOMe.

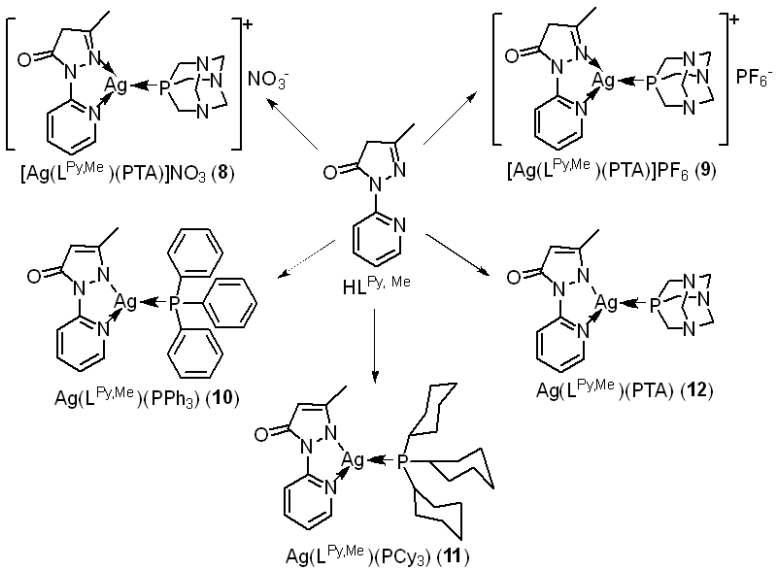

Scheme 4. Synthesis of derivatives **8**–**12**.

Derivative **13** has been synthesized by reaction of $HL^{Py, Ph}$ with PTA and $AgNO_3$ in methanol. Subsequently, derivatives **14-16** were obtained by interaction of $HL^{Py, Ph}$ with $AgNO_3$ and several phosphorus donors (PPh_3, PCy_3, and PTA) with different electronic and steric features, in the presence of NaOMe, respectively.

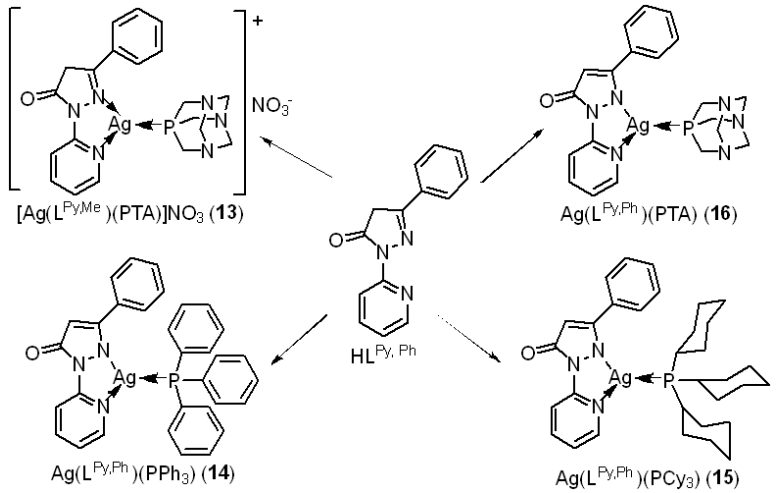

Scheme 5. Synthesis of derivatives **13**–**16**.

Derivatives **8-18** are air-stable solid compounds. The cationic structures of **1**, **2**,

and **13** and neutral structures of **10-12** and **14-16** were determined based on the dates mentioned in the experimental section. The ν(C=O) absorptions in the IR spectra of **9-16** are found essentially unchanged with respect to the neutral ligands ($HL^{Py, Me}$ and $HL^{Py, Ph}$), in accordance with the coordination of ligands primarily through the N atoms of the pyrazole and pyridine rings. In the IR spectra of derivatives **11** and **15**, containing PCy_3, absorptions at 2920 and 2850 cm^{-1} confirm the presence of $–CH_2$ groups (**Figure 11**).

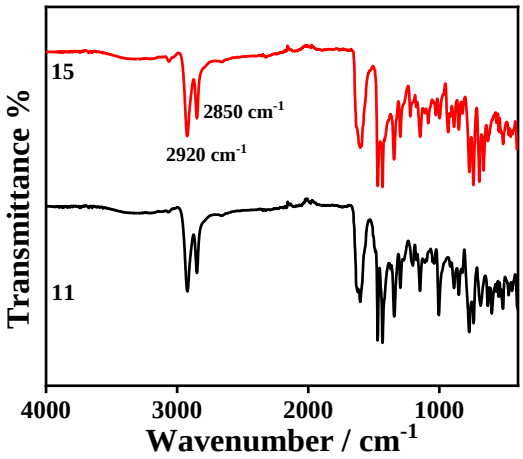

Figure 11. IR spectra of derivatives **11** and **15**.

In the ^{1}H, ^{13}C and ^{31}P NMR spectra, derivatives **8** was measured in D_2O, derivatives **10-11** and **14-15** were tested in $CDCl_3$. While derivatives **9**, **12-13** and **16** were carried out in DMSO-d_6. The proton and carbon NMR spectra of derivatives **8-16** show a unique broad set of resonances. The integrations of the signals are in accordance with the proposed formulation. The ^{1}H spectra of **8**, **10**, **13** and **14** have been presented in **Figures 12-15**, respectively. The ^{13}C NMR spectra of **8**–**16** exhibit one set of carbon resonances, and the presence of doublets due to C–P coupling help

to assign the signals arising from the C atoms of the phosphine ligand.

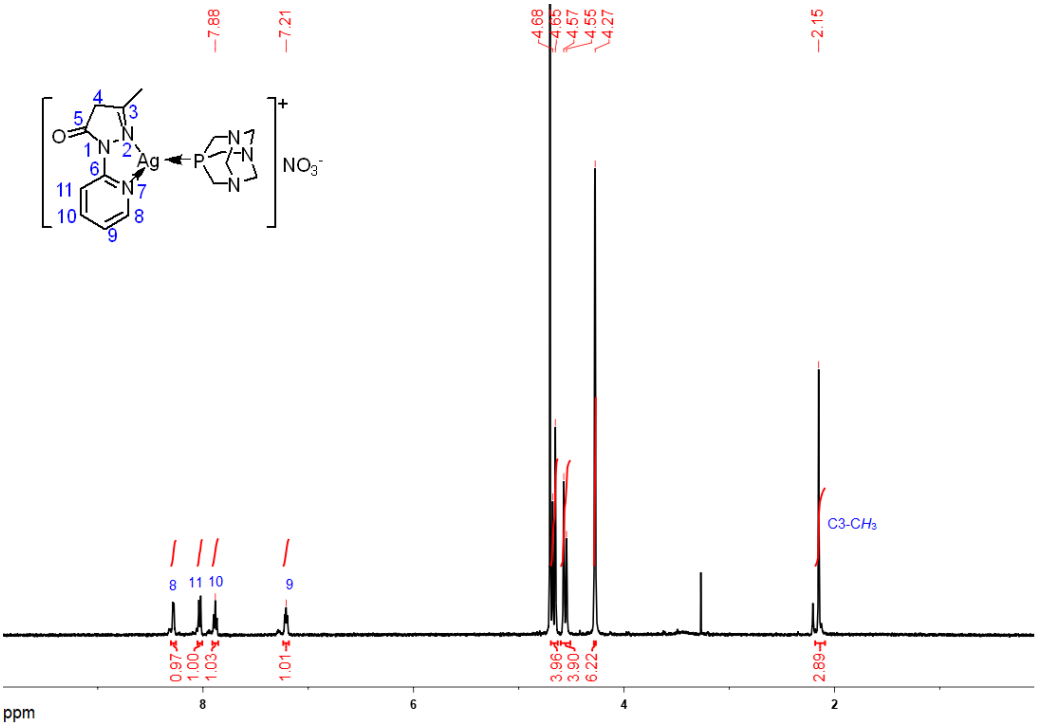

Figure 12. ^{1}H NMR spectrum of [Ag($L^{Py, Me}$)(PTA)]NO_3, **8**.

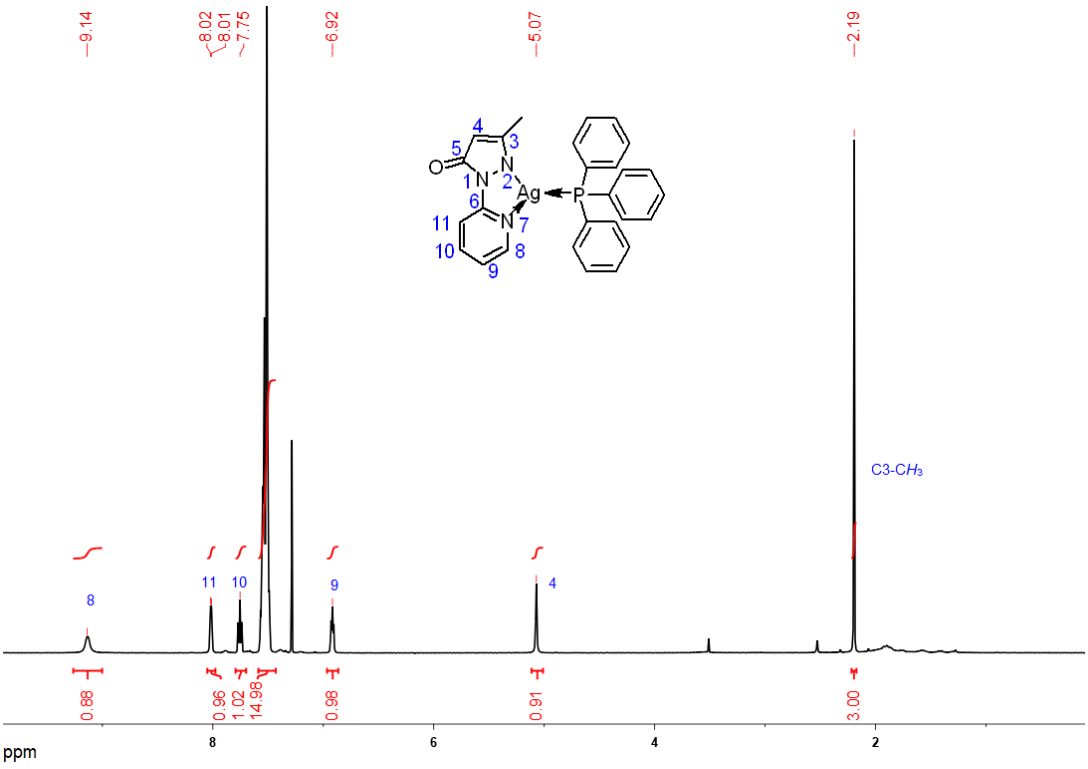

Figure 13. ^{1}H NMR spectrum of [Ag($L^{Py, Me}$)(PPh_3)], **10**.

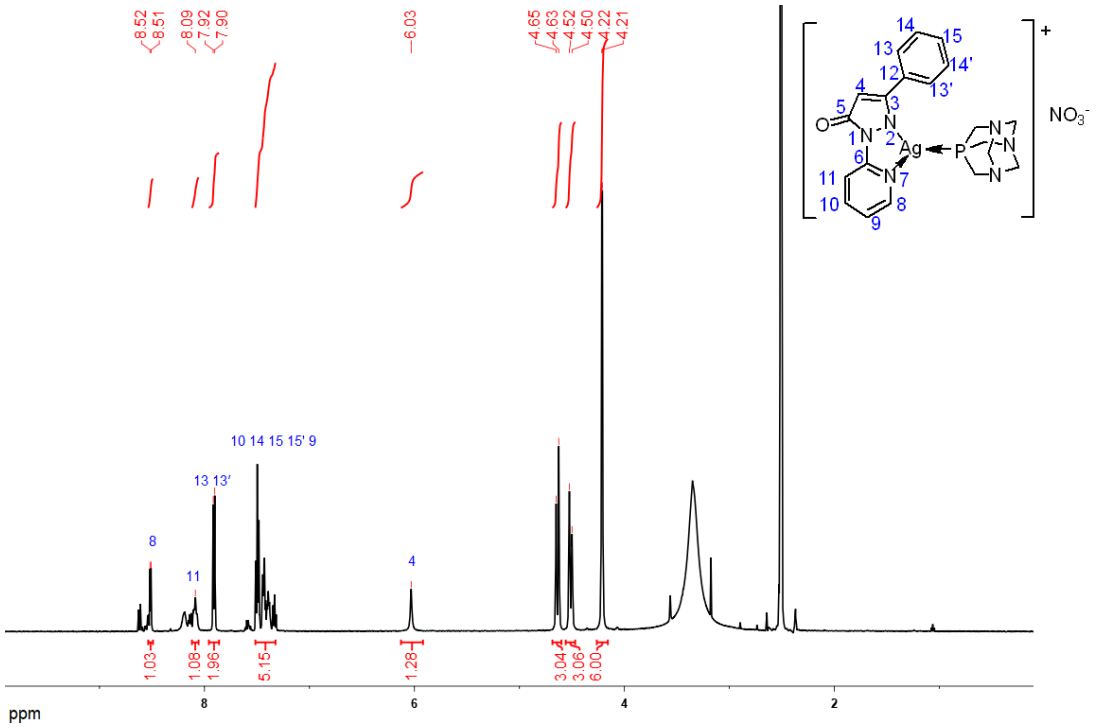

Figure 14. ^{1}H NMR spectrum of [Ag($L^{Py, Ph}$)(PTA)]NO_3, **13**.

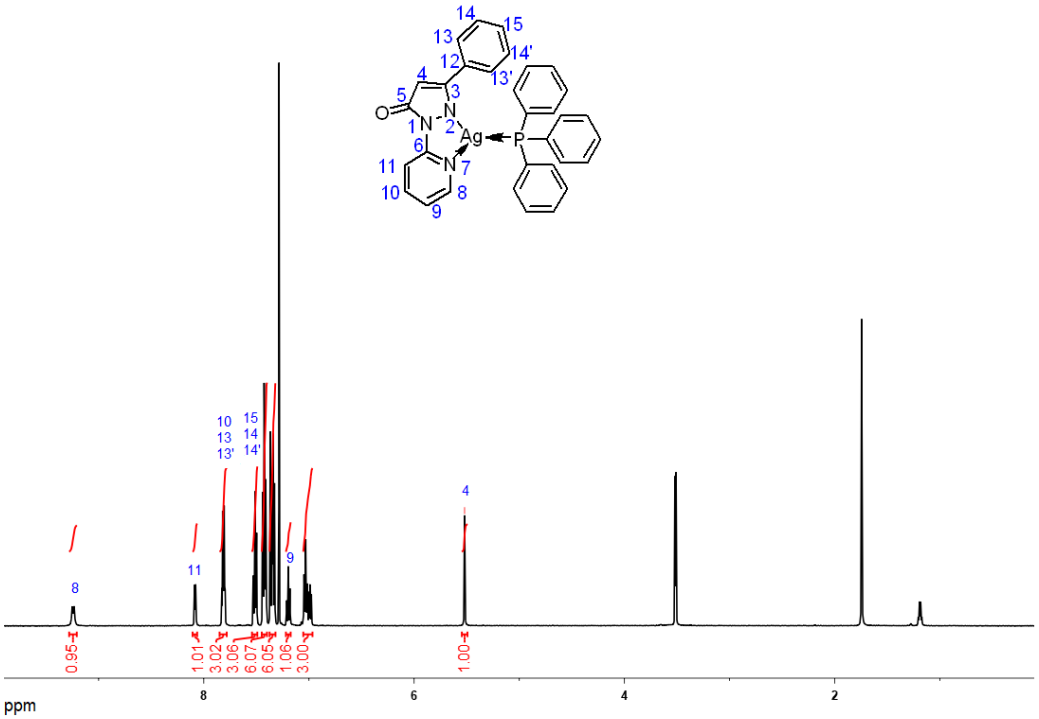

Figure 15. ^{1}H NMR spectrum of [Ag($L^{Py, Ph}$)(PPh_3)], **14**.

Moreover, the ^{31}P NMR studies at 25 °C have been recorded for **8**-**16**, also at -20 °C and -50 °C for **10** and **14**. In the ^{31}P NMR spectra of **8**, **12**, **13** and **16**, only one resonance has been detected at room temperature. In the ^{31}P NMR spectra of **9**, two different resonances were detected at -80.4 and -144.2 ppm, which could be explained by the presence of PTA and the formation of Ag-P species. The ^{31}P NMR spectra of **10** and **14** at room temperature show only one single resonance, while on cooling the sample this signal splits into one or two double doublets, from which the coupling constants of $^{1}J(^{31}P–^{109}Ag)$ and $^{1}J(^{31}P–^{107}Ag)$ can be determine. The values of coupling constant ^{1}J(P–Ag) are indicative of the number of phosphine ligands bond. Finally, the ^{31}P NMR spectra of **11** and **15** recorded at room temperature exhibit a pair of doublets at 43.2 and 42.2, respectively, with $^{1}J_{P\text{-}Ag}$ values higher than 600 Hz (typical for compounds containing only one phosphines bound to silver).

ESI-MS spectrum of **9** was measured in acetonitrile, **10**-**11** and **14**-**15** were measured in methanol. The signals correspond to species containing the ligand, silver and phosphorous donors. TGA analyses show that **8**–**16** are thermally stable species, with decomposition after 180 °C for **10** and **12**, above 230 °C for **8**-**9**, **11**, and **13**-**16**.

The X-ray crystal structure determination was performed on complexes **10**, **12** and **14**, confirming their molecular structures proposed in **Schemes 4** and **5**. As shown in **Figure 16**, the geometry on silver is essentially trigonal planar, the coordination environment being composed by a pyrazolone ligand acting as anionic chelating N_2-donor, through the nitrogen atoms of pyridine and of pyrazole, and by the phosphorus atom of the triphenylphosphine in **10** and **14** and tricyclohehyl phosphine

in **12**.

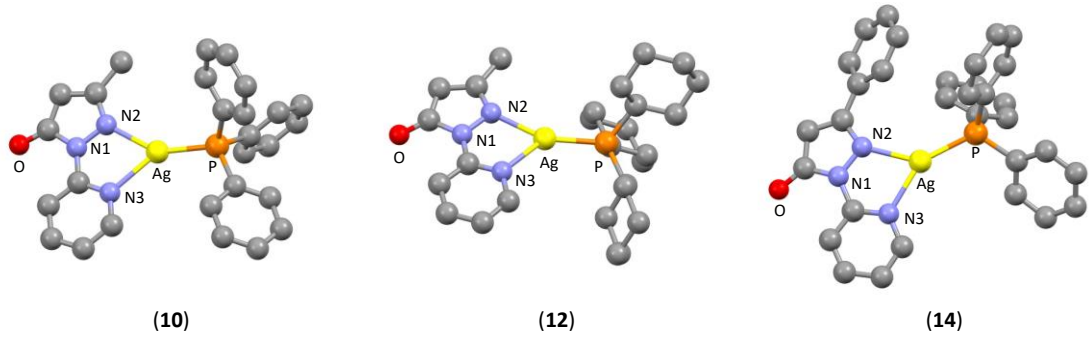

Figure 16. X-ray molecular structure of complexes **10**, **12** and **14**.

3.4 Conclusion

Novel silver(I) complexes have been synthesized by interaction pyrazolone ligands with $AgNO_3$, triphenylphosphine were selected as ancillary donors. The coordination of pyrazolone ligand to silver through the N_2-chelating mode, cationic species $[Ag(L^{Py,\ Me})(PTA)]NO_3$, $[Ag(L^{Py,\ Me})(PTA)]PF_6$, and $[Ag(L^{Py,\ Ph})(PTA)]NO_3$, and have been obtained. In the presence of $NaOCH_3$, neutral species $[Ag(L^{Py,\ Me})(PR_3)]$, $[Ag(L^{Py,\ Me})(PTA)]$, $[Ag(L^{Py,\ Ph})(PR_3)]$, and $[Ag(L^{Py,\ Ph})(PTA)]$ (R=Ph or Cy) were obtained.

CHAPTER 4

Copper-based polymer-metal-organic framework embedded with Ag nanoparticles: long-acting and intelligent antibacterial activity and accelerated wound healing

4.1 Introduction

Efficient wound healing is essential in the therapy of infected wounds caused by trauma, emergency surgery, and battlefield rescue [37]. Four steps, i.e., hemostasis, inflammation, cell proliferation, and tissue remodeling, are often involved in the wound healing process [88], in which bacterial infection should be effectively inhibited to improve the therapeutic effect [89]. Despite conventional antibiotics have superior antibacterial ability, their abuse usually result in the persistent drug resistance of organism [90]. In addressing these shortcomings, different antimicrobial agents have been developed along with the progress of nanotechnology and nanomaterials for treating bacterial infection [91]. These nanomaterials exhibit excellent antibacterial performances, bacterial killing via physical contact damage [92], chemical damage (oxidative stress) [93], or photo-induced damages (including photocatalytic therapy [94], photothermal therapy [95], and antimicrobial photodynamic therapy [96]). Some common nanomaterials such as MoS_2 [97], CuO [98], ZnO [99], Ag_3PO_4 [100], Ag [101], and TiO_2 [102] can be directly used as antibacterial agents to kill bacteria. However, these metal/metal oxides cannot provide sustained antibacterial effect and high durability due to metal agglomeration and oxidation.

To date, some efficient scaffolds such as yeast-derived microparticles [103], microgels [104], liposomes [105], graphene [106], graphene oxide [107], single-walled nanotubes [108], MXene [109], glycosylated nanoparticles [110], porous-organic frameworks (such as MOFs [111] and covalent-organic frameworks

[112]), and polymeric nanoparticulates [113] are often used as delivery vehicles for loading metal/metal oxide antimicrobial agents [114]. Among these scaffolds, MOFs synthesized by coordinating metallic nodes of single metal ions or few metal ion clusters with organic linkers, as a hybrid crystalline material with a periodic structure and porous interior, have been flourished and extensively applied in biomedical fields, because of their high specific surface area, tunable porosity, flexible skeletons, and adjustable and modifiable channels [115]. Varieties of metal nanoparticles, such as Ag, Cu, ZnO, TiO_2, and Fe_3O_4, with outstanding bacterial abilities are often combined with MOFs [116]. These MOF-based composites, as novel antibacterial systems, can exhibit multiple bacteriostatic mechanisms [117]. Among different metal NPs, Ag NPs, as an excellent broad-spectrum antibacterial agent [118], can be delivered to cell walls to destroy bacterial cells and then cause the leakage of intracellular contents through comprehensive functions such as physical interactions, generation of ROS, and ion release, overcoming the bacterial resistance to Ag NPs antimicrobial therapeutics [119]. However, the exploitation of Ag NPs is greatly inhibited because of size selection, for which only Ag NPs with diameters of 1-10 nm exhibit a preferential antibacterial effect [120] and feasible oxidation [121]. The integration of diverse MOFs with Ag NPs can merge antibacterial effect caused by the controlled release of Ag^+ and metal ions from MOF matrices.

Apart from MOFs, polymeric networks often serve as platforms for carrying Ag NPs for effective wound healing because of their tunable architecture, biocompatibility, biodegradability, hemostatic effects, and antimicrobial properties

[122]. Meanwhile, polymer materials with uniform pores can provide a scope to encapsulate Ag NPs [123]. Considering the merits of polymers and MOFs as antibacterial platforms, constructing a novel polymer-MOF-based scaffold is desirable for loading Ag NPs to improve the integrated antibacterial efficiency. Recently, polymer MOFs (polyMOFs) have been reported as a new class of hybrid metallopolymer material that combines features of polymers (such as the facile fabrication of films, good processability, and chemical stability) and crystalline MOFs (such as high crystallinity, well-determined structures, and permanent porosity) [124]. Consequently, polyMOFs prepared using polymer as ligand have enhanced stability, hierarchical porosity [125], and controlled morphologies [126]. Moreover, in comparison with MOFs developed using small molecules as ligands, the solution stability of polyMOFs can be significantly improved because of the existence of a cross-linking ligand [127].

Herein, we have prepared a copper-based polymer-MOF (denoted as polyCu-MOF) using polyether containing 1,4-benzenedicarboxylic acid (H_2BDC) units as building block, 4,4′-bipyridine as co-ligand, and copper ions as metal-coordinated centers (**Scheme 6**). Subsequently, the gained polyCu-MOF serves as a novel carrier for loading abundant Ag NPs (represented as polyCu-MOF@AgNPs). The antibacterial performances against the Gram-positive bacteria, *Staphylococcus aureus*, and the Gram-negative bacteria, *Escherichia coli*, were investigated using the growth curve and plate colony counting method. The antibacterial properties of Cu-MOF@AgNPs constructed using H_2BDC as ligand was

also carried out for comparison. After assessing the cytocompatibility and hemocompatibility of polyCu-MOF@AgNPs, wound healing rate, histopathological examinations, and plate counting method were also used to evaluate the *in vivo S. aureus*-infected wound therapeutic effects. The present work not only extends the biomedical application of MOF-based platforms, but also provides a potential and robust strategy for healing bacteria-infected wound.

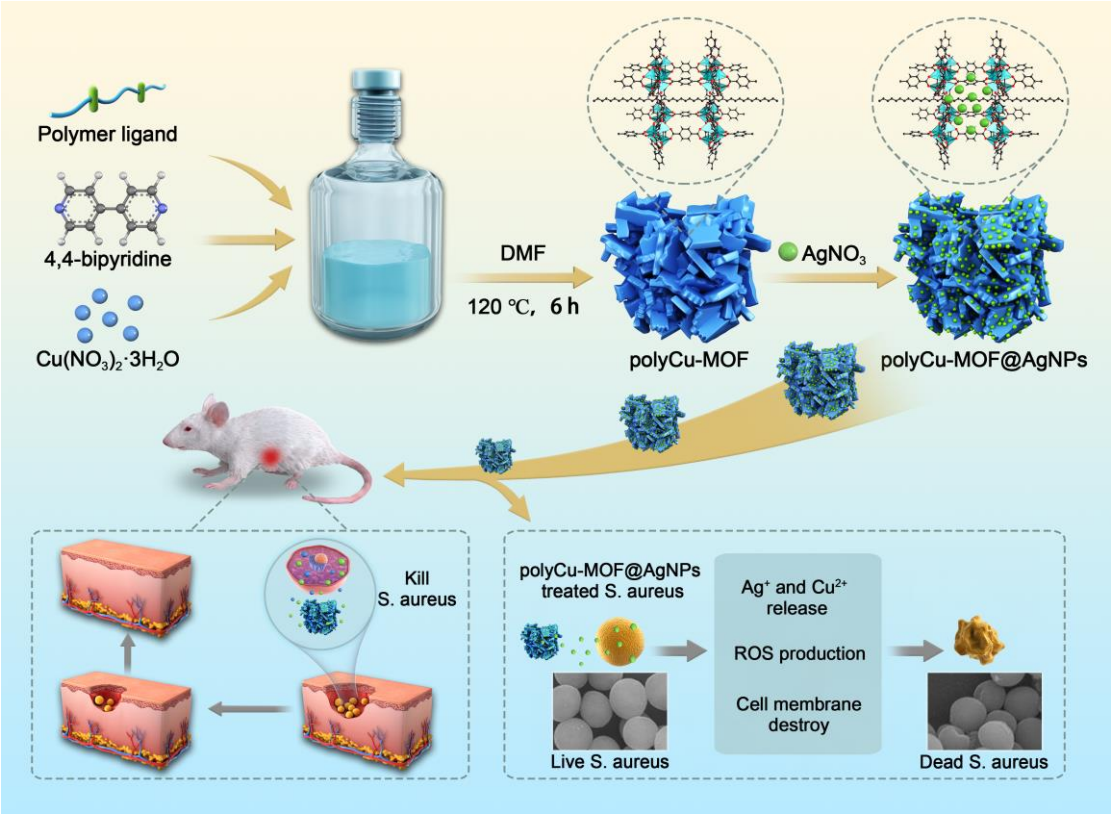

Scheme 6. Schematic diagram of the synthesis procedure and antibacterial and wound healing activities of polyCu-MOF@AgNPs hybrid.

4.2 Experimental section

4.2.1 Chemicals and regents

2,5-Dihydroxy terephthalic acid, 1,8-dibromooctane, and 4'-bipyridine were

purchased from Aladdin Chemical Regent Co., Ltd. (Shanghai, China). Sodium bicarbonate ($NaHCO_3$), silver nitrate ($AgNO_3$), sodium borohydride ($NaBH_4$), potassium carbonate (K_2CO_3), and sodium hydroxide (NaOH) were bought from Sinopharm Chemical Regent Co., Ltd. (Shanghai, China). Sulfuric acid (H_2SO_4, 98%), hydrochloric acid (HCl, 37%), methanol, tetrahydrofuran (THF), ethanol (EtOH), and dichloromethane (CH_2Cl_2) were supplied by Tianjin Fuyu Fine Chemical Reagent Co., Ltd. (Tianjin, China). Live & Dead Bacterial Staining Kit (40274ES60) was from Yeasen Biotech Co., Ltd. (Shanghai, China), while 2′,7′- dichlorodihydrofluorescein diacetate (H_2-DCFDA) was purchased from Beijing Solarbio Science & Technology Co., Ltd (China). *Escherichia coli* (*E. coli*) (ATCC25922) and *Staphylococcus aureus* (*S. aureus*) (ATCC6538) were provided by Beijing Biobw Biotech Co., Ltd. (China). All solvents and reagents were of analytical grade and used as received. All solutions were prepared with Milli-Q water (≥ 18.2 MΩ cm).

4.2.2 Synthesis of the polymer ligand

Preparation of diethyl 2,5-dihydroxyterephthalate: According to the previous literature, the fabrication procedure of as follows [128]. 2,5-Dihydroxyterephthalic acid (1.98 g, 10 mmol) was dissolved in 100 mL of methanol and introduced to a 250 mL round bottom flask. Afterward, 4 mL of concentrated H_2SO_4 was slowly added and heated at 80 °C for 12 h. After cooling to room temperature, the saturated solution of $NaHCO_3$ was introduced to the mixture until pH = 7. The crude product was extracted with dichloromethane three times. The organic solution was removed by

rotary evaporator. Finally, yellow solid compound was obtained.

Synthesis of the poly(diethyl terephthalate) ligand (L8-e): The mixture of prepared diethyl 2,5-dihydroxyterephthalate (1.06 g, 4.7 mmol), 1,8-dibromooctane (1.28 g, 4.7 mmol), K_2CO_3 (2.6 g, 19 mmol), and 20 mL of DMF was stirred at 100 °C for 24 h under N_2 atmosphere. The reaction mixture was filtered to remove potassium carbonate. After that, the filtrate was poured into water. Then the precipitation obtained from water was washed with methanol for three times and dried in a vacuum oven at 60 °C.

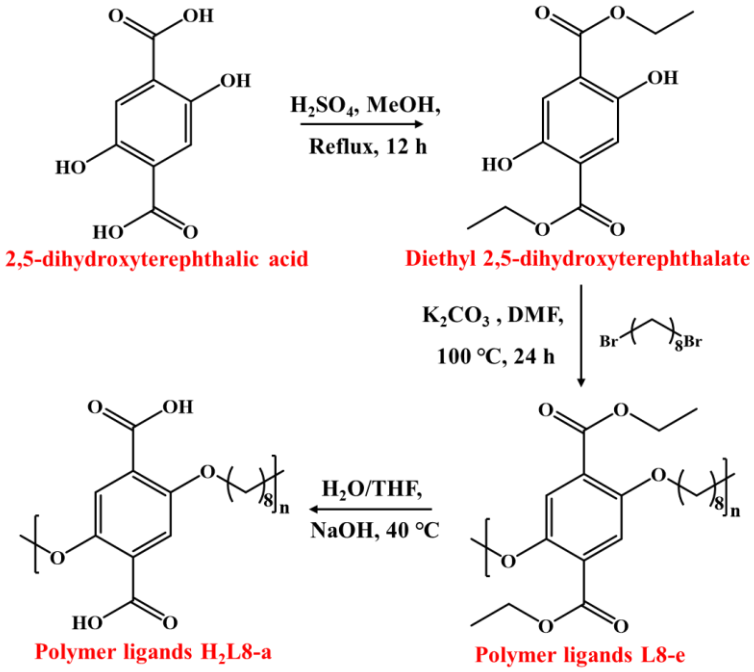

Scheme 7. Synthesis procedure of the polymer ligand.

Synthesis of the poly(terephthalic acid) ligand (H_2L8-a): The polymer ligand of L8-e was added to H_2O/THF (1:1, 40 mL), following by introducing NaOH (300 mg). The mixture was stirred at 40 °C to form a transparent solution. The solution was acidified to pH = 1 using a 4 M HCl solution after the evaporating reaction of THF

under reduced pressure. The resultant solid was collected by vacuum filtration and washed with water.

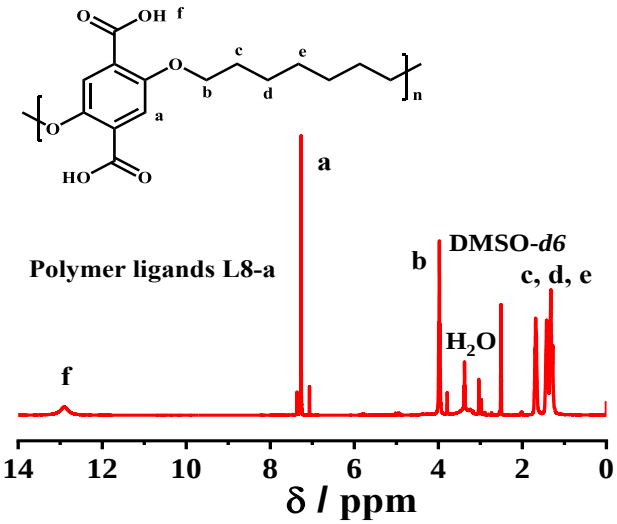

Figure 17. ^{1}H-NMR spectrum of the polymer ligand.

As shown **Figure 17**, the 1H-NMR spectrum of H_2L8-a gave the carboxyl group signal H_f at 12.92 ppm, thereby confirming the fabrication of carboxyl group through by hydrolysis of ester group. The signal located at 7.25 ppm was ascribed to the benzene ring signal H_a. Moreover, the signals at 3.98, 1.68, 1.42, and 1.32 ppm were derived from the aliphatic (H_{b-e}) protons, confirming the successful preparation of H_2L8-a by Williamson ether synthesis route.

4.2.3 Preparation of polyCu-MOF and Cu-MOF

Poly(terephthalic acid) ligand (H_2L8-a 0.25 mmol by monomer repeat unit), 4,4'-bipyridine (19.5 mg, 0.125 mmol), and $Cu(NO_3)_2 \cdot 3H_2O$ (60.4 mg, 0.25 mmol) were dissolved into the mixture of DMF (5 mL) and ethanol (0.25 mL) and

thoroughly stirred. The obtained homogeneous solution was heated at 85 °C for 24 h. After slowly cooling down to room temperature, polyCu-MOF with green color was isolated by centrifugation, following by washed with DMF and CH_2Cl_2. Further, Cu-MOF was synthesized with the same approach by replacing polymer-ligand and 4,4'-bipyridine with H_2BDC.

4.2.4 Preparation of polyCu-MOF@AgNPs and Cu-MOF@AgNPs hybrids

The polyCu-MOF@AgNPs hybrid was synthesized through a simple wet chemical method at room temperature. Briefly, 150 mg polyCu-MOF and 50 mg $AgNO_3$ were dispersed into 20 mL of methanol. The mixed suspension was stirred for 3 h in dark to ensure that Ag^+ ions were fully absorbed into polyCu-MOF, and rinsed with deionized water to remove possible residuals. Then, 2 mL of $NaBH_4$ (10 mg mL^{-1}) was added to the formed suspension and stirred for further 30 min, guaranteeing the reduction of Ag^+ ions to Ag NPs. Finally, polyCu-MOF@AgNPs hybrid was formed. As comparison, the Cu-MOF@AgNPs composite was prepared by the similar method, but replacing polyCu-MOF with Cu-MOF.

4.2.5 Basic characterizations

Powder X-ray diffraction measurements (PXRD) patterns were taken on a Rigaku D/Max-2500 X-ray diffractometer with Cu Kα radiation (λ = 0.15406 nm). Fourier transform infrared (FT-IR) spectra were recorded on a Bruker TENSOR27 spectrometer. Raman spectra were taken on a Renishaw inVia spectrometer. X-ray

photoelectron spectroscopy (XPS) were recorded to analyze the chemical environment on an AXIS HIS 165 spectrometers (Kratos Analytical, Manchester, U.K.) with a monochromatized Al Kα X-ray source (1486.71 e KαV photons). The surface morphology of the as-prepared samples was investigated by field emission scanning electron microscope (FE-SEM, JSM-6490LV, Japan) and high-resolution transmission electron microscopy (HR-TEM, FEI TECNAI G2 F30, United States) with a field emission gun of 200 kV. The elemental distribution was analyzed via energy dispersive spectrometer (EDS) on FESEM. Brunauer-Emmett-Teller (BET) method was employed to determine the specific surface area of samples by using a Micromeritics ASAP2022 instrument.

4.2.6 *In vitro* antibacterial effect

Antibacterial ability of the polyCu-MOF@AgNPs hybrid was investigated by taking two bacterial strains, *S. aureus* and *E. coli*, as model bacteria and using both the growth curve and plate colony counting method. Meantime, polyCu-MOF, Cu-MOF, and Cu-MOF@AgNPs were employed for comparison. To evaluate the effect of the material dosage on the bacterial growth, bacteria with the initial density of 1×10^6 CFU mL^{-1} were incubated with different concentrations of polyCu-MOF@AgNPs and Cu-MOF@AgNPs suspensions (2, 5, 10, 20, and 50 μg mL^{-1}). As for polyCu-MOF and Cu-MOF, the final concentrations of 20, 50, 100, 200, and 500 μg mL^{-1} were applied. For comparison, metal compounds of $Cu(NO_3)_2$ and $AgNO_3$ were used for providing free metal ions of Cu^{2+} and Ag^+, respectively, as well

as their mixture, in which their concentration was set as same as the determined release amount of Cu^{2+} and Ag^{+} from polyCu-MOF@AgNPs. All suspensions were separately transferred to a tube containing 5 mL LB, and continuously shaken at 200 rpm for 10 h (37 °C). The mixture was drawn every 2 h, and the value of optical density at 600 nm (OD_{600}) was measured to obtain the bacterial growth curves of treatments. To construct the growth curves, the OD of the LB medium was subtracted from the bacterial OD in all groups. For these groups treated with MOF, corresponding blank control (i. e., medium without bacteria and containing MOFs) was also measured to eliminate errors caused by MOF aggregation.

To quantitate the antibacterial activity of all samples, colony counting was employed on an LB agar plate. Different nanomaterials were separately incubated with the bacteria suspension (1×10^6 CFU mL^{-1}) for 8 h. The resulting mixture (100 μL) was diluted 10,000 times with LB media. After that, the diluted solution (10 μL) was dispersed onto LB agar plates and stood for 24 h. The antibacterial ratio was obtained by counting the bacterial colonies and calculated using the following formula:

$$\text{Antibacterial rate (\%)} = \left(1 - \frac{\text{CFU(experimental group)}}{\text{CFU(control group)}}\right) \times 100\%$$

The membrane damage was investigated by Live/Dead kit containing calcein acetoxymethyl ester (Calcein-AM, green fluorescent dye for live bacteria) and propidium iodide (PI, red fluorescent dye for dead bacteria). *S. aureus* and *E. coli* (1×10^6 CFU mL^{-1}) were treated with different materials (10 μg mL^{-1}) for 12 h,

followed by centrifuged at 5000 rpm at 4 °C. The precipitation was re-suspended in fresh LB medium. Then, the mixture solution of Calcein-AM and PI was added and incubated for 20 min at 37 °C. The images of these samples were recorded by a confocal laser scanning microscope (CLSM LSM710, ZEISS, Germany).

4.2.7 Bacterial morphological studies

FE-SEM analysis was carried out to probe the morphological change of bacteria before and after incubated with materials. Bacteria (1×10^6 CFU mL^{-1}) were incubated with different suspensions of polyCu-MOF, Cu-MOF, polyCu-MOF@AgNPs, Cu-MOF@AgNPs (10 μg mL^{-1}), $Cu(NO_3)_2$ (0.9 μg mL^{-1}), $AgNO_3$ (1.1 μg mL^{-1}), the mixture of $Cu(NO_3)_2$ and $AgNO_3$ for 12 h. Meanwhile, bacteria in LB medium without material were used as the control. Afterward, the treated bacteria were centrifuged and fixed with 2.5% glutaraldehyde for 4 h, followed by rinsed with 0.1 M phosphate buffer solution (PBS) and dehydrated in an ascending ethanol series (30, 50, 70, 80, 90, and 100%) for 15 min. After thoroughly drying and sputtering gold, the surface morphologies of bacteria were recorded by FE-SEM.

4.2.8 Release behaviors of Cu^{2+} and Ag^{+} ions *in vitro*

To study the release behaviors of Cu^{2+} and Ag^{+} ions, polyCu-MOF@AgNPs, Cu-MOF@AgNPs, polyCu-MOF and Cu-MOF (2 mg) were separately dispersed into 40 mL of PBS (pH=7.4, 37 °C), in which the diffusion media were taken out at different intervals (2, 4, 8, 12, 24, and 48 h). Afterward, the obtained mixture was

centrifuged, while the supernatant was filtered through a 0.22 μm membrane to ensure only Cu^{2+} and Ag^{+} ions remained in the solution. The release behaviors of Cu^{2+} and Ag^{+} ions from polyCu-MOF@AgNPs (10 μg mL^{-1} and 50 μg mL^{-1}) in LB medium at different pH (6.0, 6.5, and 7.0) were also measured by the same procedure. The concentrations of Cu^{2+} and Ag^{+} ions were determined by inductively-coupled plasma atomic emission spectrometry (ICP-AES, Analytik Jena, contrAA 700).

4.2.9 Detection of the intracellular ROS level

The generated efficiency of ROS was evaluated using the fluorescent dye H_2-DCFDA assay. Briefly, *S. aureus* and *E. coli* (1×10^6 CFU mL^{-1}) were separately and initially incubated with H_2-DCFDA (200 μM) for 0.5 h at 37 °C in dark, followed by adding different concentrations of polyCu-MOF@AgNPs (2, 5, 10, 20, and 50 μg mL^{-1}). The bacterium suspensions were further incubated for another 4 h, for which the fluorescence intensity was recorded at 523 nm with excitation at 495 nm by a microplate reader. Cu-MOF@AgNPs, polyCu-MOF and Cu-MOF (50 μg mL^{-1}) were determined by the same way. Moreover, H_2O_2 was used as a positive control for ROS production in a concentration of 1 mM, while untreated bacterium cells were used as the negative control.

4.2.10 Cytotoxicity assay and hemolysis assay *in vitro*

The cytotoxicity of Cu-MOF, polyCu-MOF, Cu-MOF@AgNPs, and polyCu-MOF@AgNPs were certified by 3-(4, 5-dimethylthiazol-2-yl)-2,

5-diphenyltetrazolium bromide (MTT) assay using fibroblast cells (L929 cells). The cells (8×10^3 cells $well^{-1}$) were cultured on 96-well plates at a density of 8000 cells $well^{-1}$ and kept in an atmosphere of 5% CO_2 at 37 °C for 24 h. Then, the cells were washed with PBS twice, and recultured with Dulbecco's Modified Eagle's Medium (DMEM) for 12 h. After treatment, MTT (5 mg mL^{-1}, 20 μL) was added to each well for cultured another 4 h. Finally, the medium was removed, and the purple formazan crystals were dissolved in 200 μL DMF. The absorbance at 490 and 630 nm were measured by using a microplate reader (Thermo K3, USA).

In addition, the hemolysis assay was performed using a fresh human blood sample (The First Affiliated Hospital of Zhengzhou University). The red blood cells were separated from the blood by centrifugation at 4000 rpm. Then, PBS (negative control), deionized water (positive control), and different concentrations of nanomaterial (2, 5, 10, 20, and 50 μg mL^{-1}) were added into red blood cells suspension. Subsequently, the samples were incubated at 37 ℃ for 4 h and centrifuged at 4000 rpm. The percentage of hemolysis of the supernatants was measured at 540 nm absorbance by UV–vis spectrophotometer (T6, PERSEE General, China).

$$\text{Hemolysis}(\%) = \frac{\text{Abs}_{\text{sample}} - \text{Abs}_{\text{PBS}}}{\text{Abs}_{\text{water}} - \text{Abs}_{\text{PBS}}} \times 100\%$$

4.2.11 Wound disinfection and healing assay *in vivo*

All animal experiments were performed with the Care and Use of Experimental Animals and approved by the animal ethics committee of the Yanxuan Biotechnology

(Hangzhou) Co., Ltd. (HZYX-2021-005), the female BALB/c mice (20 ± 2 g, 5 – 6 weeks old) were raised in the SPF animal room with food and water supplied 24 h. The rats were divided into three groups (six rats in each group), control group, polyCu-MOF group, and polyCu-MOF@AgNPs group. The rats were anaesthetized with chloral hydrate, and full thickness wound of circular diameter (5 mm) was made on the back of each rate. Then, 20 μL of *S. aureu*s suspensions (1×10^6 CFU mL^{-1}) were spread on the wound for constructing the infected wound model. After 24 h, 20 μL suspension of different samples (PBS, polyCu-MOF, and polyCu-MOF@AgNPs) was dropped into the wound region in the corresponding groups. The developed antibacterial agents were added every day and bound up with hospital gauze. The mice weight was recorded daily. Subsequently, photos of the infected wounds were taken and the sizes of wounds were measured using a digital Vernier caliper every day. The wound healing rate was calculated according to the following equation: wound healing rate (%) = $(Area_{Day0} - Area_{DayX})/Area_{Day0}\times100\%$, $Area_{Day0}$ and $Area_{DayX}$ were the wound area of the Day0 and DayX, respectively. On the tenth day, the wound was excised and incubated in PBS for 24 h at 37 °C. After that, the culture solution was diluted 100-fold and cultured on LB agar plates at 37 °C for 24 h for counting the number of bacterial colonies. For histological analysis, the skin of the wound tissues (day 6 and day 10) from each group of mice were harvested and fixed in 10% formaldehyde for 4 h, dehydrated in 30% sucrose for 12 h, further staining and hematoxylin and eosin (H&E) analysis.

4.2.12 Statistical analysis

All experiments were performed in triplicate and obtained data were evaluated as the mean value ± standard deviation. Statistical significance between two groups was analyzed by the Student's t-test. Differences were considered significant if $*P < 0.05$, $**P < 0.01$, and $***P < 0.001$.

4.3 Results and discussion

4.3.1 Basic characterizations of polyCu-MOF@AgNPs

The morphologies and microstructures of polyCu-MOF@AgNPs were investigated by FE-SEM and TEM. **Figures 18a** and **b** indicate polyCu-MOF demonstrates the flower-like shape, which can be confirmed by its TEM image (**Figures 19a-d**). **Figures 19c** and **d** show that polyCu-MOF@AgNPs is composed of disorderly cubes with a side length of ~600 nm and height of ~100 nm. In addition, the majority of nanoparticles are presented over the cube rough surface.

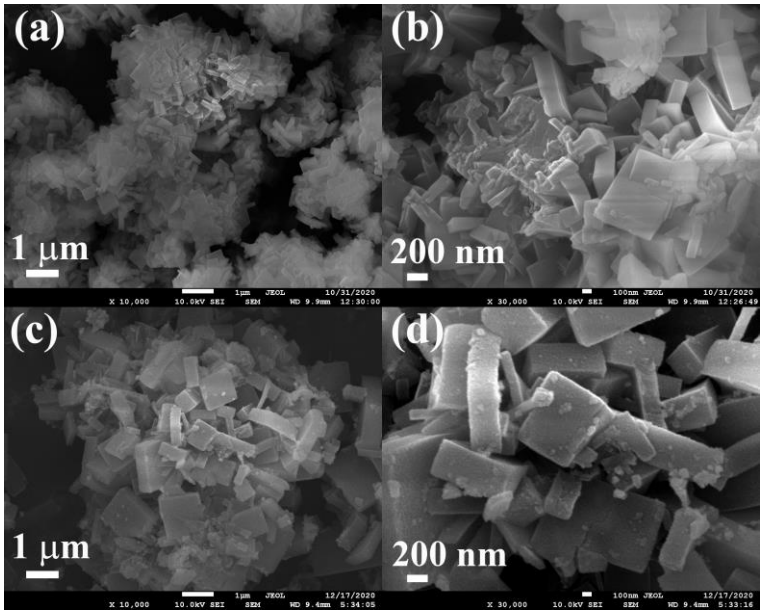

Figure 18. Low- and high-magnification SEM images of (a, b) polyCu-MOF and (c, d) polyCu-MOF@AgNPs.

The TEM image of polyCu-MOF@AgNPs (**Figure 19e**) illustrates that a number of nanoparticles are encapsulated within the polyCu-MOF network. Also, large amounts of Ag NPs with uneven size can be found in the HR-TEM image (**Figure 19f**) of polyCu-MOF@AgNPs. Furthermore, the lattice diffraction fringe of 0.236 and 0.204 nm is obtained in the HR-TEM image of polyCu-MOF@AgNPs (**Figure 19g**), corresponding to the (111) and (200) plane of Ag (JCPDS no. 04–0783) [129], respectively, suggesting the presence of Ag NPs. The selected area diffraction pattern image shows multiple-crystal diffraction features, and the four diffraction rings from inner to outer can be indexed as (111), (200), (220), and (311) reflections of face-centered cubic Ag. Moreover, elemental mappings in scanning TEM energy-dispersive X-ray spectroscopy of polyCu-MOF@AgNPs (**Figure 19h**) display the homogenous distribution of Ag, Cu, C, and O, whereas Ag is primarily found in the nanoparticle region.

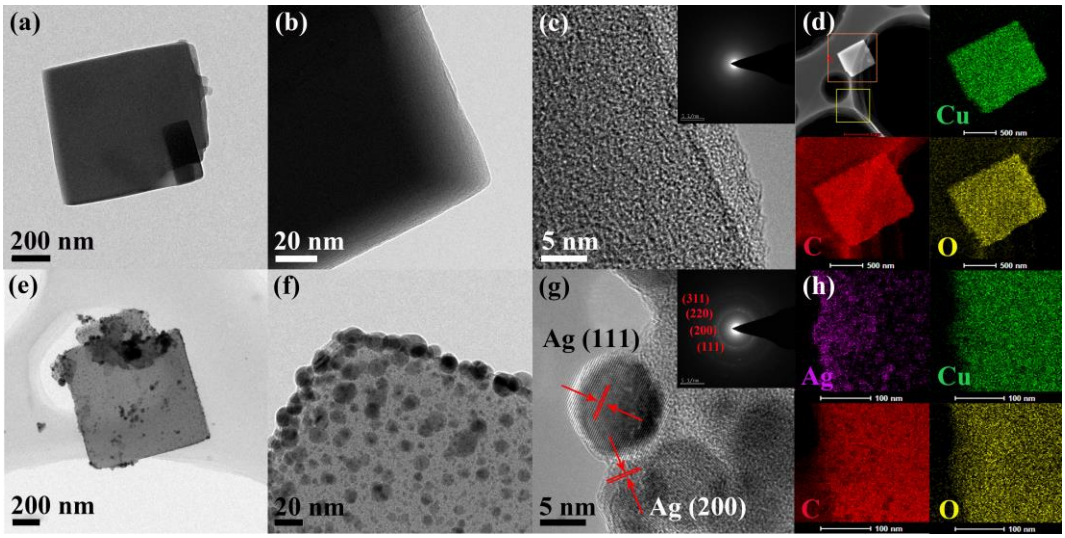

Figure 19. Low-, high-magnification, and HR-TEM images of (a-c) polyCu-MOF and (e-g) polyCu-MOF@AgNPs (Insert: the SAED pattern of (c) polyCu-MOF and (g) polyCu-MOF@AgNPs). Elemental mapping spectra of (d) polyCu-MOF and (h)

polyCu-MOF@AgNPs (Ag: purple, Cu: green, C: red, and O: yellow).

Figures 20a and **b** depict that Cu-MOF is composed of cubic-like structure with irregular shape. Furthermore, no substantial lattice fringe and diffraction ring are observed in HR-TEM and selected area diffraction patterns (SAED) images (**Figure 21b**). After doped with Ag NPs, a new stacked layer structure is observed in SEM images of Cu-MOF@AgNPs (**Figures 20c** and **d**), totally different with the pristine Cu-MOF. It can be explained that the structure of bulk-like Cu-MOF is destroyed during the Ag-doping process, suggesting an unsteady chemical state of Cu-MOF under alkaline environment. **Figure 21d** clearly shows that abundant Ag NPs are embedded within the Cu-MOF network, and the crystal lattice in HR-TEM image is calculated to 0.236 and 0.204 nm (**Figure 21e**), which corresponded to the (111) and (200) plane of Ag, respectively.

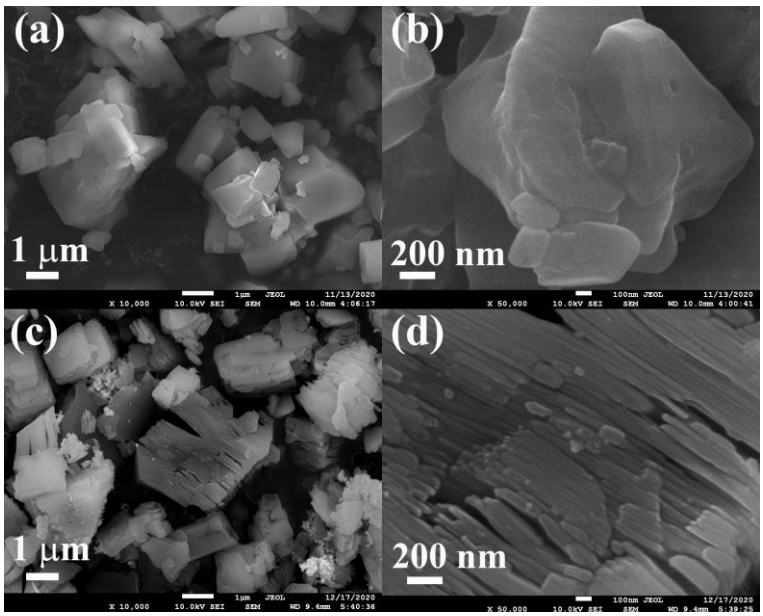

Figure 20. Low- and high-magnification SEM images of (a, b) Cu-MOF, and (c, d) Cu-MOF@AgNPs.

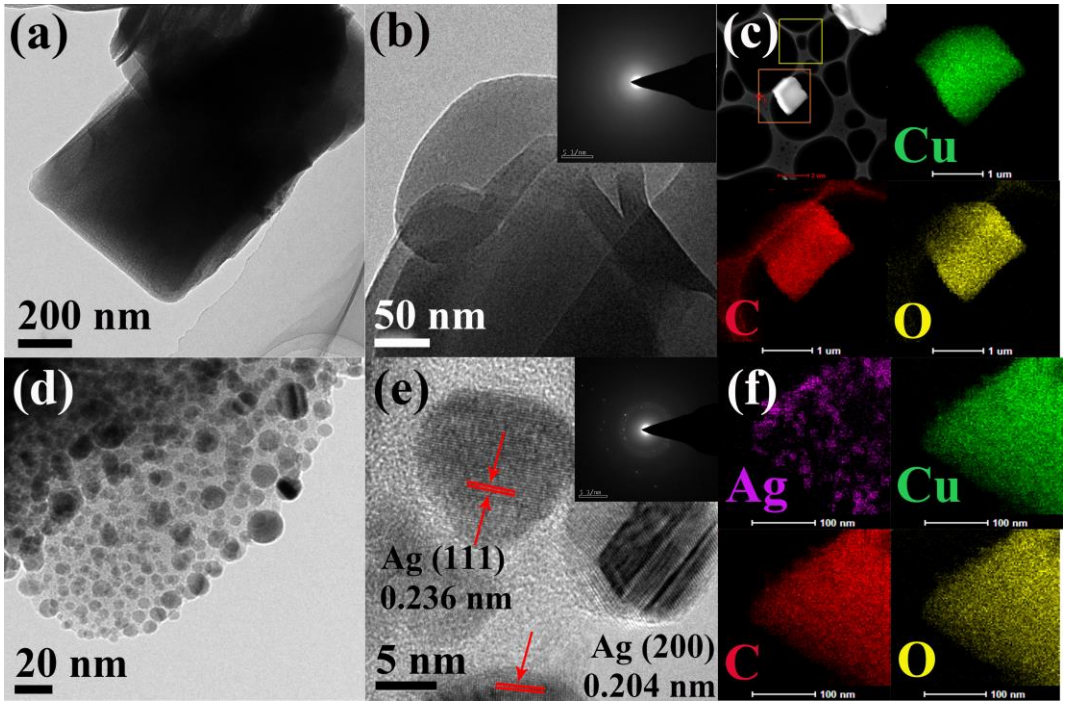

Figure 21. Low-magnification and HR-TEM images of (a, b) Cu-MOF and (d, e) Cu-MOF@AgNPs (Insert: the SAED patterns of (b) Cu-MOF and (e) Cu-MOF@AgNPs). Elemental mapping of homogenously distributed Cu (green), Ag (purple), C (red), and O (yellow) containing in (c) Cu-MOF and (f) Cu-MOF@AgNPs, as well as Ag in Cu-MOF@AgNPs.

The corresponding atomic% of C, O, Cu, and Ag elements in all samples is summarized in **Table 2**. The atomic% of C in polyCu-MOF (72.75%) is substantially larger than that of Cu-MOF (65.58%) because of the long carbon chain of polymer ligand. Furthermore, polyCu-MOF@AgNPs and Cu-MOF@AgNPs involve 7.24% and 3.45% of Ag, respectively. It indicates the high adsorption capacity of polyCu-MOF toward Ag^+ ions, which can be ascribed to the synergistic effect caused by the electrostatic interaction between Ag^+ and negatively charged carboxyl groups, coordination interaction between nitrogen atoms on bipyridine moieties and Ag^+, and

encapsulation effect of Ag^{+} into the pores of polyCu-MOF. Therefore, larger number of Ag NPs were formed through the reduction of Ag^{+} in MOF skeleton. By contrast, the atomic% of Cu in Cu-MOF@AgNPs (6.02%) is higher than that of polyCu-MOF@AgNPs (3.46%). Therefore, polyCu-MOF exhibits lower toxicity due to small amounts of Cu^{2+} ions than Cu-MOF, but showing outperformed antibacterial property to Cu-MOF because of the high loading capacity of Ag NPs.

Table 2. The atomic% of C, O, Cu and Ag elements in Cu-MOF, polyCu-MOF, Cu-MOF@AgNPs, and polyCu-MOF@AgNPs.

Samples	Atomic %			
	C	O	Cu	Ag
Cu-MOF	65.58	26.74	7.67	-
polyCu-MOF	72.75	23.50	4.15	-
Cu-MOF@AgNPs	63.28	27.25	6.02	3.45
polyCu-MOF@AgNPs	72.79	16.50	3.46	7.24

N_2 sorption–desorption isotherms were examined at 77 K to explore the porosity and pore-size distributions of of polyCu-MOF, Cu-MOF, polyCu-MOF@AgNPs, and Cu-MOF@AgNPs. Cu-MOF and polyCu-MOF show type-I adsorption-desorption isotherms (**Figure 22a**), which present high adsorption at low relative pressure. This finding reveals the microporous characteristics of the two MOFs. The Brunauer-Emmett-Teller surface area of polyCu-MOF is approximately 598.15 $m^2 g^{-1}$, which is substantially smaller than that of Cu-MOF (1121.7 $m^2 g^{-1}$), because of pore filling by the polymer ligand [41, 125]. In addition, the corresponding pore-size

distribution of polyCu-MOF and Cu-MOF using the Horvath–Kawazoe method indicates a narrow distribution of the micropores at approximately 5.1 and 5.4 Å, respectively. polyCu-MOF and Cu-MOF exhibit an analogous microporous structure (**Figure 22b)**. However, after being doped with Ag NPs, the specific surface areas of polyCu-MOF@AgNPs and Cu-MOF@AgNPs significantly decrease to 45.39 and 43.95 m^2 g^{-1}, respectively. Large amounts of Ag NPs are embedded within the pores of MOFs, and they partly occupied the pore volume of MOFs, thereby declining the specific surface area. This appearance is consistent with the TEM results of the two MOFs.

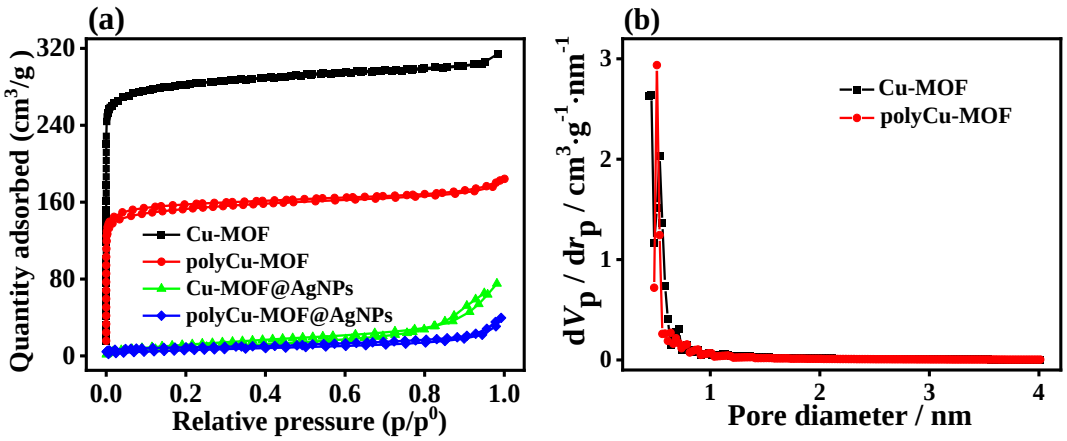

Figure 22. (a) Nitrogen adsorption-desorption isotherms and (b) pore size distribution of Cu-MOF, polyCu-MOF, Cu-MOF@AgNPs and polyCu-MOF@AgNPs.

Moreover, the crystal structures of the four samples were determined by PXRD (**Figure 23a**). The PXRD pattern of Cu-MOF shows the diffraction peaks at 2θ = 10.1°, 12.0°, 17.0°, 20.2°, and 24.7°, which matched well with the reported structure (a simulated pattern based on the single-crystal data of $C_{11}H_{11}CuNO_5$ [CCDC no.

687690]) [130]. The network of polyCu-MOF is composed of two-dimensional square grids of $[Cu_2(L8)_2(bpy)]_n$ units, which are pillared by bipyridine coligands **(Figure 23b)** [131]. Apart from the peaks of Cu-MOF, the PXRD patterns of polyCu-MOF@AgNPs and Cu-MOF@AgNPs indicate additional peaks at 2θ = 38.1°, 44.2°, and 64.4°, belonging to the (111), (200), and (220) planes of Ag, respectively. Thereto, Ag NPs were integrated with two Cu-MOFs.

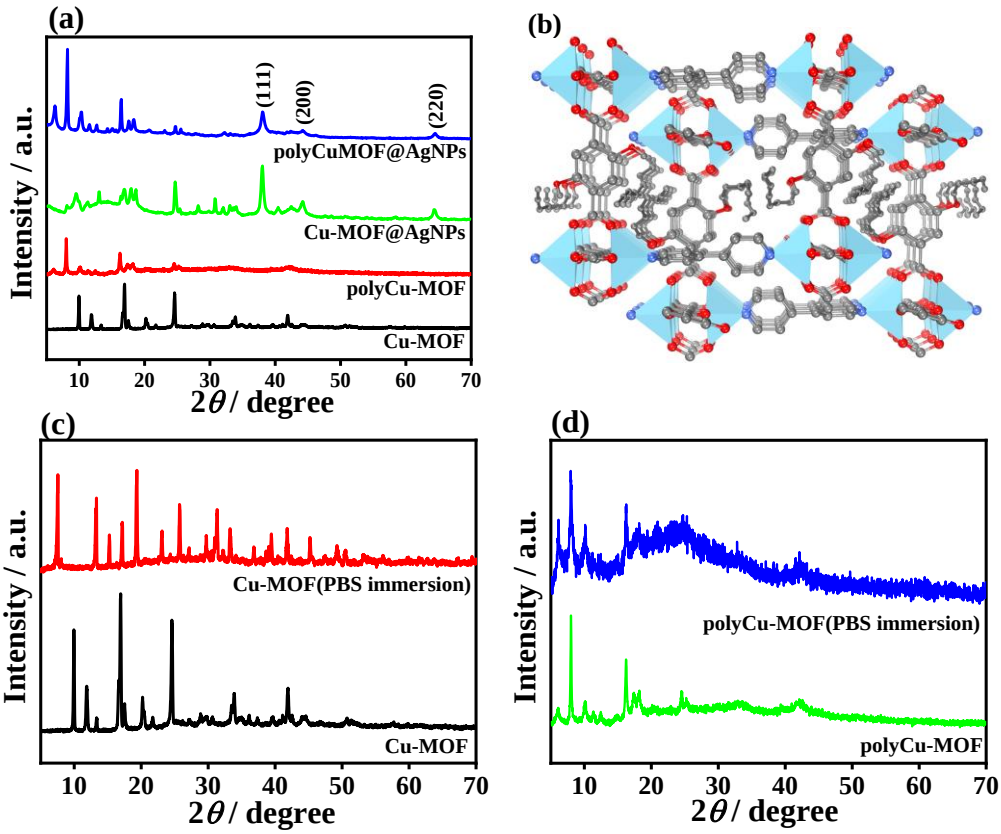

Figure 23. (a) PXRD patterns of Cu-MOF, polyCu-MOF, Cu-MOF@AgNPs and polyCu-MOF@AgNPs. (b) The crystal structure of polyCu-MOF ($[Cu_2(L8)_2(bpy)]_n$, Cu, blue; C, gray; O, red; N, dark blue). PXRD patterns of (c) Cu-MOF and (d) polyCu-MOF before and after immersed in PBS for 24 h at 37 °C.

After immersed in PBS for 24 h, the PXRD pattern of Cu-MOF completely

changed (**Figure 23c**), indicating its poor solution stability. By contrast, the PXRD pattern of polyCu-MOF (**Figure 23d**) was virtually unchanged over the same period. This finding indicates that the solution stability of polyCu-MOF outperformed to Cu-MOF, showing the potential extended long-acting antibacterial applications.

In addition, Fourier-transform infrared spectra of polyCu-MOF and polyCu-MOF@AgNPs show a characteristic peak around 2945 cm^{-1} (**Figure 24a**), corresponding to the stretching frequency of C–H on alkyl chain, further confirming the presence of a polymer ligand within the framework [132]. The two bands at 1611 and 1383 cm^{-1} are attributed to the antisymmetric and symmetric stretch modes of the C=O group, respectively [133]. As for Cu-MOF and Cu-MOF@AgNPs, the observed bands at 1508, 1155, and 1019 cm^{-1} are associated with benzene rings of the H_2BDC ligand and C-O-Cu stretching at 1106 cm^{-1}. Furthermore, the strong peaks at 1397 cm^{-1} correspond to asymmetric and symmetric vibrations of the carboxyl group on the polymer ligand. In addition, other bands in the fingerprint region can be assigned to the adsorbed water or C-H characters [130], whereas the band at 1665 cm^{-1} can be found in four samples, which is due to the carbonyl group.

XPS characterizations of all samples were performed to evaluate the chemical structure and components. The XPS survey scan spectra (**Figure 24b**) show the coexistence of C 1*s* (284.3 eV), O 1*s* (531.4 eV), and Cu 2*p* (935.0 eV) in four samples. Notably, the additional Ag 3*d* (371.6 eV) signal is observed in both Cu-MOF@AgNPs and polyCu-MOF@AgNPs. The high-resolution XPS spectra of all elements in four samples are analyzed by Gaussian fitting to investigate chemical

valences and environments of each element.

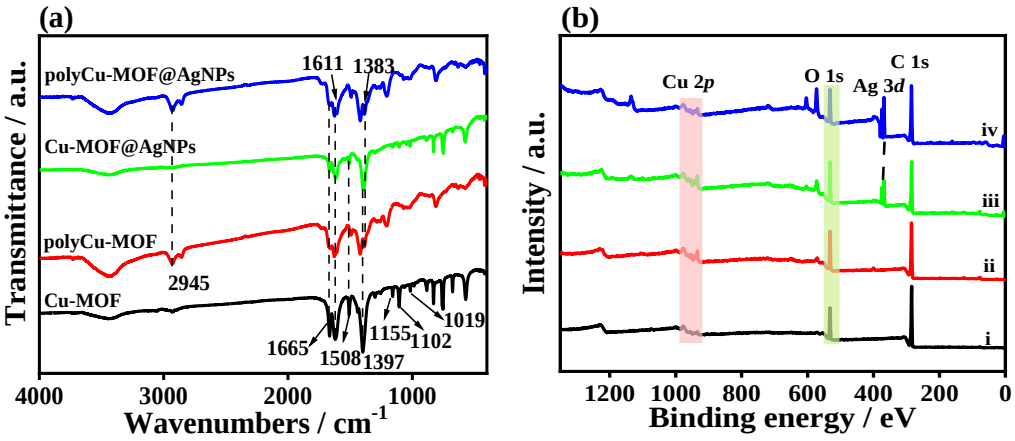

Figure 24. (a) FT-IR spectra and (b) XPS survey spectra of (i) Cu-MOF, (ii) polyCu-MOF, (iii) Cu-MOF@AgNPs, and (iv) polyCu-MOF@AgNPs.

The Cu 2*p* XPS spectrum of polyCu-MOF@AgNPs (**Figure 25a**) is divided into two weak peaks at binding energies (BEs) of 932.5 and 952.5 eV, which is attributed to Cu $2p_{3/2}$ and Cu $2p_{1/2}$ of Cu^{+} species, respectively, whereas the peaks at BEs of 934.5 and 954.5 eV are assigned to Cu $2p_{3/2}$ and Cu $2p_{1/2}$ of Cu^{2+}, respectively. Moreover, the peaks at BEs of 939–943 eV and 959–963 eV are due to the satellite peaks of Cu^{+} and Cu^{2+}, respectively. The existence of Cu^{+} species indicates that Cu^{2+} ions were partially reduced during the preparation of polyCu-MOF. As for the Ag 3*d* spectrum (**Figure 25b**), two clear peaks at BEs of 368.2 and 374.1 eV are observed because of Ag $3d_{5/2}$ and Ag $3d_{3/2}$ of Ag^{0}, respectively. This result implies that Ag NPs are embedded within the polyCu-MOF network. **Figure 25c** shows that the C 1*s* XPS spectrum of polyCu-MOF@AgNPs comprises four main peaks at BEs of 284.5, 285.5, 286.3, and 288.5 eV, corresponding to the C–C, C–O, C=O, and COO/N–C=O groups,

respectively. Among the groups, the peak area of C–C/C–H is the largest, indicating its high content in the organic component, which results from the long carbon chain of polymer ligand in the preparation of polyCu-MOF. The O 1*s* XPS spectrum of polyCu-MOF@AgNPs (**Figure 25d**) can be split into three peaks at BEs of 531.1, 531.8, and 532.9 eV, which are ascribed to O vacancies, C=O, and C−O, respectively. Abundant O vacancies indicate strong tendency to adsorb and activate oxygen to generate O_2^-, thereby improving the antibacterial performance of MOFs [134].

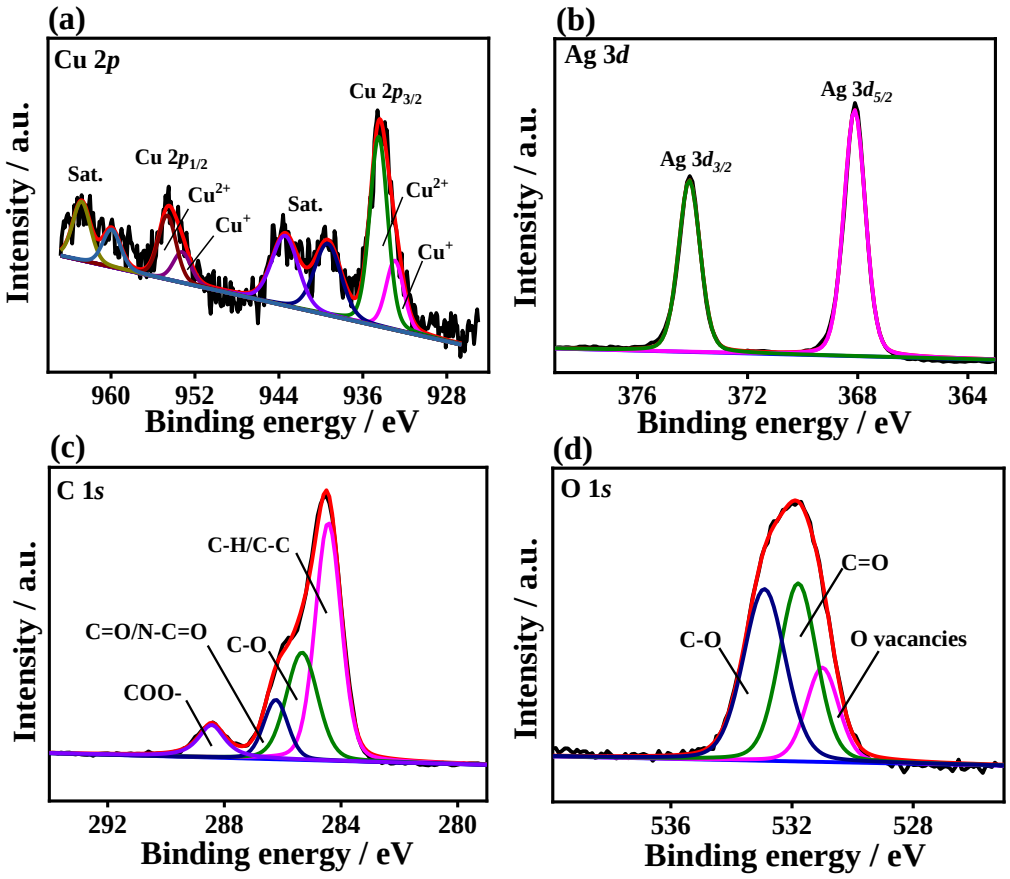

Figure 25 High-resolution (a) Cu 2*p*, (b) Ag 3*d*, (c) C 1*s* and (d) O 1*s* XPS spectra of polyCu-MOF@AgNPs.

As for polyCu-MOF, similar deconvoluted peaks of the Cu 2*p*, C 1*s*, and O 1*s*

XPS spectra are obtained (**Figure 26a**), indicating the analogous chemical structures of polyCu-MOF before and after the addition of Ag ions. Moreover, the high-resolution XPS spectra of each element in Cu-MOF and Cu-MOF@AgNPs were analyzed (**Figures 26b** and **c**). Similar deconvoluted XPS results between Cu-MOF and Cu-MOF@AgNPs are obtained, but with a slight difference in peak intensities. By contrast, the peak intensities of the C=O and C−O groups in the C 1*s* XPS spectra of polyCu-MOF and polyCu-MOF@AgNPs are remarkably higher than those of Cu-MOF and Cu-MOF@AgNPs. As aforementioned, the used polymer ligand has an undistributed molecular chain, and it contains abundant ether groups, thereby leading to the reservation of C−O.

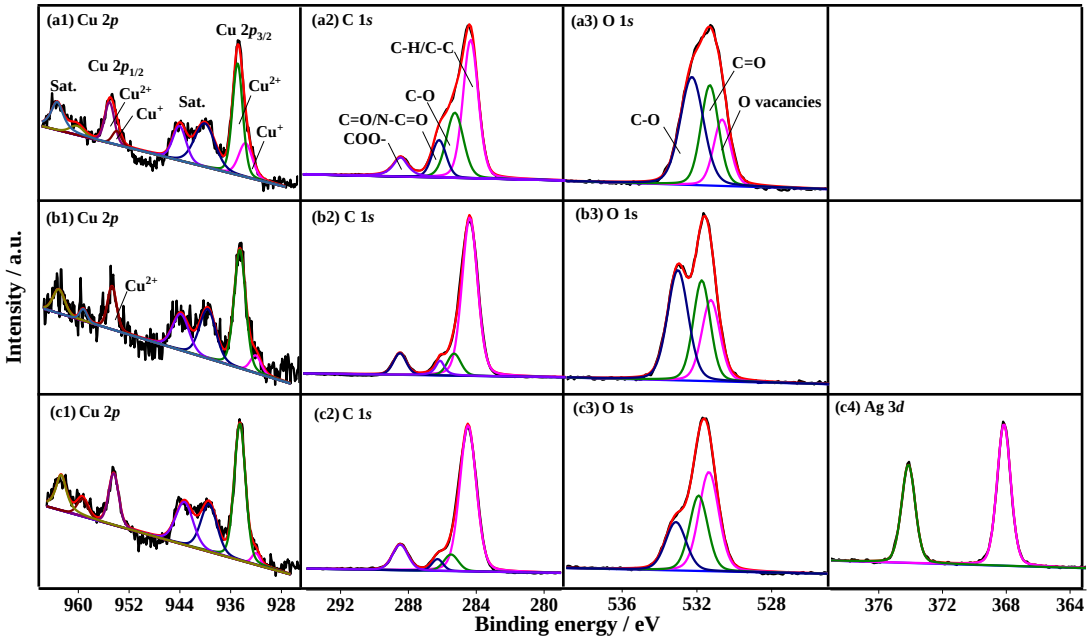

Figure 26. High-resolution Cu 2*p*, C 1*s*, O 1*s*, and Ag 3*d* XPS spectra of the (a) polyCu-MOF, (b) Cu-MOF and (c) Cu-MOF@AgNPs.

TGA analysis was conducted to evaluate the thermal stability of the prepared

samples (**Figure 27**). The TGA curve of polyCu-MOF exhibits a gradual weight loss with the increase of temperature to 245 °C, illustrating the loss of guest and coordinated solvent molecules in pores. Subsequently, the weight of polyCu-MOF decreases with the increase of temperature from 245 °C to 700 °C because of the degradation of the polymer ligand unit, thereby resulting in the complete collapse of the MOF frameworks. Finally, approximately 11.63% weight is remained because CuO residue is formed at 700 °C. Moreover, the weight residue after degradation of the polyCu-MOF@AgNPs hybrid (27.87%) is higher than that of polyCu-MOF, corresponding to the formation of Ag_2O after combustion. As for Cu-MOF, the thermal degradation of Cu-MOF occurs at 280 °C, whereas the substantial weight loss can be observed within the temperature range of 280 °C–430 °C because of the decomposition of BDC^{2-} (1,4-benzenedicarboxylate) linkers [130]. By contrast, the weight reservation of Cu-MOF (27.24%) is higher than that of polyCu-MOF, indicating the high Cu-related content. A similar degradation trend for the Cu-MOF@AgNPs hybrid is found but with steep degradation and 40.81% weight reservation.

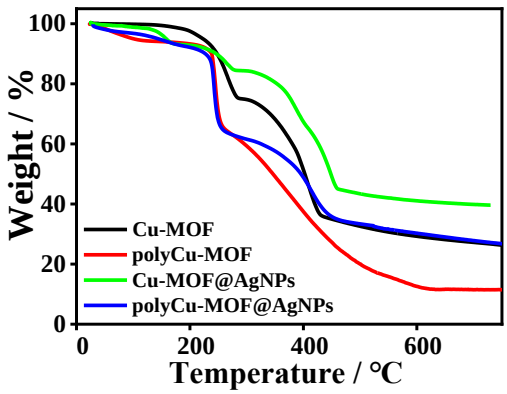

Figure 27. TGA curves of Cu-MOF, polyCu-MOF, Cu-MOF@AgNPs, and

polyCu-MOF@AgNPs.

4.3.2 Antibacterial property of polyCu-MOF@AgNPs

S. aureus and *E. coli* were selected as representative Gram-positive and Gram-negative bacteria, respectively, to investigate the antibacterial abilities of polyCu-MOF@AgNPs, Cu-MOF@AgNPs, polyCu-MOF, and Cu-MOF. The growth curves and antibacterial efficiency of bacteria cocultured with polyCu-MOF@AgNPs were measured. Bacterial growth was evaluated by monitoring the OD_{600} values based on the turbidity of the bacterial suspension. For the untreated control, the OD_{600} values of *S. aureus* and *E. coli* rapidly increase to 1.35 and 1.73 after incubation for 10 h **(Figure 28)**, respectively. By contrast, the OD_{600} values of bacterial cultures treated with Cu-MOF and polyCu-MOF are slightly smaller than those of the untreated control, suggesting that the released Cu^{2+} ions only have limited ability to inhibit bacterial growth. Nonetheless, the growth of *S. aureus* and *E. coli* is significantly inhibited by Cu-MOF@AgNPs (10 μg mL^{-1}) within the initial 6 h, which is ascribed to the bacterial destructive effect of Ag NPs embedded in Cu-MOF. After incubating for 6 h, the turbidity of bacterial suspension increases gradually, indicating that Cu-MOF@AgNPs cannot completely eradicate bacteria, leading to bacterial proliferation. Furthermore, the growth of *S. aureus* and *E. coli* is inhibited completely by polyCu-MOF@AgNPs in 10 h, implying that the antibacterial activity can be remarkably strengthened by loading Ag NPs within the polyCu-MOF network. As aforementioned, large amounts of Ag^{+} ions can be adsorbed within the

three-dimensional polyCu-MOF network. Compared with Cu-MOF, the polymer chain in polyCu-MOF can absorb a large number of Ag^{+} ions, generating large amounts of Ag NPs. Thereto, it provides polyCu-MOF@AgNPs a superior antibacterial performance for killing diverse bacteria.

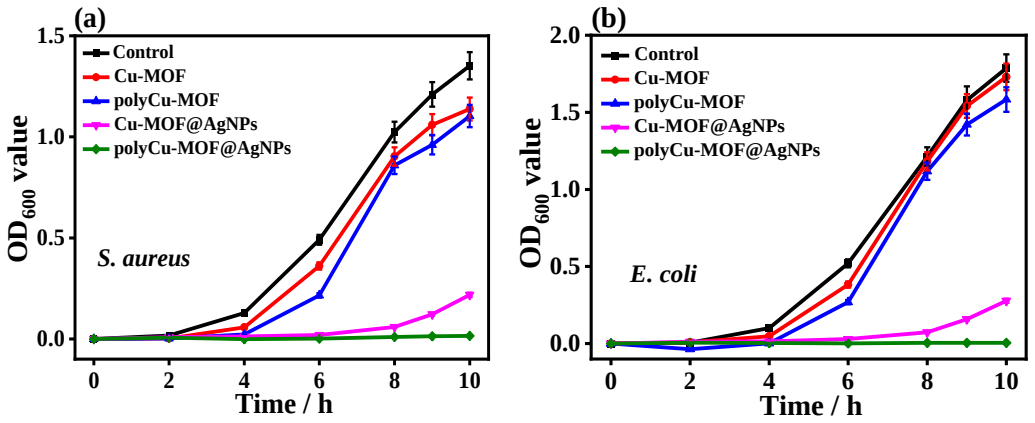

Figure 28. OD_{600} values of (a) *S. aureus* and (b) *E.coli* treated with different materials (10 μg mL^{-1}), including Cu-MOF, polyCu-MOF, Cu-MOF@AgNPs, and polyCu-MOF@AgNPs.

In addition, the MIC values of all samples were studied. Compared with the untreated control, the initial lag phase of the two bacteria incubated with polyCu-MOF@AgNPs is observed at low concentration (**Figure 29a**), for which the growth of *S. aureus* is significantly inhibited by incubating with polyCu-MOF@AgNPs suspension (5 μg mL^{-1}). Furthermore, *S. aureus* is completely killed in the 10 μg mL^{-1}polyCu-MOF@AgNPs suspension. Consequently, this concentration can be defined as MIC of polyCu-MOF@AgNPs for inhibiting the growth of *S. aureus*. Therefore, polyCu-MOF@AgNPs exhibits good antibacterial activity against *S. aureus*, indicating its concentration-dependent behavior. Moreover,

the MIC values of Cu-MOF@AgNPs (20 μg mL^{-1}), polyCu-MOF (200 μg mL^{-1}), and Cu-MOF (500 μg mL^{-1}) against *S. aureus* were evaluated (**Figures 29b–d**) using the same method.

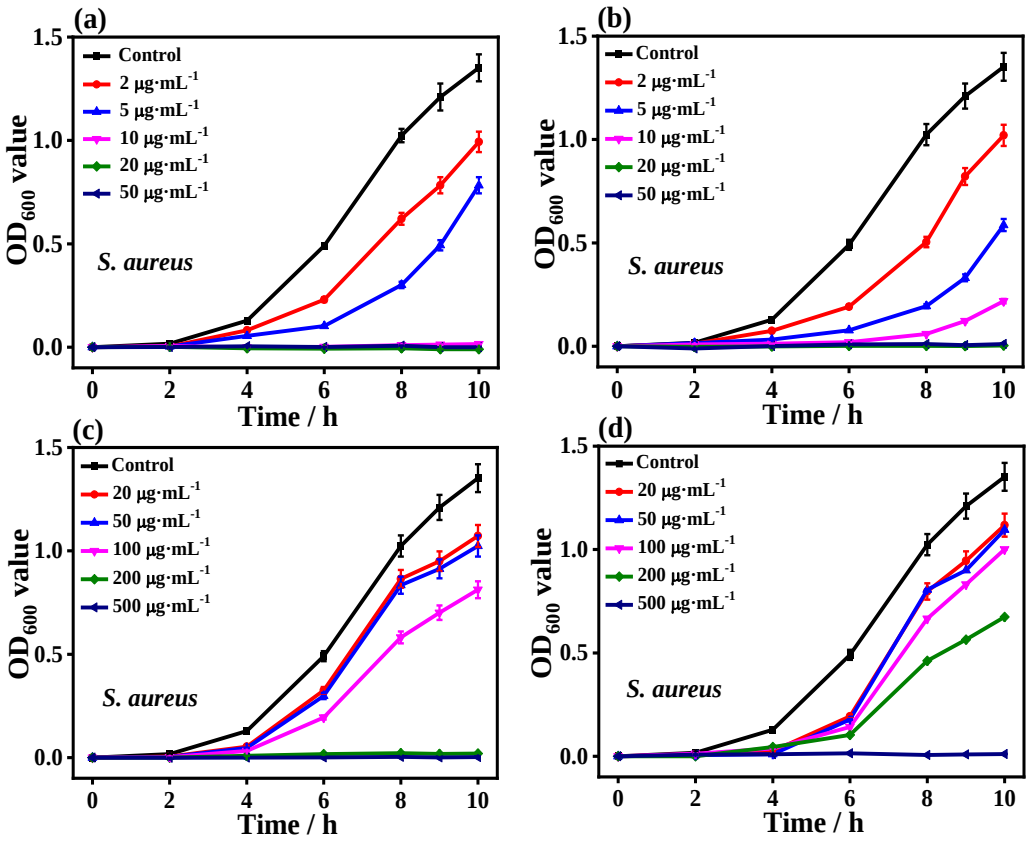

Figure 29. Growth curves of *S. aureus* after incubating with different concentrations of (a) polyCu-MOF@AgNPs, (b) Cu-MOF@AgNPs, (c) polyCu-MOF, and (d) Cu-MOF.

The MICs for polyCu-MOF@AgNPs, Cu-MOF@AgNPs, polyCu-MOF, and Cu-MOF against *E. coli* (**Figure 30)** are deduced to be 10, 20, 200, and 500 μg mL^{-1}, respectively. Furthermore, the inhibition efficiency of polyCu-MOF@AgNPs toward *E. coli* is higher than that against *S. aureus* at low concentration (2 and 5 μg mL^{-1}).

This result may be attributed to the presence of a thick peptidoglycan layer in Gram-positive bacteria, which protects the penetration of antibacterial agents [135].

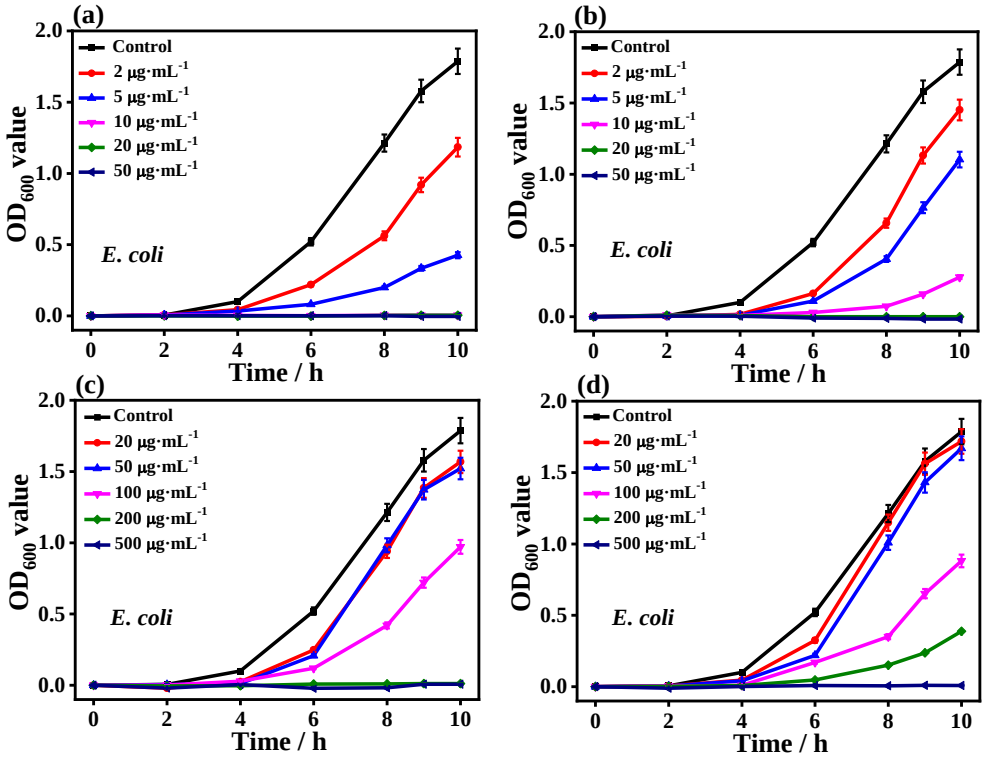

Figure 30. Growth curves of *E. coli* after incubating with different concentrations of (a) polyCu-MOF@AgNPs, (b) Cu-MOF@AgNPs, (c) polyCu-MOF, and (d) Cu-MOF.

The antibacterial efficiency of polyCu-MOF@AgNPs and Cu-MOF@AgNPs were analyzed by using the colony counting method to confirm their antibacterial properties against *S. aureus* and *E. coli*. When *S. aureus* was treated with 5 μg mL^{-1} of polyCu-MOF@AgNPs and Cu-MOF@AgNPs (**Figure 31c**), the antibacterial efficacy is about 78.57% and 49.14%, respectively. Moreover, when the concentration of polyCu-MOF@AgNPs increases to 10 μg mL^{-1}, the killing efficiency of polyCu-MOF@AgNPs against *S. aureus* reaches 100%, higher than that of

Cu-MOF@AgNPs toward *S. aureus* (94.71%). With regard to *E. coli* (**Figure 31d**), the killing efficiencies of polyCu-MOF@AgNPs and Cu-MOF@AgNPs at a low concentration (5 μg mL^{-1}) are 94.14% and 82.29%, respectively. Furthermore, at 10 μg mL^{-1}, the killing efficiencies of polyCu-MOF@AgNPs and Cu-MOF@AgNPs increase to 100% and 98.87%, respectively. It further indicate that the effective antibacterial property of polyCu-MOF@AgNPs is in agreement with the trend of growth curves.

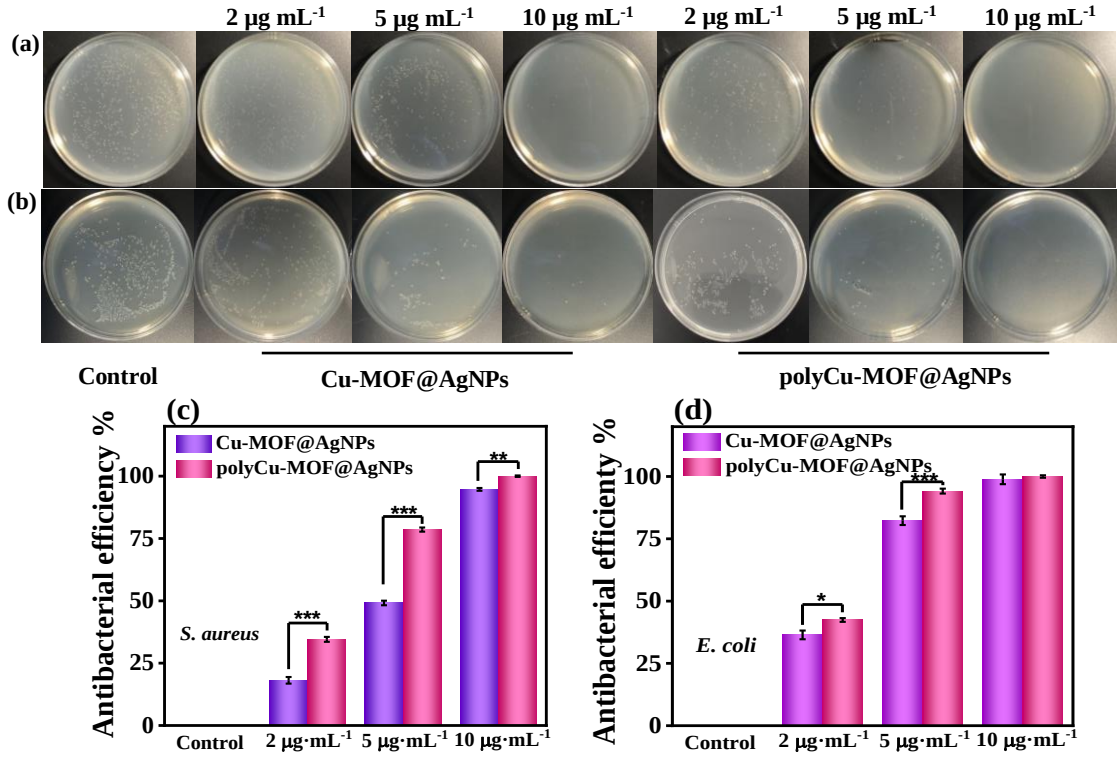

Figure 31. Photographs of bacterial colonies formed by (a) *S. aureus* and (b) *E. coli* treated with Cu-MOF@AgNPs and polyCu-MOF@AgNPs by using the plate count method. The corresponding Killing ratios of (c) *S. aureus* and (d) *E. coli* after different treatments.

In addition, a live/dead bacterial staining assay was used to investigate the survival condition of bacteria after being incubated with different materials. Calcein-AM was used to stain live bacteria with green fluorescence, whereas PI was employed to stain dead bacteria with red fluorescence. After treatment with PBS, almost all bacteria in the control group show green fluorescence, indicating that they are alive. On the contrary, the polyCu-MOF@AgNPs group only presents red fluorescence. This result displays that nearly all bacteria are killed by polyCu-MOF@AgNPs (10 μg mL^{-1}) after 12 h cultivation, showing enhanced destructive effect on the bacterial structure. As for the Cu-MOF@AgNPs group, the red fluorescence indicates the partial death of bacteria. **Figures 32a** and **b** show that bacteria contacted with the Cu-MOF and polyCu-MOF groups present green fluorescence, indicating the negligible antibacterial ability of Cu-MOF and polyCu-MOF at low concentration. FE-SEM characterizations were conducted to probe the direct damage to bacterial membranes induced by polyCu-MOF@AgNPs and investigate the morphological changes using Cu-MOF and polyCu-MOF as control. After treatment with PBS, the SEM images of *S. aureus* and *E. coli* (**Figures 32c1** and **d1**) retain smooth and complete membranes, which are typically round and rod shape, respectively. However, in the case of polyCu-MOF@AgNPs, the membranes of bacteria is seriously distorted and ruptured (**Figures 32c5** and **d5**), for which partial bacteria demonstrate intracellular component leakage (as indicated by the arrows). This result indicates that treatment using polyCu-MOF@AgNPs can remarkably disrupt the bacterial integrity. After being incubated with

Cu-MOF@AgNPs, the surface of partial bacteria tends to be wrinkled with a change in the shape of the bacterium. Therefore, many bacteria reverse their well-formed structures. By contrast, almost all bacteria incubated with Cu-MOF and polyCu-MOF suspensions maintain an intact surface and typical morphologies, indicating a negligible impact on the integrity of the bacterial membrane. These results further prove that polyCu-MOF@AgNPs hybrid displays a superior antibacterial effect by causing the bacterial membrane damage, thereby leading to the death of bacteria.

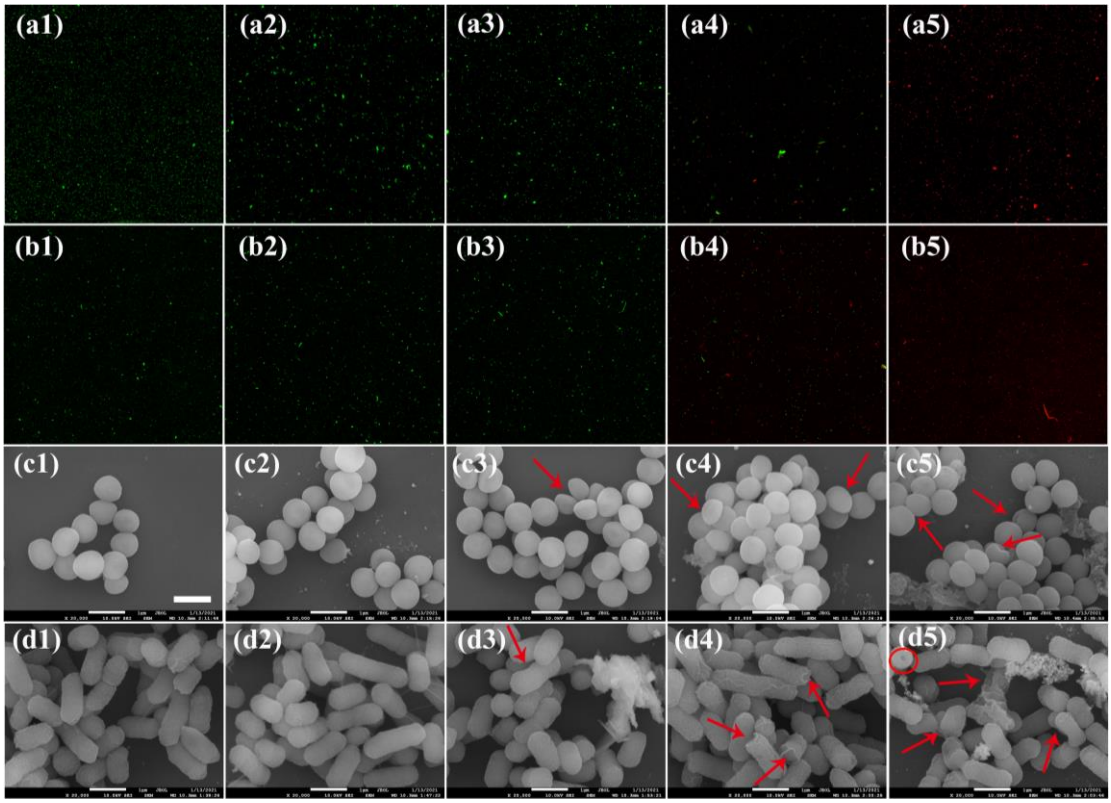

Figure 32. Confocal fluorescent live/dead stain images for *S. aureus* (top panel) and *E. coli* (bottom panel) after treatment with (a1, b1) PBS, (a2, b2) Cu-MOF, (a3, b3) polyCu-MOF, (a4, b4) Cu-MOF@AgNPs, and (a5, b5) polyCu-MOF@AgNPs at the concentration of 10 μg mL^{-1} for 12h. FE-SEM images of (c1, d1) PBS, (c2, d2) Cu-MOF, (c3, d3) polyCu-MOF, (c4, d4) Cu-MOF@AgNPs, and (c5, d5)

polyCu-MOF@AgNPs groups.

4.3.3 Antibacterial mechanism of polyCu-MOF@AgNPs

4.3.3.1 Release behavior of Ag^+ and Cu^{2+} ions

As reported, varieties of MOFs can be used as reservoirs of metal ions, for which the gradual release of metal ions by diffusion or degradation can provide MOF-sustained antibacterial effect [136]. Metal ions released from MOF networks can damage the bacterial membrane, which is regarded as the main mechanism for killing bacteria. Nonetheless, considering that metal ions at high concentrations might cause damage to normal tissue, the release kinetics of metal ions must be controlled below the threshold [137]. The release behavior of Cu^{2+} and Ag^+ ions in PBS was monitored by ICP-AES for 2, 4, 8, 12, 24, and 48 h. **Figure 33a** shows the release kinetics of Cu^{2+} ions separately from Cu-MOF, polyCu-MOF, Cu-MOF@AgNPs, and polyCu-MOF@AgNPs. The amount of Cu^{2+} ions released increases substantially within 12 h. Afterward, the release of Cu^{2+} gradually slows down and approaches to an equilibrium after 24 h. By contrast, the amount of Cu^{2+} ions released from polyCu-MOF@AgNPs continuously increases to a small value of 3.2 μg mL^{-1}, which is less than that of Cu-MOF (5.08 μg mL^{-1}), polyCu-MOF (4.53 μg mL^{-1}), and Cu-MOF@AgNPs (4.06 μg mL^{-1}). The amount of Cu^{2+} released from polyCu-MOF@AgNPs is below the toxic level (7.8 μg mL^{-1}) [138].

Ag NPs can be oxidized in aqueous solutions, resulting in the release of Ag^+ under acidic conditions.

$$4Ag + O_2 \rightarrow 2AgO_2$$

$$AgO_2 + 4H^+ \rightarrow 4Ag^+ + 2H_2O$$

Excessive Ag^+ ions can burst blood cells and cause some undesirable side effects. Therefore, achieving the function of Ag (e.g., antibacterial ability) within a healthy range of concentration without damaging the tissues is of significance [139]. The released behavior of Ag^+ ions from polyCu-MOF@AgNPs and Cu-MOF@AgNPs was assessed (**Figure 33b**). Consequently, Ag^+ ions can be fast released from polyCu-MOF@AgNPs and Cu-MOF@AgNPs within the initial 12 h. Subsequently, the release of Ag^+ ions decreases slowly and approaches to a plateau after 12 h. After 50 h, the amount of Ag^+ ions released from polyCu-MOF@AgNPs is approximately 3.08 μg mL^{-1}, which is 1.3-fold that of Cu-MOF@AgNPs (2.37 μg mL^{-1}). As discussed, an amount of Ag NPs, which is larger than that of Cu-MOF, are anchored into polyCu-MOF, thereby leading to high amount of Ag^+ ions released. In addition, the release of Ag^+ ions in the presence of bacterial cells could increase because Ag NPs can interact with the sulfur-containing proteins of the cell walls [140]. When cultured with bacteria, Ag^+ ions can be slowly and sustainably released from polyCu-MOF@AgNPs, thereby boosting the growth inhibition ability of bacteria. In this regard, although polyCu-MOF@AgNPs release a small amount of Cu^{2+}, approximately 2/3-fold of Cu-MOF, good bactericidal abilities against the two kinds of bacteria indicate that the release Cu^{2+} ions is not responsible for the inactivation of bacteria.

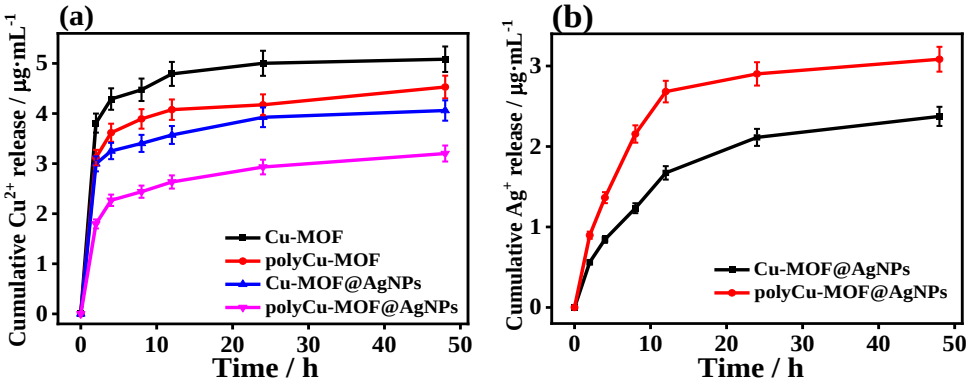

Figure 33. Cumulative (a) Cu^{2+} and (b) Ag^{+} release properties of Cu-MOF, polyCu-MOF, polyCu-MOF@AgNPs, and Cu-MOF@AgNPs (50 μg mL^{-1}).

4.3.3.2 Generation efficiencies of ROS from polyCu-MOF@AgNPs

In general, metal NPs and metal ions can generate ROS such as superoxide ($•O_2^-$), hydrogen peroxide (H_2O_2), and hydroxyl radical (•OH) during aerobic metabolism, which can damage the cell membrane and induce oxidative stress in cells [141]. The generation efficiencies of ROS from all samples were investigated using an H_2-DCFDA probe. The nonpolar, nonionic H_2-DCFDA diffused within cells can be hydrolyzed into non-fluorescent H_2-DCF (dichlorodihydrofluorescein) by intracellular esterase. With the production of ROS, H_2-DCF was oxidized to form the green fluorescent product, DCF [142]. **Figures 34a** and **b** show the relative contents of ROS in *S. aureus* and *E. coli* cells after interacting with different concentrations of polyCu-MOF@AgNPs. The fluorescence intensity of the H_2-DCFDA probe increases with the increase of the concentration of polyCu-MOF@AgNPs, indicating the increased amount of generated ROS. Therefore, the ROS production rates of polyCu-MOF@AgNPs at different concentrations toward the two bacteria are

summarized in **Figure 34c**. For polyCu-MOF@AgNPs at 2 μg mL^{-1}, no significant increase in fluorescence intensity is observed in comparison with the negative control group. When the concentration increases to 5 μg mL^{-1}, the ROS contents are 19.6% and 17.7% of the positive control group toward *S. aureus* and *E. coli*, respectively. However, when the concentration of polyCu-MOF@AgNPs is higher or equal to 10 μg mL^{-1}, the generation of ROS in *S. aureus* and *E. coli* cells increases significantly, illustrating that polyCu-MOF@AgNPs can cause oxidative damage to bacterial cells. Compared with the positive control, the content of ROS in *S. aureus* and *E. coli* is 61.9% and 52.8%, respectively, when treated with polyCu-MOF@AgNPs at 50 μg mL^{-1}. These results indicate that abundant ROS can be generated in bacteria in the presence of polyCu-MOF@AgNPs. Consequently, the combined effect of the generation of ROS and release of Ag^{+}/Cu^{2+} ions plays an important role in the antibacterial effect of the developed polyCu-MOF@AgNPs.

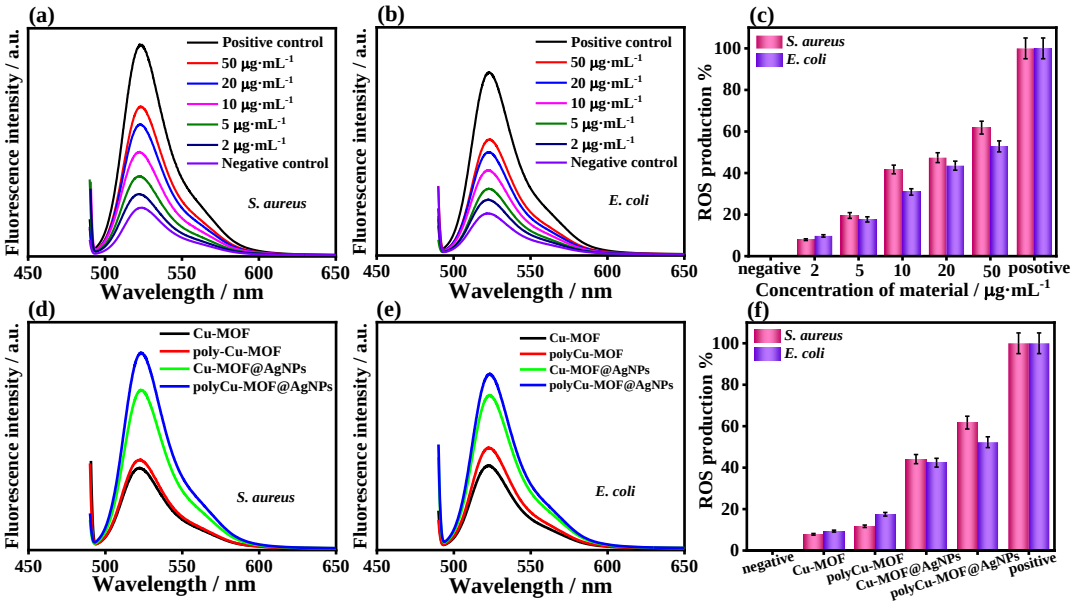

Figure 34. (a, b) H_2-DCFDA probe for detection of intracellular ROS production after treated with different concentration of polyCu-MOF@AgNPs. (c) Concentration

dependent ROS production of the polyCu-MOF@AgNPs hybrid in treated bacteria. H_2-DCFDA probe for detection of intracellular ROS production after treated with different materials at 50 μg mL^{-1} for (d) *S. aureus* and (e) *E. coli*. (f) ROS generation in bacteria treated with Cu-MOF, polyCu-MOF, polyCu-MOF@AgNPs, and Cu-MOF@AgNPs (50 μg mL^{-1}).

Furthermore, fluorescence spectra of the quantification of the ROS level in bacterial cells after being treated with Cu-MOF, polyCu-MOF, and Cu-MOF@AgNPs were studied (**Figures 34d** and **e**), whereas the ROS levels are indicated in **Figure 34f**. By treating with Cu-MOF and polyCu-MOF, no substantial change in the ROS level is obtained in comparison with the negative control in *S. aureus* and *E. coli*. In general, the ROS level is closely correlated with the antibacterial activity of antibacterial substance [143]. The Cu-MOF and polyCu-MOF groups cannot kill bacteria efficiently because of low ROS production, leading to the unobvious inhibition effect. By contrast, the ROS production level in *S. aureus* and *E. coli* treated with polyCu-MOF@AgNPs is 61.9% and 52.8%, respectively, which is substantially higher than those treated with Cu-MOF@AgNPs (44.1% and 42.4%, respectively). Consequently, the polyCu-MOF@AgNPs hybrid exhibits boosted antibacterial performance because of the high ROS generation in bacteria.

Based on the abovementioned results, we hypothesize that the outstanding antibacterial ability of polyCu-MOF@AgNPs is ascribed to the following factors: (i) in an acidic environment, which is caused by the metabolic behavior of bacteria, H^+

ions can trigger Ag NPs, resulting in efficient and continuous release of Ag^+ ions from polyCu-MOF@AgNPs [101]. The efficient and controlled Ag^+ ions from polyCu-MOF@AgNPs are dominant in the antibacterial mechanism; (ii) Ag^+ released from polyCu-MOF@AgNPs can wreck the integrity of cell membrane, thereby causing morphological change, increasing membrane permeability, and causing the leakage of internal nutrients and other contents, which finally kill bacteria [144]; (iii) when Ag NPs and metal ions enter into the cell, they can interact with the cell nucleus and damage DNA or proteases, resulting in cell death or loss of division and proliferation abilities [145]. (iv) In addition, Ag NPs and metal ions can induce cells to produce intracellular ROS, which further accelerate the rupture of bacterial wall and induce bacterial death [140]. The abovementioned multiple factors can cause a synergistic effect, thereby killing bacteria without drug resistance.

4.3.4 *In vitro* biocompatibility

The potential hemolysis and cytotoxicity performances were investigated to evaluate the biocompatibility of polyCu-MOF@AgNPs. Considering that metal ions released from MOFs could increase the cytotoxicity to normal cells, the toxicity of all samples toward human normal L929 cells was tested via the MTT assay. **Figure 35a** indicates that no significant toxicity is found for polyCu-MOF@AgNPs within a range of 2–20 μg mL^{-1}. Furthermore, a high cell viability of 82.2% is obtained at 50 μg mL^{-1}. The decline of the cell viability at the high sample dosage is primarily attributed to the toxicity of the produced ROS during cell culture. Therefore,

polyCu-MOF@AgNPs exhibit negligible toxicity at antibacterial concentration, providing great potential in biomedical treatments. Moreover, more than 92% of L929 cells survive after being treated with Cu-MOF and polyCu-MOF at a high concentration of 50 μg mL^{-1}, suggesting low-toxicity MOFs. The excellent biocompatibility of Cu-MOFs may be due to the low level of released Cu^{2+} ions from MOFs, which is below the threshold and far from cytotoxicity. Furthermore, a hemolysis test was performed to assess the biocompatibility of all samples. Here, venous blood samples were collected and separately incubated with deionized water, PBS, Cu-MOF, polyCu-MOF, Cu-MOF@AgNPs, and polyCu-MOF@AgNPs for 4 h.

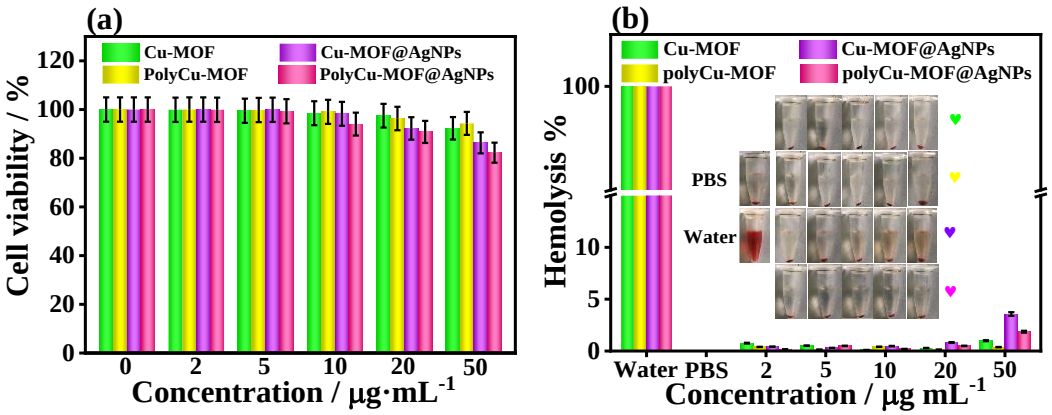

Figure 35. (a) Cell viability of L929 cells treated with different concentrations of Cu-MOF, polyCu-MOF, Cu-MOF@AgNPs, and polyCu-MOF@AgNPs. (b) Hemolysis assay of Cu-MOF, polyCu-MOF, Cu-MOF@AgNPs, and polyCu-MOF@AgNPs (inset: photos from the hemolytic activity assay of all samples).

The inset of **Figure 35b** shows an insignificant hemolytic effect for all test groups and PBS control group. However, the positive control group exhibits complete

hemolysis, resulting in bright-red solution. In addition, the quantitative data indicate that the hemolysis ratio increases with the increase of the concentration of the polyCu-MOF@AgNPs suspension (0.16%–1.86%). This finding can be ascribed to the high structural stability of polyCu-MOF, which is conductive to a long-acting antibacterial effect. Furthermore, polyCu-MOF can reduce the interaction with the blood cell membrane, thereby decreasing the potential hemolysis caused by Ag NPs [146]. Consequently, polyCu-MOF@AgNPs are regarded as suitable antibacterial agents because of their low cytotoxicity and hemolysis.

4.3.5 Wound disinfection and healing assay *in vivo*

Given the superior antibacterial capability and excellent biocompatibility of polyCu-MOF@AgNPs, polyCu-MOF@AgNPs can be applied in treating *in vivo S. aureus*-infected wound. The infected wound model of BALB/c mice was used to evaluate the therapeutic effect of the polyCu-MOF, polyCu-MOF@AgNPs, and control groups. After being infected with *S. aureus*, mice were separately injected with different materials every subsequent day (**Figure 36a**). The wound images of mice treated with PBS, polyCu-MOF, and polyCu-MOF@AgNPs at different durations are obtained (**Figure 36b**), from which the corresponding wound healing rates are deduced (**Figure 36c**). After 4 days, the infected wound area of mice seems to decrease, and the scars appear in polyCu-MOF- and polyCu-MOF@AgNPs-treated groups. On the contrary, mice treated with PBS and polyCu-MOF exhibit 62.5% and 68.74% closure, respectively. The wound closure ratio in the

polyCu-MOF@AgNPs-treated group reaches 79.06%, indicating the efficient wound healing trend. After 8 days, the wound area of the polyCu-MOF@AgNPs-treated group remarkably shrinks to 1.2 mm^2, corresponding to a wound healing rate of 97.18%, which is 22.84% and 9.16% higher than that of polyCu-MOF and control groups, respectively. After 10 days, the wounds disappear in the polyCu-MOF@AgNPs group compared with the other groups. In addition, the treatment with polyCu-MOF@AgNPs can promote wound healing and improve the anti-bactericidal ability against *S. aureus*. Furthermore, the wound healing activity of polyCu-MOF@AgNPs was confirmed by H&E staining (**Figure 36d**). The broken epidermis could be observed in tissues in the control group. Meanwhile, the wound tissue collected from the control and polyCu-MOF groups of mice shows weak repair, leading to the appearance of abundant neutrophils. On the contrary, complete re-epithelialization and significantly reduced inflammation can be observed after treatment with polyCu-MOF@AgNPs. In the polyCu-MOF@AgNPs treatment group, extensive development of hair follicles can be observed at wound sections, which is close to the healthy tissue, indicating remarkable healing efficiency. In addition, a slight increase in body weight during treatment indicates the biosafety of polyCu-MOF@AgNPs on mice (**Figure 36e**). We further examine the *in vivo* antimicrobial effect of polyCu-MOF@AgNPs on the wound tissue healing at day 10 by using the plate counting method (**Figure 36f**). Compared with the other groups, the polyCu-MOF@AgNPs group exhibits the lowest bacterial colonies, indicating its highly effective antibacterial ability for *S. aureus in vivo*.

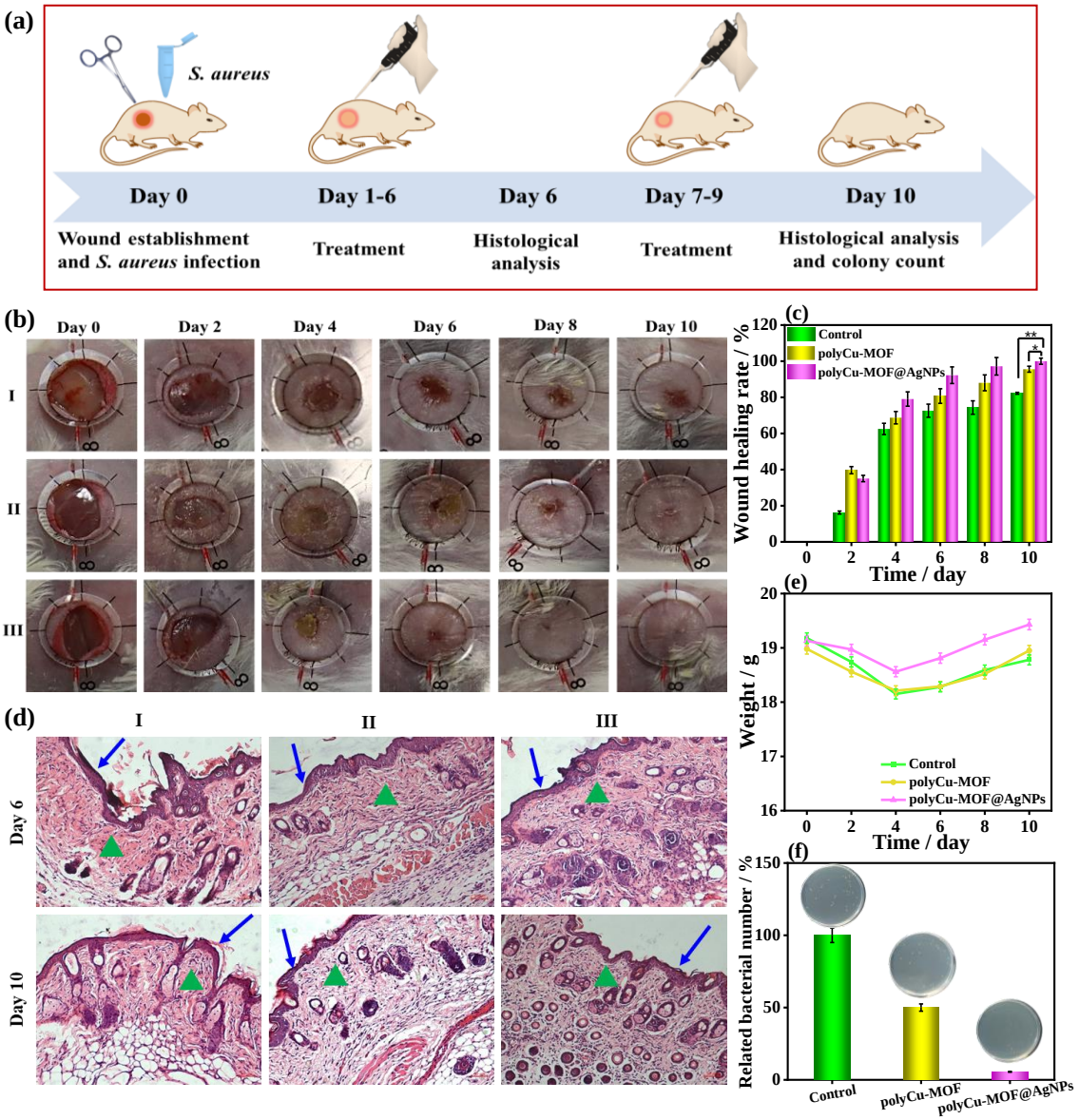

Figure 36. (a) Schematic illustration for *S. aureus*-infected wound construction and treatment model. (b) Photographs of infected wounds with different treatments at 0, 2, 4, 6, 8, and 10 days. Group I to III were treated with PBS, polyCu-MOF, and polyCu-MOF@AgNPs (10 μg mL^{-1}), respectively. (c) Corresponding wound healing rate of wounds. (d) Histological analysis of the infected wound with different treatments at day 6 and day 10 by H&E staining (arrows and triangles designate the epidermal and dermal, respectively. (e) Body weight measurement of mice. (f) The relative bacteria number derived from the skin tissue of infected wound after different

treatments for 10 days (insets: corresponding images of the bacteria colonies).

4.4 Conclusion

We have provided a novel antibacterial platform based on polyCu-MOF nanoplates by loading Ag NPs, which has been used for healing bacteria-infected wound. Compared with Cu-MOF synthesized using terephthalic acid as ligand, polyCu-MOF exhibited analogous nanostructure and skeleton but with higher carboxyl functionality, smaller copper clusters, and higher structural stability. Given the synergistic effect caused by the electrostatic interaction between Ag^+ ions and COO^- of polyCu-MOF, coordination interaction between N atoms on bipyridine and Ag^+ ions, and encapsulation effect of Ag^+ ions, polyCu-MOF showed high loading amount of Ag NPs. Therefore, the developed polyCu-MOF@AgNPs hybrid displayed superior antibacterial performance toward *S. aureus* and *E. coli*, resulting in an MIC value of approximately 10 μg mL^{-1}, which was substantially lower than the antibacterial agent used in the reported literature. Cytotoxicity and hemolysis tests revealed that polyCu-MOF@AgNPs had excellent cytocompatibility and hemocompatibility, whereas in vivo wound-healing evaluation indicated that polyCu-MOF@AgNPs improved the wound healing capability of *S. aureus*-infected mice. The enhanced efficiency for wound healing of the present polyCu-MOF@AgNPs was primarily attributed to the sustained release of Ag^+ and generated ROS. This work presented a potential antibacterial alternation based on the polyMOF network with long-acting effect and accelerated in vivo healing of

bacteria-infected wound.

CHAPTER 5

Semiconductive Cu_xNi_{3-x}(hexahydroxytriphenylene)$_2$ framework for electrochemical aptasensing of C6 glioma cells and epidermal growth factor receptor

5.1 Introduction

Recently, a new group of graphene-like 2D MOFs with high electrical conductivity has been developed [147], which can be constructed by six-connected linkers with phenylene or triphenylene backbones [148, 149], such as benzenehexathiol, 1,2,5,6,9,10-triphenylenehexathiol, 2,3,6,7,10,11-hexaiminotriphenylene, hexaaminobenzene, and HHTP. In comparison with the traditional porous conductive materials, such as porous carbons and porous metals, these crystalline MOFs exhibit narrow size distributions, regular channels, tunable band gaps, and designable charge transport pathways [150]. Owing to the high electrochemical activity and large specific area, these graphene-like MOFs will be highly promising as the scaffolds for adsorbing aptamer strands and then serve as the platforms for construction of novel electrochemical aptasensors.

Glioma is the most common malignant brain tumor in adults [151]. According to the Global Cancer Observatory 2018 report, this illness is diagnosed in ~100,000 people, and is associated with substantial mortality and morbidity [152]. Circulating biomarker-based liquid biopsies are useful, minimally invasive approaches for the early diagnosis of glioma, the dynamic real-time assessment of tumor growth, and therapeutic response compared with traditional tissue biopsies [153]. Various detection techniques for glioma liquid biopsies have been developed, such as telomerase promoter-based assay, next-generation sequencing, reverse transcriptase-polymerase chain reaction, Raman spectroscopy, and SPR. However, these methods are of high costs, time-consuming, and rely on sophisticated

instrumentation and skilled technologists. In this context, aptasensors have been widely used for living cancer cell detection owing to their high specificity, fast response, and high binding affinity [154]. The cancer markers, such as isocitrate dehydrogenase, O6-methylguanine-DNA-methyltransferase, telomerase reverse transcriptase, and EGFR, which are overexpressed in C6 cells, can act as indicators for the early diagnosis and prognosis monitoring of cancer. Though the detection of cancer markers or living cancer cells has been thoroughly explored, a bifunctional aptasensor for the simultaneous detection of both is rarely known [155, 156].

In this work, a bimetallic $Cu_xNi_{3-x}(HHTP)_2$ MOF was proposed to act as the sensitive scaffold **(Scheme 8)** for anchoring the EGFR-targeted aptamer, that is, 5′-GTA CTT CCA TTT GTG TTT GCC CGG AGC CTT AGT CTG TTC AAA AGT-3′, and was further explored to determine C6 cells and its corresponding biomarker EGFR. $Cu_3(HHTP)_2$ displays a honeycomb-like porous structure and has excellent electronic conductivity [157], whereas mixed Cu and Ni ions as coordinated centers could result in the heterostructure of $Cu_xNi_{3-x}(HHTP)_2$. This modified structure allows the aptamer strands to anchor tightly on the surface of $Cu_xNi_{3-x}(HHTP)_2$ and penetrate into the porous network via the π–π stacking interaction [158], the coordination force between Cu or Ni centers and N atom on aptamer [159], and intermolecular force [160]. The EGFR-targeted aptamer can specifically recognize some biomarkers located in the nucleus of C6 cells45. As such, the aptamer strands immobilized on MOF would change its conformation to combine with the biomarkers to form the G-quadruplex. As one of the biomarkers for glioma

cells, EGFR can be detected by the proposed aptasensor. Compared with the reported MOFs-based electrochemical biosensors, the proposed electrochemical sensing approach exhibits three unique features, including (i) bifunctional sensing both living cancer cells and biomarker with a pristine semiconducting bimetallic MOF; (ii) the feasible preparation of $Cu_xNi_{3-x}(HHTP)_2$ without any postsynthesis modification or pyrolysis; and (iii) the presence of $Cu^0/Cu^+/Cu^{2+}$ and Ni^{2+}/Ni^{3+} mixed valences of metal centers and graphene-like MOF network endowing the amplified electrochemical signal for biosensing. The optimized aptasensor based on $Cu_xNi_{3-x}(HHTP)_2$ exhibits a promising platform for the early diagnosis of cancers, which can also extensively broaden the applications of MOFs in sensing fields.

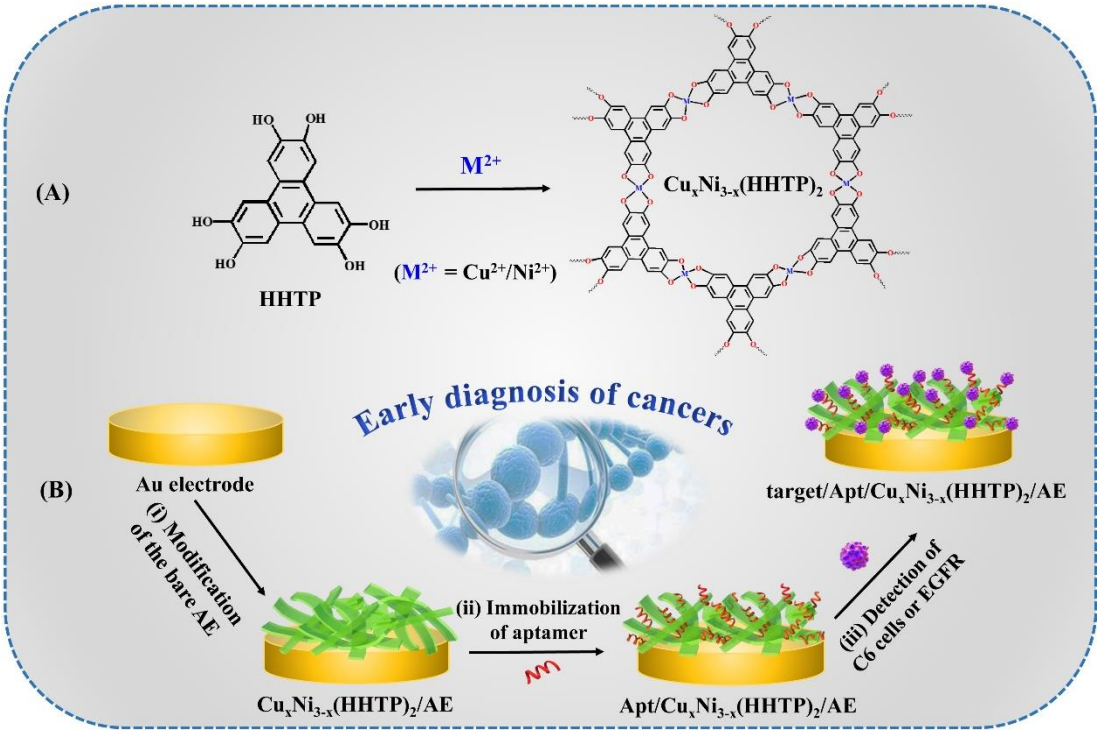

Scheme 8. (A) Preparation of $Cu_xNi_{3-x}(HHTP)_2$. (B) Fabrication of the bifunctional aptasensor based on $Cu_xNi_{3-x}(HHTP)_2$ for detecting C6 cells and EGFR, including (i) modification of the bare Au electrode (AE) with $Cu_xNi_{3-x}(HHTP)_2$, (ii) immobilization

of C6 cell-targeted aptamer strands, and (iii) detection of C6 cells and EGFR.

5.2 Experimental section

5.2.1 Reagents and materials

$Cu(NO_3)_2 \cdot 3H_2O$·and $Ni(NO_3)_2 \cdot 6H_2O$ were from Aladdin Reagent Co. Ltd. (Shanghai, China). KH_2PO_4, Na_2HPO_4, KCl, NaCl, $K_3[Fe(CN)_6]$ and $K_4[Fe(CN)_6]$ were from Sinopharm Chemical Reagent Co. Ltd. (Beijing, China). EGFR, immunoglobulin G (IgG), bovine serum albumin (BSA), vascular endothelial growth factor 165 ($VEGF_{165}$), Alpha fetoprotein (AFP), CEA, CA 125, and carbohydrate antigen 199 (CA 199) were obtained from Solarbio Bioengineering Ltd. Company (Beijing, China). The aptamer sequence, which was from SBS Genetech Co. Ltd., is as follow: 5′-GTA CTT CCA TTT GTG TTT GCC CGG AGC CTT AGT CTG TTC AAA AGT-3′. All of the chemicals were of analytical reagent grade and used as received. All solutions were prepared with Milli-Q ultrapure water (≥ 18.2 MΩ·cm).

5.2.2 Preparation of $Cu_3(HHTP)_2$, $Ni_3(HHTP)_2$, and $Cu_xNi_{3-x}(HHTP)_2$

$Cu_3(HHTP)_2$ was prepared based on literature method with a slight change [161]. Briefly, $Cu(NO_3)_2 \cdot 3H_2O$ (16 mg) was dissolved in deionized water (2.5 mL) to produce solution **A**. HHTP (20 mg) was dissolved in deionized water (2.5 mL) to produce solution **B**. Then, solution **A** was mixed with solution **B** in a vessel, which was heated in an oven at 80 °C for 24 h and subsequently, cooled to room temperature.

The product was washed with ethanol three times and dried in an oven at 60 °C to obtain $Cu_3(HHTP)_2$. $Ni_3(HHTP)_2$ was prepared by the same method, except for the replacement of $Cu(NO_3)_2·3H_2O$ with $Ni(NO_3)_2·6H_2O$. Similarly, $Cu(NO_3)_2·3H_2O$ (16 mg) and $Ni(NO_3)_2·6H_2O$ (20 mg) were concurrently dissolved in deionized water for the preparation of $Cu_xNi_{3-x}(HHTP)_2$.

5.2.3 Pre-treatment of the bare AE

The bare AE with a diameter of 3.0 mm was applied as working electrode and cleaned prior to use. Firstly, the AE was polished with 0.3 and 0.05 μm alumina powder to obtain a mirror-like surface, following by washing thoroughly with piranha solution (H_2SO_4/H_2O_2 = 7/3, v/v) and ethanol, respectively, for 15 min. Afterwards, the AE was washed with Milli-Q water and dried under nitrogen. The AE was electrochemically activated in 0.5 M H_2SO_4 within the potential cycling between −0.2 V and 1.6 V. Finally, the AE was rinsed with Milli-Q water and dried under nitrogen again, and stored for further use.

5.2.4 Preparation of solutions

PBS (0.01 M, pH 7.4) was prepared by mixing 0.24 g KH_2PO_4, 1.44 g $Na_2HPO_4·12H_2O$, 0.20 g KCl, and 8.0 g NaCl. The electrolyte solution for electrochemical tests was prepared immediately before use by dissolving 1.65 g $K_3[Fe(CN)_6]$, 2.11 g $K_4[Fe(CN)_6]$, 8.0 g and 7.45 g KCl in 1.0 L of PBS. The stock solutions of aptamer, IgG, BSA, $VEGF_{165}$, AFP, CEA, CA 125, and CA 199 were

prepared using PBS. All solutions were prepared immediately before each test and stored at 4 ℃ until use.

5.2.5 Electrochemical measurements

EIS and cyclic voltammetry (CV) were conducted on a CHI 660E electrochemical station. A traditional three-electrode system was used in the electrochemical measurements, including a bare or modified AE as the working electrode, an Ag/AgCl (3M KCl) as the reference electrode, and a platinum wire as the auxiliary electrode. EIS was carried out within the frequency range of 0.01 Hz–100 kHz with amplitude of 5 mV under open circuit potential of 0.22 V (**Scheme 9**). The EIS spectra were analyzed using ZView software obtained from Scribner Associates Incorporated, which utilizes nonlinear least-squares fitting to determine the parameters in the equivalent circuit (**Scheme 9** inset). The equivalent circuit consists of solution resistance (R_s), charge-transfer resistance (R_{ct}), constant-phase element (CPE), and Warburg impedance (W_o). CV curves was taken from −0.2 to 0.8 V at a scan rate of 50 $mV \cdot s^{-1}$ in PBS containing 5 mM $[Fe(CN)_6]^{3-/4-}$.

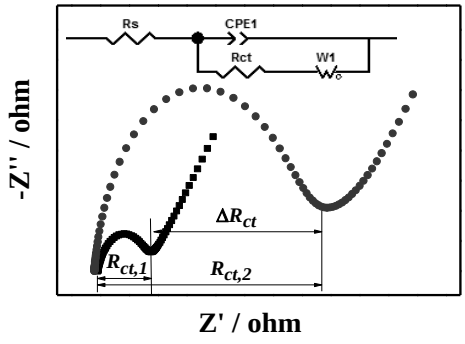

Scheme 9 Typical EIS Nyquist plots and equivalent circuit.

5.2.6 Fabrication of electrochemical aptasensors

In this work, the bimetallic $Cu_xNi_{3-x}(HHTP)_2$ MOF was proposed to construct aptasensor for determining C6 cells and EGFR, while $Cu_3(HHTP)_2$ and $Ni_3(HHTP)_2$ were also similarly used to develop aptasensors for comparison. In detail, the fabrication of $Cu_xNi_{3-x}(HHTP)_2$-based aptasensor was described below as an example. First, 5.0 μL of the $Cu_xNi_{3-x}(HHTP)_2$ suspension was dropped on the surface of pre-treated bare AE and the modified AE with $Cu_xNi_{3-x}(HHTP)_2$ was represented by $Cu_xNi_{3-x}(HHTP)_2$/AE. Then, $Cu_xNi_{3-x}(HHTP)_2$/AE was incubated with aptamer solution at 4 ℃ to develop the corresponding aptasensor (represented by Apt/$Cu_xNi_{3-x}(HHTP)_2$/AE), which was explored to detect diverse analytes of C6 cells and EGFR.

Parameters for tests, including the dosage of $Cu_xNi_{3-x}(HHTP)_2$, concentration of aptamer, and binding time of C6 cells, were determined to obtain the optimal sensing performances. A series of aptasensors were fabricated by modifying the electrode with $Cu_xNi_{3-x}(HHTP)_2$ at different dosages (0.2, 0.5, 1, 2, and 5 mg mL^{-1}) to evaluate its effect on sensing performance. $Cu_xNi_{3-x}(HHTP)_2$/AE was incubated with the aptamer solution at different concentrations (20, 50, 100, 200, and 500 nM) to investigate its influence on the sensitivity of aptasensor. The proposed $Cu_xNi_{3-x}(HHTP)_2$-based aptasensor was also used to determine C6 cells (1000 cell·mL^{-1}), measured by EIS technique and recorded at different durations to obtain the optimal binding time.

The LOD of the $Cu_xNi_{3-x}(HHTP)_2$-based aptasensor for C6 cells was tested under optimal experimental conditions, by separately incubating the modified electrode with

the suspension of C6 cells of different concentrations (50, 1×10^2, 5×10^2, 1×10^3, 5×10^3, 1×10^4, 5×10^4, and 1×10^5 cells mL^{-1}). The calibration plot was obtained between EIS responses and logarithm of the concentration of C6 cell suspension, from which the LOD was deduced according to the criterion of International Union of Pure and Applied Chemistry (IUPAC) recommendation [162]. The LOD of the $Cu_xNi_{3-x}(HHTP)_2$-based aptasensor for EGFR was achieved by the similar method, where the modified electrode was incubated with the EGFR solution with different concentrations (0.001, 0.01, 0.1, 1, 10, 1×10^2, 1×10^3, and 5×10^3 pg mL^{-1}).

L929 cells were used as the interferent to assess the specificity of aptasensor for detecting living C6 cells. The aptasensor was explored to determine L929 cells (1×10^3 cells mL^{-1}) by EIS technique, from which the EIS response was obtained and compared with the determination of C6 cells. The selectivity of aptasensor for EGFR was evaluated with interferents that possibly coexist with EGFR in biological system. These interferents include IgG, BSA, $VEGF_{165}$, Alpha fetoprotein AFP, CEA, CA 125, and CA 199 with the concentration of 100 pg mL^{-1}, which is 1000-folds of the EGFR concentration (0.1 pg mL^{-1}), and their mixed solution (0.1 ng mL^{-1}).

Five independently Apt/$Cu_xNi_{3-x}(HHTP)_2$/AEs were applied to determine C6 cells (1×10^3 cells mL^{-1}) to assess the reproducibility of aptasensor by comparing their detection results. The stability of aptasensor was tested by storing C6/Apt/$Cu_xNi_{3-x}(HHTP)_2$/AE in refrigerator (4 °C) for 15 days and continuously measuring C6 cells by EIS technique each day. The reproducibility and stability of aptasensor for detecting EGFR (1 pg mL^{-1}) were also taken by the same way. The

regenerability of aptasensor for EGFR detection was assessed by washing EGFR/Apt/$Cu_xNi_{3-x}(HHTP)_2$/AE in 0.05 M H_2SO_4 for 2 min and rinsing three times with Milli-Q water. The refreshed aptasensor was then reused to detect EGFR (1 pg mL^{-1}) by EIS. The same operation was repeated until the EIS response of the fabricated aptasensor is up to the original level.

5.2.7 Real samples

Serum samples were obtained from the First Affiliated Hospital of Zhengzhou University after informed consent of the patient. The study protocol was in accordance with the ethical standards of the 1964 Declaration of Helsinki and its later amendments and was approved by the ethics committee of the First Affiliated Hospital of Zhengzhou University. The applicability of cytosensor based on $Cu_xNi_{3-x}(HHTP)_2$ for real samples was evaluated by adding C6 cells suspension with different concentrations (50, 1×10^2, 5×10^2, 1×10^3, 5×10^3, 1×10^4, 5×10^4, and 1×10^5 cells mL^{-1}) into human serum samples through standard addition method. The concentration of C6 cells was detected by the proposed sensor according to calibration curves and compared with the real value. The same method was used for testing the applicability of aptasensor in detecting EGFR with different levels (0.001, 0.01, 0.1, 1, 10, 1×10^2, 1×10^3, and 5×10^3 pg mL^{-1}) in human serum.

5.2.8 Cytotoxicity and *in vitro* cell uptake

For assessing the cell viability against the MOFs, C6 cells and normal cells of

mice, i.e., L929 cells, were cultured in a 96-well plate for 24 h in a humidified atmosphere (5% CO_2, 37 °C). Then, the medium was replaced by the fresh media containing MOFs at various concentrations of 10, 20, 50, 80, and 200 μg·mL^{-1}. After incubating with the suspension of C6 cells for 12 h, the cells were washed with PBS twice, following by adding 200 mL of DMEM to each well. After further incubating for 12 h at 37 °C, 20 μL of MTT (5 mg·mL^{-1}) was added into each well for culturing for 4 h. Finally, the media was removed and the cells were dispersed in 150 mL of DMSO. Then, the absorbance of each well was measured at 490 and 630 nm using a microplate reader.

Prior to the investigation of in *vitro* cellular uptake, the Cy3-labeled EGFR-targeted aptamer (Cy3-Apt) was immobilized over MOFs, denoted by Cy3-Apt/$Cu_3(HHTP)_2$, Cy3-Apt/$Ni_3(HHTP)_2$, and Cy3-Apt/$Cu_xNi_{3-x}(HHTP)_2$, respectively. Afterwards, L929 and C6 cells were cultured in laser confocal culture dish for 12 h in a humidified atmosphere (5% CO_2, 37 °C) with a medium containing Cy3-Apt/$Cu_3(HHTP)_2$, Cy3-Apt/$Ni_3(HHTP)_2$ and Cy3-Apt/$Cu_xNi_{3-x}(HHTP)_2$. For comparison, the blank experiments were also taken. After the media were removed, the cells were softly rinsed with PBS twice and fixed with 4% paraformaldehyde solution for 15 min. The nuclei were then stained with Hoechst 33342 (20 μg·mL^{-1} in PBS) for 20 min and washed with PBS thrice. Finally, the fluorescence images were observed on a CLSM.

5.3 Results and discussion

5.3.1 Characterizations of $Cu_3(HHTP)_2$, $Ni_3(HHTP)_2$, and $Cu_xNi_{3-x}(HHTP)_2$

Characterizations of the chemical and crystal structures of the series of 2D MOFs were taken prior to the study of their sensing performances. The XRD patterns (**Figure 37a**) are similar to previous reports [163]. Prominent peaks at 2θ = 4.7°, 9.5°, 12.6°, and 16.5°corresponding to (100), (200), (001), and (220) plane, indicate the long-range order within the *ab* plane. Additionally, the broad peaks at 2θ = 27.3° can be indexed to the (002) plane, demonstrating the long-range order along the c direction, as expected for covalently linked layered materials. The $Cu_xNi_{3-x}(HHTP)_2$ MOF possesses the identical peak positions with those of $Cu_3(HHTP)_2$ and $Ni_3(HHTP)_2$ MOFs, demonstrating that they are isostructural. The PXRD pattern of the Ni_3HHTP_2 MOF displays an additional diffraction peak around 13.9°, suggesting the alternative stacking mode present in $Ni_3(HHTP)_2$ due to the intercalated layer. Moreover, the FT-IR spectra of $Cu_3(HHTP)_2$, $Ni_3(HHTP)_2$, and $Cu_xNi_{3-x}(HHTP)_2$ (**Figure 37b**) show the peaks of –OH at 3400 cm^{-1}, the asymmetric vibration of O=C−O at 1640 and 1436 cm^{-1}, and C–O at 1308 and 1218 cm^{-1}. The characteristic peaks of Cu–O appear at 568 cm^{-1} in $Cu_3(HHTP)_2$ and $Cu_xNi_{3-x}(HHTP)_2$. An extremely weak peak at 464 cm^{-1} of $Ni_3(HHTP)_2$ is due to Ni–O, which suggests that the coordination of Cu^{2+} with HHTP is dominant in formation of $Cu_xNi_{3-x}(HHTP)_2$. The Raman spectra of $Cu_3(HHTP)_2$, $Ni_3(HHTP)_2$, and $Cu_xNi_{3-x}(HHTP)_2$ MOFs (**Figure 37c**) show the Raman-allowed first-order G band at about 1580 cm^{-1} and the so-called disorder-induced D_1 band at ca. 1350 cm^{-1} of the graphene-like nanostructure [157]. The weak and broad peaks at 2720 and 3180 cm^{-1} can be assigned to the 2D and 2D′ peaks [164], respectively. These results reveal that the

as-obtained 2D MOFs exhibit graphene-like structure. For further analysis, five-band fitting procedures were applied to three MOFs, as shown in **Figure 37d**. Apart from the G band at ~1580 cm^{-1}, other four bands of D_1, D_2, D_3 and D_4, which are typically for disordered carbon structure, are observed at ~1360 cm^{-1}, ~1620 cm^{-1}, ~1530 cm^{-1} and ~1180 cm^{-1}, respectively. The area ratios of D_1/G of $Cu_3(HHTP)_2$ and $Ni_3(HHTP)_2$ MOFs are 3.036 and 3.257, respectively, greater than that of $Cu_xNi_{3-x}(HHTP)_2$ MOF (2.957), hinting that the $Cu_xNi_{3-x}(HHTP)_2$ MOF exhibits low defective structure with a high degree of graphitization. It further reveals that the introduction of Ni ions can improve the graphitization of semiconducting MOF, which can boost the conductivity of the MOF network and aptamer immobilization.

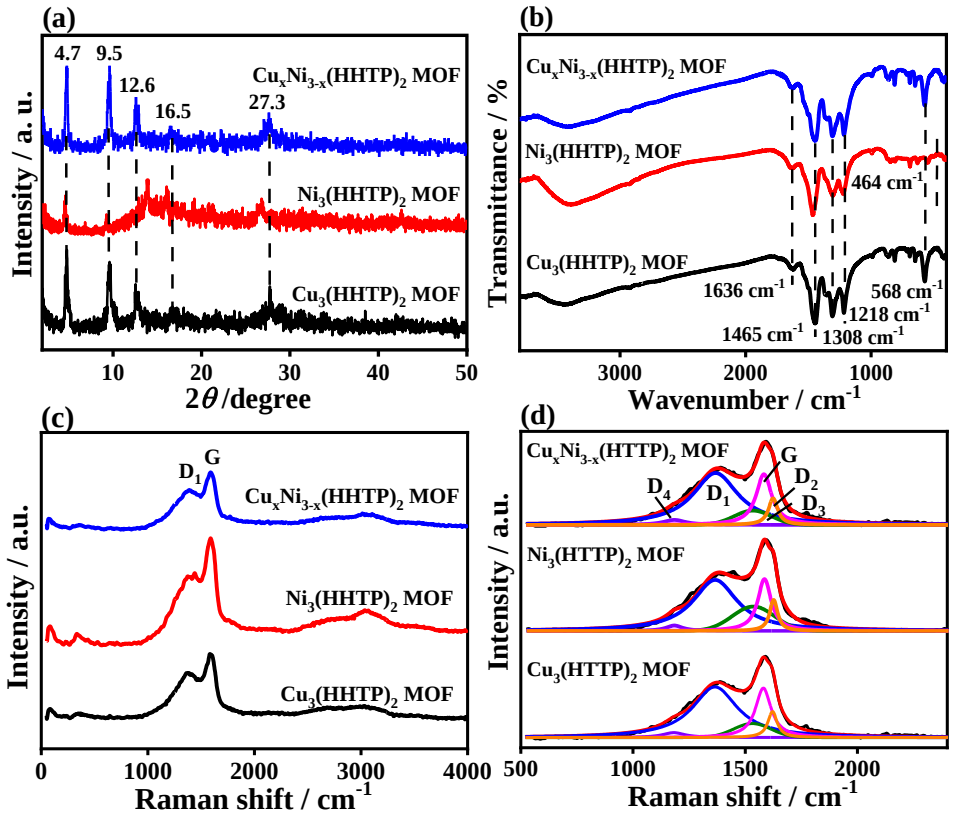

Figure 37. (a) XRD patterns, (b) FT-IR, (c) Raman, and (d) Raman with Gaussian split-peak fitting spectra of $Cu_3(HHTP)_2$, $Ni_3(HHTP)_2$, and $Cu_xNi_{3-x}(HHTP)_2$.

The XPS survey scan spectra (**Figure 38**) exhibit the coexistence of C 1*s* and O 1*s* signals from the HHTP linker. Additionally, the weak Cu 2*p* signal appears in $Cu_3(HHTP)_2$ and the weak Ni 2*p* signal is found in $Ni_3(HHTP)_2$.

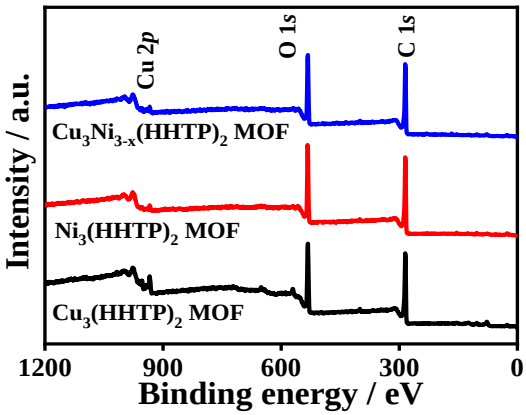

Figure 38. XPS survey scan spectra of $Cu_3(HHTP)_2$, $Ni_3(HHTP)_2$, and $Cu_xNi_{3-x}(HHTP)_2$.

The high-resolution XPS spectra were analyzed by XPSPEAK1 to probe the valence state of each element in the three MOFs. The Cu 2*p* XPS spectrum of $Cu_xNi_{3-x}(HHTP)_2$ (**Figure 39a**) can be separated into two doublets of Cu $2p_{3/2}$ and Cu $2p_{1/2}$ at the binding energies (BEs) of 934.4 and 954.4 eV. The peaks at the BEs of 932.5, 934.5, and 936.6 eV are respectively attributed to the metal Cu state (Cu^0), Cu^+, and Cu^{2+} species of Cu $2p_{3/2}$, whereas those at 940.1 and 943.3 eV are assigned to the satellite peaks of Cu^+ and Cu^{2+}, respectively. The components at the BEs of 952.2 and 954.2 eV are due to the Cu^+ and Cu^{2+} species of Cu $2p_{1/2}$, along with their satellite peaks at the BEs of 961.7 and 963.1 eV, respectively. The existence of Cu^0 and Cu^+ species hints the partial reduction of Cu^{2+} ions during synthesis of $Cu_3(HHTP)_2$,

which is necessary to drive the redox reaction [165] and boosts the electron transfer at electrode/electrolyte interface [166]. The Ni 2*p* XPS spectrum (**Figure 39b**) shows two couples of peaks at the BEs of 858.6 and 875.7 eV, which are attributed to Ni $2p_{3/2}$ and Ni $2p_{1/2}$, respectively. BE components at 855.8 and 858.5 eV in the Ni $2p_{3/2}$ region can be ascribed to Ni^{2+} and Ni^{3+} species of Ni $2p_{3/2}$, along with their satellite peaks at 861.2 and 863.9 eV. Components at the BEs of 873.4 and 875.8 eV are assigned to the Ni^{2+} and Ni^{3+} species of Ni $2p_{1/2}$, respectively, accompanying their satellite peaks at 878.2 and 880.8 eV. The C 1*s* region (**Figure 39c**) shows four main peaks at the BEs of 284.1, 285, 286, and 288.3 eV that are respectively attributed to C–C/C=C, C–O, C=O, and COO groups, and a weak π–π^* peak at the BE of 290.8 eV. This region indicates that $Cu_xNi_{3-x}(HHTP)_2$ has a highly conjugated structure, which can greatly boost the immobilization of aptamer strands [167]. Here, the C–C/C=C and π–π^* bonds are aroused from the benzene rings of organic linkers. The coexistence of C=O and COO groups are due to the oxidation of C–OH. The O 1*s* deconvolutions (**Figure 39d**) are composed of three peaks at the BEs of 530.7, 531.7, and 533 eV, corresponding to the O vacancies, C=O, and C-O groups, respectively, along with a weak peak of OH at 535.6 eV. The appearance of abundant O vacancies can greatly improve the electrochemical performance of MOF [168]. These results reveal that $Cu_xNi_{3-x}(HHTP)_2$ is composed of mixed valences $Cu^0/Cu^+/Cu^{2+}$ and Ni^{2+}/Ni^{3+}, and has a highly conjugated nanostructure and abundant O vacancies, leading to its excellent electrochemical activity.

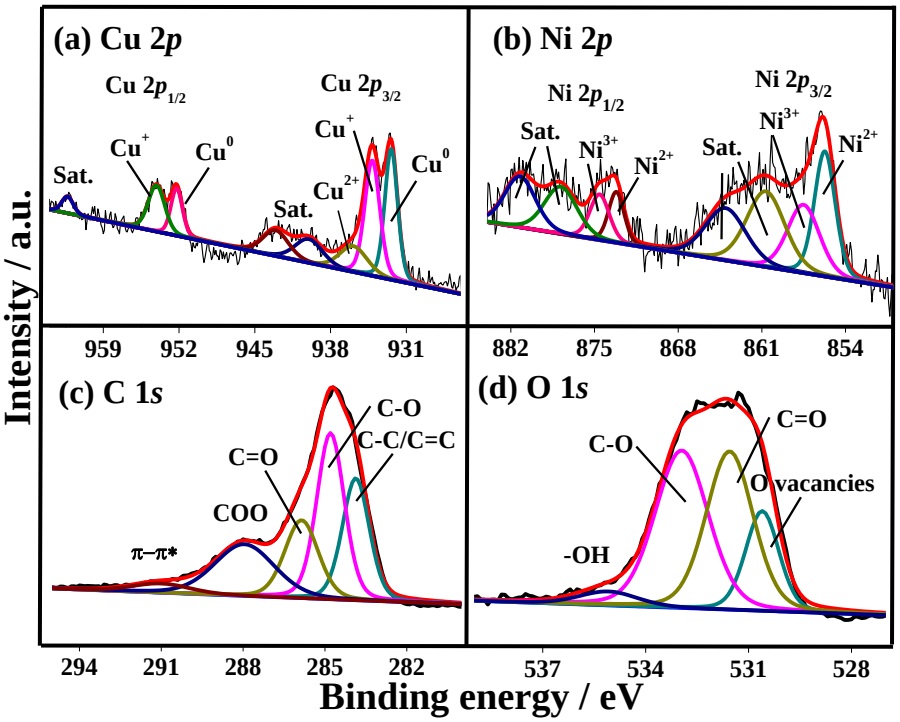

Figure 39. High-resolution (a) Cu 2*p*, (b) Ni 2*p*, (c) C 1*s* and (d) O 1*s* XPS spectra of $Cu_xNi_{3-x}(HHTP)_2$.

The permanent porosity of $Cu_3(HHTP)_2$, $Ni_3(HHTP)_2$, and $Cu_xNi_{3-x}(HHTP)_2$ MOFs are illuminated by N_2 adsorption at 77 K (**Figure 40a**), which display type-I adsorption-desorption isotherms as archetypal microporous materials apparently. The BET surface areas of $Cu_3(HHTP)_2$, $Ni_3(HHTP)_2$, and $Cu_xNi_{3-x}(HHTP)_2$ MOFs are calculated to be 754.01, 516.24 and 789.32 $cm^3 \cdot g^{-1}$, respectively. It is clear that the $Cu_xNi_{3-x}(HHTP)_2$ MOF displays the largest surface area, which can greatly facilitate the aptamer immobilization. All of the three samples reveal narrow distributions centered at 0.5−1 nm and 1−2 nm (**Figure 40b**), indicating the microporous structure of the samples.

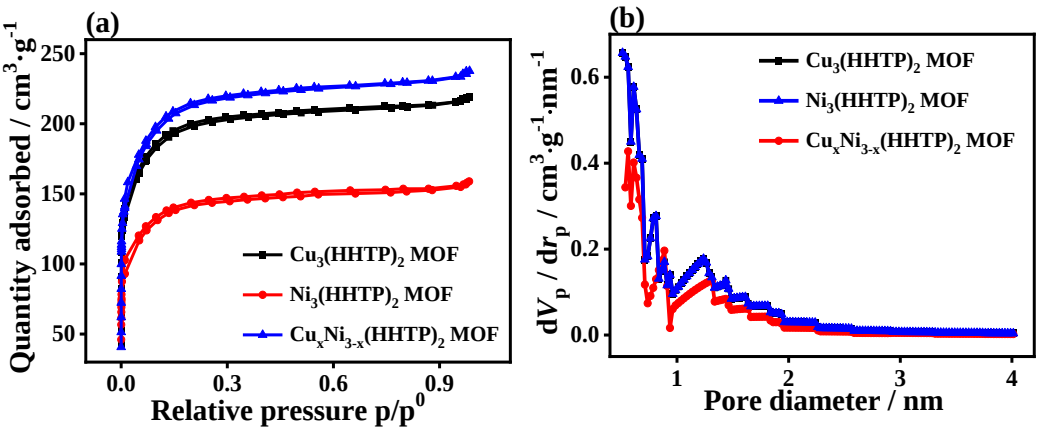

Figure 40. (a) Nitrogen adsorption-desorption isotherms and (b) pore size distribution of $Cu_3(HHTP)_2$, $Ni_3(HHTP)_2$, and $Cu_xNi_{3-x}(HHTP)_2$ MOFs.

The TEM images (**Figure 41**) confirm the appearance of nanorods that are aggregated to the homogeneous-packed structure. As illustrated in the high-magnification TEM (HR-TEM) (**Figure 41c**), the distance of 1.81 nm between lattice fringes corresponds to the hexagonal crystal system and can be assigned to (100) lattice face, indicating a top view of *ab* plane. Meanwhile, the lattice spacing of 0.37 nm suggests the stacking of layers along c-axis, which nearly coincides with the simulated distance between layers of $Cu_3(HHTP)_2$ MOF. The honeycomb structure of the porous framework of $Ni_3(HHTP)_2$ MOF along the plane (001) reveals a hexagonal unit cell agreeing well with the results observed for pure $Ni_3(HHTP)_2$ MOF. As shown in the HR-TEM image (**Figure 41f**), the clear lattice fringe with a spacing of 0.67 nm attributes to the (210) face of $Ni_3(HHTP)_2$ MOF nanorods. The HR-TEM image of $Cu_xNi_{3-x}(HHTP)_2$ MOF (**Figure 41i**) shows the lined patterns parallel to the c-axis, which is characteristic for the $Cu_3(HHTP)_2$ MOF structure.

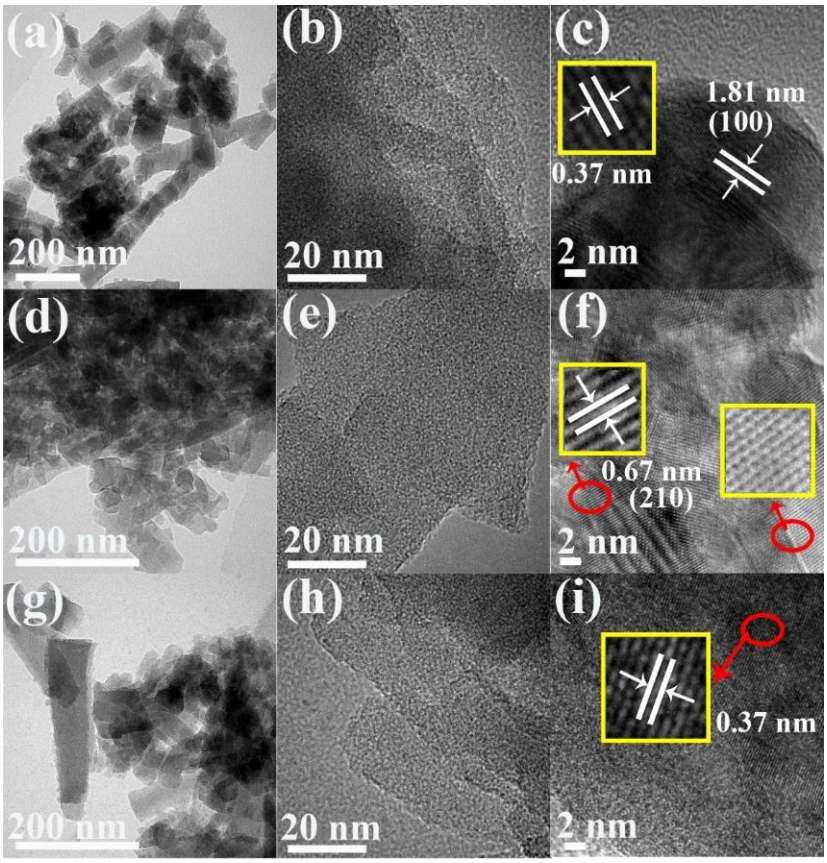

Figure 41. TEM and HR-TEM images of (a, b, c) $Cu_3(HHTP)_2$, (d, e, f) $Ni_3(HHTP)_2$, and (g, h, i) $Cu_xNi_{3-x}(HHTP)_2$ MOFs.

5.3.2 Biocompatibility of $Cu_3(HHTP)_2$, $Ni_3(HHTP)_2$ and $Cu_xNi_{3-x}(HHTP)_2$

Cell viability of the series of MOFs were evaluated by incubating with the suspension of living L929 and C6 glioma cells, and tested via MTT experiments. **Figure 42a** reveals that the cytotoxicity of three MOFs against L929 cells slightly decreases with the incubating time going on. About 74.5% L929 cells remain alive when the concentration of $Cu_xNi_{3-x}(HHTP)_2$ is 200 $\mu g \cdot mL^{-1}$. C6 glioma cells show a comparable survival rate (76.2%) at the same concentration (**Figure 42b**). Similar results are also obtained for $Cu_3(HHTP)_2$ and $Ni_3(HHTP)_2$. The results reveal the good biocompatibility of such MOFs, which could be potentially used for detection of

living cells.

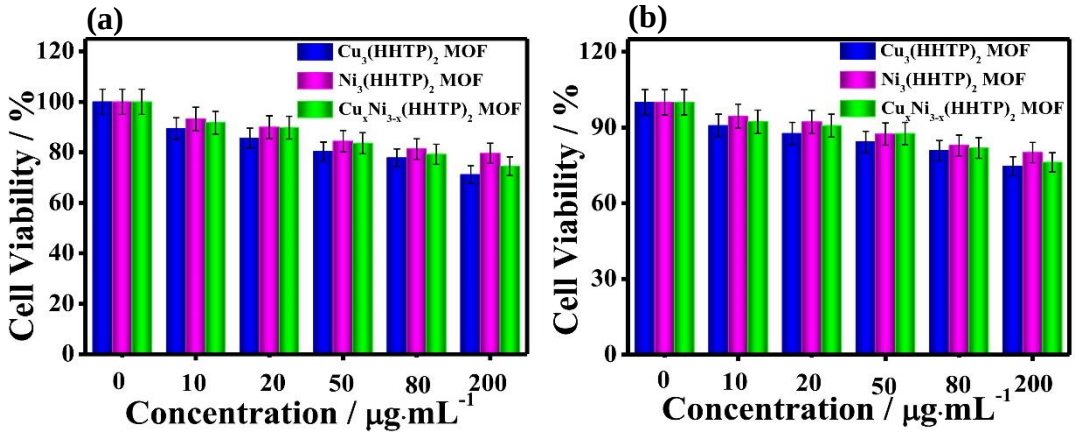

Figure 42. Cell viabilities of $Cu_3(HHTP)_2$, $Ni_3(HHTP)_2$, and $Cu_xNi_{3-x}(HHTP)_2$ against (e) L929 and (f) C6 rat glioma cells.

5.3.3 Electrochemical sensing performances of 2D MOFs toward C6 cells

Among the diverse electrochemical techniques, the impedimetric sensing has ultra-low sensitivity, depending on the impedance measurement of an electrochemical system subject to alternating current in a range of frequencies [169]. As EIS enables to determine the change in electrochemical activity caused by modification of electrode or adsorption of biomolecule, it is substantially benefited in electrochemical biosensing. Herein, both EIS and CV methods were explored to record the electrochemical performances of each procedure for sensing C6 glioma cells, including the modification with MOFs, the immobilization of aptamer strands, and the detection of C6 glioma cells. EIS can be graphically represented by Nyquist plots where the experimental values are fitted with a Randles theoretical model and used to estimate the charge-transfer resistance (R_{ct}) at the working electrode [170]. R_{ct} is most

commonly used to assess the level of targets. The increase of R_{ct} correlates with the blockage of electron transfer, and the successful modification of working electrode. **Figure 43** show the EIS Nyquist plots for the determining procedures of C6 cells by using the impedimetric sensors based on MOFs. The R_{ct} values for each step of the construction of aptasensors and detection of C6 cells are summarized in **Table 3**.

Table 3. R_{ct} values of each step during the detection procedures for C6 cells using the cytosensors based on $Cu_3(HHTP)_2$, $Ni_3(HHTP)_2$, and $Cu_xNi_{3-x}(HHTP)_2$.

Electrode materials	R_{ct} (Ω)			
	Bare AE	Modification of electrode	Immobilization of aptamer	Detection of C6 cells
$Cu_3(HHTP)_2$	72.5	659.5	797.9	950.9
$Ni_3(HHTP)_2$	60.2	631.2	819.6	981.6
$Cu_xNi_{3-x}(HHTP)_2$	118.9	381	647.3	1128.3

The analysis of $Cu_xNi_{3-x}(HHTP)_2$-based aptasensor is considered as an example to illustrate the electrochemical behaviors for determining C6 cells. As shown in **Figure 43c**, the EIS Nyquist plot of the bare AE shows a small diameter of the semicircle of small R_{ct} value of 118.9 Ω, which indicates good electrochemical activity. The $Cu_xNi_{3-x}(HHTP)_2$/AE shows a larger semicircle of the EIS Nyquist plot, with a higher R_{ct} value (381 Ω) than the bare AE. Nevertheless, this R_{ct} value is much smaller than those of the reported MOFs or MOF-derived materials, which can greatly enlarge the electrochemical signal, and thus enhance the detection sensitivity of the

corresponding aptasensor. Further, the Apt/$Cu_xNi_{3-x}(HHTP)_2$/AE shows an even larger R_{ct} value (647.3 Ω). This result suggests that the binding aptamer strands can reduce the electrochemical performance. Afterwards, the specific recognition of aptamer strand toward C6 cells further causes the increase of R_{ct} value (1.13 kΩ) for C6/Apt/$Cu_xNi_{3-x}(HHTP)_2$/AE.

Quantitative comparison of the change of R_{ct} value for each step ($\Delta R_{ct} = R_{ct,\,i+1} - R_{ct,\,i}$) of three kinds of aptasensors is feasible to analyze their detection sensitivity toward C6 cells. As illustrated in **Figure 43d**, the $Cu_3(HHTP)_2$/AE and $Ni_3(HHTP)_2$/AE exhibit comparable ΔR_{ct} values for each step during the aptasensor fabrication, revealing their equivalent electrochemical activities and sensing performances. In comparison, the $Cu_xNi_{3-x}(HHTP)_2$/AE exhibits smaller ΔR_{ct} value (262.1 Ω) for AE modification and larger ΔR_{ct} values for aptamer immobilization (266.3 Ω) and C6 cell detection (481 Ω). This result suggests that the bimetallic MOF has superior electrochemical activity and sensing performance, which can be ascribed to the following factors. (i) The isomorphic substitution of Cu sites in $Cu_3(HHTP)_2$ by Ni centers can modify the MOF surface, and further, improve the sorption ability toward aptamers [171], as indicated by the slightly larger ΔR_{ct} for $Ni_3(HHTP)_2$. (ii) The bimetallic MOFs can produce structural defect that leads to some metal centers connected to auxiliary terminals (e.g. solvent). Those unsaturated open metal centers can increase the adsorption affinity toward biomolecules, compared to fully coordinated metal centers [164]. (iii) The abundant O vacancies and different metal valences of $Cu^{2+}/Cu^{+}/Cu^{0}$ and Ni^{2+}/Ni^{3+} offer $Cu_xNi_{3-x}(HHTP)_2$ with good redox

properties and reoxidation ability, thereby showing more active sites and efficiently reducing the resistance of charge transfer, which is beneficial to improve electrochemical sensing performances [172]. (iv) Large specific surface area of the 2D $Cu_xNi_{3-x}(HHTP)_2$ MOF also remarkably enhances the adsorption of aptamer strands and detection efficiency toward targets [173].

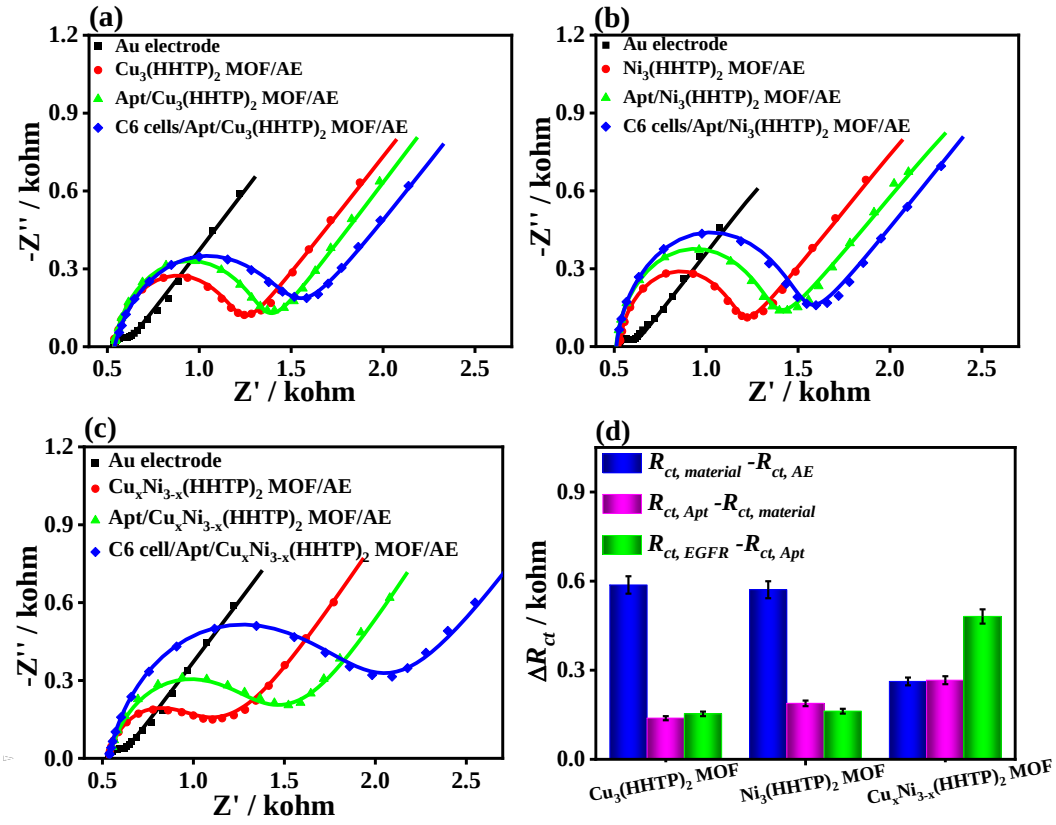

Figure 43. EIS Nyquist plots of (a) $Cu_3(HHTP)_2$, (b) $Ni_3(HHTP)_2$ and (c) $Cu_xNi_{3-x}(HHTP)_2$-based aptasensor for detecting C6 cells (1×10^3 cells mL^{-1}) in 0.1 M PBS (pH 7.4) containing 5.0 mM $[Fe(CN)_6]^{3-/4-}$ redox. (d) Variations in R_{ct} values for the modification with three kinds of MOFs ($\Delta R_{ct} = R_{ct,\ materials} - R_{ct,\ AE}$), the immobilization of aptamer strands ($\Delta R_{ct} = R_{ct,\ Apt} - R_{ct,\ materials}$), and detection of C6 cells ($\Delta R_{ct} = R_{ct,\ C6} - R_{ct,\ Apt}$).

The CV curve (**Figure 44**) of AE shows typical quasi-reversible oxidation and

reduction wave peaks of $[Fe(CN)_6]^{3-/4-}$, which acts as redox-active probe to indicate the electron transfer between electrolyte and working electrode [174].

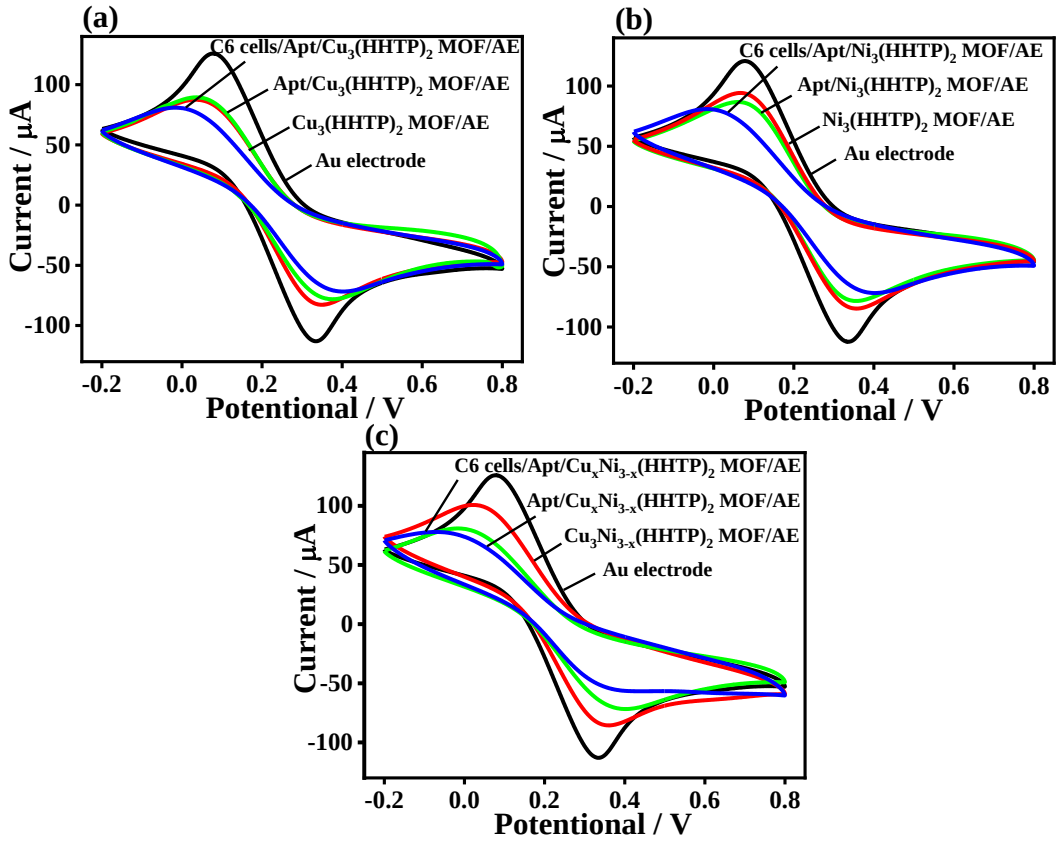

Figure 44. CV curves of the aptasensors based on (a) $Cu_3(HHTP)_2$, (b) $Ni_3(HHTP)_2$, and (c) $Cu_xNi_{3-x}(HHTP)_2$ for detecting C6 cells in PBS containing 5.0 mM $[Fe(CN)_6]^{3-/4-}$ redox.

Regarding $Cu_xNi_{3-x}(HHTP)_2$/AE, the enclosed area of CV curve becomes smaller than AE, and peak current density also decreases. These results suggest that $Cu_xNi_{3-x}(HHTP)_2$ slightly hinders the electron transfer at the electrode/electrolyte interface [175]. The Apt/$Cu_xNi_{3-x}(HHTP)_2$/AE displays a reduced enclosed area and peak current density. The aptamer strand can be ionized in water, which leads to the production of the negative charge of phosphate groups. Thus, a strong repulsion

between the negative charge of phosphate groups and the $[Fe(CN)_6]^{3-/4-}$ redox can prevent the electron transferring, resulting in a decrease of the electrochemical activity for the electrode [176]. The current density of CV curve of C6/Apt/$Cu_xNi_{3-x}(HHTP)_2$/AE continuously declines, suggesting the strong binding between aptamer strands and C6 cells [177]. Further, aptasensors based on $Cu_3(HHTP)_2$ and $Ni_3(HHTP)_2$ were investigated for detecting C6 cells using CV technique. The change trend in their peak current density and enclosed area is very close, revealing similar sensing performances. The dissimilarity among CV curves clearly suggests different detection ability or sensitivity of the three kinds of aptasensors.

5.3.4 Selectivity of the $Cu_xNi_{3-x}(HHTP)_2$-based cytosensor toward C6 cells

The $Cu_xNi_{3-x}(HHTP)_2$-based aptasensor was used to detect L929 cells via EIS and CV to confirm its specificity for detecting C6 cells. The EIS Nyquist plots (**Figure 45a**) show that even a large change in the semicircle diameter for the aptamer immobilization over $Cu_xNi_{3-x}(HHTP)_2$/AE, a slight increase of the semicircle diameter value for determining L929 cells is observed. This finding indicates a good specificity of the $Cu_xNi_{3-x}(HHTP)_2$-based aptasensor for detecting C6 cells. Also, the corresponding CV curves give the closest result (**Figure 45b**), showing a negligible change in the peak current density for the detection of L929 cells.

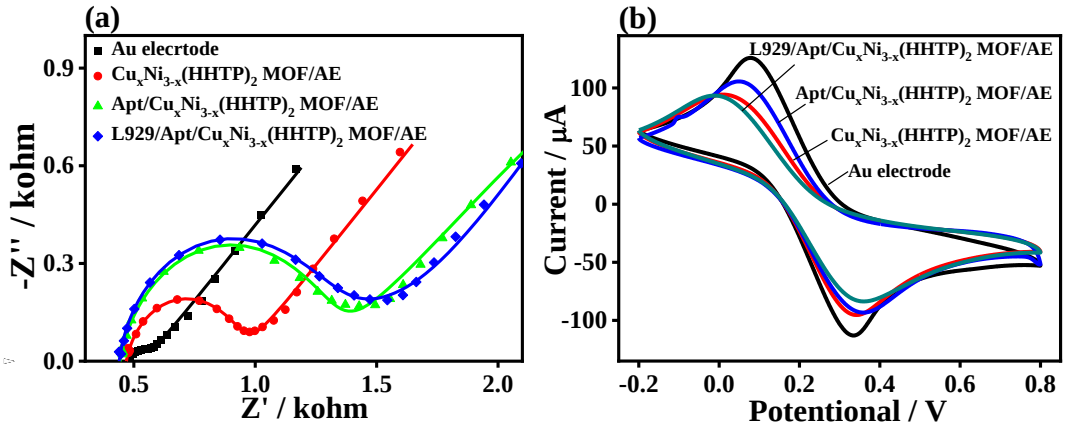

Figure 45. (a) EIS Nyquist plots and (b) corresponding CV curves for the $Cu_xNi_{3-x}(HHTP)_2$-based aptasensor for detecting L929 cells in PBS containing 5.0 mM $[Fe(CN)_6]^{3-/4-}$ redox.

The specificity of $Cu_xNi_{3-x}(HHTP)_2$-based aptasensor was further investigated in living cells via CLSM (**Figure 46**). As the overexpressed nucleolin on the cell membrane of C6 cells (nucleolin$^+$) can be recognized by the Cy3-Apt, bright yellow fluorescent signals are observed around C6 cells; whereas no noticeable yellow fluorescent signal is found for L929 cells (nucleolin$^-$). Thus, it could infer that Cy3-Apt/$Cu_xNi_{3-x}(HHTP)_2$ is mostly identified and attached to C6 cells by the efficient receptor-mediated recognition. Besides, the black dots outside the C6 and L929 cells in the bright field are the aggregated $Cu_xNi_{3-x}(HHTP)_2$ under the physiological medium. Similar appearances of Cy3-Apt/$Cu_3(HHTP)_2$ and Cy3-Apt/$Ni_3(HHTP)_2$ against L929 and C6 cells are also found, which hint the good specificity of these cytosensors.

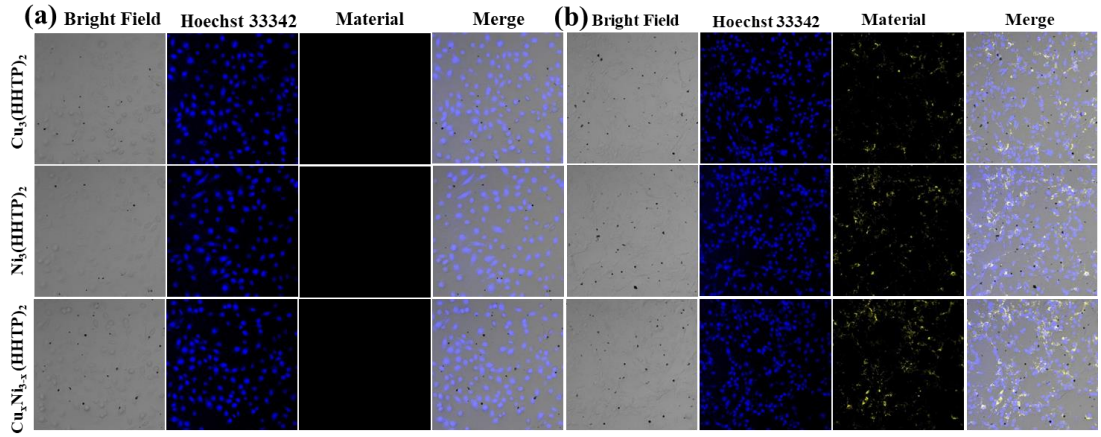

Figure 46 CLSM images of Cy3-Apt/$Cu_3(HHTP)_2$, Cy3-Apt/$Ni_3(HHTP)_2$, and Cy3-Apt/$Cu_xNi_{3-x}(HHTP)_2$ against (a) L929 and (b) C6 cells.

5.3.5 Detection of C6 cells using the $Cu_xNi_{3-x}(HHTP)_2$-based cytosensor

Screening the experimental parameters for electrochemical measurements, such as the dosage of $Cu_xNi_{3-x}(HHTP)_2$, the aptamer concentration, and the binding time toward C6 cells, is essential to achieve the optimal sensing performances. A series of $Cu_xNi_{3-x}(HHTP)_2$-based aptasensors were constructed under the same condition by using different dosages of $Cu_xNi_{3-x}(HHTP)_2$ (0.2, 0.5, 1.0, 2.0, and 5.0 $mg \cdot mL^{-1}$) for determining C6 cells (1000 cells·mL^{-1}). The ΔR_{ct} value before and after modification of AE with $Cu_xNi_{3-x}(HHTP)_2$ increases along with increasing its dosage (**Figure 47a**). This observation reveals that the thick $Cu_xNi_{3-x}(HHTP)_2$ layer can substantially hinder the electron transfer at the solid/liquid interface. However, the ΔR_{ct} values stimulated by aptamer immobilization and C6 cells detection first arises with the increasing $Cu_xNi_{3-x}(HHTP)_2$ dosage from 0.2 to 1 mg·mL^{-1}, and then declines when the $Cu_xNi_{3-x}(HHTP)_2$ dosage is larger than 1.0 mg·mL^{-1}. During the electrochemical measurement, it can be observed that partial $Cu_xNi_{3-x}(HHTP)_2$ will be released from

the electrode surface ($Cu_xNi_{3-x}(HHTP)_2$ dosage: 2.0 mg·mL^{-1}), which reveals that excessively thick MOF layer is not stable in water. As a result, $Cu_xNi_{3-x}(HHTP)_2$ with a concentration of 1.0 mg·mL^{-1} is selected to develop the cytosensor. Prior to detecting C6 cells, the $Cu_xNi_{3-x}(HHTP)_2$-based cytosensors were separately incubated with the aptamer solutions at different concentrations of 20, 50, 100, 200, and 500 nM. The ΔR_{ct} values for each cytosensor (**Figure 47b**) show a continuous increase, with increasing the concentration of aptamer in the range of 20–100 nM. After that, the ΔR_{ct} values reach an equilibrium, which suggests a saturated binding between the aptamer strands and C6 cells. Thus, the aptamer solution of 100 nM is selected to test the electrochemical sensing.

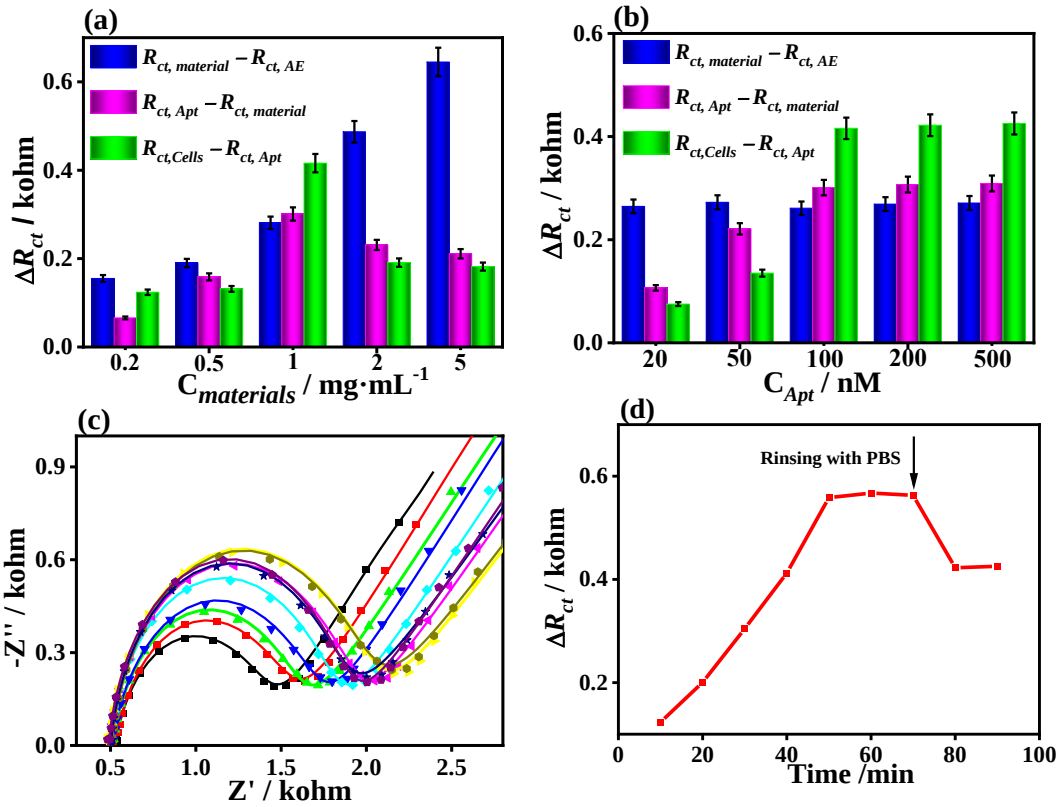

Figure 47. Effect of (a) the dosage of $Cu_xNi_{3-x}(HHTP)_2$ and (b) the concentration of aptamer strands on the variation of R_{ct} values before and after detecting C6 cells. (c)

EIS Nyquist plots of the $Cu_xNi_{3-x}(HHTP)_2$-based aptasensor incubated with C6 cells (1000 cell·mL^{-1}) for different durations and (d) their corresponding ΔR_{ct} values.

To evaluate the influence of incubation time of C6 cells on the sensing performance, the EIS Nyquist plots for the proposed $Cu_xNi_{3-x}(HHTP)_2$-based cytosensor were recorded (**Figure 47c**). The observed ΔR_{ct} value increased with the prolonged binding time of C6 cells. This finding remains at a level-off when the binding time is longer than 50 min, which implies the statured combination of aptamer and C6 cells. When washing the sensing system using excessive PBS, the ΔR_{ct} value will decrease, because some loosely adsorbed aptamer-C6 complexes fall off (**Figure 47d**).

Gradient concentrations of the C6 cell suspension under optimal conditions were used to verify the analytical capability of $Cu_xNi_{3-x}(HHTP)_2$-based cytosensor toward C6 cells. As shown in **Figure 48a**, the EIS responses of cytosensor gradually enhance with the increased concentration of cell suspension in the range of 50 to 1×10^5 cells mL^{-1}. Then, the EIS signal is up to a level-off, which hints that the combination of C6 cells with aptamer is saturated. **Figure 48b** shows the corresponding ΔR_{ct} values caused by determining C6 cells at different concentrations. A linear proportional relationship between the logarithm of suspension concentration is found (**Figure 48b** inset), and the caused ΔR_{ct} values ranging from 50 to 1×10^5 cells mL^{-1} are observed. As such, the linear equation for analyzing C6 cells is simulated as ΔR_{ct} (kΩ) = $0.24\log Con_{cell} - 0.26$ (Con_{cell} is the concentration of C6 cell suspension) with a

correlation coefficient value (R^2) of 0.9966. Thereby, the LOD is estimated by 3σ/S (σ is the standard deviation of blank signal, and S is the slope of fitting line), i.e., 21 cells mL^{-1}.

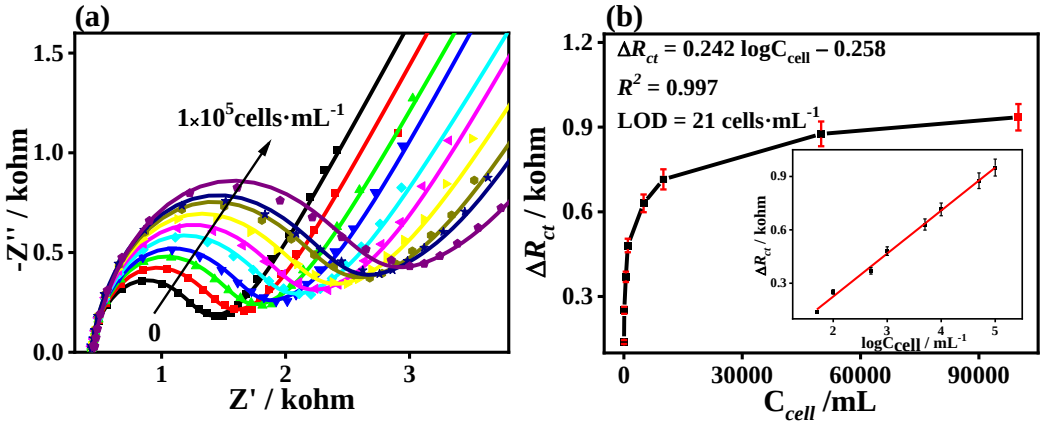

Figure 48. (a) EIS responses of Apt/$Cu_xNi_{3-x}(HHTP)_2$/AE toward C6 cells with different concentrations (0, 50, 1×10^2, 5×10^2, 1×10^3, 5×10^3, 1×10^4, 5×10^4, and 1×10^5 cells mL^{-1}). (b) The ΔR_{ct} values as a function of the concentration of C6 cells (inset: the linear fitting plot of ΔR_{ct} as a function of the logarithm of C6 cells concentration, the error bars are standard deviations for n = 3).

Compared with the reported cytosensors for analyzing C6 cells or other cancer cells (**Table 4**), the $Cu_xNi_{3-x}(HHTP)_2$-based cytosensor shows a lower LOD and superior sensing performance. As mentioned, $Cu_xNi_{3-x}(HHTP)_2$ substrate for immobilizing aptamer strands exhibits large specific area and intrinsic channels, which not only anchors the aptamers on its surface via the π–π stacking, Vander Waals, and electrostatic interactions [178], but also impel the aptamers to penetrate into its interior. Moreover, the good biocompatibility of $Cu_xNi_{3-x}(HHTP)_2$ also enhances the adhesion of living cancer cells, which further boosts the stability of the complex of

aptamer and cells.

Table 4 Comparison with the reported sensing techniques for detection of living cancer cells.

Materials	Detection method	Cell type	Detection range (cell·mL^{-1})	LOD (cell·mL^{-1})	Refs.
Au NCs/MWCNT	EIS	MCF-7 cells	1×10^2–1×10^6	80	[179]
p-COF	EIS	MCF-7 cells	5×10^2–1×10^5	61	[155]
Tb-MOF-on-Fe-MOF	EIS	MCF-7 cells	1×10^2–1×10^5	19	[73]
Catalytic hairpin assembly	DPV	A549 cells	50–1×10^6	30	[180]
DNA bridge-AgNCs	DPV	HepG2 cells	50–2×10^6	15	[181]
GQD-ConA@Fe_3O_4	DPV	HeLa cells	5×10^2–1×10^5	273	[182]
$Cu_xNi_{3-x}(HHTP)_2$	**EIS**	**C6 cells**	**50–1×10^5**	**21**	**This work**

A549 cells: lung cancer cells, HepG2 cells: hepatocellular carcinoma cells, HeLa cells: cervical cancer, DPV: differential pulse voltammetry

To evaluate the reproducibility of the $Cu_xNi_{3-x}(HHTP)_2$-based cytosensor, five independently cytosensors were constructed and incubated with the C6 cell suspensions at different concentrations of 1×10^2, 5×10^2, and 1×10^3 cells mL^{-1}. Then, EIS responses of the cytosensors for determination of C6 cells were recorded in 0.1 M PBS (pH = 7.4) containing $[Fe(CN)_6]^{3-/4-}$. The ΔR_{ct} values (**Figure 49a**) show RSD of 7.1%, 4.9%, and 2.4%, respectively, for analyzing C6 cells at different concentrations, hinting an acceptable reproducibility of this sensing system. Furthermore, the stability

of cytosensor was investigated by storing three groups of C6/Apt/$Cu_xNi_{3-x}(HHTP)_2$/AEs binding with C6 cells at different concentrations (1×10^2, 5×10^2, and 1×10^3 cells mL^{-1}) for 15 days. The obtained ΔR_{ct} values (**Figure 48b**) provides RSD of 5%, 4.8%, and 4.3% for the cell concentrations of 1×10^2, 5×10^2, and 1×10^3 cells mL^{-1}, respectively. Apparently, the $Cu_xNi_{3-x}(HHTP)_2$-based cytosensor shows not only an acceptable reproducibility but also good stability for analyzing C6 cells in biological system.

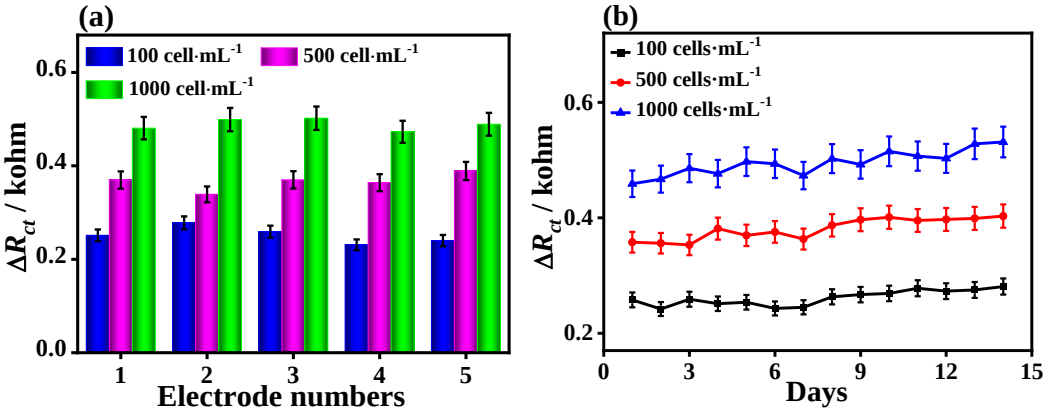

Figure 49. (e) Reproducibility of $Cu_xNi_{3-x}(HHTP)_2$-based cytosensor for detecting living C6 cells. (f) Stability of the $Cu_xNi_{3-x}(HHTP)_2$-based cytosensor toward C6 cells (concentrations: 1×10^2, 5×10^2, and 1×10^3 cells mL^{-1}) within 15 days.

C6 cell suspensions at different concentrations were spiked into the pretreated human serum to probe the applicability of the $Cu_xNi_{3-x}(HHTP)_2$-based cytosensor, and the real cell concentration was deduced from the calibration plot (**Figure 48b** inset). **Table 5** summarizes the values, recoveries, and RSD deduced from the EIS results, revealing the high accuracy of the $Cu_xNi_{3-x}(HHTP)_2$-based cytosensor for C6 cell detection in serum samples, with recoveries ranging from 99.4 to 108% and RSD

values ranging from 1.59 to 4.36%.

Table 5 Detection of C6 cells in human serum using the $Cu_xNi_{3-x}(HHTP)_2$-based cytosensor.

Amount added (cells·mL^{-1})	ΔR_{ct} (kohm)	Found (cells·mL^{-1})	Apparent recovery (%)	RSD (%)
50	0.159	53	106	3.18
1×10^2	0.234	108	108	2.67
5×10^2	0.400	527	105.4	4.36
1×10^3	0.467	994	99.4	2.86
5×10^3	0.645	5367	107.3	1.59
1×10^4	0.712	10187	101.9	1.76
5×10^4	0.882	51684	103.4	2.56
1×10^5	0.867	105418	105.4	3.46

5.3.6 EGFR sensing performances of the $Cu_xNi_{3-x}(HHTP)_2$-based aptasensor

In addition to the determination of living C6 cells by the $Cu_xNi_{3-x}(HHTP)_2$-based aptasensor, EGFR overexpression in C6 cells was also investigated via EIS and CV techniques. For comparison, the $Cu_3(HHTP)_2$- and $Ni_3(HHTP)_2$-based aptasensors were also utilized to detect EGFR under the same conditions (**Figures 50a** and **b**). For all aptasensors, similar electrochemical behaviors were achieved in the different steps of electrode modification, aptamer immobilization, and EGFR detection, from which the gradual increase in R_{ct} values was obtained along with the fabrication of aptasensors and on-going EGFR detection. The ΔR_{ct} value of the

$Cu_xNi_{3-x}(HHTP)_2$-based aptasensor is the largest (625.8 Ω), hinting its superior sensing performance toward EGFR, which is consistent with the detection result of living C6 cells.

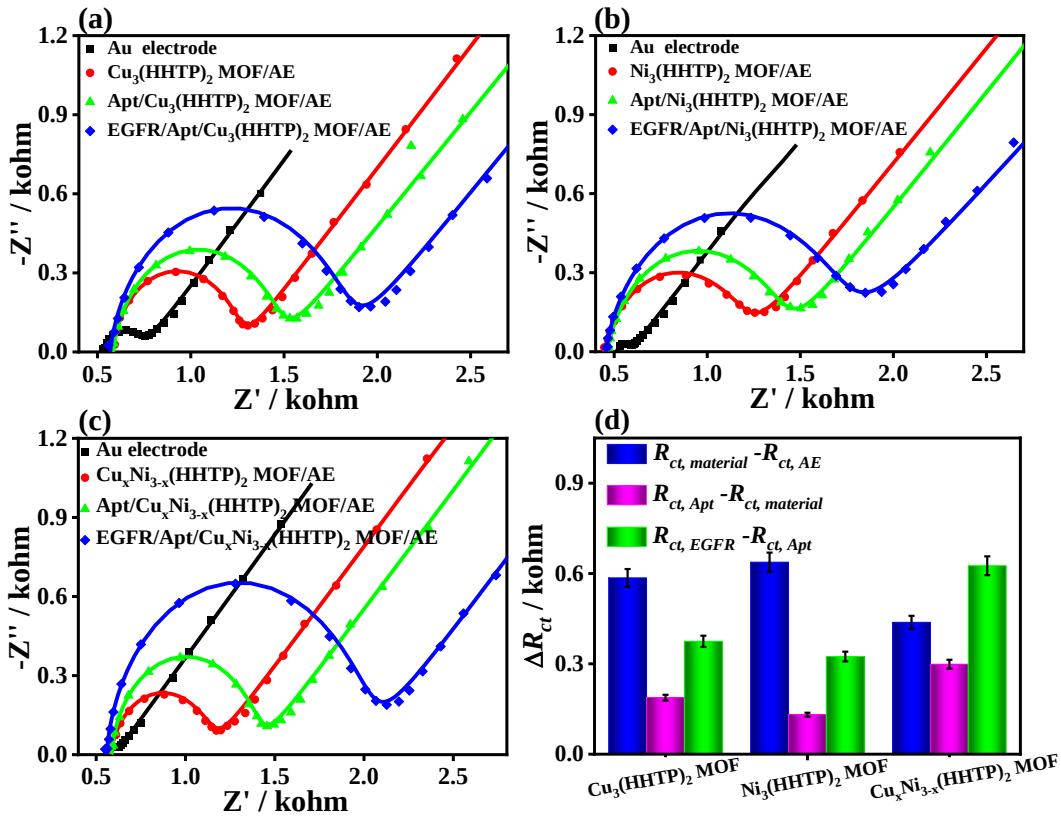

Figure 50. EIS Nyquist plots of the aptasensor based on (a) $Cu_3(HHTP)_2$, (b) $Ni_3(HHTP)_2$ and (c) $Cu_3Ni_{3-x}(HHTP)_2$ for detecting EGFR (1 pg mL^{-1}) in 0.1 M PBS (pH 7.4) containing 5.0 mM $[Fe(CN)_6]^{3-/4-}$ redox. (d) Variations in R_{ct} values for each stage in the fabrication procedure of aptasensors based on $Cu_3(HHTP)_2$, $Ni_3(HHTP)_2$, and $Cu_3Ni_{3-x}(HHTP)_2$ for detecting EGFR (1 pg mL^{-1}).

Under the optimized condition, the LOD of the developed $Cu_xNi_{3-x}(HHTP)_2$-based aptasensor was determined by analyzing EGFR at different concentrations (0.001, 0.01, 0.1, 1, 10, 1×10^2, 1×10^3, and 5×10^3 pg mL^{-1}) and recorded

by EIS technique (**Figure 51a**). The result reveals that the observed ΔR_{ct} values for detecting EGFR increase with rising EGFR concentration within the range from 1 fg mL^{-1} to 2 ng mL^{-1} (**Figure 51b**). When the EGFR concentration is larger than 2 ng mL^{-1}, the ΔR_{ct} value reaches a constant level, which suggests a saturated interaction between aptamer and EGFR. As deduced from the calibration curve (**Figure 51b** inset), the LOD can be evaluated as 0.72 fg mL^{-1} from the equation of ΔR_{ct} (kohm) = $0.14\log C_{EGFR} + 0.6$ by $3\sigma/S$ (σ is the standard deviation of the blank signal and S is the slope of the fitting line).

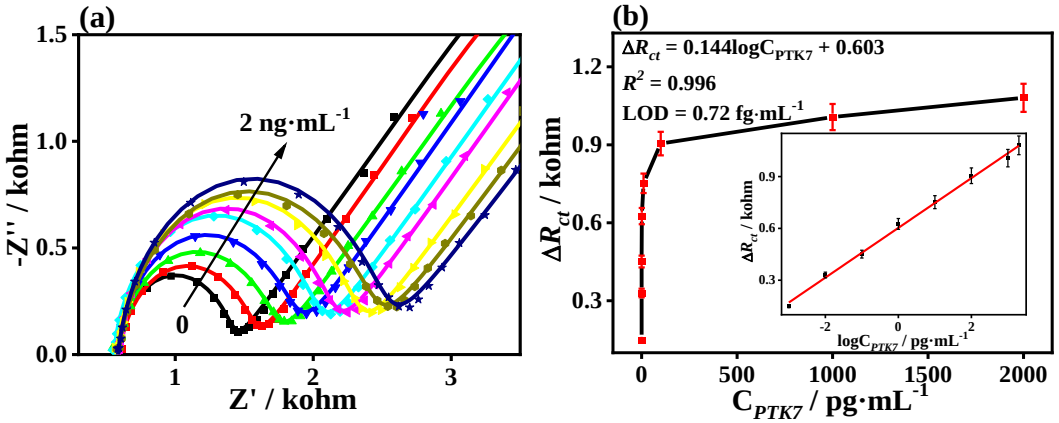

Figure 51. (a) EIS Nyquist plots for detecting EGFR with different concentrations (0.001, 0.01, 0.1, 1, 10, 100, 1000 and 5000 pg mL^{-1}) with the $Cu_3Ni_{3-x}(HHTP)_2$-based aptasensor; (b) The calibration curves between ΔR_{ct} and EGFR concentrations (inset: the linear fitting plot of ΔR_{ct} as a function of the logarithm of EGFR concentration, the error bars are standard deviations for n = 3).

Compared to the known aptasensors for detecting EGFR (**Table 6**), the $Cu_xNi_{3-x}(HHTP)_2$-based aptasensor has excellent sensing performances with lower LOD and higher sensitivity toward EGFR.

Table 6 Comparison with the reported sensing techniques for detection of EGFR.

Materials	Detection method	Detection range ($pg \cdot mL^{-1}$)	LOD ($fg \cdot mL^{-1}$)	Refs.
Cysteamine/PDITC/protein G/AuNPs	Impedimetry	$1–10^6$	340	[183]
CMK3-p(AC-co-MDHLA)-Ab_{EGFR}-AMS	Amperometry	$10–5\times10^4$	3030	[184]
primer 1 + primer 2	Fluorescence	$0.17–1.7\times10^5$	27.2	[185]
Ferrocene-labeled peptide ligand	DPV	$0.1–1\times10^3$	37	[186]
Fe_3O_4/N-trimethyl chitosan/Au	DPV	$0\text{-}10^3$	50	[187]
p-COF	DPV	0.05–100	5.64	[155]
$Cu_xNi_{3-x}(HHTP)_2$	**EIS**	**$0.001–2\times10^3$**	**0.72**	**This work**

The selectivity of this aptasensor was tested using some possible cancer markers ($VEGF_{165}$, CEA, AFP, CA 125, and CA 199) or proteins (IgG and BSA) with 1000-fold concentration of EGFR (**Figure 52a**), and their mixture with EGFR. Insignificant EIS responses (ΔR_{ct}) for detecting these interferents are found, whereas detecting EGFR leads to a large variation in R_{ct} value. The observed ΔR_{ct} caused by determining the mixture of all interferents and EGFR is ca. 107.6% of EGFR. All results prove the high selectivity of the present aptasensor for detecting EGFR. Further, the stability and reproducibility of the proposed aptasensor toward EGFR were investigated (**Figures 52b and c**), also showing satisfied results. The regeneration of aptasensor was tested by washing the EGFR/Apt/

$Cu_xNi_{3-x}(HHTP)_2$/AE electrode with H_2SO_4. The recycled electrode was then used for detecting EGFR (1 pg mL^{-1}). The EIS response (ΔR_{ct}) of the developed aptasensor (**Figure 52d**) shows adequate stability as there is only a negligible change after ten regeneration cycles, revealing that the developed aptasensor could be regenerated in a feasible way.

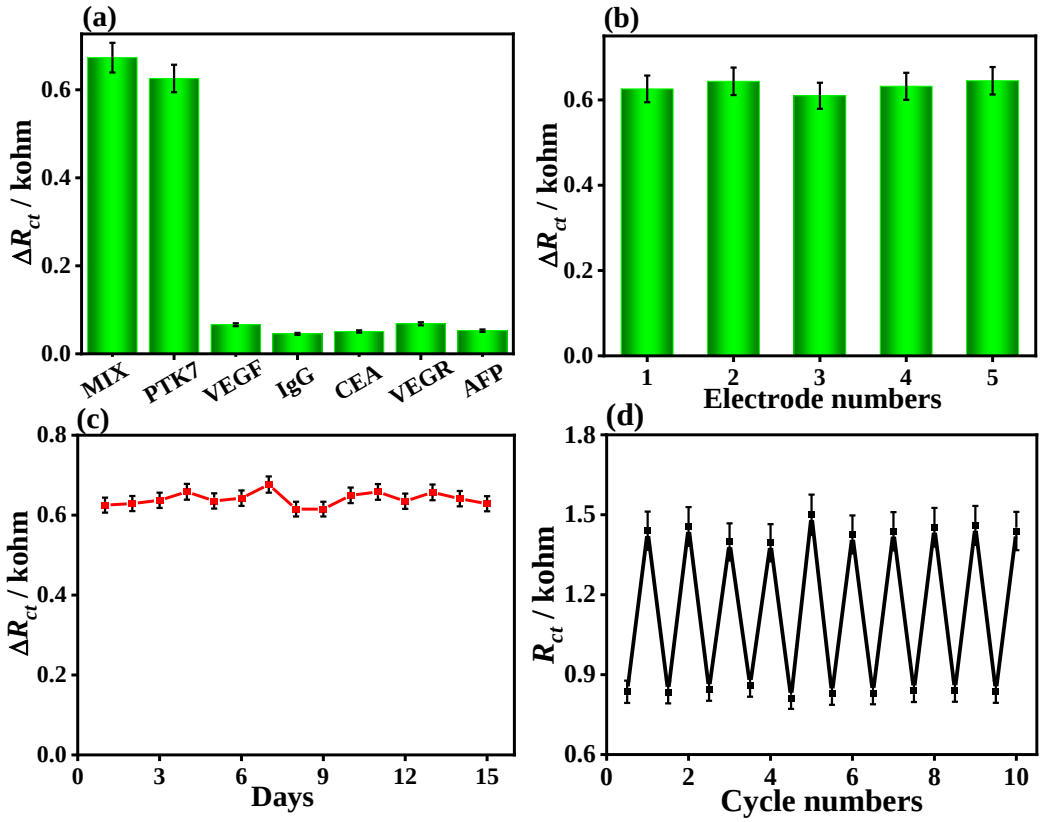

Figure 52. (a) Selectivity, (b) reproducibility, (c) stability, and (d) regenerability of the aptasensor for detecting EGFR (1 pg mL^{-1}) (n = 3).

Considering the good sensing performances of the proposed aptasensor for EGFR detection, its applicability in real samples was further also explored. As shown in **Table 7**, the real sample analysis using spike method in human serum (adding

EGFR to human serum) was performed with EIS. The recovery for EGFR detection is between 95.7% and 103%, with RSD lower than 2.37%. This finding suggests the acceptable applicability of the present aptasensor, which therefore can be used for practical diagnosis of cancer markers.

Table 7 Detection of EGFR in human serum sample by the $Cu_xNi_{3-x}(HHTP)_2$-based electrochemical aptasensor.

Amount added ($fg \cdot mL^{-1}$)	ΔR_{ct} (kohm)	Found ($fg \cdot mL^{-1}$)	Recovery (%)	RSD (%)
0.001	0.172	0.00103	103.0	2.92
0.01	0.458	0.0984	98.4.	4.18
0.1	0.463	0.106	106	3.67
1	0.600	0.957	95.7	2.35
10	0.748	10.232	102.3	2.13
100	0.892	102.1	102.1	1.05
1000	1.035	1007	100.7	1.57
20000	1.179	10054	100.54	1.10

5.4 Conclusion

The present work provides a new application of semiconductive bimetallic $Cu_xNi_{3-x}(HHTP)_2$ MOF as a novel scaffold of the electrochemical aptasensor for simultaneous detection of living C6 cells and its biomarker of EGFR without any modification and post-synthesis. This MOF exhibits high porosity, excellent

biocompatibility, remarkable electrochemical activity, rich chemical functionality, and active metal sites. As a result, the $Cu_xNi_{3-x}(HHTP)_2$-based aptasensor shows superior sensing performances toward living cells and EGFR, compared with other conventional MOFs or MOF-derivatives as well as its monometallic analogues $Cu_3(HHTP)_2$ and $Ni_3(HHTP)_2$, showing an extremely low detection limit of 21 cells mL^{-1} and 0.72 fg mL^{-1} for detecting C6 cells and EGFR, with high selectivity, good stability, and acceptable reproducibility. This contribution will provide a promising approach for detecting cancer biomarkers and living cancer cells, which also extends the applications of MOFs in the biomedical and biosensing fields.

CHAPTER 6

Structural hybridization of bimetallic zeolitic imidazolate framework (ZIF) nanosheets and carbon nanofibers for efficiently sensing α-synuclein oligomers

6.1 Introduction

Parkinson's disease (PD) is a progressive neurodegenerative disease which affects neuromotor function [188] and PD patients can also develop other nonmotor function-related symptoms. The increase of PD patients has currently become a social problem [189]. Intraneuronal protein aggregates, which are composed of α-Syn oligomers, are found in all patients with PD [190]. Therefore, the high levels of the soluble oligomeric form of α-Syn oligomers may indicate a pathogenic species in PD. Several methods have been developed for detecting α-Syn oligomers, such as confocal nanoscanning [191], enzyme-linked immunosorbent assay (ELISA) [192], electrochemiluminescence [193], fluorescent assays [194], SPR [195], and electrochemical techniques [196]. However, ELISA requires expensive and poorly stable antibodies for molecular recognition [197]. On the other hand, most organic dyes applied in fluorescence assays cannot be used to discriminate α-Syn oligomers from other α-Syn aggregates; this limitation results in determination deviation. Thus, exploring simple and economically analytical methods for α-Syn oligomers detection is very necessary. In this context, electrochemical biosensors have been developed, because of their low cost, convenient operation, portability, and ultrasensitivity [198].

The structural hybridization of two-dimensional (2D) nanosheets and one-dimensional (1D) nanofibers has attracted increasing attention because of their excellent synergistic effect [199]. Considering the unique features of ZIFs and 1D/2D hierarchical nanostructures, this work aims to design and construct a series of integrated 1D/2D nanohybrids of CoMn-ZIF nanosheets (CoMn-ZIF NSs) and CNFs,

as potential electrode materials for α-Syn oligomers biosensors (**Scheme 10**).

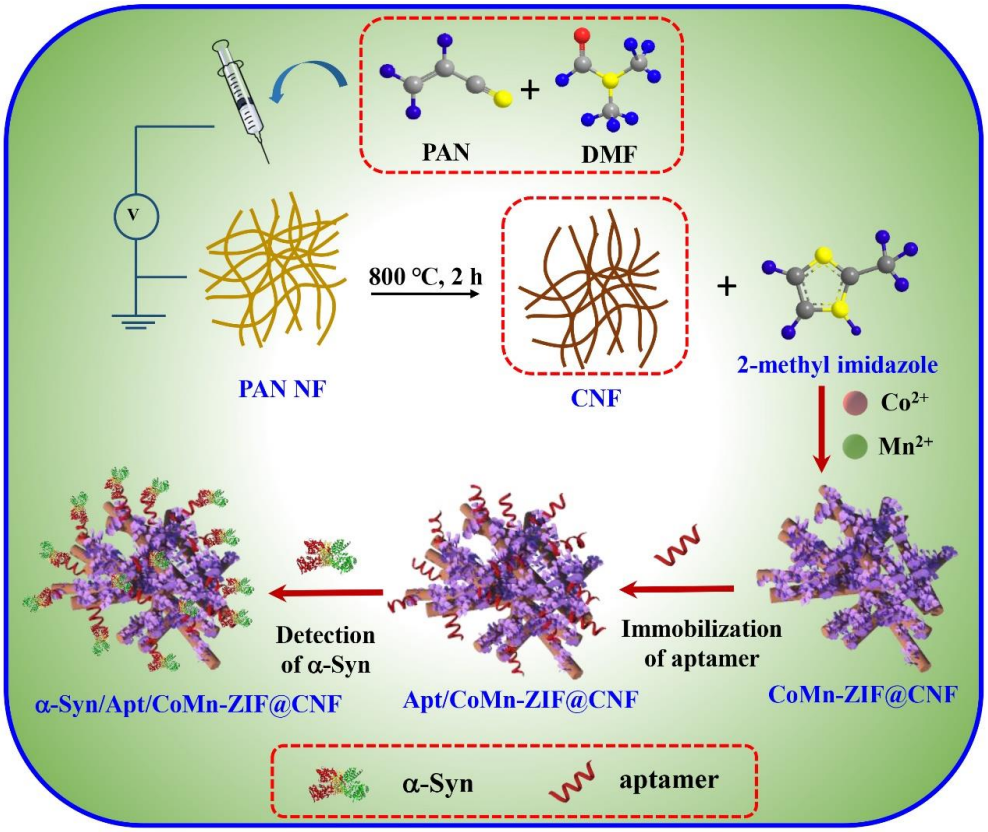

Scheme 10. Schematic diagram of the CoMn-ZIF@CNF-based aptasensor for detecting α-Syn oligomers, for which the whole procedure includes the synthesis of CoMn-ZIF@CNF composites, the immobilization of aptamer, and the detection of α-Syn oligomers.

The obtained CoMn-ZIF@CNF nanohybrids were used to anchor the α-Syn oligomers aptamer strands *via* π-π stacking between aptamer and ligand of CoMnZIF or CNF [200], hydrogen-bonding interaction between nitrogen-containing ligands and aptamer [201], and coordination effect between metal ions and N-element of aptamer [202]. Moreover, the weak electrostatic interaction between amino groups bearing on CNF and negatively charged phosphate groups of aptamer strands in the aqueous

solution can further lead to α-Syn oligomers aptamer anchoring [203]. The hierarchical structural hybridization of CoMn-ZIF NSs and CNF further enlarges this effect, with good electrochemical activity. Thus, the aptamer strands anchored over the CoMn-ZIF@CNF nanohybrid can strongly bind with α-Syn oligomers [204]. The proposed CoMn-ZIF@CNF nanohybrids can possess several features such as large specific surface areas, the intrinsic cavities of porous frameworks, the strong bioaffinity toward oligonucleotides, and good electrochemical activity. All these merits can remarkably facilitate α-Syn oligomers aptamer anchorage and enhance α-Syn oligomers sensing. Moreover, the sensing performances of the aptasensor can be modulated by the CoMn-ZIF@CNF nanocomposites, via changing the Co^{2+}-to-Mn^{2+} ratios of CoMn-ZIF.

6.2 Experimental section

The other experiment parts of basic characterizations, pre-treatment of the bare AE, preparation of all solutions, and electrochemical measurements are described in the **5.2**.

6.2.1 Materials and reagents

$Co(NO_3)_2 \cdot 6H_2O$ and $Mn(NO_3)_2 \cdot 4H_2O$ and 2-methyl imidazole were obtained from Aladdin Reagent Co. Ltd.. PAN (M_w = 150,000) was obtained from Aldrich Corporation. DMF (AR) was purchased from Sinopharm Chemical Reagent Co., Ltd.. Alpha-synuclein (α-Syn), OPN, prostate specific antigen (PSA), myoglobin (Myo),

and cardiac troponin-T (cTnT) were purchased from Solarbio Life Sciences Reagent Co. Ltd.. The sequence of the α-Syn oligomers aptamer is 5'-TTTTTGGTGGCTGGAGGGGGCGCGAACG-3'. All chemicals were of analytical grade and used without further purification. Milli-Q water (18.2 MΩ cm) was used throughout the experiments.

6.2.2 Synthesis of CNF and the series of CoMn-ZIF@CNF nanohybrids

Herein, the used PAN NFs were prepared by electrospinning technique according to the reported literature [205]. The obtained PNA NFs were annealed in a tube furnace at 800 °C for 3 h with a heating rate of 2 °C min^{-1} under a gas flow of 95% Ar and 5% H_2. Thus, the obtained CNF was further applied as the template for preparation of CoMn-ZIF NSs.

CoMn-ZIF NSs grown on CNF were synthesized using the approach reported previously with slight modification [206]. Taking the preparation of CoMn-ZIF@CNF(1-3) as an example, the synthesis route was shown as below. $Co(NO_3)_2 \cdot 6H_2O$ (2 mM, 0.58 g) and $Mn(NO_3)_2 \cdot 4H_2O$ (6 mM, 1.506 g) were dissolved in 30 mL of methanol under magnetic stirring to form the Solution **I**. CNF (1 g) was dispersed in 30 mL of methanol and sonicated for 15 min. 2-methyl imidazole (16 mM) was added to the CNF solution to form the Solution **II**. Subsequently, the Solution **I** and Solution **II** were mixed under magnetic stirring to obtain a homogeneous solution. Afterward, the mixture was washed by methanol, following by dispersed in 15 mL of methanol and mixed with the Solution **I**. Then, the

mixture was transferred to 100 mL Teflon-lined stainless-steel autoclaves and heated at 120 ℃ for 1 h. After cooling to room temperature, the product was washed with ethanol and then dried at 60 ℃ for 12 h, which was referred to as CoMn-ZIF@CNF(1-3). According to the ratios of $Co(NO_3)_2 \cdot 6H_2O$: $Mn(NO_3)_2 \cdot 4H_2O$ (i.e., 1:1 and 3:1), the nanohybrids were represented by CoMn-ZIF@CNF(1-1) and CoMn-ZIF@CNF(3-1), respectively. Additionally, the pure CoMn-ZIF(1-3) were also prepared using the similar approach without CNF.

6.2.3 Development of the series of CoMn-ZIF@CNF-based aptasensors

In the present work, different aptasensors were developed based on CNF, CoMn-ZIF, and the series of CoMn-ZIF@CNF nanohybrids for the detection of α-Syn oligomers. Taking the construction of CoMn-ZIF@CNF(1-3)-based aptasensor as an example, the procedure was described as below. CoMn-ZIF@CNF(1-3) with different usages (1, 2, 5, and 10 mg) was separately added to Milli-Q water (10 mL) and sonicated fully to obtain a homogeneous suspension with various concentrations of 0.1, 0.2, 0.5, and 1 mg mL^{-1}. The effect of the CoMn-ZIF@CNF(1-3) dosage on the sensing performance toward α-Syn oligomers was investigated. Then, 10.0 μL of CoMn-ZIF@CNF(1-3) suspension was dropped onto the pre-treated bare AE and dried under N_2 atmosphere at room temperature (denoted by CoMn-ZIF@CNF(1-3)/AE). Subsequently, the modified AE was immersed into the aptamer solution with diverse concentrations of (10, 20, 50, 100, 200, and 500 nM) for 1 h at 4 ℃, followed by rinsed with PBS and dried over a gentle stream of N_2 to

complete the fabrication of Apt /CoMn-ZIF@CNF (1-3)/AE aptasensor. As such, the influence of the concentration of aptamer solution on the detection efficiency of α-Syn oligomers was evaluated. Further, CoMn-ZIF@CNF(1-1)- and CoMn-ZIF@CNF(3-1)-based aptasensors were developed by the same procedure. For comparison, the CNF- and CoMn-ZIF-based aptasensors were also constructed for detecting α-Syn oligomers. All developed aptasensors were stored in refrigerator at 4 °C when not used.

6.2.4 Electrochemical measurements

The detection procedure of α-Syn oligomers was tested by CV and EIS techniques, by using the aptasensors based on CNF, CoMn-ZIF, and the series of CoMn-ZIF@CNF. To assess the detection limit of the CoMn-ZIF@CNF-based aptasensor, the Apt/CoMn-ZIF@CNF/AE was incubated with α-Syn oligomers solutions of different concentrations and recorded by EIS. For evaluation of the selectivity of aptasensor, the Apt/CoMn-ZIF@CNF/AE was immersed with the interferences and proteins, including OPN, PSA, IgG, BSA, Myo, or cTnT of 1.0 pg mL^{-1} (100-folds concentration of α-Syn oligomers) and their mixture with α-Syn oligomers and then, measured by EIS. The reproducibility was investigated by developing five parallel aptasensors and assessed by EIS for comparing their sensing performances. Meanwhile, the stability of aptasensor was characterized by storing the α-Syn/Apt/CoMn-ZIF@CNF/AE in a refrigerator (4 °C) for 15 days and determined by EIS every day. The regenerability of aptasensor was assessed by washing

α-Syn/Apt/CoMn-ZIF@CNF(1-3)/AE with 1.0 M NaOH for 2 min, following by rinsing with Milli-Q water for three times. The refreshed aptasensor was then reused to detect α-Syn oligomers (0.1 pg mL^{-1}) by EIS. Given that the EIS response of the fabricated aptasensor reached the original level, the same operation was repeated. As for the applicability of aptasensor, the α-Syn oligomers solution with different concentrations were spiked into the human serum for 1 h. After rinsing the electrode with Milli-Q water, the modified Apt/CoMn-ZIF@CNF/AE electrode was detected and recorded by EIS. Based on the concentration titration equation, the actual concentration of α-Syn oligomers was fitted out and compared with the used dosage.

6.3 Results and discussion

6.3.1 Basic characterizations of CoMn-ZIF@CNF nanohybrids

The SEM image of CNF (**Figure 53a**) shows the continuous nanofiber structure. The diameter of nanofibers is in range from 200 to 350 nm (**Figure 53b**). The smaller diameter of the fibers leads to the higher specific surface area which is supposed to facilitate the CoMn-ZIF growth. Raman spectrum of CNF shows two characteristic peaks at 1341 and 1597 cm^{-1}, corresponding to D and G bands of graphitic carbon, respectively (**Figure 53c**). The weak peak at 248.3 cm^{-1} is attributed to CN_x group [207], suggesting that CNF calcined from PAN is comprised of mesoporous carbon doped with N. The high-resolution XPS spectra of C 1*s*, N 1*s*, and O 1*s* of CNF were analyzed. The C 1s XPS spectrum (**Figure 53d**) can be deconvoluted into four parts, including the peaks at the BEs of 284.8, 285.4, 286.4, and 289.2 eV, corresponding to

C−C, C−N/C−O, C=O, and N−C−O groups, respectively. Only two peaks are found in the N 1*s* XPS spectrum (**Figure 53e**) at the BEs of 399 and 400.15 eV, due to pyridyl N and amine N. As for the O 1*s* XPS spectrum (**Figure 53f**), three main components can be simulated out, including C=O, C−O, and O−H groups. All of these results hint that the N element was oxidized during calcination, whereas PAN was transferred into CNF.

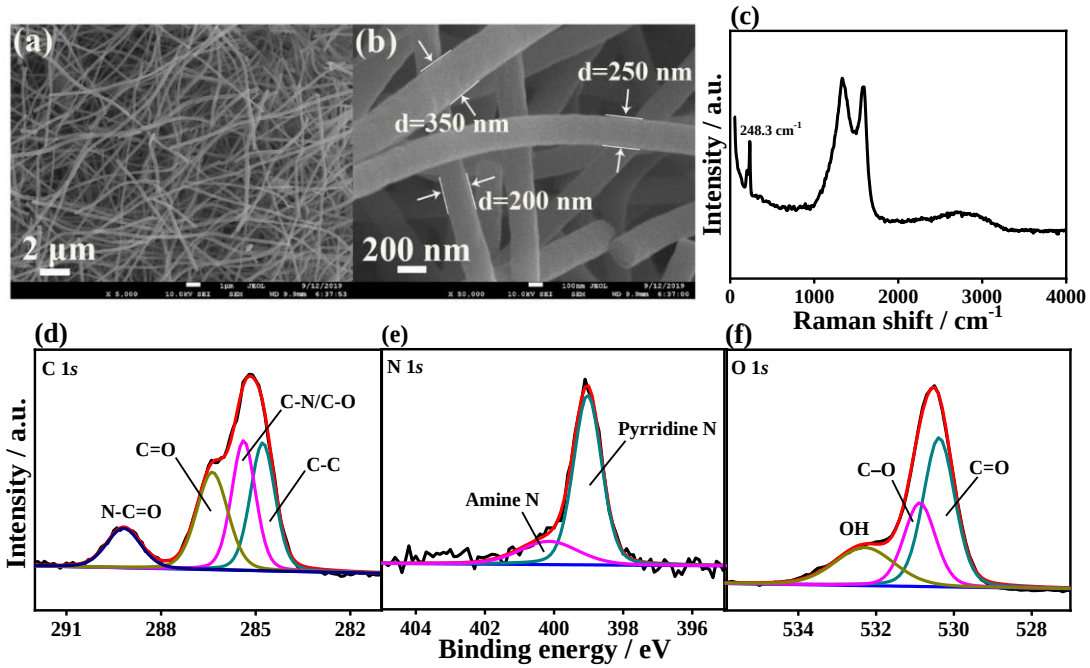

Figure 53. (a, b) Low- and high-magnification SEM images of CNF. (c) Raman spectrum, and high-resolution XPS spectra of (d) C 1*s*, (e) N 1*s*, and (f) O 1*s* of the CNF.

As shown in the SEM images (**Figures 54a** and **b**), the CoMn-ZIF comprises nanospheres, which are assembled with a large amount of NSs. As illustrated in the TEM image (**Figure 54c**), the CoMn-ZIF nanospheres are dispersed into large amounts of nanosheets along with several spheres. The CoMn-ZIF nanospheres

shown in the HR-TEM image (**Figure 54d**) are smaller than those observed in the SEM image due to the homogeneous dispersion in aqueous solution. Two clear lattice spacings of 0.220 and 0.241 nm attributed to the (220) and (311) planes of CoO and Co_3O_4, respectively, are observed (**Figure 54e**). The addition of excessive Co^{2+} and Mn^{2+} during the preparation of CoMn-ZIF results in the formation of small CoO and Co_3O_4 nanoparticles filled in the nanosheets, which has been similarly observed in our previous work [208].

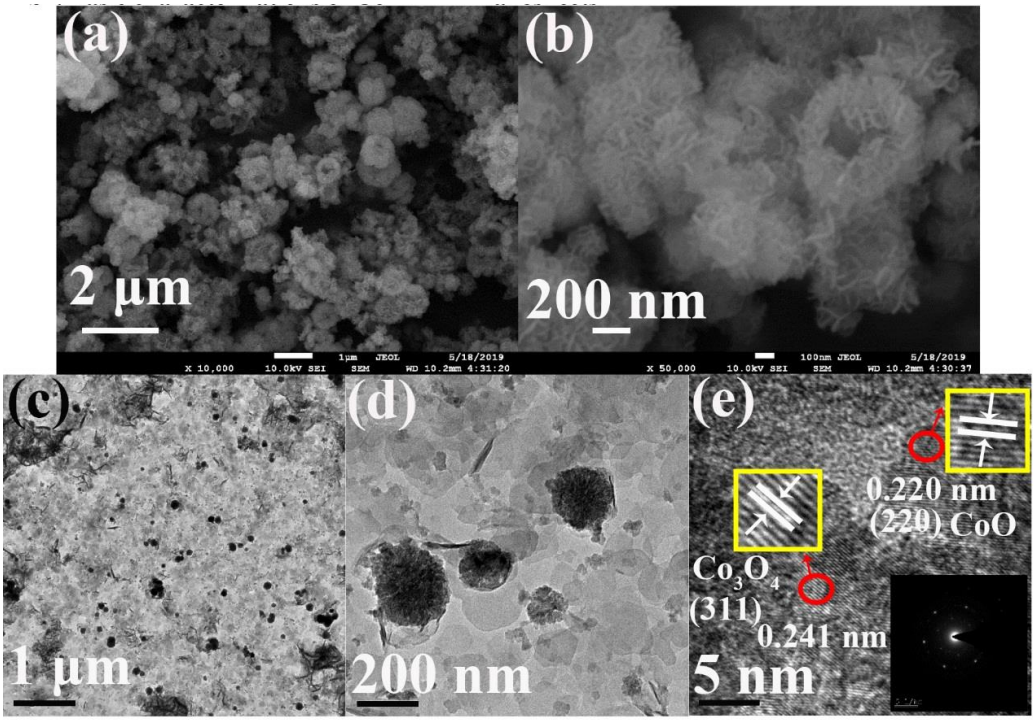

Figure 54. (a, b) Low- and high-magnification SEM images and (b, c, d) TEM and HR-TEM images of CoMn-ZIF NSs.

The TEM image of CoMn-ZIF@CNF(1-3) nanohybrid shows that the ultrathin CoMn-ZIF NSs are tightly tacked on the CNFs (**Figures 55a** and **b**). The HR-TEM image (**Figure 55c**) shows interplanar distances of 0.213 and 0.22 nm ascribable to

the (200) plane of CoO [209].

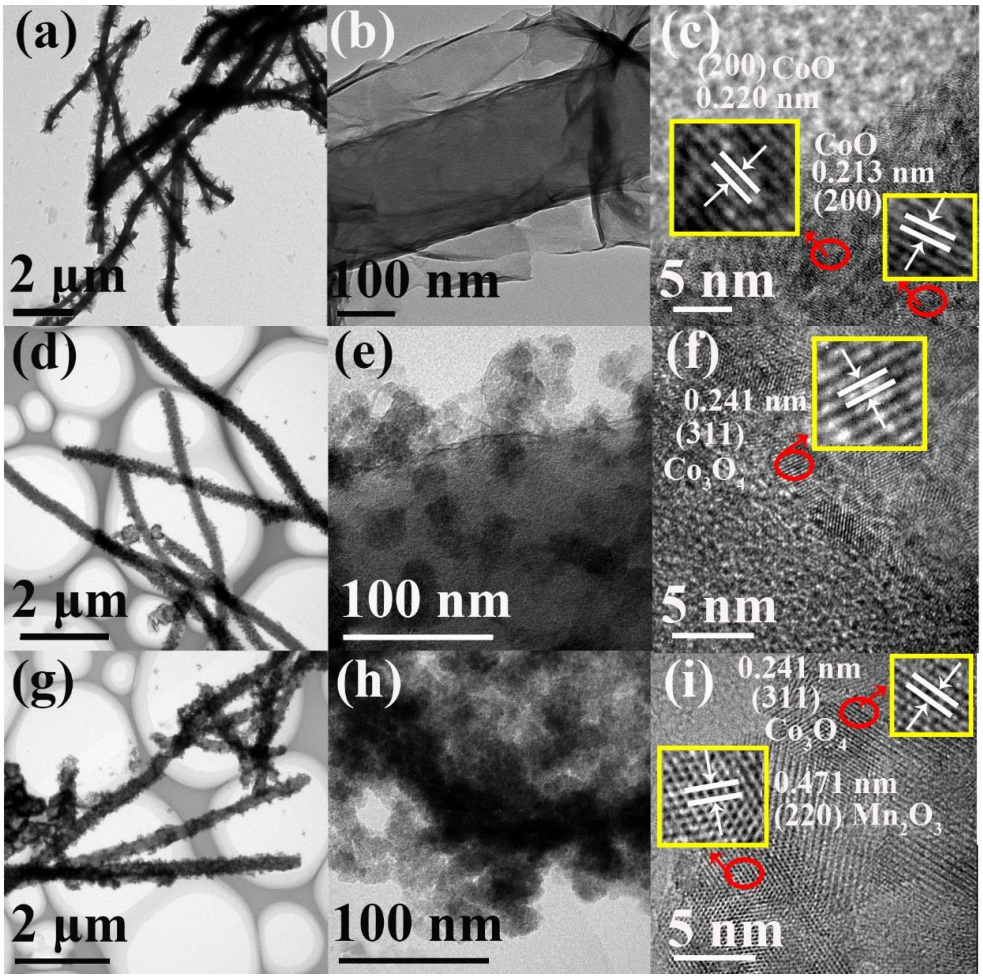

Figure 55. TEM and HR-TEM images of (a, b, c) CoMn-ZIF@CNF(1-3), (d, e, f) CoMn-ZIF@CNF(1-1) and (g, h, i) CoMn-ZIF@CNF(3-1) nanohybrids (inset: the SEAD patterns of each nanohybrid).

The SEM images reveal that some nanoparticles anchor on the surfaces of CoMn-ZIF NSs in CoMn-ZIF@CNF(1-1) (**Figure 55e**). The measured two sets of the crystalline lattices of 0.241 and 0.471 nm in the HR-TEM image (**Figure 55f)** are attributed to the (311) and (220) planes of Co_3O_4 and Mn_2O_3 phases, respectively [210]. Small CoMn-ZIF NSs are loosely stacked on the CNF surfaces, as shown in the

TEM image of CoMn-ZIF@CNF(3-1) (**Figure 55h**). The lattice spacing of 0.241 nm in the HR-TEM image matches well with the (311) plane of Co_3O_4 (**Figure 55i**) [211]. These results confirm that 2D/1D hierarchical heterostructure can be obtained, which consists of ultrathin CoMn-ZIF NSs and 1D CNFs. 1D CNFs have the advantages of large surface area with an optimal length/diameter ratio and high charge utilization efficiency with a short transfer distance when compared with 2D nanosheet structures [212]. Therefore, these hierarchical heterostructures fully integrate the advantages of both structures with different dimensions, which are beneficial for improving the sensing performances [213].

Various characterization methods, including XRD, FTIR, Raman, and XPS spectroscopy, were performed to further understand the chemical and crystal structures of CoMn-ZIF and the series of CoMn-ZIF@CNF nanohybrids. The XRD pattern of CoMn-ZIF NSs shows the diffraction peaks at 10.3, 20.5, 33.6, 37.4, and 58.9° (**Figure 56a**), which are ascribed to the (003), (006), (012), (015), and (110) planes of CoMn-ZIF [214]. XPD patterns of the three CoMn-ZIF@CNF nanohybrids lack clear difference and are similar to that of CoMn-ZIF. The absence of CNF characteristic peak is indicative of an amorphous structure. The FT-IR spectra of CoMn-ZIF@CNF nanohybrids (**Figure 56b**) exhibit the characteristic peak at 3430 cm^{-1}, which is ascribed to the O–H stretching vibration of adsorbed water molecules [215]. This wide peak is absent in the FT-IR spectrum of CoMn-ZIF NSs. Two weak bands at 2915 and 2810 cm^{-1} are attributed to C–H stretching vibration. The characteristic peaks at 1635 and 1380 cm^{-1} are associated with the C=N and CH_3

groups of 2-methyl imidazole. The peak located at 1050 cm^{-1} is the typical –OH stretching vibration caused by residual methanol. Moreover, the peak at 550 cm^{-1} is the characteristic absorption peak caused by the stretching vibration of M–O (M = Co or Mn). When CNFs are covered by CoMn-ZIF NSs, the peak distribution of CoMn-ZIF@CNFs becomes similar to that of CoMn-ZIF NSs.

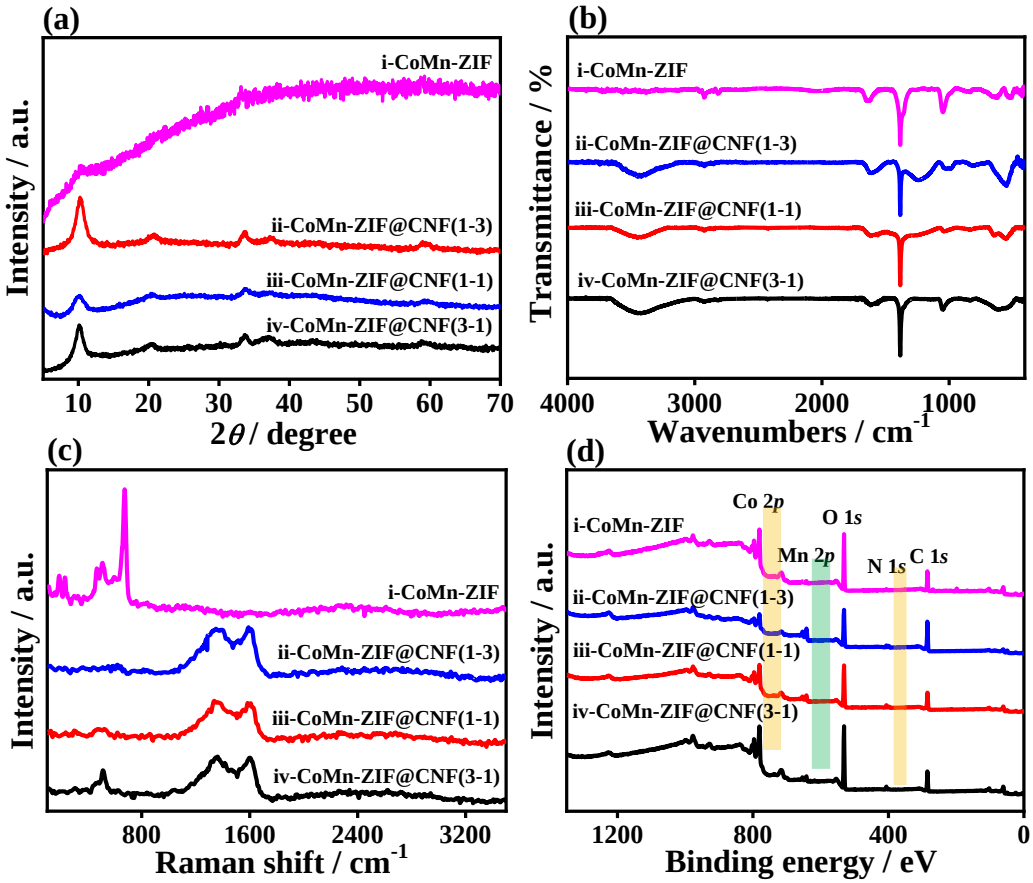

Figure 56. (a) XRD patterns, (b) FT-IR spectra, (c) Raman spectra, and (d) XPS survey spectra of (i) CoMn-ZIF, (ii) CoMn-ZIF@CNF(1-3), (iii) CoMn-ZIF@CNF(1-1), and (iv) CoMn-ZIF@CNF(3-1) nanohybrids.

The Raman spectra of CoMn-ZIF and the series of CoMn-ZIF@CNF nanohybrids were collected to evaluate their chemical structures (**Figure 56c**). The

peaks located at 465.3 and 510.6 cm^{-1} for pure CoMn-ZIF are the vibrational modes of E_g and $F_{2g}{}^2$ crystalline Co–O, respectively. The intense Raman peak at 673.06 cm^{-1} is assigned to the A_{1g} mode of the Co–O crystalline phase [216]. In contrast, the typical Raman spectra of CoMn-ZIF@CNF nanohybrids exhibit the characteristic disordered carbon of the D band and E_{2g}-mode phonons of the sp^2 G bands of graphitic carbon arising from CNFs, which are insubstantial for CoMn-ZIF. A weak peak at 510.6 cm^{-1} ($F_{2g}{}^2$ crystalline Co-O) remains in the Raman spectrum of CoMn-ZIF@CNF(3-1). XPS characterizations were conducted to investigate the chemical components and environments of CNF, CoMn-ZIF, and the series of CoMn-ZIF@CNF nanohybrids (**Figure 56d**). C 1s, N 1s and O 1s signals are observed in the XPS survey of CNF. For others, all XPS survey spectra exhibit the Co 2*p* (787.7 eV), O 1s (531.9 eV), and C 1s (285.1 eV) signals, as well as the weak signals of Mn 2*p* (664.7 eV) and N 1*s* (404.9 eV). Here, the higher peak intensity of Co 2*p* than that of Mn 2*p* implies a higher content of Co species in CoMn-ZIF NSs. The atomic% values of each element in CoMn-ZIF@CNF nanohybrids were also deduced from XPS (**Table 8**). In CoMn-ZIF NSs, the atomic% of Co 2*p* is 14% and that of Mn 2*p* is only 1.08%. In comparison, the atomic% values of Co 2*p* and Mn 2*p* in CoMn-ZIF@CNF(1-3) prepared under the same conditions are 5.47% and 3.64%, respectively. These results demonstrate that CNFs can facilitate the coordination of Mn^{2+} with the ligand due to their strong adsorption ability toward metal ions [217].

Table 8 The atomic% of each element in CoMn-ZIF and the series of

CoMn-ZIF@CNF nanohybrids.

Samples	Atomic%				
	C 1*s*	N 1*s*	O 1*s*	Co 2*p*	Mn 2*p*
CoMn-ZIF	34.9	2.54	36.7	14	1.08
CoMn-ZIF@CNF(3-1)	33.4	4.7	37.5	12.3	1.88
CoMn-ZIF@CNF(1-1)	37.7	6	33.7	9.69	2.75
CoMn-ZIF@CNF(1-3)	50.2	5.42	25.6	5.47	3.64

To further probe the chemical environment and valence state of each element in the samples, the high-resolution XPS spectra were deconvoluted using the XPSPEAK1 software (**Figure 57**). The Co 2*p* XPS spectra of CoMn-ZIF NSs and CoMn-ZIF@CNF nanohybrids (**Figures 57a1-d1**) are separated to two groups of peaks centered at the BEs of 779.4 and 794.6 eV that correspond to Co $2p_{3/2}$ and Co $2p_{1/2}$, respectively. The spin-energy separation of 15.2 eV between Co $2p_{3/2}$ and Co $2p_{1/2}$ indicates the existence of Co^{2+} and Co^{3+} in all samples. Moreover, the other two peaks located at the BEs of 797.6 and 780.9 eV are assigned to the Co^{2+} peak of two orbits, further proving the coexistence of Co^{2+} and Co^{3+}. Analyzing the Mn 2*p* XPS spectra of the CoMn-ZIF and the series of CoMn-ZIF@CNF nanohybrids (**Figures 57a2-d2**) reveals that the binding energy peaks of Mn $2p_{3/2}$ and Mn $2p_{1/2}$ are centered at the BEs of 641.6 and 653.5 eV, respectively. The Mn $2p_{3/2}$ signal is further resolved to two parts at the BEs of Mn^{3+} (641.4 eV) and Mn^{4+} (642.5 eV), whereas the Mn $2p_{1/2}$ component is deconvoluted into other two parts at the BEs of Mn^{3+} (652.9 eV) and Mn^{4+} (654.4 eV), respectively. This finding reveals that Mn^{3+} and Mn^{4+} are

concurrently present and are accompanied by Co^{2+}/Co^{3+}.

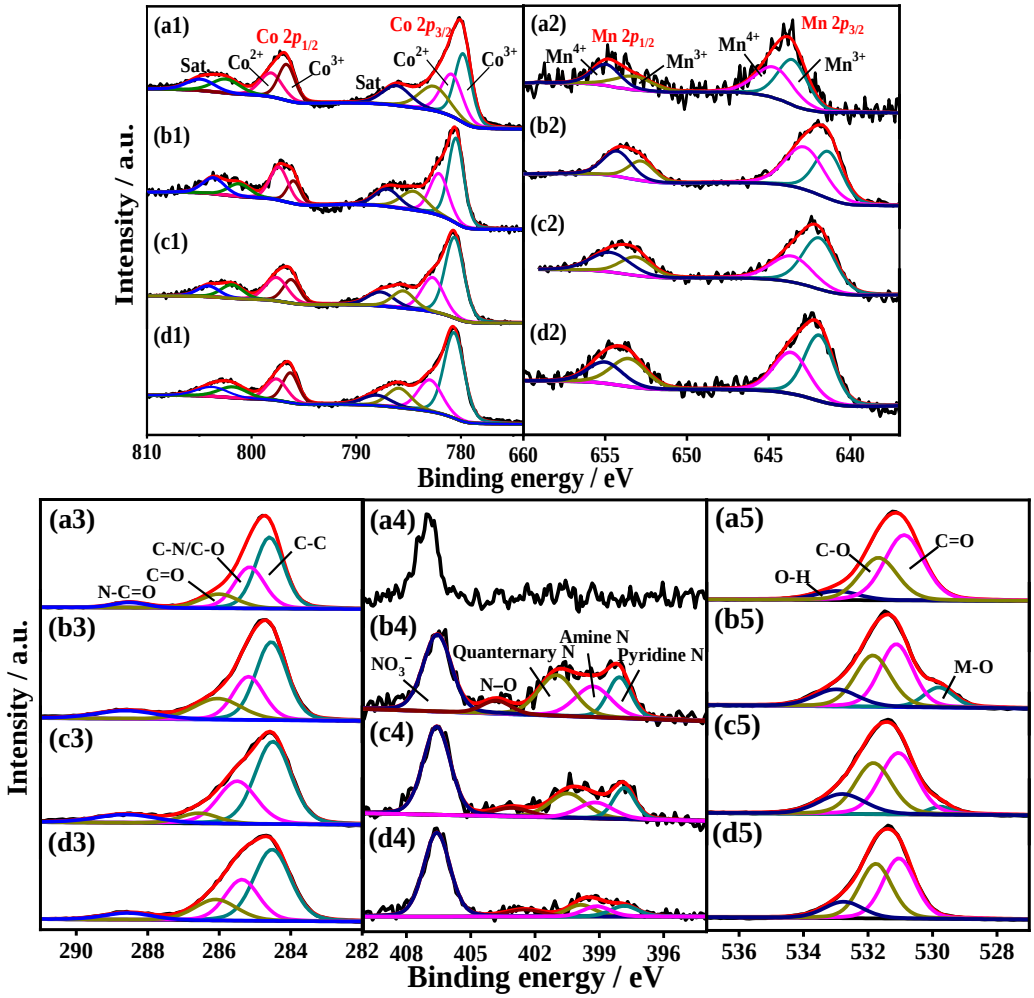

Figure 57. High-resolution Co 2*p*, Mn 2*p*, C 1*s*, N 1*s*, and O 1*s* XPS spectra of (a) CoMn-ZIF, (b) CoMn-ZIF@CNF(1-3), (c) CoMn-ZIF@CNF(1-1), and (d) CoMn-ZIF@CNF(3-1).

The coordination metal centers in CoMn-ZIF are Co^{2+} and Mn^{2+} ions. Given that excessive Co^{2+} and Mn^{2+} ions were added into the synthesis system to form CoMn-ZIF nanosheet structures, some metal ions do not coordinate with 2-methyl imidazole. During the preparation, these excessive metal ions are oxidized into their high valence states (e.g. Co^{3+}, Mn^{3+}, and Mn^{4+}). The percentage of each component

can be deduced from their corresponding areas in the high-resolution XPS spectra. As summarized in **Table 9**, the percentages of Co^{2+} for CoMn-ZIF@CNF(1-3), CoMn-ZIF@CNF(1-1), and CoMn-ZIF@CNF(3-1) are 63%, 67%, and 69%. The remarkably higher Co^{2+} percentage of the CoMn-ZIF@CNF nanohybrids than that of CoMn-ZIF NSs hint that the CNFs can promote the coordination. Similar result is also observed for the percentage of Mn^{2+} in all samples, where the percentage of Mn^{2+} of the series of CoMn-ZIF@CNF nanohybrids is higher than that of CoMn-ZIF NSs. Moreover, the percentage of Mn^{2+} of the series of nanocomposites is less than 30%. This result suggests that only a small part of Mn^{2+} ions are coordinated with N atoms, whereas a large amount of Mn^{2+} ions are oxidized during the preparation procedure of CoMnZIF. The percentage of the Mn^{4+} ions in CoMn-ZIF@CNF(1-3) (45%) is the largest among all nanomaterials and can greatly improve aptamer immobilization.

Table 9 The ratios of Co^{2+}/Co^{3+} and Mn^{3+}/Mn^{4+} in CoMn-ZIF and the series of CoMn-ZIF@CNF nanohybrids.

Samples	Co^{2+} (%)	Co^{3+} (%)	Mn^{2+} (%)	Mn^{3+} (%)	Mn^{4+} (%)
CoMn-ZIF	0.55	0.45	0.14	0.51	0.35
CoMn-ZIF@CNF(3-1)	0.63	0.37	0.21	0.34	0.45
CoMn-ZIF@CNF(1-1)	0.67	0.33	0.29	0.44	0.27
CoMn-ZIF@CNF(1-3)	0.69	0.31	0.23	0.42	0.35

The high-resolution C 1*s*, N 1*s*, and O 1*s* XPS spectra of CNF, CoMn-ZIF, and the CoMn-ZIF@CNF nanohybrids were analyzed. The four parts of C 1*s* XPS

spectrum (**Figures 57a3-d3**)at the BEs of 284.5, 285.2, 286.1, and 288.6 eV are attributed to C−C, C−N/C−O, C=O, and N−C=O, respectively. The presence of C−O, C=O, or N−C=O groups indicates that the N element of PAN is oxidized during pyrolysis at high temperature. This result can be confirmed by analyzing the N 1*s* XPS spectrum of CNFs (**Figures 57a4-d4**), where the two fitted peaks at the BEs of 399.0 and 400.1 eV correspond to pyridyl and amine N, respectively. However, no substantial N-related group, except for the peak of NO_3^- at the BE of 406.6 eV, is obtained. In the spectrum of CoMn-ZIF NSs, the three components of pyridinic N (298.1 eV), pyrrolic N (399.3 eV), and graphitic N (401 eV) are fitted, and the peaks at the BEs of 403.8 and 406.6 eV are ascribed to the oxidized N and NO_2. The contents of pyridinic, pyrrolic and graphitic N of CoMn-ZIF@CNF(1-3) nanohybrid is the largest among all samples. The nitrogen-rich functionality, metal-oxygen clusters and porosity promote the aptamer immobilization and further boost the sensing performance. As for the O 1s XPS spectrum **(Figures 57a5-d5)**, three main components can be simulated out, including C=O, C−O, and O−H groups.

6.3.2 Electrochemical sensing performances of the series of CoMn-ZIF@CNF nanohybrids

Considering the hierarchical nanostructures and rich functional groups of the prepared CoMn-ZIF@CNF nanohybrids, their electrochemical sensing was investigated, including the modification of bare electrodes with different materials, the immobilization of aptamer strands, and the α-Syn oligomers detection, by various

electrochemical techniques such as EIS and CV. For comparison, CNFs and CoMn-ZIF NSs were also used for α-Syn oligomers detection (**Figure 58**). As depicted in the EIS Nyquist plots for the CNF-based aptasensor (**Figure 58a**), the R_{ct} of the bare AE is 62.7 Ω. This small R_{ct} value suggests the excellent electrochemical activity of AE [73]. The smaller R_{ct} value (17.1 Ω) of the CNF-modified electrode than that of the bare AE hints the excellent electrochemical performance of CNF, in which the carbon component endows CNF with remarkable electron transfer ability [218]. After anchoring the aptamer strands, the R_{ct} value of Apt/CNF/AE increases to 153.9 Ω. Given that the phosphate groups of adsorbed aptamer strands can be ionized into a large amount of negative charges, a strong repulsive interaction exists between them and the $[Fe(CN)_6]^{3-/4-}$ redox. This interaction will prevent electron transferring at the interface between electrode and electrolyte [219], thus increasing the R_{ct} value. Exploring the detecting ability of CNF-based aptasensor to α-Syn oligomers in aqueous solution shows that the R_{ct} value continuously increases to a large value of 255.1 Ω. The binding of aptamer strands and α-Syn oligomers leads to formation of the G-quadruplex complex [220]. α-Syn oligomers is a biomarker that is insulated and can decrease electron transfer, resulting in high R_{ct} [221]. The results are consistent with their CV curves (**Figure 58b**). The bare AE exhibits a typical redox peak that corresponds to the electrochemical signal index of $[Fe(CN)_6]^{3-/4-}$. However, the enclosed area of the CV curve for CNF/AE is larger than that of the bare AE. The subsequent reduction in the enclosed areas of Apt/CNF/AE and α-Syn/Apt/CNF/AEα-Syn detection hints that the electrochemical activity for these

two steps declines. In terms of the ability of the CoMn-ZIF-based aptasensor to sense α-Syn oligomers (**Figure 58c**), the modification of AE with CoMn-ZIF NSs results in a large R_{ct} value (387.4 Ω), which is remarkably higher than that of CNFs. After aptamer anchorage and α-Syn oligomers detection, the corresponding R_{ct} value subsequently increases to 491 and 606.4 Ω. This trend is similar to that shown by the CNF-based sensor. Apparently, the presence of CNFs can substantially improve the electron transfer of CoMn-ZIF NSs.

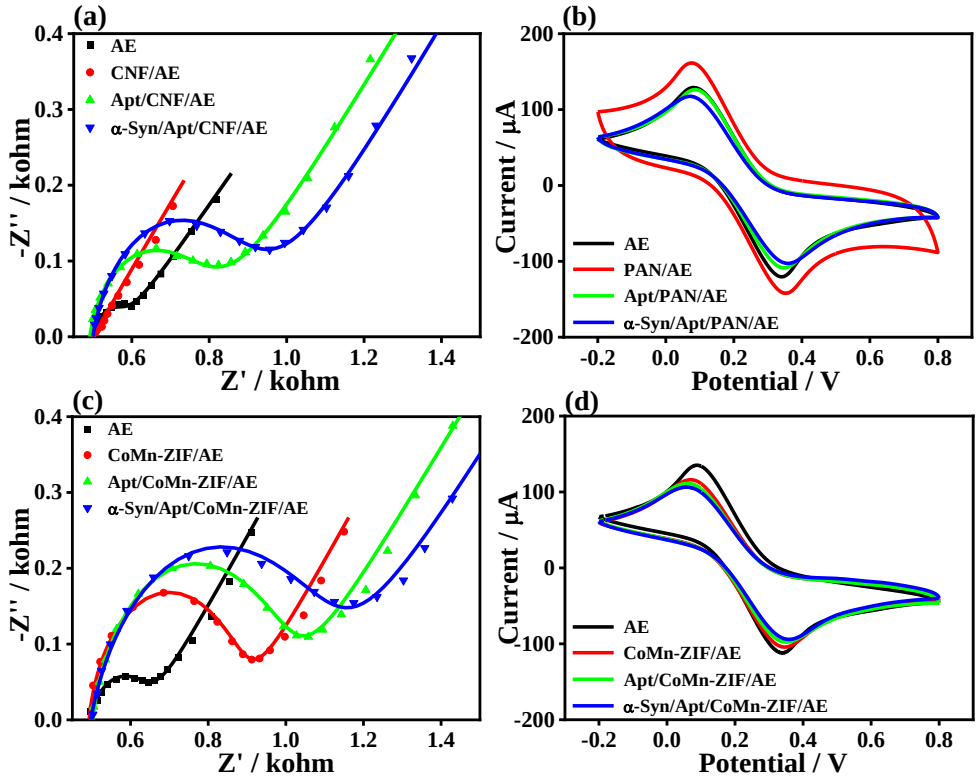

Figure 58. CV curves of AEs modified with (a) CNF and (b) CoMn-ZIF, EIS Nyquist plots of AEs modified with (a) CNF and (b) CoMn-ZIF for detecting α-Syn oligomers, including the bare AE, the modification of AE with CNF or CoMn-ZIF/AE, the immobilization of probe DNA, and the detection of α-Syn oligomers.

Consequently, the series of CoMn-ZIF@CNF nanohybrids show intermediate

electrochemical activity. All samples present similar trends for aptamer immobilization and α-Syn oligomers detection even when different aptasensors were used. The CoMn-ZIF@CNF(1-3)-based aptasensor was analyzed as an example (**Figure 59a**) and the sensing performance is discussed below. The R_{ct} of CoMn-ZIF@CNF(1-3)/AE increases to 198 Ω. After aptamer adsorption and α-Syn oligomers detection, the successive increase in value to 408 and 714.6 Ω of the modified electrode indicates that aptamer strand immobilization and target determination can further hinder the electron transfer. The CV measurements of the CoMn-ZIF@CNF(1-3)-based biosensor for α-Syn oligomers detection were also collected (**Figure 59d**). The results that are consistent with those of EIS Nyquist plotting. The simulated R_{ct} values of each step for different aptasensors based on CNF, CoMn-ZIF, and the series of CoMn-ZIF@CNF nanohybrids are summarized in **Table 10**.

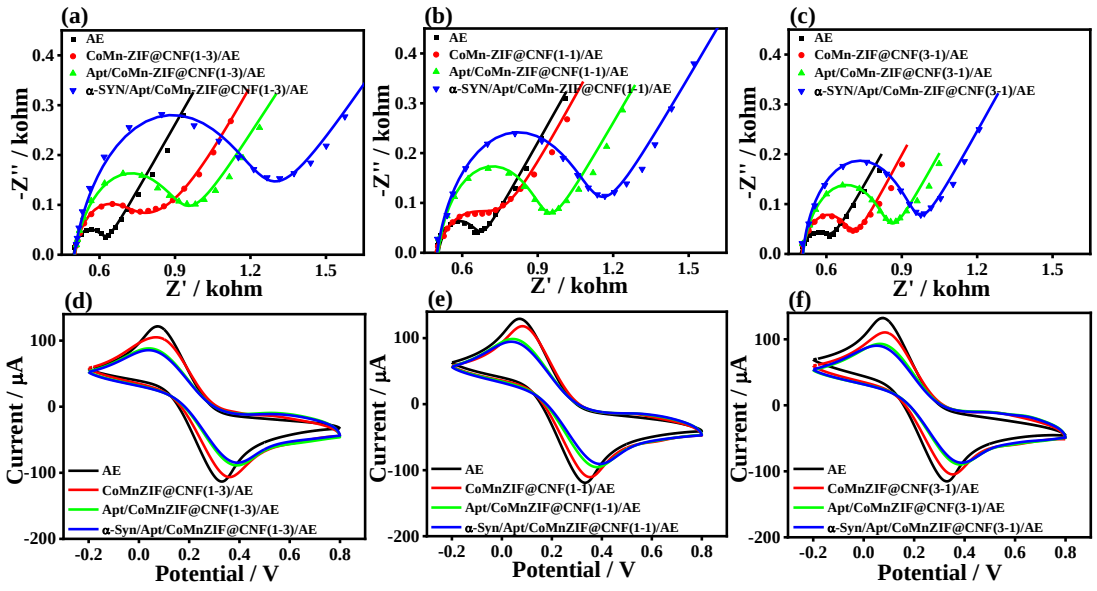

Figure 59. EIS Nyquist plots and CV curves of AEs modified with (a, d) CoMn-ZIF@CNF(1-3), (b, e) CoMn-ZIF@CNF(1-1) and (c, f) CoMn-ZIF@CNF(3-1)

for detecting α-Syn oligomers, including modification of AE with diverse nanohybrids, immobilization of probe DNA and detection of α-Syn oligomers.

Table 10 R_{ct} values of each step during the detection procedures of α-Syn oligomers using the aptasensors based on the CNF, CoMn-ZIF, and series of CoMn-ZIF@CNF.

Electrode materials	R_{ct} (Ω)			
	AE	Materials/AE	Apt/materials /AE	α-Syn/Apt/ materials/AE
CNF	62.7	17.1	153.9	255.1
CoMn-ZIF	152.2	387.4	491	606.4
CoMn-ZIF@CNF(1-3)	111.7	210	408	714.6
CoMn-ZIF@CNF(1-1)	153.2	254.7	404.5	605.7
CoMn-ZIF@CNF(3-1)	107.3	191.5	327.5	430.2

Although the different biosensors have similar appearances, they show various R_{ct} values as deduced from EIS Nyquist plots and the peak current densities of the CV curves and thus, exhibit different α-Syn oligomers sensing performances. As reported, the difference in the R_{ct} values of each step ($\Delta R_{ct} = R_{ct,\,i+1} - R_{ct,\,i}$) can represent the amount of the additional layer [222]. Therefore, the ΔR_{ct} values of each step can be utilized to compare the sensing sensitivity of various biosensors (**Figure 60**). Among the five kinds of aptasensors, the CNF-modified electrode shows a negative ΔR_{ct} value due to its good electrochemical activity. Even the variation in the electrochemical signal (ΔR_{ct}) arising from the anchorage of the aptamer over CNF (136.8 Ω) is slightly larger than the ΔR_{ct} of the CoMn-ZIF-based aptasensor (103.6 Ω).

The comparable ΔR_{ct} values of the two aptasensors originating from α-Syn oligomers detection demonstrate that the sensing efficiency of the CoMn-ZIF-based sensor is superior to that of the CNF-based sensor. Moreover, the ΔR_{ct} (235.2 Ω) of CoMn-ZIF/AE is higher than that of CoMn-ZIF@CNF/AE. This result hints that the presence of CNF nanowires can remarkably enhance the electrochemical activity of CoMn-ZIF NSs and thus, intensify the electrochemical signal for α-Syn oligomers detection. The comparable ΔR_{ct} values of the three CoMn-ZIF@CNF nanohybrids indicates their equal electrochemical activity. After aptamer immobilization, CoMn-ZIF@CNF(1-3) exhibits the largest ΔR_{ct} value (198 Ω), hinting its superior ability to anchor aptamer strands. It further exhibits the largest ΔR_{ct} value (306.6 Ω) in α-Syn oligomers detection, revealing its excellent detection efficiency. The CoMn-ZIF@CNF nanohybrids possess N-rich functionality, porous nanostructure, low crystallinity, and large specific surface area. Their synergistic effect can promote aptamer strand immobilization and stabilize the complex formed between aptamer and α-Syn oligomers. Therefore, the CoMn-ZIF@CNF(1-3) nanohybrid was chosen as the optimal sensing nanomaterial for α-Syn oligomers detection.

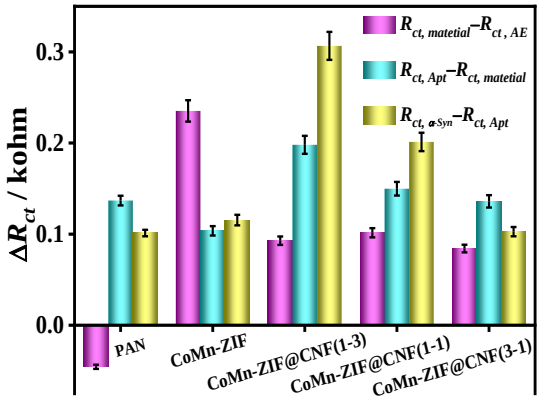

Figure 60. (d) Variations in R_{ct} values for each stage in fabrication procedure of

aptasensors for detecting α-Syn oligomers, for which the ΔR_{ct} represents the difference of R_{ct} caused by each step ($\Delta R_{ct} = R_{ct,\,i+1} - R_{ct,\,i}$).

6.3.3 Optimization of sensing performances for α-Syn oligomers detection

To construct the CoMn-ZIF@CNF(1-3)-based aptasensor with optimal detection ability toward α-Syn oligomers, the influence of CoMn-ZIF@CNF(1-3) dosage, aptamer concentration, and α-Syn oligomers binding are considered. The EIS Nyquist plots of the fabrication of the α-Syn oligomers aptasensor based on CoMn-ZIF@CNF(1-3) with different dosages of 0.1, 0.2, and 0.5 mg mL^{-1} are shown in **Figure 61**.

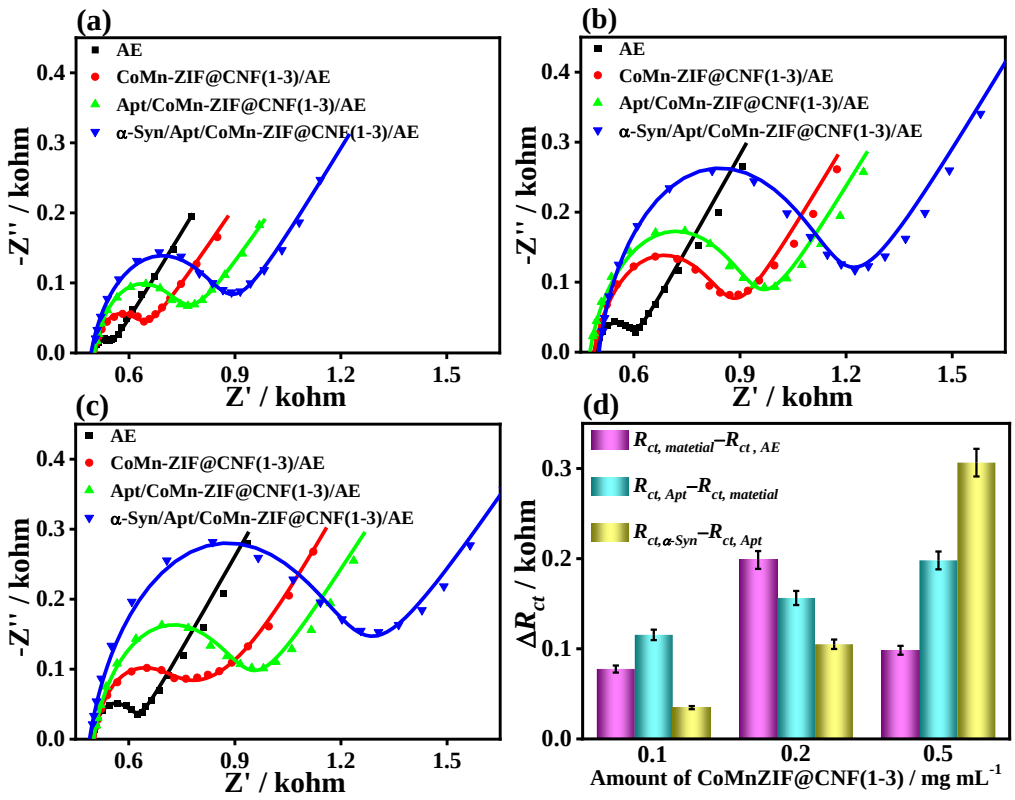

Figure 61. EIS Nyquist plots of AEs modified with (a) CoMn-ZIF@CNF(1-3) with the concentration of (a) 0.1, (b) 0.2, and (d) 0.5 mg mL^{-1} for detecting α-Syn

oligomers. (d) The effect of the concentration of CoMn-ZIF@CNF(1-3) dispersion on sensor fabrication and α-Syn oligomers detection, which is represented by the caused ΔR_{ct} values for each step.

In comparison, the AE modified with 0.2 mg mL^{-1} CoMn-ZIF@CNF(1-3) exhibits the largest R_{ct} value, whereas those modified with 0.1 and 0.5 mg mL^{-1} CoMn-ZIF@CNF(1-3) show comparable R_{ct} values. The ΔR_{ct} values caused by aptamer immobilization and α-Syn oligomers detection will increase as the dosage of CoMn-ZIF@CNF(1-3) is increased. A small dosage of CoMn-ZIF@CNF(1-3) cannot fully cover the electrode surface, thus leading to inferior sensing performance. However, when the dosage exceeds 0.5 mg mL^{-1}, the material layer is likely removed from the electrode surface due to the increased thickness, which also results in inferior sensing ability of the aptasensor. Consequently, CoMn-ZIF@CNF(1-3) (0.5 mg mL^{-1}) was selected for sensor construction and further measurements.

To probe the influence of aptamer concentration on α-Syn oligomers detection, the CoMn-ZIF@CNF(1-3)-based sensor immobilized with aptamer strands at concentrations of 10, 20, 50, 100, and 200 nM were utilized to determine α-Syn oligomers and tested by EIS. The ΔR_{ct} values caused by aptamer immobilization and α-Syn oligomers detection are summarized in **Figure 62a**. The results verify that the ΔR_{ct} values deduced from aptamer anchorage increase as the aptamer concentration is increased from 10 nM to 100 nM. Owing to the increased adsorption of aptamer strands, an increased number of α-Syn molecules can be detected via the formation of

G-quadruplex complex, which in turn leads to the gradual increase in ΔR_{ct}. Then, the ΔR_{ct} value reaches a plateau. Thus, the aptamer concentration of 100 nM was used for developing the CoMn-ZIF@CNF(1-3)-based aptasensor.

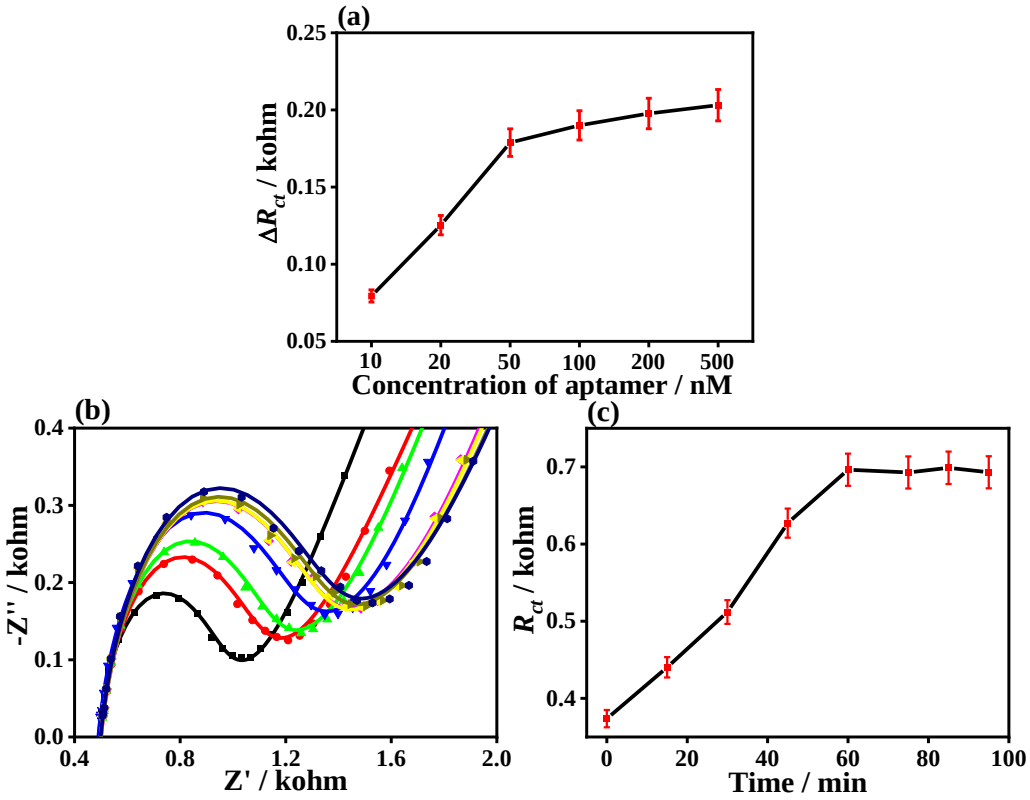

Figure 62. (a) The effect of the concentration of the aptamer solution on detection of α-Syn oligomers, which is represented by the caused ΔR_{ct} values for detecting α-Syn oligomers. (b) EIS Nyquist plots of the CoMn-ZIF@CNF(1-3)-based aptasensor for detecting α-Syn oligomers recorded at different binding times and (c) corresponding ΔR_{ct} values obtained at diverse binding times.

The binding kinetics of the CoMn-ZIF@CNF(1-3)-based aptasensor during α-Syn oligomers detection was also investigated using EIS (**Figure 62b**), for which the obtained EIS Nyquist plots were recorded in accordance with the binding time of

α-Syn oligomers. The calculated ΔR_{ct} values increase linearly within 60 min (**Figure 62c**) and then reach an equilibrium, which hints that the combination of α-Syn oligomers and aptamer strands is saturated. Given the above results, the optimal measurement condition with the CoMn-ZIF@CNF-based aptasensor involves incubating the CoMn-ZIF@CNF(1-3) (0.5 mg mL^{-1})-modified electrode immobilized with aptamer strands (100 nM) for 60 min. These parameters were used for the further investigation of sensing performances, such as detection limit, selectivity, stability, reproducibility, and applicability.

6.3.4 Detection sensitivity of the CoMn-ZIF@CNF(1-3)-based aptasensor

Sensitivity is a vital parameter for evaluating the sensing performance of aptasensor and can be deduced from the LOD [223]. Herein, concentration titration experiments were taken by EIS to determine the LOD of developed aptasensor for α-Syn oligomers detection. The EIS Nyquist plots for detecting different concentrations of α-Syn oligomers by the aptasensor were recorded (**Figure 63a**). The corresponding ΔR_{ct} values are shown in **Figure 63b**. The diameters of semicircles in EIS Nyquist plots linearly increase as α-Syn oligomers concentration is increased in the range of 0.001–200 pg mL^{-1}. This result verifies that an increasing number of α-Syn molecules are bound with the aptamer strands anchored over the CoMn-ZIF@CNF(1-3) nanohybrid, producing additional G-quadruplex complexes. The deduced R_{ct} values then reach a plateau, suggesting that the binding interaction of the aptamer strands with α-Syn oligomers is saturated. Therefore, the binding

interaction between aptamer and α-Syn oligomers using the developed aptasensor complies with the Langmuir-Freundlich isotherm. The LOD was graphically calculated from the calibration plot with the steep slope encompassing the first four data points (**Figure 63b**). On the basis of IUPAC, the LOD was deduced to be 0.87 fg mL^{-1} (45.7 fM) within the α-Syn oligomers concentration range from 0.1 fg mL^{-1} (52.6 fM) to 0.2 ng mL^{-1} (0.1 nM) by using the following equation: LOD = $3S_b/m$, in which S_b represents the standard deviation, and m represents the slope in reference to the gradient of calibration graph.

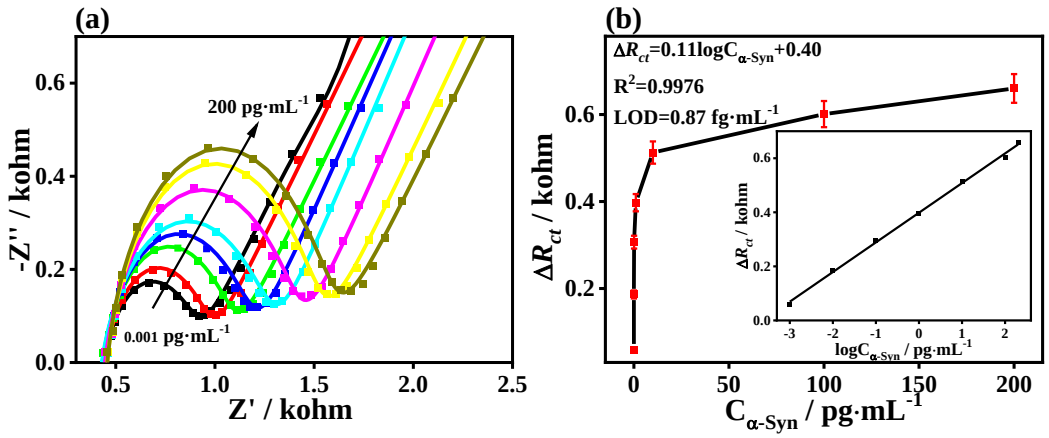

Figure 63. (a) EIS Nyquist plots for detecting α-Syn oligomers with different concentrations (0, 0.001, 0.01, 0.1, 1, 10, 100, and 200 pg mL^{-1}) using the CoMn-ZIF@CNF(1-3)-based aptasensor, (b) the calibration curves between ΔR_{ct} and α-Syn oligomers concentrations (inset: the linear fit plot of ΔR_{ct} as function of the logarithm of α-Syn oligomers concentration.

The sensing ability of the CoMn-ZIF@CNF(1-3)-based aptasensor is superior to that of previously reported sensors for α-Syn oligomers (**Table 11**). Ultrahigh

sensitivity or low LOD can be attributed to the integration of the features of CoMn-ZIF@CNF nanohybrids, electrochemical techniques and aptasensors. (i) The 2D nanostructured CoMn-ZIF NSs possess intrinsic cavities, large specific surface area, and excellent biocompatibility that can endow them with remarkable adsorption ability to aptamer strands [224]. (ii) The hierarchical CoMn-ZIF@CNF structure produced by hybridization of 2D/1D nanostructures can boost aptamer immobilization and stabilize the G-quadruplex formed between α-Syn oligomers and targeted aptamers [225]. (iii) The mixed metal ions in CoMn-ZIF [226] and conductive CNF [226] can enhance electron transfer, further intensifying electrochemical signals and enhancing sensing performances.

Table 11 Comparison of this work with reported techniques for α-Syn oligomers detection.

Materials	Detection method	Detection range	LOD	Refs.
Aptamer-complementary strand	DPV	60 pM−150 nM	10 pM	[227]
AuNPs	SPR	0−5 μM	8 pM	[198]
Cellular prion protein	EIS	1 pM−1 μM	0.5 pM	[228]
AuNPs	DPV	0.5 nM−30 nM	100 pM	[229]
U-shaped fiber optic probe immobilized with Au NPs	LSPR	70 nM−0.7 μM	70 nM	[230]
Three push-pull benzothiazole	Fluorescent	48 nM−353 nM	40 nM	[194]
CoMn-ZIF@CNF(1-3)	**EIS**	**52.6 fM−0.1 nM**	**45.7 fM**	**this work**

LSPR: localized surface plasmon resonance

6.3.5 Selectivity, reproducibility, stability, and regeneration of the

CoMn-ZIF@CNF(1-3)-based aptasensor

PD-related biomarkers such as Myo and cTn1 proteins, proteins in human serum (IgG and BSA), other cancer markers (OPN and PSA), and their mixtures with α-Syn oligomers were taken as the interferents, to investigate the selectivity of CoMn-ZIF@CNF(1-3)-based aptasensor. The Apt/CoMn-ZIF@CNF(1-3)/AE was used to detect solutions with different interferents (OPN, PSA, IgG, BSA, Myo, and cTnT) and the mixture of α-Syn oligomers with these interferents. The EIS signals of electrodes were recorded in 0.1 M PBS (pH 7.4) containing $[Fe(CN)_6]^{3-/4-}$ (**Figure 64a**). The concentrations of interferents (10.0 pg mL^{-1}) is 100-fold larger than that of the α-Syn oligomers solution (0.1 pg mL^{-1}). Notably, no remarkable EIS signal is found when the Apt/CoMn-ZIF@CNF(1-3)/AE is incubated with the pure interfering solution, and by contrast, the resulting EIS signal is strong when Apt/CoMn-ZIF@CNF(1-3)/AE is incubated with the pure α-Syn oligomers. This finding can be attributed to the specifically detecting ability of the CoMn-ZIF@CNF(1-3)-based aptasensor to trace amounts of α-Syn oligomers. Notably, the EIS signal for a mixed solution of α-Syn oligomers and interferent is ca. 106.8% of that obtained in the α-Syn oligomers solution at the same concentration. All these results confirm the high selectivity of the constructed aptasensor for α-Syn oligomers detection. The intra- and interassay stabilities were also tested to evaluate the reproducibility of the constructed biosensor in response to incubation with 0.1 pg mL^{-1} α-Syn oligomers. The EIS signals of five independent biosensors were used to probe interassay stability (**Figure 64b**), in which the obtained relative standard

deviation (RSD) is only ca. 5.17%.

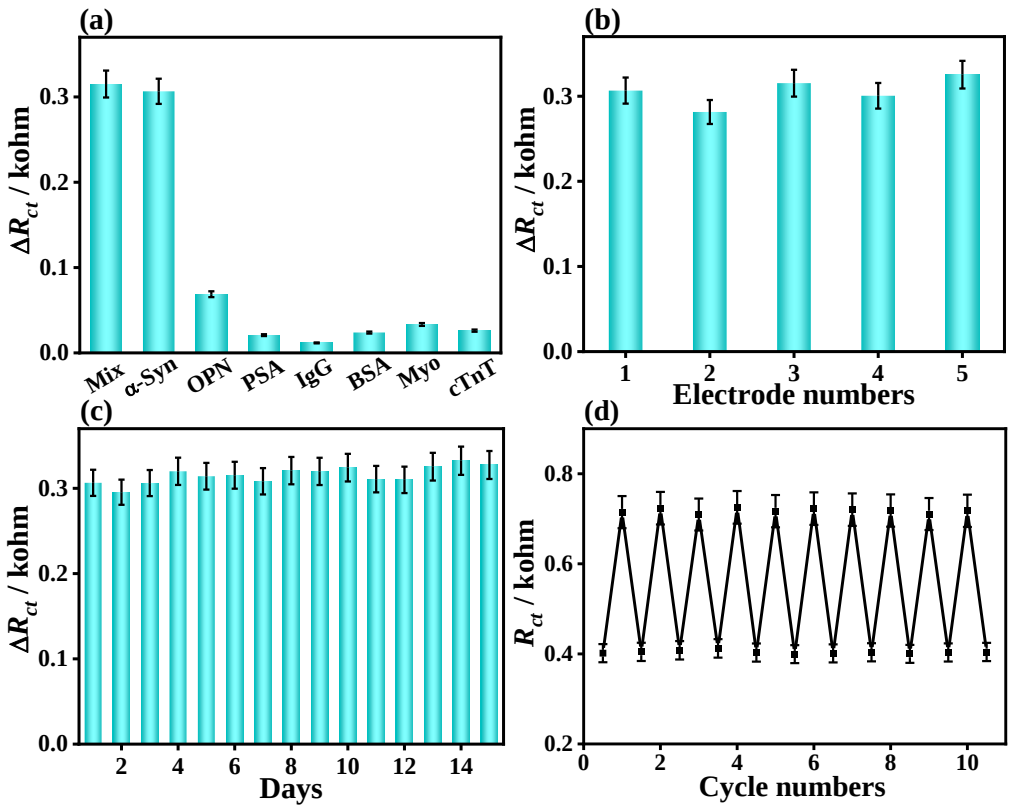

Figure 64. (a) Selectivity, (b) reproducibility, (c) stability, and (d) regenerability of the proposed aptasensor for detection of α-Syn oligomers (n = 3).

The day-to-day intra-assay stability of the aptasensor for α-Syn oligomers detection was also investigated. As shown in **Figure 64c**, the obtained ΔR_{ct} of the CoMn-ZIF@CNF-based aptasensor remains consistent after 15 days. All these results reveal the good stability of the aptasensor. The regenerability of aptasensor was assessed by washing α-Syn/Apt/CoMn-ZIF@CNF(1-3)/AE with 1.0 M NaOH for 2 min, following by rinsing with Milli-Q water for three times. The refreshed aptasensor was then reused to detect α-Syn oligomers (0.1 pg mL^{-1}) by EIS. Given that the EIS response of the fabricated aptasensor reached the original level, the same operation

was repeated. A slight decline in the resulting R_{ct} values of the proposed aptasensor over 10 regeneration runs indicates its excellent regenerability (**Figure 64d**). The developed CoMn-ZIF@CNF(1-3)-based sensor has considerable potential applications in detecting real samples, considering its high sensitivity and selectivity, good stability and acceptable regenerability.

The feasibility of the constructed aptasensor was also confirmed by investigating its applicability and reliability in detecting α-Syn oligomers in spiked samples. To avoid interference from background signals, varying amounts of α-Syn oligomers were added to human serum diluted 100-fold. Recovery experiments were then performed to detect α-Syn oligomers spiked at different concentrations by the standard addition method. The results in **Table 12** clearly show that recoveries range from 91.2% to 118.0%, and RSD values range from 2.42% to 4.09%. These results indicate that the proposed aptasensor can be applied to establish a platform for detecting α-Syn oligomers in real samples.

Table 12 Detection of α-Syn oligomers oligomers in human serum sample using the developed electrochemical CoMn-ZIF@CNF(1-3)-based aptasensor.

Added amounts (pg mL^{-1})	**Found amounts (pg mL^{-1})**	**Recovery (%)**	**RSD (%)**
0.001	0.00118	118	3.38
0.01	0.011	110	2.42
0.1	0.104	104	2.70
1.0	1.07	107	4.09

10	9.12	91.2	2.98
100	106.3	106.3	2.82

6.4 Conclusion

Novel 1D/2D hierarchical nanostructure of CoMn-ZIF@CNF has been developed and explored as the platform for strongly anchoring aptamer strands to detect the PD biomarker α-Syn oligomers. The series of CoMn-ZIF@CNF nanocomposites demonstrate adjustable functionality by modulating the ratios of Co and Mn precursors. The integration of hierarchical 1D/2D nanostructure, high electrochemical activity of CNF, rich N-related functional groups, diverse valences of metal ions (Co^{2+}/Co^{3+} and Mn^{3+}/Mn^{4+}), and low crystallinity of CoMn-ZIF@CNF(1-3) result in the anchorage of large amounts of aptamer strands and the ability to stabilize the formed G-quadruplex complex. These characteristics lead to high sensitivity toward α-Syn oligomers. Consequently, under optimal determination condition, the CoMn-ZIF@CNF(1-3)-based aptasensor has an ultralow detection limit of 0.87 fg mL^{-1} (45.7 fM) over a wide linear range of 0.1 fg mL^{-1} (52.6 fM) to 0.2 ng mL^{-1} (0.1 nM). Concurrently, the developed aptasensor shows good selectivity toward other possible interferents, high stability, improved reproducibility and regeneration, and acceptability in human serum. The present work provides new insight into the development of electrochemical biosensors and the sensing applications of hierarchical nanostructures.

References

[1] Z. Zhang, M.J. Zaworotko, Chem. Soc. Rev., 43 (2014) 5444-5455.

[2] T.R. Cook, Y.-R. Zheng, P.J. Stang, Chem. Rev., 113 (2013) 734-777.

[3] A. Carné, C. Carbonell, I. Imaz, D. Maspoch, Chem. Soc. Rev., 40 (2011) 291-305.

[4] W.N. Konings, S.-V. Albers, S. Koning, A.J.M. Driessen, Anton. van Leeuw., 81 (2002) 61-72.

[5] D. Megrian, N. Taib, J. Witwinowski, C. Beloin, S. Gribaldo, Mol. Microbiol., 113 (2020) 659-671.

[6] T.D. Tavares, J.C. Antunes, J. Padrão, A.I. Ribeiro, A. Zille, M.T.P. Amorim, F. Ferreira, H.P. Felgueiras, Antibiotics, 9 (2020).

[7] T. Tran Truc, D. Panesso, N. Mishra Nagendra, E. Mileykovskaya, Z. Guan, M. Munita Jose, J. Reyes, L. Diaz, M. Weinstock George, E. Murray Barbara, Y. Shamoo, W. Dowhan, S. Bayer Arnold, A. Arias Cesar, J. Projan Steven, mBio, 4 00281-00213.

[8] S.K. Nandanwar, H.J. Kim, ChemistrySelect, 4 (2019) 1706-1721.

[9] D.-L. Ma, H.-Z. He, K.-H. Leung, D.S.-H. Chan, C.-H. Leung, Angew. Chem. Int. Edit., 52 (2013) 7666-7682.

[10] L. Lu, L.-J. Liu, W.-c. Chao, H.-J. Zhong, M. Wang, X.-P. Chen, J.-J. Lu, R.-n. Li, D.-L. Ma, C.-H. Leung, Sci. Rep-UK, 5 (2015) 14544.

[11] P. Biegański, Ł. Szczupak, M. Arruebo, K. Kowalski, RSC Chem. Biol., 2 (2021) 368-386.

[12] A. Frei, J. Zuegg, A.G. Elliott, M. Baker, S. Braese, C. Brown, F. Chen, C.G. Dowson, G. Dujardin, N. Jung, A.P. King, A.M. Mansour, M. Massi, J. Moat, H.A. Mohamed, A.K. Renfrew, P.J. Rutledge, P.J. Sadler, M.H. Todd, C.E. Willans, J.J. Wilson, M.A. Cooper, M.A.T. Blaskovich, Chem. Sci., 11 (2020) 4531-4531.

[13] J. Jimenez, I. Chakraborty, A.M. Del Cid, P.K. Mascharak, Inorg. Chem., 56 (2017) 4784-4787.

[14] S. Celik, S. Yurdakul, B. Erdem, Inorg. Chem. Commun., 131 (2021) 108760.

[15] I. Chakraborty, M. Pinto, J. Stenger-Smith, J. Martinez-Gonzalez, P.K.

Mascharak, Polyhedron, 172 (2019) 1-7.

[16] P.G. Esquezaro, C.M. Manzano, D.H. Nakahata, I.A. Santos, U.E.A. Ruiz, M.B. Santiago, N.B.S. Silva, C.H.G. Martins, D.H. Pereira, F.R.G. Bergamini, A.C.G. Jardim, P.P. Corbi, J. Mol. Struct., 1246 (2021) 131261.

[17] M.Z. Ghdhayeb, K.J. Sabah, A.W. Salman, M.M. Kadhim, J. Mol. Struct., 1245 (2021) 131254.

[18] P.O. Asekunowo, R.A. Haque, M.R. Razali, S.W. Avicor, M.F.F. Wajidi, Eur. J. Med. Chem., 150 (2018) 601-615.

[19] M.A. Neelakantan, K. Balamurugan, C. Balakrishnan, L. Subha, Appl. Organomet. Chem., 32 (2018) e4259.

[20] Z. Albobaledi, M. Hasanzadeh Esfahani, M. Behzad, A. Abbasi, Inorg. Chim. Acta, 499 (2020) 119185.

[21] S. Thakurta, J. Chakraborty, G. Rosair, R.J. Butcher, S. Mitra, Inorg. Chim. Acta, 362 (2009) 2828-2836.

[22] K. Dhahagani, M.P. Kesavan, K. Gujuluva Gangatharan Vinoth, L. Ravi, G. Rajagopal, J. Rajesh, Mat. Sci. Eng. C, 90 (2018) 119-130.

[23] P.D. Akrivos, Coordin. Chem. Rev., 213 (2001) 181-210.

[24] O. Evangelinou, A.G. Hatzidimitriou, E. Velali, A.A. Pantazaki, N. Voulgarakis, P. Aslanidis, Polyhedron, 72 (2014) 122-129.

[25] O.A. El-Gammal, F.S. Mohamed, G.N. Rezk, A.A. El-Bindary, J. Mol. Liq., 326 (2021) 115223.

[26] A. Prakash, R. Malhotra, Appl. Organomet. Chem., 32 (2018) e4098.

[27] M.K. Koley, N. Duraipandy, M.S. Kiran, B. Varghese, P.T. Manoharan, A.P. Koley, Inorg. Chim. Acta, 466 (2017) 538-550.

[28] M. Azarkish, A. Akbari, T. Sedaghat, J. Simpson, J. Mol. Struct., 1156 (2018) 34-42.

[29] Y. Qian, F. Zhang, H. Pang, Adv. Funct. Mater., 31 (2021) 2104231.

[30] C. Pettinari, R. Pettinari, C. Di Nicola, A. Tombesi, S. Scuri, F. Marchetti, Coordin. Chem. Rev., 446 (2021) 214121.

[31] Y. Liu, L. Zhou, Y. Dong, R. Wang, Y. Pan, S. Zhuang, D. Liu, J. Liu, RSC Med.

Chem., 12 (2021) 915-928.

[32] W. Nong, J. Wu, R.A. Ghiladi, Y. Guan, Coordin. Chem. Rev., 442 (2021) 214007.

[33] F. Hu, S.-s. Xia, Y. He, Z.-l. Huang, H. Ke, J.-Z. Liao, Colloid. Surface. B, 213 (2022) 112425.

[34] Z. Wang, W. Guo, K. Zhang, Y. Ye, Y. Wang, D. Sui, N. Zhao, F.-J. Xu, Sci. China Technol. Sc., 65 (2022) 1052-1058.

[35] P. Li, J. Li, X. Feng, J. Li, Y. Hao, J. Zhang, H. Wang, A. Yin, J. Zhou, X. Ma, B. Wang, Nat. Commun., 10 (2019) 2177.

[36] S. Chen, J. Lu, T. You, D. Sun, Coordin. Chem. Rev., 439 (2021) 213929.

[37] S. Yao, J. Chi, Y. Wang, Y. Zhao, Y. Luo, Y. Wang, Adv. Healthc. Mater., 10 (2021) 2100056.

[38] H.N. Rubin, B.H. Neufeld, M.M. Reynolds, ACS Appl. Mater. Inter., 10 (2018) 15189-15199.

[39] K. Gwon, I. Han, S. Lee, Y. Kim, D.N. Lee, ACS Appl. Mater. Inter., 12 (2020) 20234-20242.

[40] M. Shen, F. Forghani, X. Kong, D. Liu, X. Ye, S. Chen, T. Ding, Compr. Rev. Food Sci. F., 19 (2020) 1397-1419.

[41] S. Shakya, Y. He, X. Ren, T. Guo, A. Maharjan, T. Luo, T. Wang, R. Dhakhwa, B. Regmi, H. Li, R. Gref, J. Zhang, Small, 15 (2019) 1901065.

[42] S. Lin, X. Liu, L. Tan, Z. Cui, X. Yang, K.W.K. Yeung, H. Pan, S. Wu, ACS Appl. Mater. Inter., 9 (2017) 19248-19257.

[43] F. Duan, X. Feng, Y. Jin, D. Liu, X. Yang, G. Zhou, D. Liu, Z. Li, X.-J. Liang, J. Zhang, Biomaterials, 144 (2017) 155-165.

[44] S. Duan, X. Zhao, Z. Su, C. Wang, Y. Lin, ACS Appl. Bio Mater., 3 (2020) 3673-3680.

[45] P. Zhang, Y. Li, Y. Tang, H. Shen, J. Li, Z. Yi, Q. Ke, H. Xu, ACS Appl. Mater. Inter., 12 (2020) 18319-18331.

[46] J. Feng, W.-X. Ren, F. Kong, Y.-B. Dong, Inorg. Chem. Front., 8 (2021) 848-879.

[47] J. Su, P. Jing, K. Jiang, J. Du, Dalton T., (2022).

[48] D. Han, Y. Han, J. Li, X. Liu, K.W.K. Yeung, Y. Zheng, Z. Cui, X. Yang, Y. Liang, Z. Li, S. Zhu, X. Yuan, X. Feng, C. Yang, S. Wu, Appl. Catal. B-Environ., 261 (2020) 118248.

[49] J. Li, X. Liu, L. Tan, Z. Cui, X. Yang, Y. Liang, Z. Li, S. Zhu, Y. Zheng, K.W.K. Yeung, X. Wang, S. Wu, Nat. Commun., 10 (2019) 4490.

[50] Y. Luo, J. Li, X. Liu, L. Tan, Z. Cui, X. Feng, X. Yang, Y. Liang, Z. Li, S. Zhu, Y. Zheng, K.W.K. Yeung, C. Yang, X. Wang, S. Wu, ACS Central Sci., 5 (2019) 1591-1601.

[51] A. Taglietti, P. Pallavicini, G. Dacarro, Applied Nano, 2 (2021).

[52] Y. Yang, X. Wu, C. He, J. Huang, S. Yin, M. Zhou, L. Ma, W. Zhao, L. Qiu, C. Cheng, C. Zhao, ACS Appl. Mater. Inter., 12 (2020) 13698-13708.

[53] S. Carrasco, Biosensors, 8 (2018).

[54] M. Pohanka, P. Skládal, J. appl. biomed., 6 (2008).

[55] N.J. Ronkainen, H.B. Halsall, W.R. Heineman, Chem. Soc. Rev., 39 (2010) 1747-1763.

[56] D.R. Thévenot, K. Toth, R.A. Durst, G.S. Wilson, Biosens. Bioelectron., 16 (2001) 121-131.

[57] S. Zhang, F. Rong, C. Guo, F. Duan, L. He, M. Wang, Z. Zhang, M. Kang, M. Du, Coordin. Chem. Rev., 439 (2021) 213948.

[58] Z. Zhang, Y. Lou, C. Guo, Q. Jia, Y. Song, J.-Y. Tian, S. Zhang, M. Wang, L. He, M. Du, Trends Food Sci. Tech., 118 (2021) 569-588.

[59] J. Zhuang, A.P. Young, C.-K. Tsung, Small, 13 (2017) 1700880.

[60] L. Zhang, C. Qiao, X. Cai, Z. Xia, J. Han, Q. Yang, C. Zhou, S. Chen, S. Gao, Chem. Eng. J., 426 (2021) 130730.

[61] X.-Q. Wu, P.-Q. Feng, Z. Guo, X. Wei, Langmuir, 36 (2020) 14123-14129.

[62] L. He, F. Duan, Y. Song, C. Guo, H. Zhao, J.-Y. Tian, Z. Zhang, C.-S. Liu, X. Zhang, P. Wang, M. Du, S.-M. Fang, 2D Materials, 4 (2017) 025098.

[63] M. Rezki, N.L.W. Septiani, M. Iqbal, D.R. Adhika, I.G. Wenten, B. Yuliarto, J. Electroch. Soc., 169 (2022) 017504.

[64] S.M. El-Sheikh, D.I. Osman, O.I. Ali, W.G. Shousha, M.A. Shoeib, S.M. Shawky,

S.M. Sheta, Appl. Sur. Sci., 562 (2021) 150202.

[65] L. He, Z. Li, C. Guo, B. Hu, M. Wang, Z. Zhang, M. Du, Sensor. Actuat. B-Chem., 298 (2019) 126852.

[66] X. Liao, H. Fu, T. Yan, J. Lei, Biosens. Bioelectron., 146 (2019) 111743.

[67] H. Huang, Y. Chen, Z. Chen, J. Chen, Y. Hu, J.-J. Zhu, J. Hazardous Mater., 416 (2021) 125895.

[68] Q. Jia, Y. Lou, F. Rong, S. Zhang, M. Wang, L. He, Z. Zhang, M. Du, J. Mater. Chem. C, 9 (2021) 14190-14200.

[69] C. Gu, C. Guo, Z. Li, M. Wang, N. Zhou, L. He, Z. Zhang, M. Du, Biosens. Bioelectron., 134 (2019) 8-15.

[70] C. Guo, F. Duan, S. Zhang, L. He, M. Wang, J. Chen, J. Zhang, Q. Jia, Z. Zhang, M. Du, J. Mater. Chem. A, 10 (2022) 475-507.

[71] X. Li, X. Li, D. Li, M. Zhao, H. Wu, B. Shen, P. Liu, S. Ding, Biosens. Bioelectron., 168 (2020) 112554.

[72] N. Zhou, F. Su, C. Guo, L. He, Z. Jia, M. Wang, Q. Jia, Z. Zhang, S. Lu, Biosens. Bioelectron., 123 (2019) 51-58.

[73] M. Wang, M. Hu, Z. Li, L. He, Y. Song, Q. Jia, Z. Zhang, M. Du, Biosens. Bioelectron., 142 (2019) 111536.

[74] S. Liu, C. Lai, X. Liu, B. Li, C. Zhang, L. Qin, D. Huang, H. Yi, M. Zhang, L. Li, W. Wang, X. Zhou, L. Chen, Coordin. Chem. Rev., 424 (2020) 213520.

[75] B. Cui, G. Fu, Nanoscale, 14 (2022) 1679-1699.

[76] S. Zhou, M. Hu, X. Huang, N. Zhou, Z. Zhang, M. Wang, Y. Liu, L. He, Microchim. Acta, 187 (2020) 219.

[77] F. Stoltz, J. Prakt. Chem, 55 (1897) 145-171.

[78] F. Marchetti, R. Pettinari, C. Pettinari, Coordin. Chem. Rev., 303 (2015) 1-31.

[79] Y.A. Zolotov, N. Kuzmin, in, Nauka, Moscow, 1977.

[80] F. Marchetti, J. Palmucci, C. Pettinari, R. Pettinari, M. Marangoni, S. Ferraro, R. Giovannetti, S. Scuri, I. Grappasonni, M. Cocchioni, ACS Appl. Mater. Inter., 8 (2016) 29676-29687.

[81] F. Marchetti, J. Palmucci, C. Pettinari, R. Pettinari, S. Scuri, I. Grappasonni, M.

Cocchioni, M. Amati, F. Lelj, A. Crispini, Inorg. Chem., 55 (2016) 5453-5466.

[82] S. Scuri, F. Petrelli, I. Grappasonni, L. Idemudia, F. Marchetti, C. Di Nicola, Acta Bio Medica: Atenei Parmensis, 90 (2019) 370.

[83] F. Marchetti, J. Palmucci, C. Pettinari, R. Pettinari, F. Condello, S. Ferraro, M. Marangoni, A. Crispini, S. Scuri, I. Grappasonni, M. Cocchioni, M. Nabissi, M.R. Chierotti, R. Gobetto, Chemistry, 21 (2015) 836-850.

[84] S.A. De Pascali, D. Migoni, M. Monari, C. Pettinari, F. Marchetti, A. Muscella, F.P. Fanizzi, Eur. J. Inorg. Chem., 2014 (2014) 1249-1259.

[85] K.E. Dalle, F. Meyer, Eur. J. Inorg. Chem., 2015 (2015) 3391-3405.

[86] A. Cingolani, Effendy, §, F. Marchetti, C. Pettinari, R. Pettinari, B.W. Skelton, A.H. White, Inorg. Chem., 43 (2004) 4387-4399.

[87] F. Marchetti, J. Palmucci, C. Pettinari, R. Pettinari, F. Condello, S. Ferraro, M. Marangoni, A. Crispini, S. Scuri, I. Grappasonni, Chem–A Eur. J., 21 (2015) 836-850.

[88] D. Baltzis, I. Eleftheriadou, A. Veves, Adv. Ther., 31 (2014) 817-836.

[89] J. Zhou, D. Yao, Z. Qian, S. Hou, L. Li, A.T.A. Jenkins, Y. Fan, Biomaterials, 161 (2018) 11-23.

[90] S.B. Levy, B. Marshall, Nat. Med., 10 (2004) S122-S129.

[91] M. Yousefi, M. Dadashpour, M. Hejazi, M. Hasanzadeh, B. Behnam, M. de la Guardia, N. Shadjou, A. Mokhtarzadeh, Mater. Sci. Eng. C, 74 (2017) 568-581.

[92] Q. Xin, H. Shah, A. Nawaz, W. Xie, M.Z. Akram, A. Batool, L. Tian, S.U. Jan, R. Boddula, B. Guo, Q. Liu, J.R. Gong, Adv. Mater., 31 (2019) 1804838.

[93] H. Yang, C. Liu, D. Yang, H. Zhang, Z. Xi, J. Appl. Toxicol., 29 (2009) 69-78.

[94] W. Wang, G. Li, D. Xia, T. An, H. Zhao, P.K. Wong, Environ. Sci. Nano, 4 (2017) 782-799.

[95] P.C. Ray, S.A. Khan, A.K. Singh, D. Senapati, Z. Fan, Chem. Soc. Rev., 41 (2012) 3193-3209.

[96] M. Qi, M. Chi, X. Sun, X. Xie, M.D. Weir, T.W. Oates, Y. Zhou, L. Wang, Y. Bai, H.H. Xu, Int. J. Nanomed., 14 (2019) 6937-6956.

[97] S. Karunakaran, S. Pandit, B. Basu, M. De, J. Am. Chem. Soc., 140 (2018) 12634-12644.

[98] M. Maruthapandi, A. Saravanan, P. Das, M. Natan, G. Jacobi, E. Banin, J.H.T. Luong, A. Gedanken, ACS Appl. Polymer Mater., 2 (2020) 5878-5888.

[99] S. Baek, S.H. Joo, M. Toborek, J. Hazardous Mater., 373 (2019) 122-130.

[100] X. Xie, C. Mao, X. Liu, L. Tan, Z. Cui, X. Yang, S. Zhu, Z. Li, X. Yuan, Y. Zheng, K.W.K. Yeung, P.K. Chu, S. Wu, ACS Central Sci,, 4 (2018) 724-738.

[101] B. Ramalingam, T. Parandhaman, S.K. Das, ACS Appl. Mater. Inter., 8 (2016) 4963-4976.

[102] J. Xu, N. Liu, D. Wu, Z. Gao, Y.-Y. Song, P. Schmuki, ACS Nano, 14 (2020) 337-346.

[103] K. Huang, F. Dou, N. Nitin, ACS Appl. Mater. Inter., 11 (2019) 17204-17214.

[104] K. Lei, X. Wang, X. Li, L. Wang, Colloid. Surface. B, 175 (2019) 688-696.

[105] S. Hallaj-Nezhadi, M. Hassan, Drug Delivery, 22 (2015) 581-589.

[106] H. Ji, H. Sun, X. Qu, Adv. Drug Deliver. Rev., 105 (2016) 176-189.

[107] O. Akhavan, E. Ghaderi, ACS Nano, 4 (2010) 5731-5736.

[108] Y. Zhu, J. Xu, Y. Wang, C. Chen, H. Gu, Y. Chai, Y. Wang, Nano Research, 13 (2020) 389-400.

[109] X. Zhu, Y. Zhu, K. Jia, B.S. Abraha, Y. Li, W. Peng, F. Zhang, X. Fan, L. Zhang, Nanoscale, 12 (2020) 19129-19141.

[110] A.M. Eissa, A. Abdulkarim, G.J. Sharples, N.R. Cameron, Biomacromolecules, 17 (2016) 2672-2679.

[111] A. Ali, M. Ovais, H. Zhou, Y. Rui, C. Chen, Biomaterials, 275 (2021) 120951.

[112] S. Bhunia, K.A. Deo, A.K. Gaharwar, Adv. Funct. Mater., 30 (2020) 2002046.

[113] P. Sikder, S. Bhaduri, Racing for the Surface, (2020) 583-612.

[114] X. Zhao, M. Zheng, X. Gao, J. Zhang, E. Wang, Z. Gao, Coordin. Chem. Rev., 440 (2021) 213970.

[115] S. Yuan, L. Feng, K. Wang, J. Pang, M. Bosch, C. Lollar, Y. Sun, J. Qin, X. Yang, P. Zhang, Q. Wang, L. Zou, Y. Zhang, L. Zhang, Y. Fang, J. Li, H.-C. Zhou, Adv. Mater., 30 (2018) 1704303.

[116] M. Alavi, M. Rai, Expert Rev. Anti-infe., 17 (2019) 419-428.

[117] J. Liu, D. Wu, N. Zhu, Y. Wu, G. Li, Trend Food Sci. Tech., 109 (2021)

413-434.

[118] H.H. Lara, E.N. Garza-Treviño, L. Ixtepan-Turrent, D.K. Singh, J. Nanobiotechnol., 9 (2011) 30.

[119] G. Mi, D. Shi, M. Wang, T.J. Webster, Adv. Healthc. Mater., 7 (2018) 1800103.

[120] V.K. Sharma, R.A. Yngard, Y. Lin, Adv. Colloid. Interfac., 145 (2009) 83-96.

[121] Y.-G. Zhou, N.V. Rees, R.G. Compton, Angew. Chem. Int. Edit., 50 (2011) 4219-4221.

[122] S. Alven, X. Nqoro, B.A. Aderibigbe, Polymers, 12 (2020) 2286.

[123] C.-C. Lin, A.T. Metters, Adv. Drug Deliver. Rev., 58 (2006) 1379-1408.

[124] Z. Zhang, H.T.H. Nguyen, S.A. Miller, A.M. Ploskonka, J.B. DeCoste, S.M. Cohen, J. Am. Chem. Soc., 138 (2016) 920-925.

[125] G.E.M. Schukraft, S. Ayala, B.L. Dick, S.M. Cohen, Chem. Commun., 53 (2017) 10684-10687.

[126] S. Ayala, K.C. Bentz, S.M. Cohen, Chem. Sci., 10 (2019) 1746-1753.

[127] Y. Gu, M. Huang, W. Zhang, M.A. Pearson, J.A. Johnson, Angew. Chem., 58 (2019) 2-8.

[128] P.G.M. Mileo, S. Yuan, S. Ayala, P. Duan, R. Semino, S.M. Cohen, K. Schmidt-Rohr, G. Maurin, J. Am. Chem. Soc., 142 (2020) 10863-10868.

[129] M. Cao, Y. Guan, J. Bie, X. Zhang, H. Gong, J. Tao, Y. Sun, C. Sun, S. Zhang, Y. Jiang, Y. Shen, L. Wang, Mater. Lett., 300 (2021) 130158.

[130] Y. Zhang, P. Sun, L. Zhang, Z. Wang, F. Wang, K. Dong, Z. Liu, J. Ren, X. Qu, Adv. Funct. Mater., 29 (2019) 1808594.

[131] S. Henke, A. Schneemann, S. Kapoor, R. Winter, R.A. Fischer, J. Mater. Chem., 22 (2012) 909-918.

[132] P. Samanta, A.V. Desai, S. Sharma, P. Chandra, S.K. Ghosh, Inorg. Chem., 57 (2018) 2360-2364.

[133] K. Yazaki, M. Takahashi, N. Miyajima, M. Obata, N. J. Chem., 44 (2020) 5182-5185.

[134] L.M. Liu, B. McAllister, H.Q. Ye, P. Hu, J. Am. Chem. Soc., 128 (2006) 4017-4022.

[135] A. Gupta, S. Mumtaz, C.-H. Li, I. Hussain, V.M. Rotello, Chem. Soc. Rev., 48 (2019) 415-427.

[136] G. Wyszogrodzka, B. Marszałek, B. Gil, P. Dorożyński, Drug Discovery Today, 21 (2016) 1009-1018.

[137] J. Xiao, Y. Zhou, M. Ye, Y. An, K. Wang, Q. Wu, L. Song, J. Zhang, H. He, Q. Zhang, J. Wu, Adv. Healthc. Mater., 10 (2021) 2001591.

[138] M. Jing, R. Liu, W. Yan, X. Tan, Y. Chen, Luminescence, 31 (2016) 557-564.

[139] K.M. de la Harpe, P.P.D. Kondiah, Y.E. Choonara, T. Marimuthu, L.C. du Toit, V. Pillay, Cells, 8 (2019) 1209.

[140] Z. Song, Y. Wu, H. Wang, H. Han, Mater. Sci. Eng. C, 99 (2019) 255-263.

[141] A.L. Neal, Ecotoxicology, 17 (2008) 362.

[142] J. Wu, D. Tu, L.-Y. Yuan, H. Yuan, L.-X. Wen, Environ. Toxicol. Phar., 36 (2013) 493-500.

[143] C. Ning, X. Wang, L. Li, Y. Zhu, M. Li, P. Yu, L. Zhou, Z. Zhou, J. Chen, G. Tan, Y. Zhang, Y. Wang, C. Mao, Chem. Resear. Toxicol., 28 (2015) 1815-1822.

[144] K. Gold, B. Slay, M. Knackstedt, A.K. Gaharwar, Adv. Ther., 1 (2018) 1700033.

[145] H.A. Hemeg, Int. J. Nanomed., 12 (2017) 8211-8225.

[146] H. Madhyastha, R. Madhyastha, A. Thakur, S. Kentaro, A. Dev, S. Singh, B. Chandrashekharappa R, H. Kumar, O. Acevedo, Y. Nakajima, H.K. Daima, A. Aradhya, N. Nagaraj P, M. Maruyama, Colloid. Surface. B, 194 (2020) 111211.

[147] Y. Liang, R. Shang, J. Lu, L. Liu, J. Hu, W. Cui, ACS Appl. Mater. Inter., 10 (2018) 8758-8769.

[148] W. Zhu, C. Zhang, Q. Li, L. Xiong, R. Chen, X. Wan, Z. Wang, W. Chen, Z. Deng, Y. Peng, Appl. Catal. B-Environ., 238 (2018) 339-345.

[149] Q. Cui, G. Qin, W. Wang, G. K. R, A. Du, Q. Sun, J. Mater. Chem. A, 7 (2019) 14510-14518.

[150] T.C. Wang, I. Hod, C.O. Audu, N.A. Vermeulen, S.T. Nguyen, O.K. Farha, J.T. Hupp, ACS Appl. Mater. Inter., 9 (2017) 12584-12591.

[151] The Lancet, 359 (2002) 1011-1018.

[152] R.H. Epstein, F. Dexter, I. Cajigas, A.K. Mahavadi, A.H. Shah, N. Abitbol, R.J.

Komotar, J. Clin. Anesth., 60 (2020) 118-124.

[153] V. Bhuria, J. Xing, T. Scholta, K.C. Bui, M.L.T. Nguyen, N.P. Malek, P. Bozko, R.R. Plentz, Exp. Cell Res., 385 (2019) 111671.

[154] L. Ding, Y. Wu, W. Liu, L. Liu, F. Yu, S. Yu, Y. Tian, J. Feng, L. He, Talanta, 205 (2019) 120129.

[155] X. Yan, Y. Song, J. Liu, N. Zhou, C. Zhang, L. He, Z. Zhang, Z. Liu, Biosens. Bioelectron., 126 (2019) 734-742.

[156] N. Zhou, F. Su, Z. Li, X. Yan, C. Zhang, B. Hu, L. He, M. Wang, Z. Zhang, Microchim. Acta, 186 (2019) 75.

[157] M.S. Yao, X.J. Lv, Z.H. Fu, W.H. Li, W.H. Deng, G.D. Wu, G. Xu, Angewandte Chemie, 129 (2017) 16737-16741.

[158] C. Guo, F. Su, Y. Song, B. Hu, M. Wang, L. He, D. Peng, Z. Zhang, ACS Appl. Mater. Inter., 9 (2017) 41188-41199.

[159] Y. Wu, S. Zhan, H. Xing, L. He, L. Xu, P. Zhou, Nanoscale, 4 (2012) 6841-6849.

[160] Z. Jiang, L. Zhou, A. Liang, Chem. Commun., 47 (2011) 3162-3164.

[161] J. Park, A.C. Hinckley, Z. Huang, D. Feng, A.A. Yakovenko, M. Lee, S. Chen, X. Zou, Z. Bao, J. Am. Chem. Soc., 140 (2018) 14533-14537.

[162] A. Thapa, A.C. Soares, J.C. Soares, I.T. Awan, D. Volpati, M.E. Melendez, J.H.T.G. Fregnani, A.L. Carvalho, O.N. Oliveira, ACS Appl. Mater. Inter., 9 (2017) 25878-25886.

[163] B. Hoppe, K.D.J. Hindricks, D.P. Warwas, H.A. Schulze, A. Mohmeyer, T.J. Pinkvos, S. Zailskas, M.R. Krey, C. Belke, S. König, M. Fröba, R.J. Haug, P. Behrens, CrystEngComm, 20 (2018) 6458-6471.

[164] M.K. Smith, K.E. Jensen, P.A. Pivak, K.A. Mirica, Chem. Mater., 28 (2016) 5264-5268.

[165] S. Gu, Z. Bai, S. Majumder, B. Huang, G. Chen, J. Power Sources, 429 (2019) 22-29.

[166] B.A. Kahsay, A. Ramar, F.-M. Wang, N.-H. Yeh, P.-L. Lin, Z.-J. Luo, T.-S. Chan, C.-H. Su, J. Power Sources, 428 (2019) 115-123.

[167] M.G. Campbell, S.F. Liu, T.M. Swager, M. Dincă, J. Am. Chem. Soc., 137 (2015) 13780-13783.

[168] S. Yang, Y. Liu, Y. Hao, X. Yang, W.A. Goddard Iii, X.L. Zhang, B. Cao, Adv. Sci., 5 (2018) 1700659.

[169] M. Wang, M. Hu, J. Liu, C. Guo, D. Peng, Q. Jia, L. He, Z. Zhang, M. Du, Biosens. Bioelectron., 132 (2019) 8-16.

[170] Y. Yang, M. Kang, S. Fang, M. Wang, L. He, J. Zhao, H. Zhang, Z. Zhang, Sensor. Actuat. B-Chem., 214 (2015) 63-69.

[171] P. Cui, J. Wu, X. Zhao, D. Sun, L. Zhang, J. Guo, D. Sun, Crystal Growth & Design, 11 (2011) 5182-5187.

[172] M.K. Smith, K.A. Mirica, J. Am. Chem. Soc., 139 (2017) 16759-16767.

[173] W.-T. Koo, S.-J. Kim, J.-S. Jang, D.-H. Kim, I.-D. Kim, Adv. Sci., 6 (2019) 1900250.

[174] X. Liu, M. Hu, M. Wang, Y. Song, N. Zhou, L. He, Z. Zhang, Biosens. Bioelectron., 123 (2019) 59-68.

[175] M. Gauthier, T.J. Carney, A. Grimaud, L. Giordano, N. Pour, H.-H. Chang, D.P. Fenning, S.F. Lux, O. Paschos, C. Bauer, F. Maglia, S. Lupart, P. Lamp, Y. Shao-Horn, J. Phys. Chem. Lett., 6 (2015) 4653-4672.

[176] M. Dahbi, N. Yabuuchi, M. Fukunishi, K. Kubota, K. Chihara, K. Tokiwa, X.-f. Yu, H. Ushiyama, K. Yamashita, J.-Y. Son, Y.-T. Cui, H. Oji, S. Komaba, Chem. Mater., 28 (2016) 1625-1635.

[177] Y. Li, K. Leung, Y. Qi, Accounts Chem. Res., 49 (2016) 2363-2370.

[178] M. Habibzadeh Mashatooki, J.J. Sardroodi, A.R. Ebrahimzadeh, J. Inorg. Organomet. Poly. Mater., 29 (2019) 1252-1264.

[179] Y. Yang, Y. Fu, H. Su, L. Mao, M. Chen, Biosens. Bioelectron., 122 (2018) 175-182.

[180] Y. Zhang, S. Luo, B. Situ, Z. Chai, B. Li, J. Liu, L. Zheng, Biosens. Bioelectron., 102 (2018) 568-573.

[181] L. Li, B. Han, Y. Wang, J. Zhao, Y. Cao, Biosens. Bioelectron., 145 (2019) 111714.

[182] A. Dutta Chowdhury, A.B. Ganganboina, Y.-c. Tsai, H.-c. Chiu, R.-a. Doong, Anal. Chim. Acta, 1027 (2018) 109-120.

[183] R. Elshafey, A.C. Tavares, M. Siaj, M. Zourob, Biosens. Bioelectron., 50 (2013) 143-149.

[184] M. Regiart, M.A. Fernández-Baldo, J. Villarroel-Rocha, G.A. Messina, F.A. Bertolino, K. Sapag, A.T. Timperman, J. Raba, Anal. Chim. Acta, 963 (2017) 83-92.

[185] D. Zhang, F. Ma, Q. Zhang, C.-y. Zhang, Chem. Commun., 53 (2017) 11496-11499.

[186] R. Li, H. Huang, L. Huang, Z. Lin, L. Guo, B. Qiu, G. Chen, Electrochimica Acta, 109 (2013) 233-237.

[187] K. Omidfar, M. Darzianiazizi, A. Ahmadi, M. Daneshpour, H. Shirazi, Sensor. Actuat. B-Chem., 220 (2015) 1311-1319.

[188] P. Gómez-Vilda, D. Palacios-Alonso, V. Rodellar-Biarge, A. Álvarez-Marquina, V. Nieto-Lluis, R. Martínez-Olalla, Neurocomputing, 255 (2017) 3-16.

[189] S. Muzerengi, H. Lewis, M. Edwards, E. Kipps, A. Bahl, P. Martinez-Martin, K.R. Chaudhuri, Aging Health, 2 (2006) 967-982.

[190] S. Przedborski, Parkinsonism & Related Disorders, 11 (2005) S3-S7.

[191] I. Pérez-Pi, D.A. Evans, M.H. Horrocks, N.T. Pham, K.S. Dolt, J. Koszela, T. Kunath, M. Auer, Anal. Chem., 91 (2019) 5582-5590.

[192] I. Horvath, I.A. Iashchishyn, L. Forsgren, L.A. Morozova-Roche, ACS Chem. Neurosci., 8 (2017) 1170-1176.

[193] N. Kruse, O.M. El-Agnaf, B. Mollenhauer, Bioanalysis, 9 (2017) 621-630.

[194] H. Watanabe, M. Ono, T. Ariyoshi, R. Katayanagi, H. Saji, ACS Chem. Neurosci., 8 (2017) 1656-1662.

[195] H. Gao, Z. Zhao, Z. He, H. Wang, M. Liu, Z. Hu, O. Cheng, Y. Yang, L. Zhu, ACS Chem. Neurosci., 10 (2019) 1204-1208.

[196] Y. An, X. Jiang, W. Bi, H. Chen, L. Jin, S. Zhang, C. Wang, W. Zhang, Biosens. Bioelectron., 32 (2012) 224-230.

[197] R.S. Akhtar, J.P. Licata, K.C. Luk, L.M. Shaw, J.Q. Trojanowski, V.M.Y. Lee, J. Neurochem., 145 (2018) 489-503.

[198] K. Sun, N. Xia, L. Zhao, K. Liu, W. Hou, L. Liu, Sensor. Actuat. B-Chem., 245 (2017) 87-94.

[199] A. Knöller, C.P. Lampa, F.v. Cube, T.H. Zeng, D.C. Bell, M.S. Dresselhaus, Z. Burghard, J. Bill, Sci. Rep-UK, 7 (2017) 40999.

[200] W. Li, C.-X. Yang, X.-P. Yan, Chem. Commun., 53 (2017) 11469-11471.

[201] D. Samanta, A. Sarkar, Chem. Soc. Rev., 40 (2011) 2567-2592.

[202] S. Liu, J. Bai, Y. Huo, B. Ning, Y. Peng, S. Li, D. Han, W. Kang, Z. Gao, Biosens. Bioelectron., 149 (2020) 111801.

[203] Y. Guo, J. Zhang, W. Zhang, D. Hu, Microchim. Acta, 186 (2019) 717.

[204] Z. Li, J. Wang, Y. Li, X. Liu, Q. Yuan, Mater. Chem.y Front., 2 (2018) 423-436.

[205] X. Ma, P. Kolla, R. Yang, Z. Wang, Y. Zhao, A.L. Smirnova, H. Fong, Electrochim. Acta, 236 (2017) 417-423.

[206] X. Xiao, C.-T. He, S. Zhao, J. Li, W. Lin, Z. Yuan, Q. Zhang, S. Wang, L. Dai, D. Yu, Energy Environ. Sci., 10 (2017) 893-899.

[207] R.R. Aysin, L.A. Leites, S.S. Bukalov, A.V. Zabula, R. West, Inorg. Chem., 55 (2016) 4698-4700.

[208] Y. Liu, B. Hu, S. Wu, M. Wang, Z. Zhang, B. Cui, L. He, M. Du, Appl. Catal. B-Environ., 258 (2019) 117970.

[209] J. Li, Q. Wang, K. Liu, J. Jiang, D. Qian, J. Li, Z. Chen, Materials Letters, 186 (2017) 189-192.

[210] X. Zhang, R. Liu, Y. Zang, G. Liu, G. Wang, Y. Zhang, H. Zhang, H. Zhao, Chem. Commun., 52 (2016) 5946-5949.

[211] Y.P. Zhu, T.Y. Ma, M. Jaroniec, S.Z. Qiao, Angew. Chem. Int. Edit., 56 (2017) 1324-1328.

[212] X. He, X. Li, H. Ma, J. Han, H. Zhang, C. Yu, N. Xiao, J. Qiu, J. Power Sources, 340 (2017) 183-191.

[213] M.-S. Yao, W.-X. Tang, G.-E. Wang, B. Nath, G. Xu, Adv. Mater., 28 (2016) 5229-5234.

[214] G. Li, X. Zhang, H. Zhang, C. Liao, G. Jiang, Appl. Catal. B-Environ., 249 (2019) 147-154.

[215] X. Guo, Y. Qing, Y. Wu, Q. Wu, Int. Biol. Macromol., 83 (2016) 117-125.

[216] K. Wang, B. Liu, Y. Cao, Y. Li, D. Jia, CrystEngComm, 20 (2018) 5191-5199.

[217] J.-M. Liu, Y.-Y. Liu, D.-D. Zhang, G.-Z. Fang, S. Wang, ACS Appl. Mater. Inter., 8 (2016) 29939-29949.

[218] T. Yang, J. Xu, L. Lu, X. Zhu, Y. Gao, H. Xing, Y. Yu, W. Ding, Z. Liu, J. Electroanal. Chem., 761 (2016) 118-124.

[219] Z. Zhang, C. Guo, S. Zhang, L. He, M. Wang, D. Peng, J. Tian, S. Fang, Biosens. Bioelectron., 89 (2017) 735-742.

[220] S. Bandeira, J. Gonzalez-Garcia, E. Pensa, T. Albrecht, R. Vilar, Angew. Chem. Int. Edit., 57 (2018) 310-313.

[221] J. Luo, Q. Ma, W. Wei, Y. Zhu, R. Liu, X. Liu, ACS Appl. Mater. Inter., 8 (2016) 21028-21038.

[222] K. Brince Paul, S. Kumar, S. Tripathy, S.R.K. Vanjari, V. Singh, S.G. Singh, Biosens. Bioelectron., 80 (2016) 39-46.

[223] M. Kaplan, T. Kilic, G. Guler, J. Mandli, A. Amine, M. Ozsoz, Biosens. Bioelectron., 92 (2017) 770-778.

[224] X. Zhao, Z. Wei, Z. Zhao, Y. Miao, Y. Qiu, W. Yang, X. Jia, Z. Liu, H. Hou, ACS Appl. Mater. Inter., 10 (2018) 6608-6617.

[225] L. Li, Y. Liang, Y. Zhao, Z. Chen, Sensor. Actuat. B-Chem., 262 (2018) 733-738.

[226] B.Y. Guan, L. Yu, X.W. Lou, Angew. Chem. Int. Edit., 56 (2017) 2386-2389.

[227] S.M. Taghdisi, N.M. Danesh, M.A. Nameghi, M. Ramezani, M. Alibolandi, M. Hassanzadeh-Khayat, A.S. Emrani, K. Abnous, Biosens. Bioelectron., 123 (2019) 14-18.

[228] J.V. Rushworth, A. Ahmed, H.H. Griffiths, N.M. Pollock, N.M. Hooper, P.A. Millner, Biosens. Bioelectron., 56 (2014) 83-90.

[229] Y. Zhou, H. Zhang, L. Liu, C. Li, Z. Chang, X. Zhu, B. Ye, M. Xu, Sci. Rep-UK, 6 (2016) 35186.

[230] A. Khatri, N. Punjabi, D. Ghosh, S.K. Maji, S. Mukherji, Sensor. Actuat. B-Chem., 255 (2018) 692-700.

List of pubulications

(1) **Chuanpan Guo**, Zhenzhen Li, Fenghe Duana, Zhihong Zhang*, Fabio Marchetti*, Miao Du*, Semiconducting Cu_xNi_{3-x}(hexahydroxytriphenylene)$_2$ framework for electrochemical aptasensing of C6 glioma cells and epidermal growth factor receptor, *J. Mater. Chem. B*, **2020**, *8*, 9951.

(2) **Chuanpan Guo**, Mengyao Hu, Zhenzhen Li, Fenghe Duana, Linghao He, Zhihong Zhang*, Fabio Marchetti*, Miao Du*, Structural hybridization of bimetallic zeolitic imidazolate framework (ZIF) nanosheets and carbon nanofibers for efficiently sensing α-synuclein oligomers, *Sensor. Actuat. B-Chem.*, **2020**, *309*, 127821.

(3) Riccardo Pettinari, Fabio Marchetti, Alessia Tombesi, Corrado Di Nicola, Claudio Pettinari, **Chuanpan Guo**, Zhihong Zhang, Agustín Galindo, Farzaneh Fadaei-Tirani, Mouna Hadiji, Paul J. Dyson, Arene-ruthenium(II) complexes with pyrazole-based ligands bearing a pyridine moiety: Synthesis, structure, DFT calculations, and cytotoxicity, *Inorg. Chim. Acta*, **2021**, *528*, 120610.

(4) **Chuanpan Guo**, Fenghe Duan, Shuai Zhang, Linghao He, Minghua Wang, Junli Chen, Jianqiang Zhang, Qiaojuan Jia, Zhihong Zhang*, Miao Du*, Heterostructured hybrids of metal–organic frameworks (MOFs) and covalent–organic frameworks (COFs), *J. Mater. Chem. A*, **2022**, *10*, 475-507.

(5) **Chuanpan Guo**, Fang Cheng, Gaolei Liang, Shuai Zhang, Qiaojuan Jia, Linghao He, Shuxia, Duan, Yingkun Fu, Zhihong Zhang*, Miao Du*, Copper-based polymer-metal–organic framework embedded with Ag nanoparticles: Long-acting and intelligent antibacterial activity and accelerated wound healing, *Chem. Eng. J.*, **2022**,

435, 134915.

Acknowledgements

First of all, I would like to extend my sincere gratitude to my supervisors, Prof. Zhihong Zhang and Prof. Fabio Marchetti, for their valuable suggestions on my thesis. Their critical way of thinking and intellectual rigor have impressed me and will exert have a profound influence on my future work. Meanwhile, during the past seven years, Prof. Zhihong Zhang also provide me with valuable suggestions about my life, which may benefit me in my whole life.

At the same time, I am also grateful to Prof. Riccardo Pettinari, Prof. Claudio Pettinari and Dr. Alessia Tombesi for providing me with valuable advice on my research.

I am also deeply indebted to all the other teachers and colleagues in Zhengzhou University of Light Industry for their direct and indirect help to me.

Special thanks should go to my friend, Lixia Yuan, who has accompanied me with encouragement and friendship.

Finally, I would like to thank my parents and husband for their continuous support and encouragement.